

120

A433699

HIGH ANGULAR RESOLUTION MICROWAVE SENSING  
WITH LARGE, SPARSE, RANDOM ARRAYS

Final Scientific Report

AIR FORCE OFFICE OF SCIENTIFIC RESEARCH  
AFOSR 82-0012



DTIC  
ELFC  
MARG 1984

A

UNIVERSITY of PENNSYLVANIA

VALLEY FORGE RESEARCH CENTER

THE MOORE SCHOOL OF ELECTRICAL ENGINEERING

PHILADELPHIA, PENNSYLVANIA 19174

DTIC FILE COPY

84 03 06 010

Approved for public release;  
distribution unlimited.

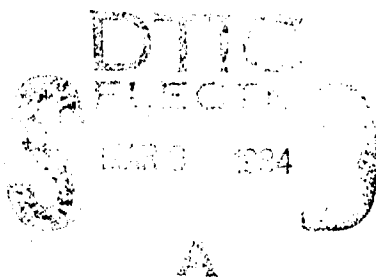
(12)  
November 1983

HIGH ANGULAR RESOLUTION MICROWAVE SENSING  
WITH LARGE, SPARSE, RANDOM ARRAYS

Final Scientific Report

AIR FORCE OFFICE OF SCIENTIFIC RESEARCH  
AFOSR 82-0012

Valley Forge Research Center  
The Moore School of Electrical Engineering  
University of Pennsylvania  
Philadelphia, Pennsylvania 19104



ABSTRACT

This document describes progress toward development of a general capability for high resolution microwave surveillance and imaging using large, sparse, self-cohering arrays. During the last five years progress has been made in the following areas: understanding of the unique advantages of large, self-cohering arrays; development of advanced system concepts, including the air-borne radio camera; enhanced self-cohering capability and experimental demonstration of that capability; and development of techniques for improving microwave image quality, including handling of the high sidelobes associated with very sparse arrays. A number of other practical issues associated with large self-cohering arrays have also been examined.

AIR FORCE OFFICE OF SCIENTIFIC RESEARCH (AFSC)  
NOTICE OF TRANSMITTAL TO DTIC  
This technical report has been reviewed and is  
approved for public release IAW AFR 190-12.  
Distribution is unlimited.  
MATTHEW J. KERNER  
Chief, Technical Information Division

**UNCLASSIFIED**

SECURITY CLASSIFICATION OF THIS PAGE (When Data Entered)

Unclassified

REPORT DOCUMENTATION PAGE		READ INSTRUCTIONS BEFORE COMPLETING FORM
1. REPORT NUMBER <b>AFOSR-TR- 84-0140</b>	2. GOVT ACCESSION NO. <i>AD-A133711</i>	3. RECIPIENT'S CATALOG NUMBER
4. TITLE (and Subtitle) <b>HIGH ANGULAR RESOLUTION MICROWAVE SENSING WITH LARGE, SPARSE, RANDOM ARRAYS</b>		5. TYPE OF REPORT & PERIOD COVERED <b>FINAL REPORT 01 OCT 81 - 30 SEP 83</b>
		6. PERFORMING ORG. REPORT NUMBER
7. AUTHOR(s) <b>C. N. Dorny</b>		8. CONTRACT OR GRANT NUMBER(s) <b>AFOSR-82-0012</b>
9. PERFORMING ORGANIZATION NAME AND ADDRESS <b>University of Pennsylvania Philadelphia, Pa. 19104</b>		10. PROGRAM ELEMENT, PROJECT, TASK AREA & WORK UNIT NUMBERS <b>2305/B1 61102F</b>
11. CONTROLLING OFFICE NAME AND ADDRESS <b>Air Force Office of Scientific Research / NE Building 410 Bolling AFB, DC 20332</b>		12. REPORT DATE <b>Nov 1983</b>
14. MONITORING AGENCY NAME & ADDRESS (if different from Controlling Office)		13. NUMBER OF PAGES <b>239</b>
		15. SECURITY CLASS. (of this report) <b>Unclassified</b>
		15a. DECLASSIFICATION/DOWNGRADING SCHEDULE
16. DISTRIBUTION STATEMENT (of this Report)  <b>Approved for public release; distribution unlimited.</b>		
17. DISTRIBUTION STATEMENT (of the abstract entered in Block 20, if different from Report)		
18. SUPPLEMENTARY NOTES		
19. KEY WORDS (Continue on reverse side if necessary and identify by block number)		
20. ABSTRACT (Continue on reverse side if necessary and identify by block number) <b>This document describes progress toward development of a general capability for high resolution microwave surveillance and imaging using large, sparse, self-cohering arrays. During the last five years progress has been made in the following areas: understanding of the unique advantages of large, self-cohering arrays; development of advanced system concepts, including the air-borne radio camera; enhanced self-cohering capability and experimental demonstration of that capability; and development of techniques for improving microwave image quality, including</b>		

Unclassified

SECURITY CLASSIFICATION OF THIS PAGE(When Data Entered)

20.

handling of the high sidelobes associated with very sparse arrays. A number of other practical issues associated with large self-cohering arrays have also been examined.

UNCLASSIFIED

SECURITY CLASSIFICATION OF THIS PAGE(When Data Entered)

# TABLE OF CONTENTS

	<u>Page</u>
Research Objectives	1
Summary of Research Effort	1
Advantages of Large Self-Cohering Arrays	2
Development of Advanced System Concepts	3
Enhanced Self-Cohering Capability and Experimental Testing	5
Interference Rejection in Self-Cohering Arrays	7
Enhanced Image Quality With Sparse Arrays	9
References	11
Publications	14
Professional Personnel	16
Interactions	17
Appendices:	
Ground-Based Radio Camera	A-1
Airborne Radio Camera	B-1
Space Based Large Array Radar	C-1
Forward-Looking Synthetic Aperture Radar	D-1
Enhanced Self-Cohering Capability and Experimental Testing	E-1
Interference Cancellation in Self-Cohering Arrays	F-1
Enhanced Image Quality with Sparse Arrays	G-1



HIGH ANGULAR RESOLUTION MICROWAVE SENSING  
WITH LARGE, SPARSE, RANDOM ARRAYS

## RESEARCH OBJECTIVES

The long-term objective of this research program was the development of a general capability for high resolution microwave surveillance and imaging. Fundamental to such a general capability is the ability to cohere large, poorly surveyed, possible flexing microwave arrays. Some form of adaptivity, referred to in this document as self-cohering, is required in order to form high quality beams with such arrays.

The specific objectives of the program were:

1. To expand understanding of self-cohering arrays in a broad range of applications.
2. To understand the effects of multipath and other propagation phenomena on the operation of large, self-cohering arrays; to devise system concepts for minimizing the degrading effects of such propagation irregularities.
3. To understand the effects of jamming and other interference phenomena on the operation of large, self-cohering arrays; to devise system concepts for minimizing the degrading effect of these interference phenomena.
4. To devise spatial and temporal signal processing techniques which optimize the beam characteristics of large, self-cohering arrays in the presence of noise, interference, multipath, and other degrading phenomena.
5. To design and perform experiments to test the models, system concepts, and theories developed in 1 through 4.

## SUMMARY OF THE RESEARCH EFFORT

Prior to the initiation of AFOSR support, two techniques for self-cohering were developed which use information external to the array (beacon signals or target reflections) to aid in beamforming. Both of these self-cohering concepts had been verified experimentally (at L-band) at our Valley Forge Research Center test range. We refer to these two techniques as (1) adaptive beamforming and scanning (suitable for narrow-angle "telephoto" imaging) and (2) self-survey (suitable for wide angle surveillance and imaging).

During the five years of support by AFOSR, program effort was focused on enhancing self-cohering capability, development of spread spectrum and nulling techniques for reducing the effects of interference on self-cohering of real and synthetic apertures, modelling the effects of multipath on self-cohered beams and experimental verification of these models, on the development of advanced system concepts (ground-based, airborne, and space-based radio cameras and forward-looking synthetic aperture radar), on refinement of our self-cohering techniques compatible with those system concepts, on hardware testing of self-cohering techniques and experimental imaging, and on the development of methods for enhancing the quality of microwave images obtained through large, sparse arrays. The results are summarized below. Many of the significant results are described in some detail in the Appendices.

#### ADVANTAGES OF LARGE SELF-COHERING ARRAYS

During the period of this AFOSR grant, study of the applicability and advantages of large self-cohering arrays for a broad range of applications has discovered the following potential advantages associated with those arrays:

1. Improvement in the range/power trade off in radar and communications as a result of the high power-aperture product (owing to large size).
2. Improvement in resolution and tracking (or pointing) accuracy owing to small beamwidth associated with large arrays.
3. Lowered probability of intercept and improved interference rejection in communications, direction finding, and radar owing to the small beamwidth associated with large arrays, and owing to the high degree of null control associated with individual-element phase control. Adaptively placed nulls can track moving interferers and ease sidelobe level requirements.
4. Extension of the capability for high resolution searching and imaging in either monostatic or bistatic operation. The technology for self-cohering of large arrays complements the imaging capability of conventional synthetic aperture radar (SAR) in two ways:
  - a. It loosens the restriction associated with conventional SAR; specifically, it provides for:
    1. Variable, loose-tolerance flight paths by means of adaptive signal processing.

- ii. Reduced data rate through aperiodic data thinning.
- iii. Reduced effects of propagation anomalies through use of adaptive signal processing.
- iv. Improved RFI suppression through adaptive signal processing.
- b. It provides a real-aperture alternative to SAR for high-resolution imaging.
  - i. No platform motion is required.
  - ii. Arbitrary array configuration is permitted owing to individual-element phase control.
  - iii. Tolerances are looser than conventional because of the adaptive signal processing.
  - iv. Aperiodic or random thinning of large arrays provides greater frugality than conventional large filled arrays.
  - v. Scanning is by sector (angle) as in conventional radar, rather than strip mapping as in conventional SAR.

#### DEVELOPMENT OF ADVANCED SYSTEM CONCEPTS

##### Ground-based Radio Camera

The articles in Appendix A describe design concepts for a ground-based radio camera. The system includes a single transmitting antenna and a separate, 1024 element two-dimensional receiving array spread over a region approximately 300 meters in diameter. The array is divided into 32 clusters in order to achieve significant sharing of processing and associated reductions in cost. The particular system proposed is designed to operate over 20° sector in horizontal and vertical planes which would intercept the approach flight pattern normally used by aircraft going into Philadelphia International Airport. The system would be capable of imaging an entire 15 meter aircraft at a 10 km range. A modified version of this ground-based radio camera is currently being developed for the purpose of imaging ground vehicles and tracking high-speed missile trajectories, under sponsorship of the Army Research Office and White Sands Missile Range [1].

##### Airborne Radio Camera

Reference [2] (See Appendix B, pp. B1 - B20) discusses the potential value of distributing a microwave antenna throughout the airframe of the aircraft. It shows that the increased antenna aperture can enormously increase the power-aperture product. Consequently, an aircraft-size aperture

will permit significantly increased detection range or, alternatively, a reduction in transmitter power at conventional range, thereby lowering the probability of intercept. Other potential values of the distributed airborne array concept result from the significantly reduced beamwidth associated with the large aperture. Specifically, the angular resolution is improved and jammer suppression is more effective in directions near the direction of the target.

A critical problem with the airborne array lies in the synchronization of the flexing aperture. Several approaches to synchronization of an airborne flexing array have been developed [4]. These techniques use doppler filters and range gates to isolate radar returns from relatively small ground or sea clutter patches. The returns are treated as beacon signals. The simplest technique permits "telephoto" imaging in the direction toward the designated clutter patch. This technique was successfully tested experimentally using airborne radar data obtained from the Naval Research Laboratory [5]. This simple technique fails, however, for an aircraft which flies over water at high sea states. This high-sea-state case is treated in [5] and [6] (under ONR sponsorship).

#### Space-Based Large Array Radar

Because of the success of the design for the airborne radio camera, some preliminary concept work has been done on the application of these techniques to space radar. One concept has been developed in which a huge (100 km) geosynchronous-altitude phased array is created from radar receivers, each on a separate vehicle. The transmitter is in a low orbiting space vehicle. The system is bistatic. The "cloud" of receivers self-synchronizes on the back radiation from the low-orbiting transmitter, the dish of which is pointing toward the ground. Data links from receivers to the ground station permit the ground facility to organize multiple receive beams that follow the transmitter. A cross range resolution of 10 to 100 meters should be achievable on the earth's surface with such a system. The proposed concept, shown in Appendix C, is under discussion with Rome Air Development Center and with NASA.

### Forward-Looking Synthetic Aperture Radar

Another potential application of large self-cohering arrays is in forward-looking synthetic aperture radar (see Appendix D). Such a system could employ a weaving motion of an airborne platform to form the synthetic aperture. The concept extends to a large, multi-platform forward-looking synthetic aperture radar such as might be formed by a number of cruise missiles. Initial analysis of such a system suggests that for a single subsonic platform a cross range resolution in the order of 0.1 meter to 1 meter may be practical at a range of 10 km. Such a system might find application in terrain following or imaging at microwave frequencies. Data thinning, for the purpose for reducing the load on a real-time signal processor, would raise the average sidelobe level to -30 dB relative to the main lobe. The peak sidelobe could be as much as 10 dB higher than the average sidelobe level. The sidelobe level can be reduced by increasing the data rate or by one of the sidelobe reduction techniques described in Appendix G. A detailed system analysis has not been performed.

### ENHANCED SELF-COHERING CAPABILITY AND EXPERIMENTAL TESTING

The papers in Appendix E describe a number of techniques for self-cohering of large distorted arrays. Reference [7] describes an algorithm for cohering a radio camera and presents experimental results for a 3 cm wavelength demonstration system using a distorted 27 m random sparse array. The measured beamwidth of 1 m<sup>r</sup> conformed to the theory, confirming the validity of the technique. When the physical distortion of an array is not known a priori, the self-cohering process must be based upon phase front measurements of the radiation from a source external to the array. The ideal adaptive synchronizing source is a point source radiating in free space. The phase fronts of realistic sources are perturbed, however. Reference [8] presents three types of practical sources and calculates conditions under which their radiation fields are acceptable for adaptive beamforming. The three sources are the passive reflector, the active beacon, and radar ground clutter. Multipath and scattering of the energy radiated from a beacon or target induce phase front distortions at the array. Reference [9] describes the effect

of these phase front distortions on the adaptive beamforming procedure. It derives a simple relationship among the loss in gain of the adaptively focused array, the strength  $S$  of the scattered field relative to the direct field, and a spatial correlation function  $\rho(\theta)$  associated with the scattering process, where  $\theta$  is the scanning angle. The article describes a series of experiments which appear to vindicate the theory and then uses the theory to determine the degradation and radio camera scanning performance for several important cases of interference caused by reflections. Reference [10] describes a two-dimensional (range-angle) radio camera imaging experiment. A 39 m, X-band (3 cm wavelength) array was formed by a cable strung between two towers, each 10 m high, on a hill. A pulsed microwave transmitter, on the hilltop, illuminated the vicinity of Phoenixville, Pennsylvania, from 7 km distance. As the receiver was moved along the cable, echoes were recorded at random positions. The time-shared receiving array was badly distorted as well as time-varying. Yet the radio camera processing produced nearly diffraction limited images of 3 city blocks at a distance of 6.5 km in the town, and details of a power plant at a distance of 8.2 km. The use of two different pilot signals or beamforming sources for the self synchronization process is demonstrated. One source is a corner reflector located in the town; the other is a target of opportunity located in the vicinity of the town.

The paragraphs mentioned above all describe work related to adaptive beamforming of a receive only array. In reference [11] the means is described for self organizing a non-rigid, distributed, transmit-receive antenna array for use in airborne radar; the techniques are applicable to ground base or shipboard radar as well. Methods are described for initializing the array using various primary microwave illuminators.

References [12-13] describe a phase multilateration technique for self cohering of antenna arrays which is suitable for systems which are to be used for wide angle surveillance and imaging. Two approaches to resolving the phase ambiguity associated with phase multilateration are described in [14] and the probability of ambiguity error is derived for each approach. For the minimum least square error method an efficient computational technique is introduced which permits element position uncertainties as large as one wavelength in the presence of phase measurement errors in the order of 1 radian. The multiple

frequency method permits element position uncertainties significantly larger than 1 wavelength; the probability of ambiguity error is shown to be acceptably small if the RMS phase measurement errors are in the order of 0.5  $\lambda$  or smaller.

In reference [15] the phase multilateration concept is generalized in order to permit locating the elements of a flexible phased array sufficiently accurately to form high quality beams without the accurate beacon location knowledge which is characteristic of radio navigation schemes. The effects of phase measurement errors and baseline measurement errors on array beam gain and pointing error are shown to be reasonably small for beam pointing directions within the spread of the beacons. The general self-survey technique is extended to near-field synthetic aperture systems in [16]. The article introduces a modification that resolves the mod  $2\pi$  ambiguity associated with phase multilateration, and shows that the self-survey technique can be used for bistatic (receive only) and monostatic (transmit-receive) systems. The validity of the technique is demonstrated by experimental self-survey and imaging with a 27 m synthetic aperture X-band (3 cm) system.

A recent study of very large arrays, arrays with aperture comparable in size to the target range, has shown ultimate limits to the resolution achievable by aperture size. The study has focused attention on the special features of very-near-field imaging. A new approach to imaging in the very-near-field has been developed. The ideas will be tested experimentally with radar data presently being taken under ARO sponsorship. This work will be presented in QPR 44 of the Valley Forge Research Center.

Kisliuk [17] (see Appendix E, pp. E113-E118) has developed techniques for flush mounting of wide band conformal antenna elements. Experimental development of these elements is continuing.

#### INTERFERENCE REJECTION IN SELF COHERING ARRAYS

Both the adaptive beamforming (narrow field of view) and self survey (wide angle) techniques for self cohering of large non-rigid antenna arrays make use of beacon signals or target reflections, as seen at the antenna elements, to aid in beamforming. Interference

can reduce or destroy the ability of the adaptive system to self cohere by use of these signals. Thus, the interference must be cancelled locally at each array element (each phase measurement point). Reference [18] introduces and analyzes three cancellation schemes which meet the local cancellation requirement for self cohering:

- 1) An element pairing approach; this approach is suitable only if the interference amplitudes are balanced at the pair inputs.
- 2) An approach which injects a signal at each element to cancel the interference; this approach is suitable only if the interference does not turn off during the instant the beacon signal phases are measured.
- 3) An approach which controls the radiation pattern of the elements (subarrays); this approach is the most versatile and promising of the three methods but requires the most hardware.

In a self cohering system the desired signals (target reflections) are under operator control. Therefore, two cancellation procedures are possible. In one procedure the system nulls the interference in the absence of target returns by minimizing the mean square of the interfering signal power at the output. After nulling, the system can observe interference-free target returns. In the other procedure, the least-mean-square algorithm minimizes the interfering signal while the imaging system is in operation; the interference cancellation is achieved in the presence of both the desired and interfering signals by utilizing the power inversion property of the canceller. The second procedure performs better only if the directions of arrival of the desired signal and the interference are closer than a bound which depends on the noise-to-desired-signal power ratio. The usual way of obtaining the reference signal required by the LMS algorithm is through a reference signal loop. The resulting phase shift of the reference signal relative to the desired signal is known to cause weight cycling and frequency distortion. A method for compensating for this phase shift is described and demonstrated by simulation in [19] (See Appendix F, pp. F1-F9).

Phase locked loops play an important role in nulling systems. Reference [20] introduces a new phase locked loop (PLL). It is superior to standard PLL's in both tracking and acquisition. The new PLL uses two phase detectors simultaneously.

Nulling of a wide-band interfering signal requires wide-band instantaneous frequency measurements, a continuously controllable delay line, and a wide-band bilinear correlator. These components are difficult to implement using standard hardware. Reference [21] describes a SAW time inversion device which, together with a SAW convolver, will provide the wide-band correlator. The voltage-controlled SAW delay line is described and analyzed in [22]. Reference [23] discusses the use of SAW devices for wide-band instantaneous frequency measurement.

#### ENHANCED IMAGE QUALITY WITH SPARSE ARRAYS

A very large array must be very sparse in order that it not be prohibitively expensive. A number of techniques have been developed to overcome the poor sidelobe properties associated with very sparse arrays. Reference [24] introduces a sequential nulling technique which, according to computer simulation results, is capable of accurately imaging target points with dynamic range greater than the average sidelobe level of the array (See Appendix G, pp. G1-G25). First, the direction of the peak of the conventional array output is determined. It is the first (strongest) estimated target direction. The target amplitude and phase are also determined. In the second scan, a null is fixed in that estimated strong-target direction while scanning the main beam across the scene. The second strongest target is determined from the second scan. In the third scan, two nulls are fixed in the directions of the two largest targets. By performing the nulling technique repeatedly, a sequence of estimated targets is determined. The technique stops when the array output (the total energy in the remaining image) is sufficiently small to indicate that all targets have been nulled. Computer simulations show that the technique has good noise tolerance and, if combined with adaptive beamforming, also has good element position

tolerance. The technique is now being applied to real radar data. The work will be submitted to the IEEE Transactions on Antennas and Propagation.

A second method [25] modifies the "clean" technique of radio astronomy to process complex images rather than real images. This method uses target subtraction rather than target nulling. Thresholds have been derived which determine when to stop the iterative process. The work will be submitted to the IEEE Transactions on Antennas and Propagation.

Image artifacts, due to high sidelobes, change their locations from image to image if the element positions are altered or the operating frequency is changed. Superimposing or averaging images tends to build up stable, correct portions of an image, while reducing, by smoothing, the image artifacts. In principle, all the sidelobe crests can be reduced to the average background level and all the troughs in the side radiation pattern will rise to this level. This theory is presented in [26] (See Appendix G, pp. G26-G34). Steinberg [27] relates the work of [26] to other diversity-based techniques which have been developed under ARO and ONR sponsorship at the Valley Forge Research Center.

## REFERENCES

- [1] "High Resolution Radar System for White Sands Missile Range", Report UP-VFRC-30-82, University of Pennsylvania, Philadelphia, PA.
- [2] B.D. Steinberg and Eli Yadin, "Distributed Airborne Array Concepts", IEEE Trans. Aerospace & Elec. Syst., Vol. AES-19, No. 2, March 1982, pp. 219-227. (See Appendix B, pp. B1-B9.)
- [3] B.D. Steinberg and Eli Yadin, "Self-cohering An Airborne Radio Camera," IEEE Trans. on Aerospace & Elec. Syst., Vol. AES-19, No. 3, May 1983, pp. 483-490. (See Appendix B, pp. B10-B17.)
- [4] Eu-Anne Lee, Report UP-VFRC-30-81, "A Generalized Self-Survey Technique for Self-cohering of a Large Array", Doctoral Dissertation in Electrical Engineering, University of Pennsylvania, 1981.
- [5] B.D. Steinberg and Eli Yadin, "Radio Camera Experiment with Airborne Radar Data", Proc. IEEE, Vol. 70, No. 1, January 1982, pp. 96-98. (See Appendix B, B18-B20.)
- [6] Eli Yadin, Report UP-VFRC-35-81, "Phase Synchronizing Distributed, Adaptive Airborne Antenna Arrays", Doctoral Dissertation in Systems Engineering, University of Pennsylvania, 1981.
- [7] B.D. Steinberg, "Radar Imaging From a Distorted Array: The Radio Camera Algorithm and Experiments", IEEE Trans. on Antennas & Propagation, Vol. AP-29, No. 5, September 1981, pp. 740-748. (See Appendix E, pp. E1-E9.)
- [8] B.D. Steinberg, "Properties of Phase Synchronizing Sources for a Radio Camera", IEEE Trans. on Antennas & Propagation, Vol. AP-30, No. 6, November 1982, pp. 1086-1092. (See Appendix E, pp. E10-E16.)
- [9] B.D. Steinberg and Eli Yadin, "Effect of Multipath and Scattering on Array Gain of a Large Adaptive Beamforming Phased Array", submitted for publication to the IEEE Trans. on Antennas & Propagation, November 1983. (See Appendix E, pp. E17-E38.)
- [10] B.D. Steinberg, William Whistler and Donald Carlson, "Two-dimensional Imaging with a Radio Camera", Proc. of IEEE, Vol. 71, No. 1, November 1983, pp. 1325-1326 (See Appendix E, pp. E39-E40.)
- [11] B.D. Steinberg, "Phase Synchronizing a Non-rigid Distributed Transmit-Receive Radar Antenna Array", IEEE Trans. on Aerospace and Electronic Systems, Vol. AES-18, No. 5, September 1982, pp. 609-620. (See Appendix E, pp. E41-E52.)
- [12] C.N. Dorny, "A Self Survey Technique for Self-cohering of Antenna Systems", IEEE Trans. on Antennas & Propagation, November 1978, pp. 877-881.

- [13] C.N. Dorny and Bernard S. Meagher, Jr., "Cohering of an Experimental Non-rigid Array By Self Survey", IEEE Trans. on Antennas & Propagation, Vol. AP-28, No. 6, November 1980, pp. 902-904.
- [14] Chung H. Lu and C.N. Dorny, "Ambiguity Resolution in Self-cohering Arrays", submitted to IEEE Trans. on Antennas & Propagation, July 1983. (See Appendix E, pp. E53-E71.)
- [15] Eu-Anne Lee and C.N. Dorny, "A Generalized Self Survey Technique for Self-cohering of Large Arrays", submitted to IEEE Trans. on Antennas & Propagation, August 1983. (See Appendix E, pp. E72-E100.)
- [16] C. N. Dorny and Tian-hu Lei, "Synthetic Aperture Near-field Self Survey," To be submitted to IEEE Trans. on Antennas & Propagation. (See Appendix E, pp. E101-E112.)
- [17] Moshe Kisliuk, "Lossy Transmission Line Model of a Microstrip Slot Antenna", Valley Forge Research Center QPR 43, University of Pennsylvania, September 1983, pp. 76-81. (See Appendix E, pp. E113-E118.)
- [18] Chung H. Lu, "Interference Cancellation in Self-cohering Arrays", UP-VFRC-18-80, Ph.D. dissertation, University of Pennsylvania, October 1980. In preparation for submission to IEEE Trans. on Aerospace and Electronic Systems.
- [19] Y. Bar-Ness, "Eliminating the Reference Loop Phase Shift in an N-element Adaptive Array", Trans. on Aerospace & Electronic Systems, Vol. AES-18, No. 1, January 1982, pp. 115-123. (See Appendix F, pp. F1-F9.)
- [20] Arie Heiman and Y. Bar-Ness, "Optimal Design of a PLL With Two Separate Phase Detectors", IEEE Trans. on Communications, Vol. COM-29, No. 2, February 1981, pp. 92-100.
- [21] Hagit Messer and Y. Bar-Ness, "Distortion Estimation of SAW Time Inversion System Based on Function Approximation", IEEE Trans. on Sonics & Ultrasonics, Vol. SU-28, No. 6, November 1981, pp. 454-459. (See Appendix F, pp. F10-F15.)
- [22] Y. Bar-Ness and Hagit Messer, "A Unified Approach to the Design of Voltage Controlled SAW Delay Lines", Report UP-VFRC-1-80, University of Pennsylvania, August 1981. To be submitted to IEEE Trans. on Sonics & Ultrasonics.
- [23] Y. Bar-Ness and Hagit Messer, "Wideband Instantaneous Frequency Measurements (IFM) Using SAW Devices", Report UP-VFRC-22-80, University of Pennsylvania, November 1980. (See Appendix F, pp. F16-F19.)
- [24] Lih-Tyng Hwang and C.N. Dorny, "A Nulling Technique for Microwave Imaging with a Random Thinned Array", Valley Forge Research Center, QPR No. 42, pp. 92-108; QPR No. 43, pp. 68-75, University of Pennsylvania, Philadelphia, PA, 1983. (See Appendix G, pp. G1-G25.)

- [25] Jenho Tsao, "A Position Error Correction Algorithm and a Revised Clean Technique for Random Thinned Array Imaging Systems", Report UP-VFRC-39-83, Ph.D. Dissertation in Systems Engineering, University of Pennsylvania, 1983.
- [26] B.D. Steinberg and El-Sayed H. Attia, "Sidelobe Reduction of Random Arrays By Element Position and Frequency Diversity", IEEE Trans. on Antennas & Propagation, Vol. AP-31, No. 6, November 1983, pp. 922-930. (See Appendix G, pp. G26-G34.)
- [27] B. D. Steinberg, Microwave Imaging with Large Antenna Arrays: Radio Camera Principles and Techniques, John Wiley & Sons, New York, 1983, Chapter 3.

## PUBLICATIONS

### Resulting From AFOSR Support

B. D. Steinberg, "Radar Imaging From a Distorted Array: The Radio Camera Algorithm and Experiments," IEEE Trans. on Antennas & Propagation, Vol. AP-29, No. 5, September 1981, pp. 740-748.

Hagit Messer and Y. Bar-Ness, "Distortion Estimation of SAW Time Inversion System Based on Delta Function Approximation," IEEE Trans. on Sonics & Ultrasonics, Vol. SU-28, No. 6, November 1981, pp. 454-459.

B. D. Steinberg and Eli Yadin, "Radio Camera Experiment with Airborne Radar Data," Proc. IEEE, Vol. 70, No. 1, January 1982, pp. 96-98.

Y. Bar-Ness, "Eliminating the Reference Loop Phase Shift in an N-element Adaptive Array," Trans. on Aerospace & Electronic Systems, Vol. AES-18, No. 1, January 1982, pp. 115-123.

B. D. Steinberg and Eli Yadin, "Distributed Airborne Array Concepts", IEEE Trans. Aerospace & Elec. Syst., Vol. AES-19, No. 2, March 1982, pp. 219-227.

B. D. Steinberg, "Phase Synchronizing a Non-rigid Distributed Transmit-Receive Radar Antenna Array," IEEE Trans. on Aerospace and Electronic Systems, Vol. AES-18, No. 5, September 1982, pp. 609-620.

B. D. Steinberg, "Properties of Phase Synchronization Sources for a Radio Camera," IEEE Trans. on Antennas & Propagation, Vol. AP-30, No. 6, November 1982, pp. 1086-1092.

B. D. Steinberg and Eli Yadin, "Self-cohering An Airborne Radio Camera", IEEE Trans. on Aerospace & Elec. Syst., Vol. AES-19, No. 3, May 1983, pp. 483-490.

B. D. Steinberg and Eli Yadin, "Effect of Multipath and Scattering on Array Gain of a Large Adaptive Beamforming Phased Array," submitted for publication to the IEEE Trans. on Antennas & Propagation, November 1983.

B. D. Steinberg, William Whistler and Donald Carlson, "Two-dimensional Imaging with a Radio Camera," Proc. of IEEE, Vol. 71, No. 1, November 1983, pp. 1325-1326.

B. D. Steinberg, Microwave Imaging with Large Antenna Arrays: Radio Camera Principles and Techniques, John Wiley & Sons, New York, 1983.

SUBMITTED OR IN PREPARATION FOR PUBLICATION

Chung H. Lu and C. N. Dorny, "Ambiguity Resolution in Self-cohering Arrays," submitted to IEEE Trans. on Antennas & Propagation, July 1983.

Eu-Anne Lee and C. N. Dorny, "A Generalized Self Survey Technique for Self-cohering of Large Arrays," submitted to IEEE Trans. on Antennas & Propagation, August 1983.

C. N. Dorny and Tian-hu Lei, "Synthetic Aperture Near-field Self Survey," To be submitted to IEEE Trans. on Antennas & Propagation.

Chung, H. Lu and C. N. Dorny, "Interference Cancellation in Self Cohering Arrays," in preparation for submission to IEEE Trans. on Aerospace & Electronic Systems.

Y. Bar-Ness and Hagit Messer, "A Unified Approach to the Design of Voltage Controlled SAW Delay Lines," to be resubmitted to IEEE Trans. on Sonics & Ultrasonics.

Lih-Tyng Hwang and C. N. Dorny, "A Nulling Technique for Microwave Imaging with a Random Thinned Array," in preparation for submission to IEEE Trans. on Antennas & Propagation.

Jenho Tsao and B. D. Steinberg, "Revised Clean Technique for Random Thinned Array Imaging Systems," in preparation for submission to IEEE Trans. on Antennas & Propagation.

Moshe Kisliuk, "Flush Mounted Microstrip Slot Antennas," in preparation for submission to IEEE Trans. on Antennas & Propagation.

## PROFESSIONAL PERSONNEL

### Professors

C. Nelson Dorny  
Bernard D. Steinberg  
Raymond S. Berkowitz  
Fred Haber  
Yehekel Bar-Ness

### Ph.D. Candidates

Chung H. Lu, "Interference Cancellation in Self-Cohering Arrays,"  
Oct. 1980. Supervisor: C. N. Dorny.

Eu-Anne Lee, "A Generalized Self Survey Technique for Self Cohering  
of a Large Array," Aug. 1981. Supervisor: C. N. Dorny.

Eli Jadlovker/Yadin, "Phase Synchronizing Distributed Adaptive  
Airborne Antenna Arrays," Oct. 1981. Supervisor: B. D. Steinberg.

Ajay K. Luthra, "Maximum Entropy Method in the Space-Angle Domain  
and a New Technique with Superior Performance," Nov. 1981. Super-  
visor: B. D. Steinberg.

Lawrence R. Burgess, "Design Constraints on a Realization of Adaptive  
Nulling Arrays," Nov. 1981. Supervisor: R. S. Berkowitz.

Paul Yeh, "Hybrid Adaptive Array Processing Utilizing Directional  
Constraints and Signal Structure," Aug. 1983. Supervisor: Fred Haber.

Jenho Tsao, "A Position Error Correction Algorithm and a Revised  
Clean Technique for Random Thinned Array Imaging Systems," Dec. 1983.  
Supervisor: B. D. Steinberg.

Lih-Tyng Hwang, "A Nulling Technique for Microwave Imaging with a  
Sparse Random Array." Expected completion date, May 1984. Supervisor:  
C. N. Dorny.

Shauh-teh Juang, "High Resolution Imaging Array Radar Techniques."  
Expected completion date, Aug. 1984. Supervisor: R. S. Berkowitz.

Tian-hu Lei, "High Resolution Imaging in the Very Near-field." Expected  
completion date, Aug. 1984. Supervisor: C. N. Dorny.

Hashem Attia, "Diversity Techniques For Sidelobe Reduction." Expected  
completion date, May 1984. Supervisor: B. D. Steinberg.

Geoffrey S. Edelson, "Diversity Techniques for Image Quality Improvement."  
Expected completion date, Aug. 1984. Supervisor: B. D. Steinberg.

### M.S.E. Candidates

Elliott Melnick, "Sidelobe Reduction Using Position and Frequency Diversity in the Random Array," Dec. 1980. Supervisor: B. D. Steinberg.

Kapil Jain, Judith Herman, James Spiegal, Marc DonVito, Dogan Tibet, Deyuan Ho.

### Research Specialists

Earl N. Powers, William Whistler, Donald Carlson.

### Visiting Scholars

Tong L. Lim, Ph.D.  
Rong Sheng Ni  
Wei Xen Xie  
Yun Long Zhang  
Hong Yuan Chen

### INTERACTIONS

De Yuan Ho and Bernard D. Steinberg, "An Array Thinning Technique," IEEE/APS Symposium and URSI Meeting, Seattle, Washington, June 1979.

Bernard D. Steinberg, "First Experimental Results from the Valley Forge Radio Camera Program," IEEE/APS Symposium and URSI Meeting, Seattle, Washington, June 1979.

C. N. Dorny and Eu-Anne Lee, "Array Self-cohering with Loosened Beacon Requirements," 22nd Midwest Symposium on Circuits and Systems, Philadelphia, Pennsylvania, June 1979. (Published in symposium proceedings.)

Raymond S. Berkowitz and Earl N. Powers, "Evaluation and Performance Prediction for a Thin Adaptive Synthetic Array Radio Camera," 2nd International Conference on Information Sciences and Systems, Patras, Greece, July 1979.

Bernard D. Steinberg, "Antenna Arrays for High Power Microwave Transmission," High Power Microwave Technology Working Group, Los Alamos Scientific Laboratory, Los Alamos, New Mexico, August 1979.

Bernard D. Steinberg, "Radio Camera, A Device for Microwave Imaging," IEEE MTT/AP-S Meeting, Philadelphia, Pennsylvania, September 1979.

H. Messer and Y. Bar-Ness, "Different Time Inversion Methods Using SAW Devices," Proceedings of the 11th Convention of the IEEE in Israel, Tel Aviv, Israel, October 1979.

A. Heiman and Y. Bar-Ness, "Optimal Design of PLL with Two Separate Phase Detectors," Proceedings of the National Telecommunication Conference, Washington, D. C., November 1979.

C. N. Dorny, "Large Self-cohering Antenna Arrays," USNC/URSI National Radio Science Meeting, Boulder, Colorado, November 1979.

Fred Haber, "Random Array as a Radio Relay," Stevens Institute of Technology, Hoboken, New Jersey, November 1979.

Bernard D. Steinberg, "High Resolution Microwave Imaging Based on Adaptive Beamforming," RCA Digital Beamforming Symposium, Princeton, New Jersey, February 1980.

Bernard D. Steinberg, "High Angular Microwave Resolution from Distorted Arrays," Society of Photo-Optical Instrumentation Engineers Technical Symposium East, Washington, D. C., April 1980. Published in SPIE Symposium Proceedings.

Ajay K. Luthra, "Single and Multiple Snapshot Maximum Entropy Image of Two Narrowband Point Sources," presented at Naval Research Laboratory Workshop on "Uncertainty Characterization: Theory and Application," Washington, D. C., May 1, 1980.

Bernard D. Steinberg, "Adaptive Signal Processing," presented at Naval Research Laboratory Workshop on "Uncertainty Characterization: Theory and Application," Washington, D. C., May 1, 1980.

Bernard D. Steinberg, "Overcoming Large Phased-Array Problems by Self-cohering Techniques," Phased Array Technology Workshop, Naval Research Laboratory, September 9-10, 1980.

Yeheskel Bar-Ness, "Phase Locked Loops (PLL): New Results and Future Research," ONR Electronic Systems Theory Program Seminar, Naval Research Laboratory, September 29, 1980.

Ajay K. Luthra, "Thinned Adaptive Radio Camera Program at VFRC," presented at University College, University of London, London, England, October 7, 1980.

Ajay K. Luthra, "Non-Linear Superresolution Techniques: Maximum Entropy Method and Prony's Method," presented at University College, University of London, October 14, 1980.

Yeheskel Bar-Ness and Hagit Messer, "Wideband Instantaneous Frequency Measurements (IFM) Using SAW Devices," 1980 Ultrasonic Symposium, Boston, MA, November 4, 1980.

Bernard D. Steinberg and Ajay K. Luthra, "Distortions in Source Estimation Due to Asymmetrical Aperture Weighting When Imaging in the Near-Field," Presented at Society of Engineering Science 17th Annual Meeting, Atlanta, GA, 16 December 1980.

Bernard D. Steinberg, "Use of a Reference Source, and its Required Properties, When Imaging with Severely Distorted Scattered-Field Measurements," (invited paper), presented at Society of Engineering Science 17th Annual Meeting, Georgia Institute of Technology, Atlanta, GA, 16 December 1980.

Bernard D. Steinberg and Eli Jadlovker, "Distributed Airborne Array Concepts," presented at National Radio Science Meeting, Session G-1, Jan. 1981, Boulder, Colorado.

W. Whistler, D. Carlson and B. D. Steinberg, "Imaging Experiments with Random, Thinned, Distorted Arrays at Valley Forge Research Center," IEEE AP/MTT-S, Benjamin Franklin Symposium on Advances in Antenna and Microwave Technology, May 16, 1981.

B. D. Steinberg and A. K. Luthra, "A Simple Theory of the Effects of Medium Turbulence Upon Scanning with an Adaptive Phased Array," presented at the International Symposium on Underwater Acoustics, Tel Aviv University, Tel Aviv, Israel, June 15-18, 1981.

Y. Bar-Ness and J. Rokah, "Cross-Coupled Boot-Strapped Interference Canceler," 1981 International Symposium on Antennas and Propagation, Los Angeles, CA, June 16-19, 1981.

Bernard D. Steinberg, "Adaptive Microwave Holography," presented at the Congress and Twelfth Assumbly of the International Commission for Optics, Aug. 31 to Sept. 5, 1981, Graz, Austria.

B. D. Steinberg, "Microwave Holography and the Radio Camera," National Radio Science Meeting, Ursi, Boulder, Colorado, 13-15 January 1982.

A. K. Luthra, "Super Resolution Techniques With Performance Better Than Maximum Entropy Method," National Radio Science Meeting, Ursi, Boulder, Colorado, 13-15 January 1982.

B. D. Steinberg, W. Whistler, D. Carlson, and E. Yadin-Yadin-Jadlovker, "Two Recent Radio Camera Experiments," Benjamin Franklin 1982 Symposium on Advances and Antenna and Microwave Technology, Philadelphia, PA, 15 May 1982.

E. H. Attia, "Sidelobe Reduction of Random Arrays by Element Position Diversity," University College, London, June 14, 1982.

E. H. Attia, "The Giant Radio Camera Project of VERC," University College, London, June 16, 1982.

B. D. Steinberg, "High Resolution Microwave Imaging From Distorted Phased Arrays," University College London, 25 Oct. 1982.

B. D. Steinberg, W. Whistler, and E. Yadin, "High Resolution Microwave Imaging Radar for White Sands Missile Range," Microwave Imaging Radar Workshop, El Paso, Texas, 4 January 1983.

B. D. Steinberg and E. Yadin, "Array Properties for High Resolution Microwave Imaging Radar," Microwave Imaging Radar Workshop, El Paso, Texas, 5 January 1983.

B. D. Steinberg, "Phase Synchronization of Distorted Imaging Antenna Arrays," Optical Society Winter '83 Topical Meeting on Signal Recovery and Synthesis with Incomplete Information and Partial Constraints, Lake Tahoe, Nevada, 12-14 January 1983.

B. D. Steinberg, "Microwave Imaging with Adaptive Antenna," Drexel University, Philadelphia, PA, 23 Feb. 1983.

B. D. Steinberg and E. H. Attia, "Reduction of Random Array Sidelobes by Diversity Techniques," Third Annual Benjamin Franklin Symposium on Advances in Antenna and Microwave Technology, Philadelphia, PA, April 30, 1983.

B. D. Steinberg and J. Tsao, "A New Method for Cohering Large Antenna Array Systems," Third Annual Benjamin Franklin Symposium on Advances in Antenna and Microwave Technology, Philadelphia, PA, April 30, 1983.

R. S. Berkowitz and S. T. Juang, "Mean and Variance of Far-Field Power Pattern of Periodic and Random Arrays with Adaptive Beamforming and Open-Loop Scanning," Third Annual Benjamin Franklin Symposium on Advances in Antenna and Microwave Technology, Philadelphia, PA, April 30, 1983.

R. S. Berkowitz, B. Yang, and S. T. Juang, "Beam Steering Algorithms for Wideband Arrays," Third Annual Benjamin Franklin Symposium on Advances in Antenna and Microwave Technology, Philadelphia, PA, April 30, 1983.

W. Whistler and D. Carlson, "Bistatic SAR Imaging Tests at Valley Forge Research Center," Third Annual Benjamin Franklin Symposium on Advances in Antenna Microwave Technology, Holiday Inn, Philadelphia, PA, April 30, 1983.

C. N. Dorny, "High Resolution Microwave Imaging," three day short course at the Northwest Telecommunications Engineering Institute, Xian, Shaanxi, People's Republic of China, May 4-14, 1983.

## Appendix A: Ground Based Radio Camera

### 3. ON THE DESIGN OF A RADIO CAMERA\*

Bernard D. Steinberg  
Raymond S. Berkowitz

Earl N. Powers  
Shuah Teh Juang

#### INTRODUCTION

This report will describe a technique for constructing a very large, random adaptive array for use as a radio camera. The radio camera is designed to provide high resolution beams suitable for imaging aircraft at a distance of a few miles. The array is assumed to operate at X-band frequency. It will have a maximum extent of about 1000 ft and is assumed to be a two-dimensional array containing about 1000 elements. The parameters which have been mentioned arise from considerations of the basic performance requirements of the array; i.e., bandwidth, sidelobe level, available terrain, and feasible economy.

Studies extending back many years have resulted in knowledge of the expected performance of such a radio camera, and experiments have produced practical experience in the types of hardware, processing, and signals which will be useful for the large array. Several designs for array elements have been developed which have the capability for reception of echo returns from targets, coherent detection, and means for communicating the detected signal (or at least its significant parameters) back to a central point for processing. Some of these designs have been experimentally evaluated. Designs have been worked out for processing and combining the outputs of array elements, techniques for conveying the various required reference and control signals over the array have been studied, and techniques for compensating for the possibly initially unknown positions of the array elements have been studied. Bistatic and monostatic configurations have been examined, as have techniques for providing transmit as well as receive capability. Current studies are exploring the subtle aspects of image formation and sidelobe suppression as well as other topics.

The building blocks are available for the design and fabrication of a large experimental system. However, the path from concept to a completed system is heavily restricted by considerations of cost. Even though the random adaptive array theory results in systems that are orders of magnitude cheaper than those available from conventional technology, they are still expensive, primarily because they must reach a certain critical mass in terms of size and number of

---

\*This work is principally supported by the Air Force Office of Scientific Research, under Grant No. AFOSR-78-3688.

elements before their potential can be realized.

In a practical application such as the proposed 1000-element array, the number of elements can generate problems (from both the viewpoint of cost and difficulty of fabricating many elements, and the difficulty of low-cost computation of the image). Unfortunately, it is also difficult to scale the size of the array to make experimentation less costly, because the array beamwidth remains a direct function of its size, and the array pattern's sidelobe level is a function of the number of array elements that are used.

The design philosophy presented herein endeavors to thread a path from design to fabrication such that the performance-to-cost ratio is kept approximately constant - thus avoiding abrupt expense thresholds as the system develops: Performance should remain commensurate with cost throughout the program.

Previous experiments have avoided the cost of large arrays by time sharing, by constructing a synthetic aperture through the movement of a receiver or antenna over the array domain and collecting the signals over an extended time period. Time sharing of the processing of the receiver outputs has also been considered. A central processor might control a set of sub-processors, each of which could service a number of elements. The synthetic aperture approach is not ultimately suitable to the large radio camera where it is desired to perform real-time imaging. Furthermore, it is difficult to "grow" a radio camera from the synthetic aperture approach; the simple addition of more elements will demand more sophisticated processing, and no major performance gain will be achieved until many elements are added. The nature of required processing will also probably change radically as the array changes from a linear synthetic one to a two-dimensional radio camera.

Multiplexing of the receiver outputs to time-share processing is certainly a useful tool, but it has not yet provided an adequate total solution since it does not influence directly the expense of the array elements. A multiplexed processor can be designed that will grow gracefully as the number of array elements increases, but useful imaging must still await the fabrication of many array elements. A solution to this problem (and the basis of the design to be presented) is to design an array element that has the same capability for easy growth as does the multiplexed processing system. The array element must be flexible enough so that useful performance is obtained when only a few elements are available and there is a continuous growth path in terms of performance as equipment and processing are added.

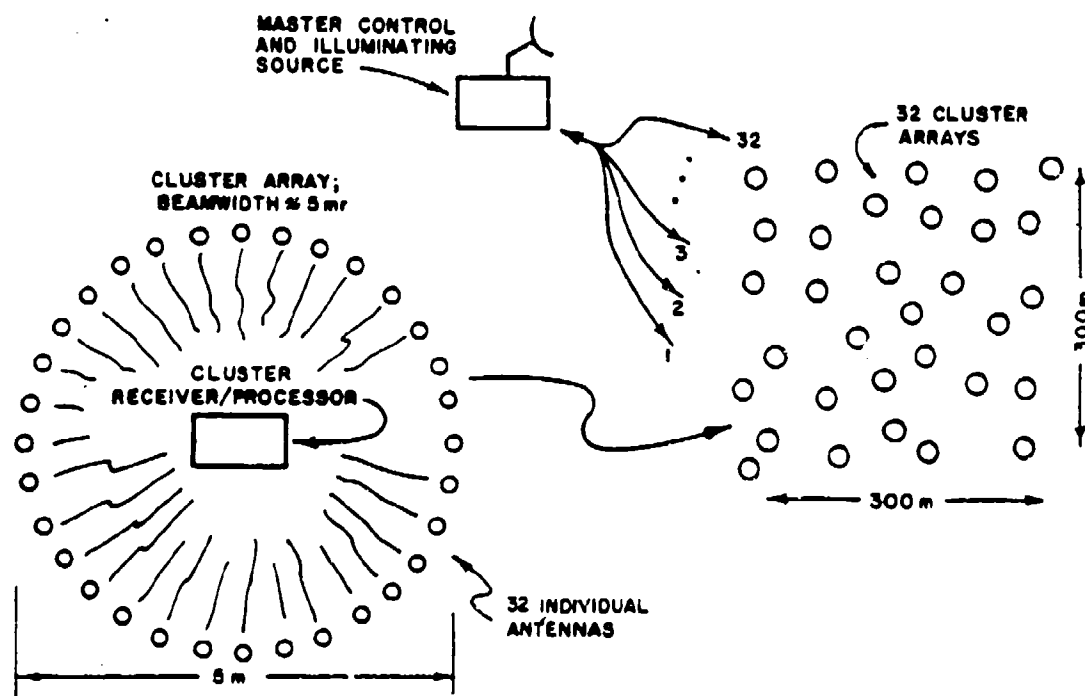


FIGURE 3.1 CLUSTER ARRAY SYSTEM

A schematic representation of an array which accomplishes these goals is shown in Figure 3.1. The array shown is not the first array which will be constructed nor is it the ultimate radio camera, but it is illustrative of a mid-sequence system design. Later reports will explain how this design evolved, and its potential extensions. This design example was chosen to illustrate sharing of system hardware among many receiving points and the use of minimal central processing capability.

An array of 1024 sampling points is spaced over a region approximately 300 meters by 300 meters. The array is divided into 32 clusters, each containing a single subarray receiver/processor. The 32 subarray receiver/processors are controlled by a single master unit. The master control will treat the array as if it were 32 monolithic antennas, each aimed at the target to be imaged. The individual cluster arrays will be automatically aimed at the target through adaptive beamforming rather than mechanical pointing as in the case of a real monolithic antenna. The mechanism and processing for the adaptive beamforming will all be contained in the receiver processor of each cluster array; the master control unit will not be involved in the individual cluster beamforming except in an overall supervisory capacity.

As indicated in Figure 3.1, each cluster array contains one receiver/processor shared by 32 receiving antennas placed in a circular array about it, and connected to it via cables. The antenna inputs will not be time-shared; there will be 32 parallel receiving and processing channels. However, there is a substantial equipment saving by centralizing the cluster system since all the local oscillator units (used only for down conversion), the frequency and phase reference systems, and the local processing can be shared among the 32 receiving channels.

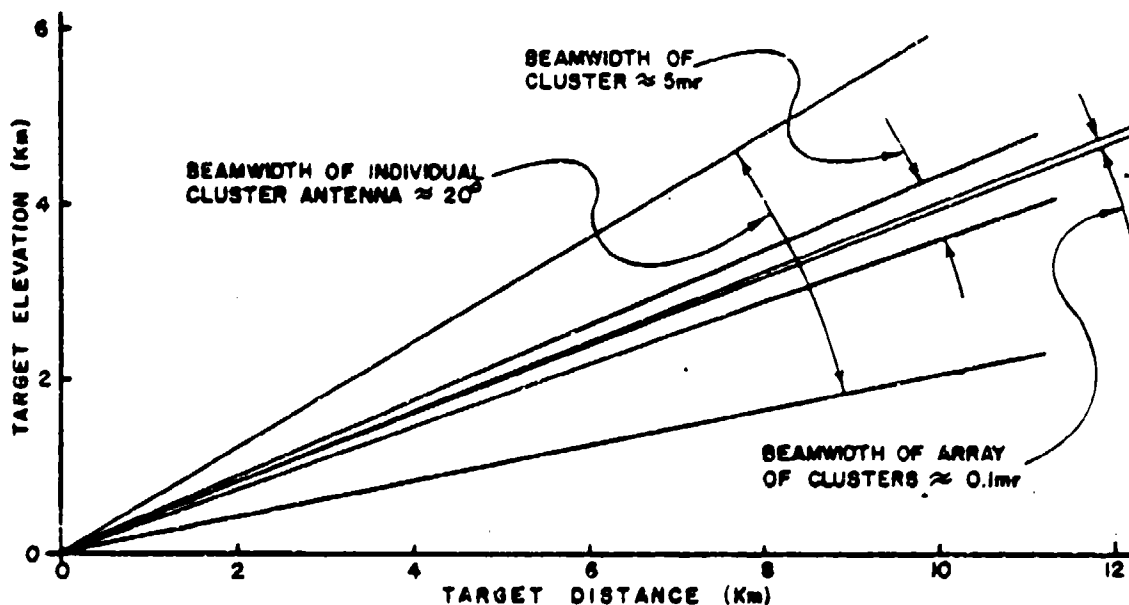


FIGURE 3.2 PATTERN COVERAGE AND BEAMWIDTHS

As shown in Figure 3.2 the individual antennas might have beamwidths of about  $20^\circ$  in horizontal and vertical planes. These antennas would be pointed to intercept the approach flight pattern normally used by aircraft landing at Philadelphia International Airport. The beamwidth of these antennas is of course arbitrary at this design level and will eventually be determined by analysis of SNR vs. angle-of-view. If the cluster array has a diameter of about 5 meters, each cluster can generate a mainlobe beamwidth of about 5 mr at X-band frequency. Since this beam is formed adaptively, it may be located anywhere within the  $20^\circ$  lobe of the individual cluster antennas; but in any case it will always be pointed at a beamforming point on the target: It is assumed that the target will be illuminated by a separate radar. When the individual cluster arrays have cohered their inputs they will generate a single sum waveform which will be returned to the master control unit. The master control unit will then adaptively beamform using these 32 inputs and

generate a 0.1 mr beam in the center of the cluster array mainlobe.

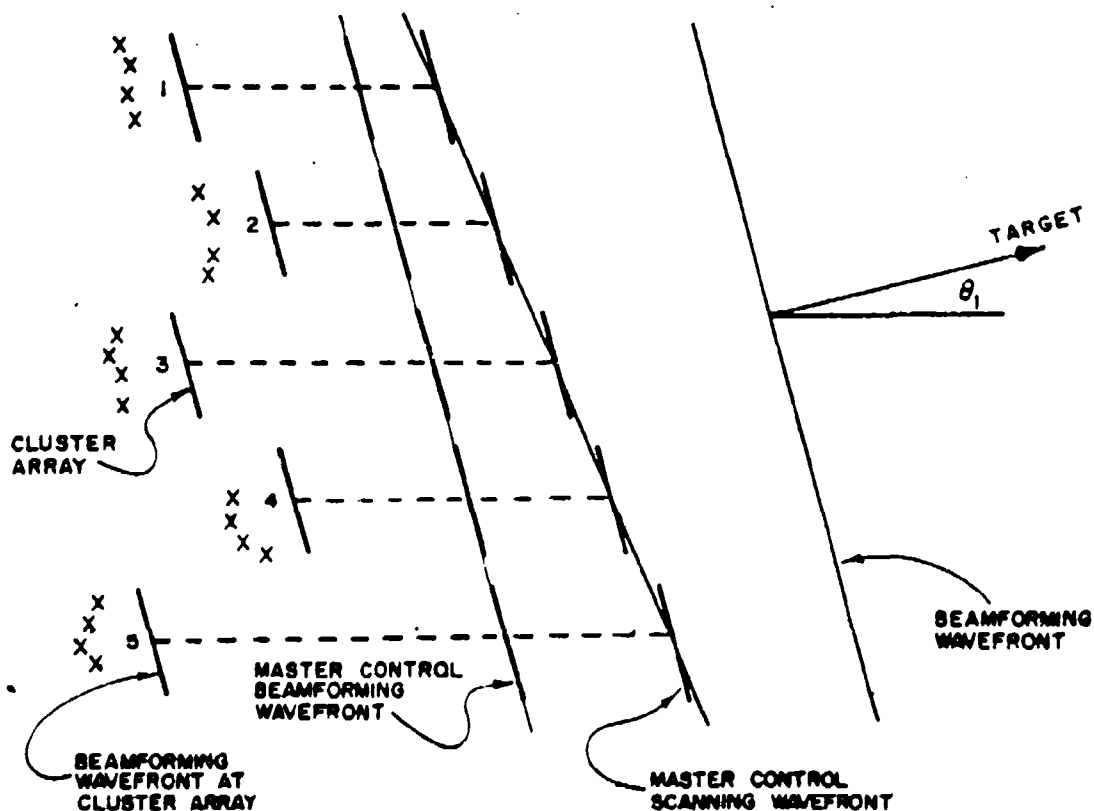


FIGURE 3.3 BEAMFORMING AND SCANNING OF CLUSTER ARRAY

Figure 3.3 shows a schematic representation of the operations performed by the individual cluster arrays, and the overall organization of the array by the master control unit. Linear arrays were assumed for ease of illustration. The individual cluster arrays will initially self-organize to place a receive beam on the far-field target located at angle  $\phi_1$ . The beamforming of the clusters and the overall array will be accomplished on a specular return from the target. As indicated, each of the cluster arrays will receive a planar wavefront which will be the source of coherence for that cluster. The master control unit will then cohere the array clusters by phase-shifting their outputs, using the planar wavefront which extends over the entire array as the beamformer source. The master control unit will then scan the array over a limited angular extent by introducing phase shifts in the signals as they are received from the outputs of the cluster arrays. In this example it is assumed that the beamwidth of the cluster array will encompass the target.

aircraft and the master control can image the aircraft by scanning within the cluster beamwidth. It is apparent from Figure 3.3 that the extent of the scan is limited, since as the overall system is scanned away from the direction of the initial beamforming source, greater and greater phase errors are introduced due to the error in the pointing direction of the individual cluster arrays. The master control can only scan the array's beam pattern over the region determined by the beamwidth of the individual clusters. As the narrow beam produced by the master control unit is scanned toward the edge of the beam pattern of the cluster array, the amplitude of the cluster signal return will begin to decrease. It will be assumed for this discussion that this is the dominant effect of scanning to the cluster beam edges and that phase remains approximately constant over the cluster array beam. This hypothesis is borne out by previous experimental work.

For this first description of the cluster array concept it has been assumed that the dimension of the cluster array is chosen so that its main lobe has a cross-section of about 50 meters at 10 km (i.e., approximately 5 m beamwidth) to permit imaging an entire aircraft; however, the ratio of the size of the individual cluster arrays to the overall dimension of the entire set of clusters is an important design parameter in this array concept. Later sections of this description will discuss the effects of increasing the cluster size to form a much narrower sub-beam, perhaps having the dimensions of only a few beamwidths of the overall cluster array. The use of large cluster arrays is of particular interest when the array is modified to function as a transmit/receive unit rather than as a bistatic unit. This cluster design lends itself well to the fabrication of a transmit/receive array system.

Earl N. Powers

#### SOME SIGNAL LEVEL CALCULATIONS FOR A GIANT RADIO CAMERA

Work has begun on the design of a giant radio camera to be installed at Valley Forge Research Center. Here we present a likely set of system parameters and point out signal level requirements for reasonable performance. A typical Giant Radio Camera can be represented by the simple model shown in Figure 3.4. The illuminator and receiving array system are operating at X-band frequency range,  $\lambda = 3$  cm. There are 1024 array elements distributed randomly over a large area such as 300 m x 300 m. The beamwidth of each element is about  $45^\circ$  and the noise figure of each

element is 10dB. Furthermore, a 2-ft diameter parabolic dish antenna is used for the operation of illuminator.

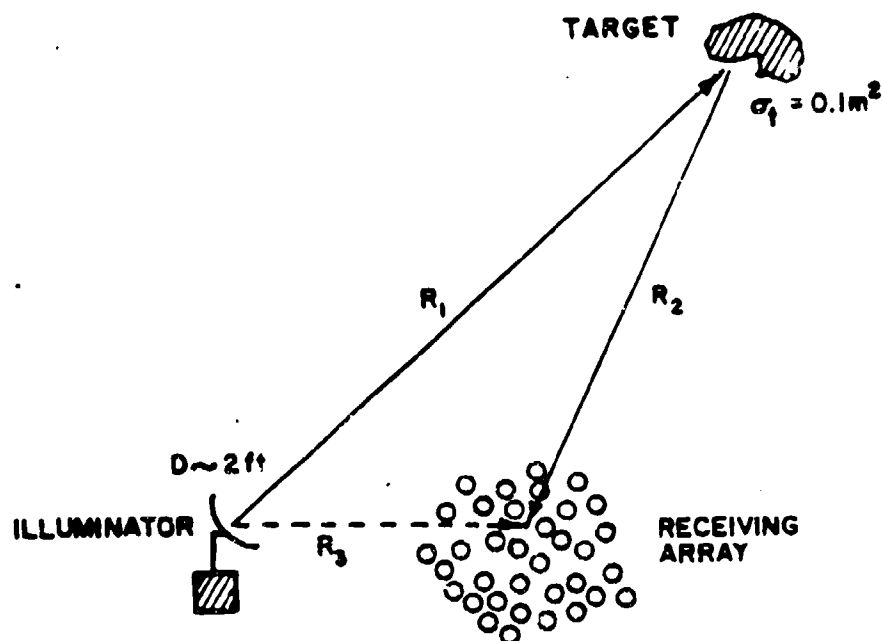


FIGURE 3.4 SIMPLE MODEL OF GIANT RADIO CAMERA

The objective here is to examine typical signal power requirements. Assumptions are made for the calculation of a typical model. For example, the target's cross-section ( $\sigma_t$ ) is taken to be  $0.1 \text{ m}^2$ . The distance between illuminator and receiving array is about 1 mile, and the distance between target and illuminator is 20 miles. The distance from target to receiving array system is also assumed to be 20 miles.

The radar equation [1] is used to calculate the signal-to-noise ratio of a single element for the reflected link. The data and result are listed below.

( $F_T$ ) = transmitted power in dBw,

( $G_T$ ) = the gain of illuminating antenna in dB,

$$G_T = \frac{4\pi A}{\lambda^2} = \frac{4\pi[\pi \times (1 \times 30.48)^2]}{3^2} = 4075.2$$

$$+ 36.1 \text{ dB}$$

$(G_{e1})$ : the gain of element's antenna in dB,

$$G_{e1} = 4\pi \times \left( \frac{1}{\text{Beamwidth(rad)}} \right)^2 = 4\pi \left( \frac{4}{\pi} \right) = 20.37 \\ \rightarrow 13.09 \text{ dB}$$

$$\lambda = 3 \text{ cm} \rightarrow 4.77 \text{ dB cm}$$

$$R_1 = R_2 = 20 \text{ miles} = 17.6 \text{ n. miles} \rightarrow 12.45 \text{ dB}_{\text{n mile}}$$

$$\sigma_t = 0.1 \text{ m}^2 \rightarrow -10 \text{ dB m}^2$$

$$\text{signal bandwidth, } 2W = 11 \text{ KHz} \rightarrow 40.41 \text{ dB Hz}$$

$$\text{noise figure, } \overline{NF}_o = 10 \text{ dB}$$

$$\text{typical loss of the link, } L_o = 4 \text{ dB}$$

$$[S/N]_r = (P_T) + (G_T) + (G_{e1}) + 2(\lambda) + (\sigma_t) - 2(R_1) - 2(R_2) - 2(W) - (\overline{NF}_o) - (L_o) \\ = (P_T) - 55.5 \quad (1)$$

where  $[S/N]_r$  is in (dB) and  $(P_T)$  in (dBw).

The direct link between illuminator and receiving array is calculated in case of the utilization of a broadcast reference signal. The result is shown as follows.

$$R_3 = 1 \text{ mile} = 0.88 \text{ n mile} = -0.555 \text{ dB}_{\text{n mile}}$$

The beacon equation can be applied here.

$$[S/N]_d = (P_T) + (G_T) + (G_{e1}) + 2(\lambda) - 2(R_3) - 2(W) - (\overline{NF}_o) - (L_o) + 77 = (P_T) + 82.43 \quad (2)$$

where  $[S/N]_d$  is in (dB) and  $(P_T)$  in (dBw).

It is seen that  $[S/N]_d$  is much larger than  $[S/N]_r$ . As a consequence, we don't have to worry about the intensity of reference signal. In addition, a cable or wire can be used to transmit the desired reference from the illuminator to the array module.

Next, the illuminated region is calculated as follows.

$$\frac{\lambda}{D} \times R_1 = \frac{3}{2 \times 30.48} \times 20 \text{ miles} = 1 \text{ mile}$$

A  $1 \times 1 \text{ mile}^2$  region is obtained. This value may not be enough for a practical system. However, it can be improved by changing the parameters of illuminator.

From T. Dzekov's dissertation [2], we can show that in the case of synchronous detection the signal-to-noise ratio is improved by a factor of  $N$  ( $N$  = number of array elements), whereas in the case of square-law detection the signal-to-noise ratio improvement factor is  $N/2$ . Thus the output signal-to-

noise ratio is given as follows.

(1) Synchronous detection:

$$[S/N]_{r_{out}} = [S/N]_r + 10 \log_{10} N, N=1024 \approx (P_T) - 25.4 \quad (3)$$

(2) Square-law detection:

$$[S/N]_{r_{out}} = [S/N]_r + 10 \log_{10} \frac{N}{2} \approx (P_T) - 28.4 \quad (4)$$

#### DISCUSSION, CONCLUSIONS

It is seen that the critical requirement is given in (1) for the single element receiver SNR as a function of  $(P_T)$ , transmitter power. For the parameters assumed,  $(P_T)$  must be 65.5 dBw ( $P_T=3.55$  Mw) to realize a 10 decibel SNR. Single element SNR is important in the beamforming phase of radio camera operation. It is possible that the  $(P_T)$  requirement can be relaxed from the following considerations.

(a) 30 or 40 dB can be gained by using a corner reflector target rather than the  $0.1 \text{ m}^2$  cross-section target assumed.

(b) A narrower effective bandwidth  $W$  can be used for beamforming.

(c) Higher gain antennas can be used.

(d) Smaller ranges can be usefully assumed.

In any event, the situation for imaging should be much better as shown in (3) or (4), gaining up to 30dB for the multiple element array.

In the next quarter more specific designs will be obtained so as to provide high resolution imaging capability.

Raymond S. Berkowitz  
Shaoh Teh Juang

#### REFERENCES

- [1] R. S. Berkowitz, "Modern Radar," Wiley, 1965, Part I, Chapter 2.
- [2] T. A. Dzekov, "Microwave Holographic Imaging of Aircraft with Spaceborne Illuminating Source," Ph.D. Dissertation, University of Penna., 1976.

### 3. CLUSTER ARRAY RECEIVER PROCESSOR \*

Raymond S. Berkowitz

Earl N. Powers  
Shauh-Teh Juang

#### INTRODUCTION

This article is a continuation of the description of the X-band cluster array concept presented in QPR No. 37. This system will employ a total of 1024 receiving points placed over a 300x300 meter area at VFRC. The purpose of this array is to produce high resolution images of aircraft travelling along the flight path to the Philadelphia airport.

#### RECEIVER/PROCESSOR

Fig. 3.1 shows a block diagram drawing of the equipment required for the implementation of the cluster array receiver/processor. In this description, it is assumed that the cluster array will consist of 32 antennas placed reasonably uniformly, but not with high accuracy, around a receiver/processor. The outputs of the antennas will be returned to the receiver/processor via cables or wave guide. Since the array dimensions are chosen to provide a 5 milliradian beamwidth, the overall size of the cluster array, i.e., 6 meters, bounds the extent of the cabling system. The relatively short distances to be traversed will limit the signal losses to few dB. Each of the antenna outputs returned to the receiver/processor will be mixed with the output from a local oscillator to generate an IF channel which will be amplified to drive a phase detector.

The oscillator supplying the local input for the bank of down converters will be shared between all, in this case, 32 channels. The local oscillator may obtain its frequency and phase reference via a cable from the master control unit as indicated, or the cable might be replaced by an RF link. The master control will supply the reference to all 32 clusters. The local oscillator will be phase locked to the reference, so that its frequency will be exactly determined and its phase will be constant, even if unknown relative to the other local oscillator in the other array clusters.

The phase angles of the 32 IF channels are measured relative to a common reference signal derived from the master control signal, and it is assumed that the SNR is adequate so that low pass filtering following the detector will

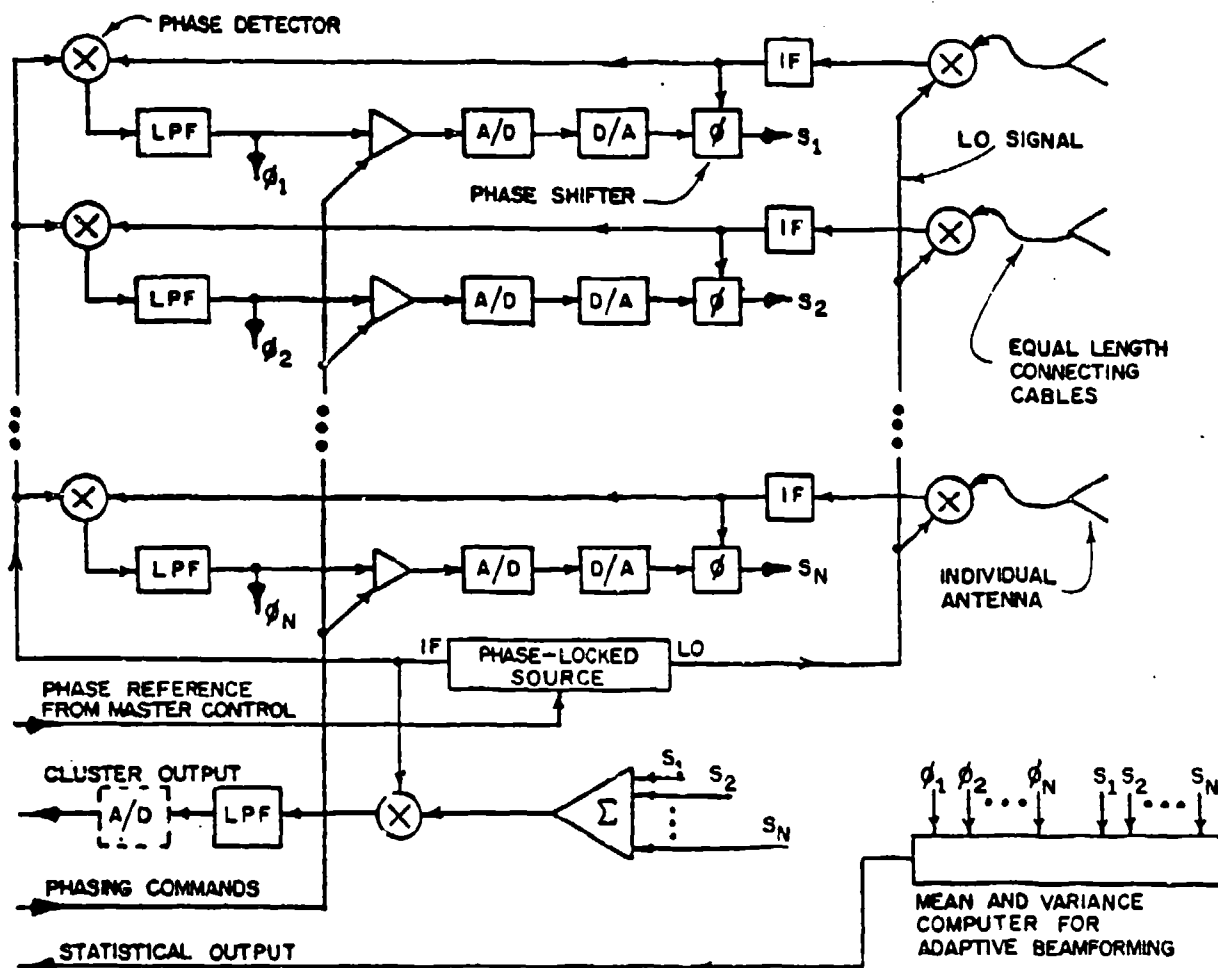


FIGURE 3.1 RECEIVE-ONLY CLUSTER ARRAY

suffice. Other applications may require more complicated integration; in this example, target range is short, relatively constant, and adequate transmit power is assumed. Similarly, considerations of doppler corrections or signal compression for range resolution have been postponed until this basic design is complete.

After passing through a gated amplifier, the outputs from the phase detector will drive phase shifters which will be used to co-phase the IF signals from each of the antennas. Figure 3.1 shows A/D conversion of the phase detector outputs, and then the complementary D/A operation. These operations were included because of the advantages of a digital phase memory. The A/D and D/A units need not be high performance, since they are used only to process the phase angles needed to adaptively place a relatively wide beam in the direction of the target. That is, the system operation will be initiated by the reception of a planar wavefront from the target; at this time, the phases of the 32 channels

will be measured, converted to digital form, and held in memory. The reconverted analog version of these stored values will drive the channel phase shifters to co-phase the signals. The planar beamforming wavefront is assumed to arrive only occasionally, and consequently the A/D and D/A units do not have to operate rapidly.

The control for activating a phasing operation will consist of a command which is returned from the master control unit; the amplifiers shown in the phase-detector phase-shifter loops are assumed to have sample and hold capability so that they can maintain the beamforming phase while the A/D process is underway. The outputs from each of the 32 channels after phase shifting are sent to an analog summer, then demodulated and converted by a single A-to-D converter and returned to the master control unit. A-to-D conversion at this point is arbitrary; it may be advantageous to return the summed analog signal directly to the master control, rather than converting it to digital.

In either case, only the combined signal from all the array elements is processed; this is in contrast to earlier system designs which typically demanded A-to-D conversion for each antenna output signal. This required either individual A-to-D converters or more probably a single high-speed converter and a multiplexing circuitry. In exchange for eliminating individual channel A/D, it has been necessary to add the phase-detector/phase-shifter network; however, the phase-detector will be required in any case and the major addition equipment is limited to the amplifier and the phase-shifter. In addition to the savings in hardware arising from combining the cluster antennas outputs, a large saving in computation and processing is accomplished through the 32-to-1 combining inherent in this cluster array system. The master processor for the array will manipulate the output from each array cluster, but not the individual components of the cluster output. Each array cluster will have the capability for adaptive beamforming, but at the current level of discussion, the cluster's adaptively formed beam will not be scanned. However it is apparent from the design, that the addition of a scanning operation would be relatively simple through use of the available phase-shifters. It would require primarily an interface between the array module and the processing system. The possibility of adding a scan capability will be discussed as the design develops.

The final major component of the cluster array system shown in Fig. 3.1 is a processor which will compute the variance of the amplitude and phase measure-

ments of the signals from the array elements. This information will be used to establish the conditions for beamforming, i.e., a minimum variance amplitude measurement, as is typical of a linear phase-front suitable for adaptive beamforming [1]. Similarly, since the array is of limited extent, a best-fit-planar surface could be used to measure the phase deviations over this cluster, and this might also be used as an indication that a suitable wavefront has arrived for adaptive beamforming. The phase angles are available at the detector outputs, but it may be necessary to add envelope detection to provide the amplitude data. The intent of this design is to minimize equipment as much as possible without limiting the performance of the system: the basic components required for independent receiving channels have been retained, but common equipment such as the local reference source is shared among all the channels. This design is a first effort and may not be optimum. The total equipment might be reduced further, but probably only at the expense of complicating the system operation. For example, in the assumed application of imaging an isolated aircraft flying along a predictable flight path, it might be possible to introduce an additional multiplexing level. The received signal from the aircraft will occupy only a small number of range bins and, if suitable delays between the array antenna outputs could be introduced, it would be possible to time-share a single mixer and IF chain between a number of antenna elements.

It should also be noted that the design of the cluster array processor/receiver is particularly attractive from the viewpoint of converting it into a transmit/receive unit. Since all the cluster antenna outputs are referenced to a single phase source, conjugation of the inputs values to the phase-shifters used for receive beamforming, could be accomplished simply. This topic will also be explored in a later section.

#### CLUSTER INSTALLATION, CALIBRATION AND OPERATION

Fig. 3.2 (repeated from QPR No. 37) shows a schematic representation of the cluster array system. The Valley Forge aircraft imaging application can be implemented by using small horns having nominal beamwidths of about  $60^{\circ}$ - $90^{\circ}$ , each aimed in the direction of the flight path along which the aircraft to be imaged will appear. The antennas are assumed fixed at approximately equal angle increments in a circular pattern about their receiver processor. This geometry was chosen because it implies an obvious phase center for the cluster. The master

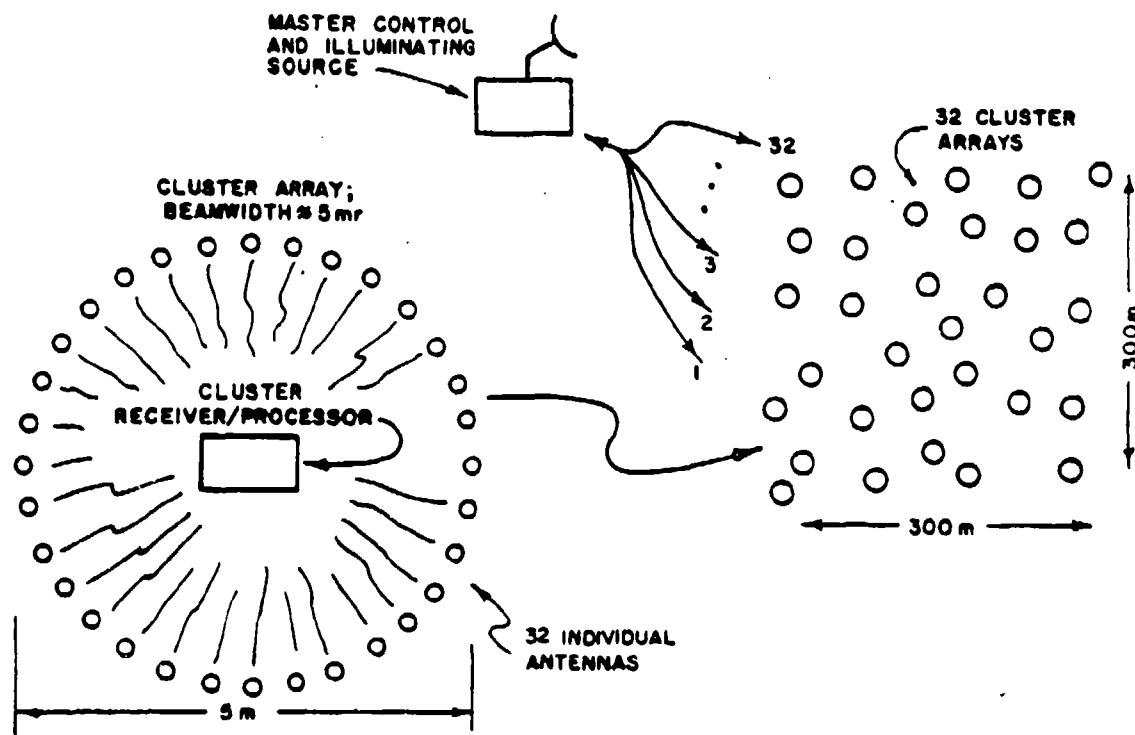


FIGURE 3.2 CLUSTER ARRAY SYSTEM

control unit must have knowledge of this phase center location for each cluster in order to scan the array. Other cluster array geometries may be superior in some respects such as sidelobe levels, and the optimum cluster geometry is a topic for future study which will be bypassed for the moment since it is beyond the scope of the current discussion. The circular geometry of each cluster should define the phase center of the array accurately enough so that determination of the exact position of each of the array elements will not be essential. However, if it is found necessary to actually measure the positions of the array elements, this might be accomplished within the cluster in a variety of ways. The simplest approach would probably be a simple mechanical measurement of the elements based upon a reference point located on the receiver; since the cluster is assumed to be about 6 meters in diameter, this measurement would not be difficult. However, if the clusters were made larger, other techniques would be indicated. More sophisticated approaches could involve an automatic distance measurement using acoustics or RF. A middle-ground approach would be to equip each of the cluster antennas with an infrared or laser reflector and

use a corresponding infrared or laser transit placed at a reference point on the processor/receiver.

It will be assumed that since the individual antenna elements are small and contain no accompanying electronic packages, they may be placed with sufficient rigidity to insure that frequent updates in the survey are not required.

Similar survey options exist for the determination of the array cluster phase centers relative to the master control unit. Probably the middle-course route of an IR or laser transit represents the simplest and most economical way of surveying the phase centers. Because of cluster approach, the survey of the array from the master control point consists only of locating the cluster centers. In the assumed example, these will number 32 so that the survey procedure is much reduced from that which would be required to survey all 1000 element locations, in order to treat them as individual elements.

The cluster array concept is also attractive from the viewpoint of electrical calibration since it can also be performed in two steps like the system survey. A portable antenna cabled to a source at the master processor might be moved sequentially to each of 32 clusters to adjust for phase shifts in the reference signal system and the return connections from the cluster arrays. A similar procedure could be used for collection of the individual receive channels in the clusters; in this case, the calibrated source would be derived from the receiver/processor in the cluster to be calibrated. It should be noted that adaptive beamforming may eliminate the need for extensive phase calibration; however, the two-step procedure described is probably more desirable than the calibration prior to assembly of the cables, amplifiers and other components of the system, and should be considered as part of the initial setup procedure for the array.

This array system will include a separate radar transmitter to illuminate the target aircraft. The individual clusters will function independently to beamform on the illuminated target. The first useful return from the target aircraft must be specular in nature if the array clusters are to adaptively beamform. In this application, the return to the cluster arrays will be limited to sidelobe clutter in the absence of a target and this level is assumed low, relative to a useful specular return from the target. Since the clusters are relatively small, any specular return may be expected to occupy a single range bin and the adaptive beamforming procedure would be initiated by peak

detecting and storing the amplitude and phase of the target signal return. A first criterion for beamforming, would be that the maximum signal was found in the same range bin in the majority of the cluster array channels. (The range bin timing would be initiated by the main-bang feed-through from the illuminating radar.)

The array cluster processor will examine the variance in amplitude across the elements of its array to determine whether the return is likely to be specular. The measured phase angle will be held while the variance information is returned to the master control, which will decide to signal all of the array clusters to freeze their phase memory at the indications produced by the previous illuminating pulse.

The decision of the master control unit is straightforward if all the clusters simultaneously identify a minimum variance condition, since this indicates that the wavefront is suitable for adaptive cohering of the entire array. The master control decision is less clear when the cluster outputs are not consistent--a condition which results either from a non-specular return, or because a specular return is visible to only part of the array. In the former case, the master control may simply not freeze the measured cluster phases, but wait for a more favorable wavefront. In the latter case, if the majority of clusters have received the specular return, the master control may simply ignore the remainder, freeze the phases and proceed to scan the target.

In summary, the phase memories of each cluster will normally be updated on each transmitted pulse unless they are deliberately frozen by the master control unit. Prior to being frozen, the cluster will examine each return, searching for peak detected signals that all occupy the same range bin. This condition suggests a possible specular return and will initiate an examination of the amplitude variation of the return across the cluster. The amplitude variance information from each cluster will be returned to the master control unit which will make the decision to freeze the cluster beamforming phases if there is an adequate indication of a specular return. Once frozen, the master control may phase-shift the outputs from the clusters to play a narrow scan across the target. This scanning procedure will involve only the introduction of phase corrections in the 32 cluster outputs returned to the master control. The master control processes only 32 inputs rather than 1,024 signals produced by the individual antennas. The major advantage, of greatly reduced processing

and required analog hardware, is possibly offset by the poor sidelobe performance of the cluster concept. In the worst case, the overall pattern of the array will be given by the convolution of the assumed identical cluster array patterns and the pattern arising from considering the 32 cluster phase centers as a random array. The near-in sidelobe may be excessively high. Future work will explore this trade-off through reducing the sidelobes by transmit/receive operation and the use of independent cluster patterns.

Earl N. Powers

#### REFERENCE

- [1] Bernard D. Steinberg, "Phase Synchronizing a Radio Camera," QPR No. 32, February 1980, pp.40-49.

---

\*This work is supported partially by the U.S.Army under contract DAAK20-80-C-0250.

# Distributed Airborne Array Concepts

BERNARD D. STEINBERG, Fellow, IEEE

ELI YADIN, Student Member, IEEE  
Valley Forge Research Center

The improvement in SNR and detection range due to distributing an antenna array throughout the airframe and skin of an aircraft is examined. SNR formulas for three system configurations are presented and compared with that of a conventional, monostatic radar. Examples given in the paper show detection range increases as large as a factor of 4. Three additional potential advantages of the distributed array are an increase in spatial signal processing capability, an improvement in azimuthal resolution, and a potential reduction in transmitter power for fixed radar performance so as to reduce the probability of intercept.

Manuscript received September 5, 1980; revised April 15 and September 14, 1981.

This work was supported by the Air Force Office of Scientific Research under Grant AFOSR-78-3688.

Authors' address: B. Steinberg, Valley Forge Research Center, Moore School of Electrical Engineering, Philadelphia, PA 19104; E. Yadin, Interspec Inc., Philadelphia, PA 19104.

18-9251/82/0300-0219 \$00.75 © 1982 IEEE

## INTRODUCTION

Radar performance in noise and jamming is a monotonic function of the power-aperture product [1, 2]. This paper evaluates the improvement in radar performance due to increasing the aperture size of airborne radar by distributing antenna elements or small subarrays throughout large portions of the skin of an aircraft. The performance measure adopted is signal to receiver noise ratio (SNR) and its equivalent, detection range of targets in noise.

The critical technical problem is that of overcoming the distortion in such a phased array due to the nonrigidity of the skin and airframe. This problem is introduced (but not solved) in the paper, and a discussion of other difficult technical problems is presented. The problem of nonrigidity must be overcome by a retrodirective [3, 4], self-adaptive technique [5, 6, 7] based upon echoes from land or sea clutter.

In addition to enhanced SNR and detection range, increasing the size of the aperture to include all or most of the airframe offers the advantages associated with small beamwidth.

One important advantage has to do with protection against jammers that are close to the axis of the beam. Rejection of jamming energy by low sidelobe design or adaptive techniques such as coherent sidelobe cancellation and adaptive nulling [8-12] are known and useful techniques. Main lobe jamming, however, is not suppressed without hazarding the suppression of target return. Increasing the size of the aperture reduces the width of the main lobe and thereby reduces the minimum angular separation between target and jammer at which sidelobe suppression techniques can operate.

A second advantage of the reduced beamwidth is the enhanced potential for target counting and classification.

An additional value of the improved detection performance is the possibility of a drastic reduction in transmitter power for a given performance so as to permit the successful design of a low probability of intercept radar.

The paper focuses upon the SNR performances of three airborne distributed array systems as compared with that of a conventional radar with a modest sized, confined antenna used both for transmitting and receiving. From the parametric relations that are developed, the conditions which produce superior detection performance can be determined. Generally speaking, it is found that the larger the aircraft and the shorter the wavelength, the greater the potential benefit. In one X-band design a potential increase in detection range by a factor of 4 is reported.

## NOMENCLATURE

$P$	Average transmitted power in watts.
$G_T$	Transmitter antenna gain.
$A_R$	Receiving antenna area in meters squared.
$\lambda$	Wavelength in meters.
$T_0$	Integration time in seconds.
$\sigma$	Target cross section in meters squared.
$R$	Target to radar distance in meters.
$k$	Boltzmann's constant ( $1.38 \times 10^{-23}$ joules per degree Kelvin).
$T$	Reference temperature (290 degrees Kelvin).
$M$	Total system and propagation loss factor (including receiver noise figure, integration loss, antenna efficiency loss, filter matching loss, etc.). Subscripts are used in the text to distinguish between the systems.
$\theta$	Azimuth beamwidth in radians.
$\theta_s$	Azimuthal surveillance sector in radians.
$\phi$	Elevation beamwidth in radians.
$\phi_s$	Elevation sector in radians.
$D$	Width of high gain antenna in meters.
$L$	Length of aircraft in meters.
$W$	Width of strip available on the fuselage for the distributed antenna array in meters.
$\eta$	Deployment efficiency (fraction of available fuselage area used as electromagnetic transducer).
$T_s$	Scan time in seconds.
$N$	Number of antenna elements.
$P_e$	Average power radiated by individual element in watts.
$A_e$	Element aperture in meters squared.

## MONOSTATIC RADAR WITH ROTATING TRANSMIT-RECEIVE ANTENNA

This is the reference system against which the distributed antenna systems are compared. Examples are the E-2 and E-3 airborne early warning (AEW) systems. The integrated output SNR is given by [2]

$$\text{SNR} \triangleq r = PG_T A_R \sigma T_0 / (4\pi)^2 R^4 k T M. \quad (1)$$

The azimuth beamwidth  $\theta = \lambda/D$ . The antenna gain is given by  $G_T = 4\pi/\theta\phi = 4\pi D/\lambda\phi$ . The receiving antenna area is given by  $A = \lambda D/\phi$ . It is assumed that the integration time  $T_0$  is equal to the time on target (time during which the target is illuminated). That time is less than  $T_s$  by the ratio of azimuthal beamwidth to  $2\pi$ , or  $T_0 = \lambda T_s / 2\pi D$  where the scan time  $T_s$  is the time for a mechanically scanning antenna to rotate  $2\pi$  rad. Making these substitutions yields

$$r = P \lambda \sigma D T_s / 8\pi^2 \phi_s^2 R^4 k T M_1, \quad (2)$$

where the subscript 1 has been given to  $M$  to designate system 1. The elevation beamwidth  $\phi$  of the

antenna is assumed to be equal to the desired elevation coverage  $\phi_s$ .

## DISTRIBUTED RECEIVING ARRAY AND HIGH GAIN ROTATING TRANSMITTING ANTENNA

Fig. 1 shows how the reference system is modified. The high gain rotating antenna is retained but is used only for transmission. The receiving system is a distributed array; a fuselage array is depicted in the figure. It consists of  $N$  receiving elements distributed in a band along the length of the fuselage. Let the length of the fuselage be  $L$  and the width of the band be  $W$  (e.g.,  $L$  and  $W$  for a Boeing 707 are approximately 45 m and 2 m). The receiving array is distributed along the aircraft surface forming an aperture of length  $L \gg D$ ; hence the receiving beamwidth is much smaller than the transmitting beamwidth. To prevent diminishing the number of hits per target, the signal processor simultaneously forms a group of adjacent receiving beams to fill the transmitting main beam. The number of receiving beams will be  $\theta_T/\theta_R = L/D$ , where  $\theta_T$  is the transmitting beamwidth and  $\theta_R$  is the receiving beamwidth. The elevation beamwidth of the receiving array ( $\lambda/W$ ) is usually much narrower than the required elevation coverage  $\phi_s$ . Hence  $W\phi_s/\lambda$  receiving beams in elevation must be formed to cover the desired sector  $\phi_s$ .

### Number of Receiving Elements

The element radiation pattern should cover the desired surveillance sector of the radar. Therefore it should have a beamwidth of  $\theta_s$  in azimuth and  $\phi_s$  in elevation. The width and length of each array element are, therefore,  $D_1 = \lambda/\theta_s$  and  $D_2 = \lambda/\phi_s$ , respectively. The fuselage area available for deploying the elements is  $LW$ . If we assume that a fraction  $\eta < 1$  of that area is used for the electromagnetic transducer, then the number of antenna elements in the fuselage array becomes

$$N = \eta LW/D_1 D_2 = \eta LW\theta_s\phi_s/\lambda^2. \quad (3)$$

Equation (3) is evaluated for two different aircrafts and the results are given in Table I. One airplane is the Boeing 707, a large aircraft which could serve an AEW function; the other is a smaller, high-performance aircraft such as the General Dynamics F-16.  $L$  and  $W$  for these aircraft are approximately 45 m and 2 m, and 10 m and 1 m, respectively. In both cases  $\eta = 0.5$  is assumed. Taking the azimuthal surveillance sector  $\theta_s = 2$  rad and the required elevation coverage  $\phi_s = 1$  rad, the number of elements is shown in Table I.

The SNR is derived by substituting the proper area  $A$  in (1).  $A$  is given by  $NA_e$ . The effective element area  $A_e$  is given by  $\lambda^2/\phi_s\theta_s$ .  $G_T$  is given by  $4\pi D/\lambda\phi_s$ ,  $N$  is given by (3), and  $T_0$  by  $\lambda T_s/2\pi D$ . Substitution yields

$$r = \eta P_0 L W T_s / 8\pi^2 \phi_s R^4 k T M_s. \quad (4)$$

It is interesting to observe from (4) that the signal to noise power ratio is not affected by the transmitting azimuth beamwidth. This is true provided that the beamwidth does not get so large that it is no longer possible to integrate coherently across the beam. In that case integration must be partially coherent and partially noncoherent, and the integration loss increases, a factor affecting the performance of system III. This is discussed numerically in a later section. Also discussed there are the relative beam-shape losses. Another relevant factor in comparing the systems is that even though the SNR might not be influenced by azimuth transmitting beamwidth, the number of receiving beams is affected by the beamwidth; hence the size of the transmitting antenna affects the complexity of the signal processor.

### DISTRIBUTED RECEIVING ARRAY AND LOW GAIN NONROTATING TRANSMITTING ANTENNA

In this design the high gain rotating transmitting antenna is eliminated and one of the array elements is substituted as a low gain, wide beam transmitter. The azimuthal width of the transmitting antenna pattern becomes equal to  $\theta_s$ . Its elevation beamwidth  $\phi_s$  is unchanged. Therefore,  $G_T = 4\pi/\phi_s \theta_s$ . The receiving antenna is formed from  $N$  such antenna elements. Therefore,  $A = NA_s = N\lambda^2/\theta_s \phi_s$ . Substituting (3) for  $N$  yields  $A = \eta L W$ .

To achieve the maximum integration gain, the signal processor simultaneously forms a group of adjacent receiving beams such that the azimuthal sector covered by the receiving beams is the same as that of the transmitting pattern. Hence, the integration time  $T_0$  will be longer than in designs I and II, which compensates for the low gain of the transmitting antenna. The relative efficiencies are discussed in a later section. As a result of the increased integration time, the integration loss also will be increased.  $M_s$  can be used to indicate this increased loss. As in system II,  $W\phi_s/\lambda$  receiving beams in elevation are formed simultaneously to cover the desired sector  $\phi_s$ . For generality the transmitter power will be indicated by  $P'$ . Making these substitutions results in

$$r = \eta P' \phi_s L W T_s / 4\pi \theta_s \phi_s R^4 k T M_s. \quad (5)$$

### DISTRIBUTED TRANSMITTING AND RECEIVING ARRAY

Here it is assumed that each element transmits and receives. The average power transmitted per element is  $P$ , and the element gain is  $G_s$ . The average power density at the target due to a single transmitter element is  $W_s = P G_s / 4\pi R^2$ . The electric field  $E$ , is proportional

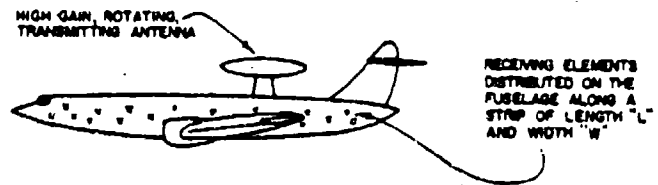


Fig. 1. Distributed receiving array and high gain rotating transmitting antenna.

TABLE I  
Number of Elements Deployable Along One Side of the Fuselage,  $\eta = 0.5$

Wavelength (m)	Aircraft	N
0.3	Boeing 707	1000
0.1	Boeing 707	9000
0.03	General Dynamics F-16	11000

to  $W_s^{1/2}$ . When the transmitting array is focused on a target the total electric field is  $E = N E_s$ , and the total average power density is  $W = N^2 W_s$ . Therefore the SNR at the receiver is

$$r = (N^2 P G_s) \phi_s (NA_s) T_0 / (4\pi)^2 R^4 k T M_s. \quad (6)$$

where  $NA_s$  is the total receiving aperture and  $T_0$  is the integration time. In this design electronic scan in azimuth and elevation for both transmit and receive beams is required. The ratio  $T_0/T_s$  is equal to the number of transmit-receive beams within the surveillance sector  $\theta_s, \phi_s$ . Therefore  $T_0 = \lambda^2 T_s / L W \theta_s \phi_s$ . For this design integration losses can be ignored since  $T_0 \ll T_s$ . (Care must be taken that  $T_0$  is not less than one interpulse period, however, a condition which the equation above may lead to at the shorter wavelengths. In such a case  $T_s$  must be lengthened or the other parameters decreased so that at least one hit per target is available to each beam.) The gain and aperture area of an element is the same as  $G_T, A$ , in design III.  $N$  is given by (3). Hence  $NA_s = \eta L W$  and  $T_0 = \eta T_s / N$ . Making these substitutions yields

$$r = \eta^2 N P \phi_s L W T_s / 4\pi \theta_s \phi_s R^4 k T M_s. \quad (7)$$

### SNR IMPROVEMENT FACTOR

The ratios of (4), (5), and (7) to (2) are the relative SNRs of the three distributed array systems to the conventional, monostatic radar. This ratio, designated the relative gain or improvement factor  $I$ , is given in the first column of Table II.

The second column of Table II is based on four assumptions: 1) the angular sector  $\theta_s$  is assumed to be about 2 rad; 2) the required elevation coverage is

TABLE II  
SNR Gains of Systems II, III, and IV Relative to System I

System	SNR Improvement Factor $I$	
	General Case	Special Case, $\theta_s = 2 \text{ rad}$ , $\phi_s = 1 \text{ rad}$ , $T_o = T_s$ , $P'/P = NP_s/P = \theta_s/2\pi$
II	$\eta M_s \phi_s LW/M_s \lambda D$	$\eta M_s LW/M_s \lambda D$
III	$2\pi \eta M_s P' T_o \phi_s LW/M_s P \theta_s \lambda D$	$\eta M_s LW/M_s \lambda D$
IV	$2\pi \eta' M_s NP_s \phi_s LW/M_s P \theta_s \lambda D$	$\eta' M_s LW/M_s \lambda D$

about 1 rad; 3)  $T_o = T_s$ , which implies that the rate at which target data are delivered to the user is the same for all systems; 4)  $P'/P = NP_s/P = \theta_s/2\pi$ , which implies the use of the same power per angular sector for all systems. It is seen that for all distributed designs  $I$  increases linearly with  $LW\phi_s/\lambda D$ .  $LW$  is the fuselage area (one side) and  $\lambda D/\phi_s$  is the aperture of the conventional fuselage area (one side) and  $\lambda D/\phi_s$  is the conventional antenna used in design I.  $LW\phi_s/\lambda D$ , therefore, is the maximum potential increase in aperture. Since  $\eta$  is the fraction of the fuselage area used to deploy the elements,  $\eta LW\phi_s/\lambda D$  is the factor by which aperture increases. It is shown later that system losses  $M_s$ ,  $M_p$ , and  $M_a$  are larger than the loss  $M_i$  of the conventional design (i.e., the fractions  $M_i/M_s$ ,  $M_i/M_p$ ,  $M_i/M_a$  are smaller than unity). Hence the aperture gain  $\eta LW\phi_s/\lambda D$  must be significantly higher than unity to make the distributed designs attractive.

## RELATIVE SYSTEM LOSSES

The parameters  $M_s/M_i$ ,  $M_p/M_i$ , and  $M_a/M_i$  represent total system and propagation losses for designs II, III, and IV relative to the conventional design I. The contributions to the system loss are compared below. Propagation losses are unaffected by choice of design.

### Beam-Shape Loss

As the beam scans over a target, the echo pulses are modulated by the antenna pattern, reaching the maximum value only when the beam points directly at the target. Blake [16, 17] showed that antenna modulation represents a loss of SNR of 1.6 dB for an antenna scanning in one dimension and a 3.2 dB loss when a pencil beam is used to scan in two dimensions. When the number of hits per scan is very low, the average loss will increase because the target might be seen only at the edge of the beam. The pattern loss for these cases are given in [18].

For the purpose of this analysis it is assumed that the conventional design (system I) has a pattern loss of 1.6 dB (0.8 dB for transmission and 0.8 dB for reception).

Design II, using the mechanically scanned transmitting antenna and the electronically scanned multiple narrow beams for receiving, has the same modulation effect both for transmitting and receiving. Therefore, the pattern loss for this design is the same as that of system I.

System III also uses multiple receiving beams. Here the receiving beams are stationary, but since they are very narrow, aircraft and target motion cause target echos to move through several receiving beams during the integration time. This is equivalent to scanning the receiving beams over the target. Therefore a pattern loss of 0.8 dB for reception is assumed.

The broad transmitting beam in system III also is stationary. Its power pattern  $G_T(\phi)$  is angle dependent. Its maximum value is at  $\theta = 0$  and it drops by 3 dB for  $\theta = \pm \theta_s/2$ . The beam-shape loss for this case is defined as the additional SNR required to maintain the same average probability of detection  $P_d$  as for the loss-free case.

The SNR depends linearly on  $G_T(\theta)$ . Since  $P_d$  is a function of SNR, it also is angle dependent, i.e.,  $P_d = g(\theta)$ . If we assume that targets are uniformly distributed in angle throughout the surveillance sector  $\theta_s$ , then the average probability of detection is given by

$$\bar{P}_d = \theta_s^{-1} \int_{-\theta_s/2}^{\theta_s/2} g(\theta) d\theta. \quad (8)$$

It is further assumed that in the interval  $-\theta_s/2 < \theta < \theta_s/2$  the one-way power pattern and, therefore, the SNR can be approximated by a constant times  $\cos^2(2\pi\theta/2\theta_s)$ . The nonlinear dependence of  $P_d$  on SNR is calculated in many radar handbooks for different false alarm rates. By using  $P_d$  (SNR) given in [1, ch. 2, fig. 4], (8) was evaluated. For a 2 rad surveillance sector and a constant probability of false alarm of  $10^{-6}$  it was found that an SNR of 14.3 dB is required to achieve an average probability of detection of 0.9. Comparing that with the required 13.2 dB SNR associated with the loss-free case and the same probability of detection, it is concluded that the beam-shape loss for transmitting is 1.1 dB. Therefore a total of 1.9 dB beam-shape loss is assumed for design II.

Design IV involves two dimensional scanning for which the loss is 3.2 dB provided that there is more than one hit per scan. In addition, the transmitting gain for each element has the same angle dependence as in design III. Therefore an additional loss of 1.1 dB is added. A total beam-shape loss of 4.3 dB is assumed for this design. Based on this analysis the estimated relative (to design I) beam-shape losses are 0

dB, 0.3 dB, and 2.7 dB for designs II, III, and IV, respectively.

### Integration Loss

The integration losses are expected to be negligible for designs I, II, and IV because their integration times will be short enough to allow coherent integration with negligible losses. The integration time for each is limited by the beamwidth of the transmitting antenna or the transmitting array and by the required scanning time through the sector. In design III, however, the total sector is continuously illuminated by the broad beamwidth, nonrotating transmitting antenna. The integration time will be limited only by the required rate at which data are to be delivered to users. Since integration over a few thousand pulses (several seconds) is expected to take place in design III, some combination of coherent and noncoherent integration will be required. Hence, integration loss relative to ideal coherent integration cannot be ignored. As an example, an integration loss of  $\sim 2.5$  dB is expected for a mixed integration process having a 2000 pulse integration time when coherent integration of only 100 pulses is possible [2, pt. IV, ch. 4].

### Receiver Noise Figure

There is no reason why the receiver noise figure should differ in the four designs.

### Adaptive Beam-Forming Loss

It is explained later that the three distributed array designs will probably require adaptive self-cohering techniques to compensate for fuselage vibrations. Calculating the loss in the self-cohering procedure is beyond the scope of this paper. However, experience with experimental adaptive beam-forming and scanning systems at the Valley Forge Research Center [13] indicates that the one-way loss can be held below 1 dB. This value will be attributed to designs II and III and a 2 dB loss will be attributed to design IV.

### Combined Relative Losses

These estimates are used in the performance examples given below. Expressed in decibels, the ratios of the loss factor  $M_i$  to the losses in systems II, III, and IV are -1dB, -3.8dB, and -4.7dB.

### INCREASE IN SNR AND DETECTION RANGE

In comparing the four systems it is tempting to assume either that their average powers are equal or that their average powers per unit azimuthal angle are equal. However, such assumptions are not necessarily

TABLE III  
SNR Gains in Decibels of Systems II, III, IV Relative to System I Due to Enlarged Aperture of Distributed Array

System	L-Band AEW on Boeing 707	S-Band AEW on Boeing 707	X-Band on General Dynamics F-16
II	13.2	18.5	23.9
III	10.4	15.7	21.1
IV	6.5	11.8	17.2

TABLE IV  
Ratios of Detection Ranges of Systems II, III, IV to System I

System	L-Band AEW on Boeing 707	S-Band AEW on Boeing 707	X-Band on General Dynamics F-16
II	2.14	2.90	3.96
III	1.82	2.47	3.37
IV	1.45	1.97	2.69

realistic.  $P$  and  $NP$ , are affected by, and therefore limited by, different physical and design phenomena.  $NP$ , can be larger or smaller than  $P$ . Because of the large possible range in their ratio it is fruitless to take it into account in comparing the relative merits of the systems. Thus, only the effect of the enhanced aperture is included in our discussion.

Table III shows the SNR improvement factors due to the enlarged aperture of the distributed array and Table IV shows the factors by which the detection ranges increase for  $\theta_s = 2$  rad,  $\phi_s = 1$  rad,  $T'_0 = T_s$ ,  $P'/P = NP_s/P = \theta_s/2\pi$ ,  $\eta = 0.5$  and for three sets of parameters: 1)  $D = 20\lambda$ ,  $L = 150\lambda$ ,  $W = 7\lambda$ ; 2)  $D = 50\lambda$ ,  $L = 450\lambda$ ,  $W = 20\lambda$ ; 3)  $D = 20\lambda$ ,  $L = 350\lambda$ ,  $W = 35\lambda$ . The first two sets are realistic for L- and S-band ( $\lambda = 0.3$  and  $0.1$  m) AEW radar on a large aircraft such as a Boeing 707; the third set is realistic for an X-band ( $\lambda = 0.03$  m) radar on a small aircraft such as a General Dynamics F-16. The value 0.5 chosen for  $\eta$  is based upon examination of aircraft models and photographs and may prove somewhat optimistic. For  $\eta = 0.25$ , systems II and III lose 3 dB in SNR gains and system IV loses 6 dB.

The SNR gains of systems II, III, and IV relative to system I (shown in Table III) are also equal to the amount by which the total transmitted powers of the distributed systems can be decreased while maintaining the same detection range as the conventional system.

### AN AEW EXAMPLE

Consider the long range detection problem with the following radar and target parameters:

TABLE V  
Average Transmitted Power Required to Achieve 650 km Detection Range

System	$\eta = 0.1$	$\eta = 0.2$	$\eta = 0.3$	$\eta = 0.4$	$\eta = 0.5$
I	83 kW (not a function of $\eta$ )				
II	5.86 kW	2.93 kW	1.95 kW	1.46 kW	1.17 kW
III	11.15 kW	5.58 kW	3.72 kW	2.79 kW	2.23 kW
IV Total per module	136.98 kW 76 W	34.25 kW 9.51 W	15.22 kW 2.52 W	8.56 kW 1.19 W	5.48 kW 0.61 W

$$\begin{aligned}
 \sigma &= 10 \text{ m}^2 & W &= 2 \text{ m} \\
 f &= 200 \text{ Hz} & \eta &= 0.5 \\
 \lambda &= 0.1 \text{ m} & P'/P &= NP_s/P = \theta_s/2\pi \\
 D &= 50\lambda & M_1/M_2 &= -1.0 \text{ dB} \\
 L &= 45 \text{ m} & M_1/M_3 &= -3.8 \text{ dB} \\
 kT &= 4 \times 10^{-21} \text{ W/Hz} & M_1/M_4 &= -4.7 \text{ dB} \\
 M_1 &= 10 \text{ dB} & \text{SNR} &= 13 \text{ dB (corresponding to 0.95 probability of detection and } 10^{-6} \text{ probability of false alarm)} \\
 T_o = T_r &= 10 \text{ s} \\
 \phi_s &= 1 \text{ rad} \\
 \theta_s &= 2 \text{ rad} \\
 R &= 650 \text{ km (desired detection range).}
 \end{aligned}$$

The average transmitted power required to achieve 650 km detection range for the four systems is shown in Table V for several different values of element deployment efficiency  $\eta$ . The differences are dramatic. Whereas an unrealistic 83 kW is required for the conventional, monostatic design, less than 5 kW suffices for a bistatic system with a large, distributed receiving array.

#### SIDELobe LEVEL OF A RANDOM ARRAY

One of the important parameters in system performance is the average sidelobe level (ASL) of the array in the receiving mode, which is  $1/N$  [7]. The pattern of the transmit-receive array is the square of the radiation pattern of the distributed receiving array and, hence, ASL for this case is  $1/N^2$ . The factor of  $N$  advantage is of considerable importance in detecting targets in clutter, which, therefore, makes system IV preferred over systems II and III. However, the improved two-way sidelobe pattern is of no advantage with respect to jamming; all systems will perform according to the  $1/N$  ASL of the receiving array. Since the one-way average sidelobe level is not likely to be less than  $-35$  dB, other electronic counter-countermeasure techniques must be designed into such a system. Adaptive nulling is very attractive in this regard [10, 12, 15].

#### POTENTIAL FOR HIGH ANGULAR RESOLUTION

The minimum available beamwidth of an aperture of length  $D$  operating at wavelength  $\lambda$  is the order of  $\lambda/D$  rad. As an example, the typical horizontal aperture of an X-band nose-mounted radar antenna is 20 wavelengths. Its beamwidth is  $1/20$  rad or  $3^\circ$ . At a radar distance of 20 km the beam cross section is 1 km. The beamwidth of the radar in the Boeing E-3A Airborne Warning and Control System (AWACS) is the order of  $1^\circ$ .

Now imagine that the receiving aperture is spread over the airframe. The effective size for any direction of view is the projected length of the airplane as seen from that direction (Fig. 2). The effective length for most aircraft is close to the length of the fuselage or the wing span regardless of direction. The fuselage of the Boeing 707 is 45 m in length. An aperture of this size at L-band (30 cm) is 150 wavelengths. The beamwidth would be  $1/150$  rad  $\approx 6.7$  mrad  $\approx 0.38^\circ$ . Table VI gives the beamwidths at several wavelengths and includes the resolving power of human optics for comparison.

It is seen that the optical resolution of the radar operator, with his eyes and brain, is the same order as the potential resolution of a distributed array installed on a large aircraft and operated at the shorter radar wavelengths. Thus, the potential exists for providing him with an all weather, all around looking, night and day, microwave imaging system with as fine a resolution as he himself has with his eyes and brain.

#### PHASE SYNCHRONIZING THE DISTRIBUTED ARRAY

The fundamental problem of cohering or phase synchronizing the array is that the airframe is not rigid and that its skin vibrates. The problem is less serious at L-band than at X-band because the positional tolerance ( $\lambda/4\pi$ ) is 10 times larger. Nonetheless techniques which compensate for element position uncertainty will be needed if the bulk of the entire airframe is to be available for the radar array. It is expected that self-cohering or adaptive beam forming

will be required. A method suitable for airborne use for systems II and III is described in [7]. It is a self-cohering process which forms a retrodirective [3, 4] beam upon echoes from land or sea clutter. The search algorithm for obtaining the reference signal for the adaptive beam forming process is described in [5, 6]. Early experimental results using this algorithm are given in [13, 19]. The transmit-receive problem (system IV) is much more complicated. Active retrodirective techniques have been designed for the solar power satellite (SPS) concept [14].

## OTHER PROBLEMS

Many other problems confront the designer, although none so fundamental as the one above. The companion problem to the adaptive phase synchronization problem is scanning the receiving array following adaptive beam forming. This problem has been solved [13, 14]. The tolerance theory regarding element position uncertainty is understood [7]. The next major problem is the development of methods of adaptive beam forming of a transmitting array on a moving aircraft. The SPS work already done will be helpful [14]. Some of the other design problems are those typical of phased array designs (types of elements, single elements versus subarrays or clusters, methods of mounting, polarization, and bandwidth) while others relate specifically to the self-cohering system (methods of phase conjugation and reference phase distribution for adaptive transmit-receive array, effects of multipath and scattering from the ground or sea surface and from reflections within the array from the aircraft structure, interconnections between elements and the signal processor, real time adaptive signal processing, and display).

## OBSERVATIONS REGARDING SNR AND DETECTION RANGE

The results shown in the tables are very attractive. They indicate that the distributed airborne array will be useful when large detection range with low transmitted power is required. In addition, the distributed airborne array is useful when adaptive nulling close to the beam axis and better angular resolution are desired.

In systems I, II, and III a single transmitter radiates the full power. System III, using a single low gain nonrotating antenna, is far superior to the other two mechanically but requires a more complicated signal processor to simultaneously form many receiving beams in azimuth as well as in elevation. In addition, it must provide efficient integration over  $T_0$ . In SNR performance, system III is slightly poorer (about 3 dB) than system II. However, by not requiring the massive rotating antenna used in II, the third

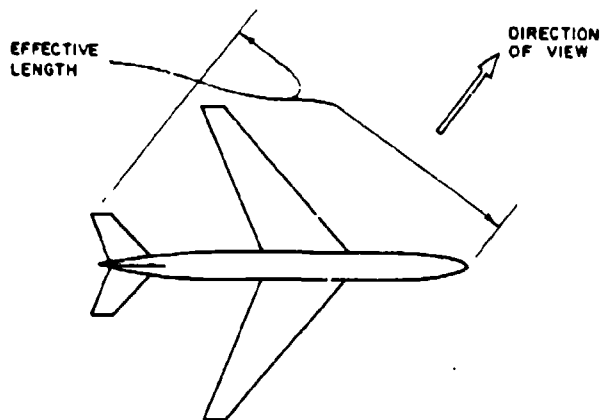


Fig. 2. Effective array length is projected extent of aircraft normal to direction of view.

TABLE VI  
Beamwidths of a 45 m Aperture and the Human Optical System

Physical Aperture	$\lambda(m)$	Beamwidth (mrad)
Boeing 707	$3 \times 10^{-1}$	6.7
Boeing 707	$3.2 \times 10^{-2}$	0.7
Boeing 707	$8.6 \times 10^{-3}$	0.2
Human eye	$5 \times 10^{-1}$	0.3

design is more attractive. System IV radiates from the distributed array. It is a much more complicated system than system III, but it offers a very much lower two-way sidelobe level. It exhibits SNR and detection range poorer than designs II and III for the same total transmitted power. SNR performance (relative to designs II, III) decreases linearly with the deployment efficiency factor  $\eta$ . Differences of nearly 4 dB and 11 dB in SNR performances relative to design III are estimated for  $\eta = 0.5$  and  $\eta = 0.1$ , respectively. Therefore design IV is preferred only if the reduced two-way sidelobe level is essential.

## SUMMARY

The improvement in SNR and detection range due to distributing an antenna array throughout the airframe and skin of an aircraft is examined. SNR formulas for three system configurations are presented and compared with that of a conventional, monostatic radar. Each of the new systems uses the distributed array for reception. One of them uses a separate, high gain, rotating transmitting antenna while another uses one of the receiving antenna elements for transmission. Both designs are bistatic. The third new system uses the entire distributed array for transmission.

SNR and detection range performances for each of the three distributed systems exceed those of conventional, monostatic radar. The X-band example given in the paper shows a potential detection range increase as large as a factor of 4.

In addition to the dramatic performance increase expected from the distributed array, it offers three additional potential advantages: an increase in spatial signal processing capability because of the enlarged size of the aperture, an improvement in azimuthal resolution, and a potential reduction in transmitter power for fixed radar performance so as to reduce the probability of intercept.

The critical problem to be solved is that of phase synchronizing the distributed array when the airframe is nonrigid.

#### REFERENCES

- [1] Skolnik, M.I. (Ed.) (1970)  
*Radar Handbook*.  
New York: McGraw-Hill, 1970.
- [2] Berkowitz, R.S. (Ed.) (1965)  
*Modern Radar*.  
New York: Wiley, 1965.
- [3] Special issue on "Active and Adaptive Antennas."  
*IEEE Transactions on Antennas and Propagation*, Mar. 1964, AP-12, 140-246.
- [4] Hansen, R.C. (Ed.) (1964)  
*Microwave Scanning Antennas*, vol. 3.  
New York: Academic Press, 1964, ch. 5.
- [5] Steinberg, B.D. (1980)  
High angular microwave resolution from distorted arrays  
*Proceedings of the 1980 International Computing Conference* vol. 23.  
Washington, D.C., Apr. 1980.
- [6] Steinberg, B.D. (1981)  
Radar imaging from a distorted array: the radio camera algorithm and experiments.  
*IEEE Transactions on Antennas and Propagation*, Sept. 1981, AP-29, 740-748.
- [7] Steinberg, B.D. (1976)  
*Principles of Aperture and Array System Design*.  
New York: Wiley, 1976.
- [8] Howells, P.A. (1965)  
Intermediate frequency sidelobe canceler.  
U.S. Patent 3-202-990, Aug. 1965.
- [9] Applebaum, S.P. (1966)  
Adaptive arrays.  
Syracuse University Research Corp., Report STLSP/L TR 66-1, Aug. 1966.
- [10] Widrow, B., et al. (1967)  
Adaptive antenna systems.  
*Proceedings of the IEEE*, 55, Dec. 1967, 2143-2159.
- [11] Brennan, L.E., and Reed, I.S. (1973)  
Theory of adaptive radar.  
*IEEE Transactions on Aerospace and Electronic Systems*, Mar. 1973, AES-9, 237-252.
- [12] Gabriel, W. (1976)  
Adaptive array—an introduction.  
*Proceedings of the IEEE*, Feb. 1976, 64, 239-272.
- [13] Steinberg, B.D., et al. (1979)  
First experimental results from the Valley Forge radio camera program.  
*Proceedings of the IEEE (Letters)*, Sept. 1979, 67, 1370-1371.
- [14] Chernoff, R. (1979)  
Large active retrodirective arrays for space applications.  
*IEEE Transactions on Antennas and Propagation*, July 1979, AP-27, 489-496.
- [15] Applebaum, S.P. (1976)  
Adaptive arrays.  
*IEEE Transactions on Antennas and Propagation*, Sept. 1976, AP-24, 585-598.
- [16] Blake, L.V. (1953)  
The effective number of pulses per beamwidth for a scanning radar.  
*Proceedings of the IRE*, June 1953, 41, 770-774.
- [17] Blake, L.V. (1953)  
Addendum to "pulses per beamwidth for radar".  
*Proceedings of the IRE (Correspondence)*, Dec. 1953, 41, 1785.
- [18] Hall, W.M., and Barton, D.K. (1965)  
Antenna pattern loss factor for scanning radars.  
*Proceedings of the IEEE (Correspondence)*, Sept. 1965, 53, 1257-1258.
- [19] Steinberg, B.D., and E. Yadin (1982)  
Radio camera experiment with airborne radar data  
*Proceedings of the IEEE (Letters)*, Jan. 1982, 67, 96-98.



**Bernard D. Steinberg** (S'48—A'50—SM'64—F'66) was born in Brooklyn, NY in 1924. He received the B.S. and M.S. degrees in electrical engineering from the Massachusetts Institute of Technology, Cambridge, in 1949 and the Ph.D. degree from the University of Pennsylvania, Philadelphia, in 1971.

He worked in the Research Division of Philco through the middle 1950's, specializing in radar backscatter and radar signal processing. He was one of the founders of General Atronics Corporation in Philadelphia in 1956 and served as its Vice President and Technical Director for 15 years. His work there was in signal processing techniques and their applications to radar, HF communications, hydroacoustics, and seismology. His most recent work is in self-adaptive signal processors, particularly in large antenna arrays. Since 1971, he has been a Professor with the Moore School of Electrical Engineering at the University of Pennsylvania, Philadelphia, and Director of its Valley Forge Research Center, where he is engaged in development of a large self-adaptive microwave imaging system called the Radio Camera. He is the author of *Principles of Aperture and Array System Design* (Wiley, 1976), in which early radio camera concepts are described, and currently is preparing a detailed book on the subject. He also is a consultant in the Airborne Radar Branch of the Naval Research Laboratory.

Dr. Steinberg is a member of U.S. Commissions B and C of the International Scientific Radio Union (URSI).



**Eli Yadin** (S'79) was born in Haifa, Israel, in 1950. He received the B.S. degree in electrical engineering from Technion—Israel Institute of Technology, Haifa, in 1972 and the M.S. degree in electrical engineering from Tel Aviv University in 1978. He recently completed the Ph.D. dissertation in systems engineering at the University of Pennsylvania, Philadelphia, 1981.

From 1972 through 1977 he was a military and electronic systems engineer in the Israeli Air Force where he was involved in areas of radar and fire control systems. From 1978 through 1981 he was a graduate student and held a research fellowship at the University of Pennsylvania. His recent research work is in the area of large self-adaptive antenna arrays. He is now employed by Interspec, Inc., Philadelphia, PA.

# Self-Cohering an Airborne Radio Camera

BERNARD D. STEINBERG, Fellow, IEEE  
Valley Forge Research Center

ZLI YADIN, Student Member, IEEE  
Interspec Inc.

By distributing antenna elements or small subarrays throughout the skin of an aircraft, a large portion of the airframe can act as an electromagnetic transducer. The basic problem associated with such a design is that uncertainties in element locations due to the nonrigidness of the airframe induce phase errors. Self-cohering techniques are required to compensate for these errors. Four such techniques are presented here.

Manuscript received March 15, 1982.

This work was supported in part by the Air Force Office of Scientific Research and in part by the Office of Naval Research.

Authors' addresses: B.D. Steinberg, Valley Forge Research Center, The Moore School of Electrical Engineering, University of Pennsylvania, Philadelphia, PA 19104; E. Yadin, Interspec Inc., Philadelphia, PA 19104.

0018-9251/83/0500-0483 \$00.75 © 1983 IEEE

## I. INTRODUCTION

The radio camera technique is a potential solution to the problem of making an airborne antenna array conform to an arbitrary surface. A radio camera normally is a large aperture system, usually at microwaves, in which the antenna array may be distorted and its surface may be varying with time [1]. The distortion may also be electrical as due to differential electrical coupling from the antenna elements to the local environment. Distortion of the phase front across the array also results when the velocity of propagation is not constant in the medium [2].

All three sources of distortion introduce phase errors into the radar echoes received at the antenna elements of the phased array. In general, these errors are random and unknown a priori. However, they can be measured if radiation having a phase front of known geometry is made to illuminate the array and if the measurements can be used to calibrate a bank of phase shifters associated with the antenna elements. Let  $\phi_{i0}$  be the expected phase of the signal received at the  $i$ th element from a known reference field, and let  $\phi_i$  be the measured phase. The difference  $\delta\phi_i = \phi_{i0} - \phi_i$  is the phase distortion due to the several sources described above. The error can be corrected completely for the reference radiation field by adding a calibration phase  $-\delta\phi_i$  to the  $i$ th phase shifter. The effect is to calibrate the array perfectly for a target located at the source of the reference field. Fortunately, the same calibration is adequate over a field of view reasonably large compared with the size of most radar targets. It has been shown that when the primary source of distortion is geometric and characterized by a standard deviation  $\sigma_x$ , the angular field of view (in radians) centered on the source of the reference field is  $\lambda/2\pi\sigma_x$ , where  $\lambda$  is the wavelength [3]. For example, if  $\sigma_x = 10\lambda$ , which is two orders of magnitude larger than conventional phased array (or dish or lens) tolerance, the field of view is about  $1/60$  rad or  $1^\circ$ . This is very large compared with most targets and target complexes. (For still larger fields of view, such as is needed for wide angle search, more than a single reference field is required [4].)

The ideal reference source is a point source in free space [5]. The reference field is planar or spherical, according to the distance to the source. A corner reflector is an excellent source, for it is physically small while it exhibits a large radar cross section. An active beacon transponder similarly makes a good phase synchronizing source. Both are practical for use with fixed, ground-based systems, but neither is practical when the system is airborne.

An airborne radio camera cannot depend upon such implanted reflectors or active sources. Instead, it must depend upon echoes from the ground or sea surface and man-made targets of opportunity. This paper discusses four techniques for self-synchronizing a nonrigid, arbitrarily conformal, distorted airborne phased array on such radar echoes.

## II. MINIMUM ECHO-AMPLITUDE VARIANCE TEST

This algorithm is described in [1]. It consists of three parts. First, the variance of the amplitudes of the group of echoes from each range bin, measured at each element in the array, is calculated. The range bin having the lowest echo variance, when normalized to the average echo power in that range bin, is selected as the reference range for the system. Second, the processor either multiplies the complex sample at each array element from each range trace by the complex conjugate of the echo at the reference range or, more simply, merely phase rotates the received echoes by the phases of the complex conjugates of the signals at the reference range. This is the adaptive part of the process. Third, the processor applies linear phase weighting across the array to electronically scan the adaptively formed beam in angle.

The object of the first step is to find a target or a clutter patch whose reradiation most closely approximates that of the point source. The object of the second step is to self-cohere the array upon that target. The object of the third step is to scan the beam in angle to the left and right of that target.

This algorithm is very simple to implement. It requires no special filtering of the radar echoes nor any complicated signal processing. It was possible to test this algorithm recently with airborne radar data [6]. The experiment used recorded data obtained from Dr. Fred Stauder of the Naval Research Laboratory (NRL). An 8-element UHF phased array was flown at 200 knots at an altitude of 15 000 to 20 000 ft over the southeastern portion of the United States. The transmitting pattern was Dolph-Chebyshev-weighted for -24 dB sidelobes. The received radar echoes were separately recorded on each of the 8 channels in a high quality digital recording system.

Demodulation was coherent and the in-phase and quadrature video channels were recorded with 10-bit precision. A functional sketch is shown in Fig. 1.

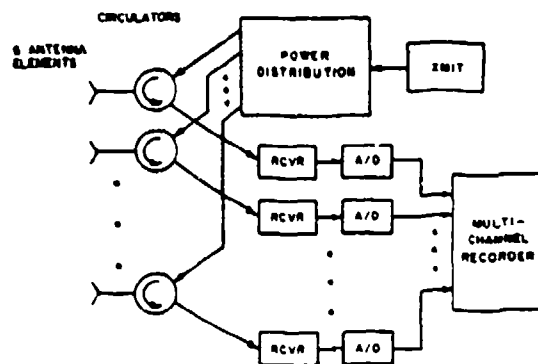


Fig. 1. NRL experimental equipment.

Although a radio camera array would be expected to be flexible and distorted, the NRL antenna was rigid. Hence, its proper performance was predictable and could be compared with the performance of the system when the adaptive algorithm was applied. That is, two beamforming algorithms were applied to the multichannel recorded data. The first was the conventional linearly phase-weighted beamforming procedure. The second was the self-cohering algorithm described above. The results are shown in Fig. 2.

The solid curve of Fig. 2 shows the pattern which resulted from the adaptive process. As is explained in [3] and [7], the beam which is formed by the adaptive procedure is directed toward the dominant scattering center in the illuminated ground patch in the range bin selected by the signal processor for adaptive beamforming. Hence,

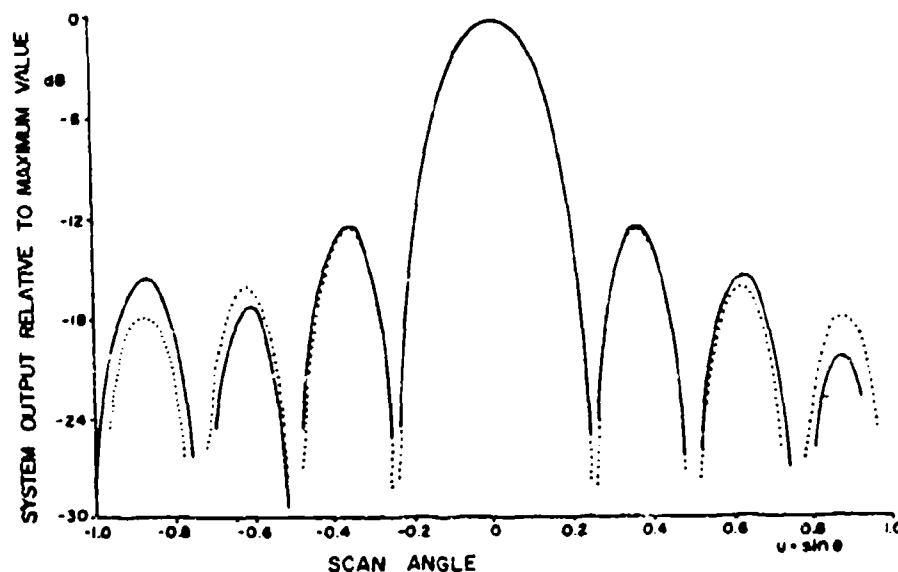


Fig. 2. Comparison of patterns formed adaptively (solid) and nonadaptively. Beam direction near ground track of aircraft.

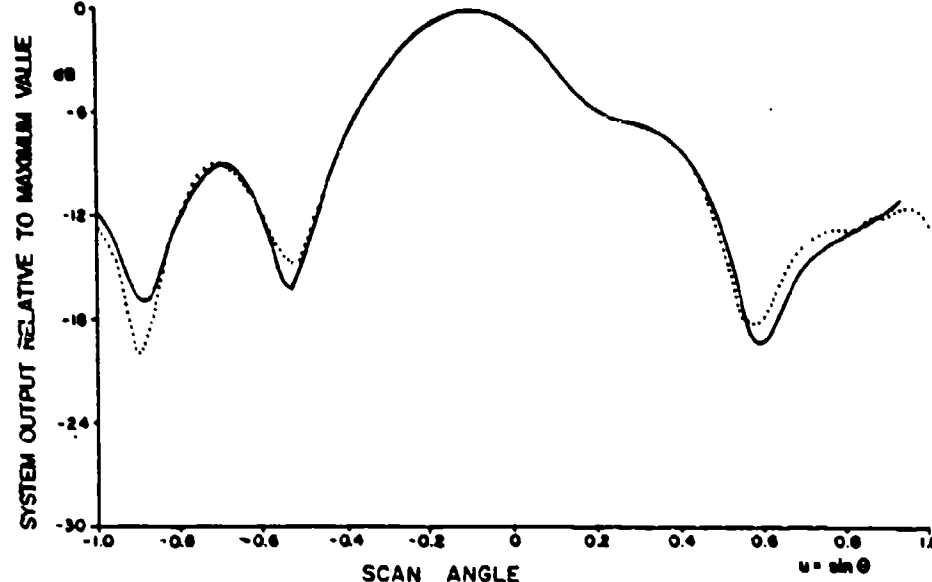


Fig. 3. Comparison of scanned outputs of adaptively (solid) and nonadaptively formed beams.

the origin will usually differ from the bearing of the transmitter array. In this experiment the difference turned out to be 0.07 rad or  $\sim 0.3 \lambda/L$ , where  $\lambda$  is the wavelength and  $L$  is the antenna length. The bearing of the transmitting array was fixed at  $0.6^\circ$  from the flight direction. The dashed curve shows the receiving pattern of a uniformly weighted 8-element array associated with conventional nonadaptive beamforming. The origin of that pattern which is the bearing of the transmitting array has been shifted by 0.07 rad so that the adaptive and nonadaptive patterns can be compared. The results are very similar, indicating that the adaptive process worked well. The smallest normalized echo variance observed was 0.0026.

A study has been made to determine the largest normalized echo amplitude variance that provides satisfactory adaptive beamforming results. Considering the radiation pattern to be acceptable when the first sidelobe has no more than doubled (risen to  $-10$  dB), it has been found that the normalized echo amplitude variance can be as large as 0.02.

The largest echo variance observed in the range traces examined was 0.77. Adaptive beamforming on such a range bin is not fruitful. The high variance, on the other hand, implies a complicated echo profile in the ground patch which therefore makes such a range bin interesting to image; it is possible to self-cohere the array on the echoes from a low-variance bin and scan the adaptively formed beam at the high-variance bin as well at all other ranges. Fig. 3 is an example. There the beam is self-cohered at the range bin used in Fig. 2 and then scanned at the range bin having the 0.77 variance (solid curve). The response of the rigid, electronically scanned phased array is shown dashed. Again the agreement is excellent, indicating that this simple algorithm has promise of being suitable for self-cohering an airborne phased array.

### III. DOPPLER-AIDED SYSTEM

While the experiment reported above and in [6] yielded highly satisfactory results, the technique contains an inherent difficulty. The problem is that the illuminated ground patch, because of its large size, is highly likely to contain more than one large radar target. When this happens, the reradiation from such a range bin is inappropriate for use as a phase synchronizing field. That the cross range dimension of the illuminated ground patch is very large compared with the sizes of reflecting structures is readily seen: its size is approximately  $\lambda R/L$ , where  $R$  is the distance to the patch. In general, the transmitting antenna will be a conventional antenna for airborne radar, which means that  $L/\lambda$  will be on the order of 20 to 50. Even at a relatively short range such as 20 km, the cross range dimension is several hundred meters. Thus notwithstanding the excellent results described above, it is possible that natural terrain and manmade target complexes will, from time to time, deny the system the ability to self-synchronize on the algorithm described above. A Doppler-aided technique described in this section helps to solve that problem.

Fig. 4 shows an aircraft flying with speed  $V$  illuminating a ground patch with a transmitting beam having beamwidth  $\Delta\theta$ . The width of the illuminated sector is  $R\Delta\theta$ . Each of the three large-cross-section reflectors shown in the illuminated patch reradiates a spherical field which is essentially planar at the aircraft (Fig. 5). The sum of the three fields has a highly nonplanar phase front, which therefore renders it inadequate for the self-cohering algorithm described earlier. The radiations from the three targets, however, originating from different bearing angles, have different Doppler shifts. Thus, narrowband filtering, akin to synthetic aperture processing, can pass the echoes from, say, the central target while re-

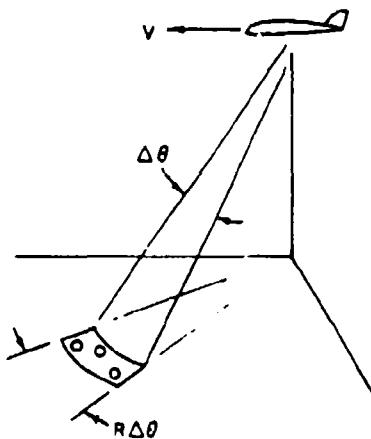


Fig. 4. Narrowband filter in receiver passes echoes from narrow strip in illuminated ground patch.

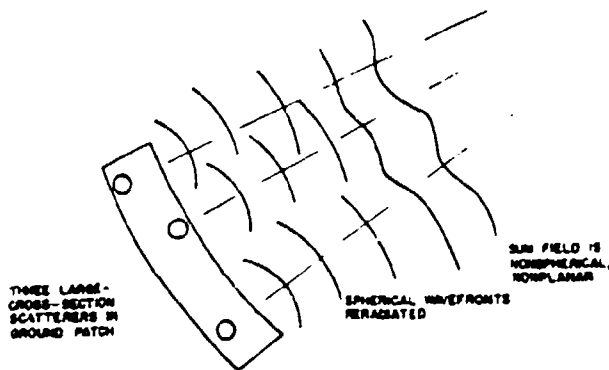


Fig. 5. Ground patch detail.

jecting the radiation fields of the others. In this way, a large, area-extensive clutter patch containing many prominent reflectors can be effectively reduced to a small, confined patch reradiating a planar wavefront at the aircraft.

To insure that the radar backscatter is essentially planar across the array, the effective cross range dimension of the scattering region must be small enough so that the lobes of the reradiation pattern from the clutter, no matter how complex or irregular, are large compared with the aircraft size. The lobe spacing at the aircraft is about  $\lambda R/T$ , where  $T$  is the cross range dimension of the reradiating patch, which must be on the order of twice the aircraft size, assuming that the entire aircraft is used for the receiving array [5]. This fact and the Doppler relation between aircraft speed, wavelength, and target angle ( $f_d = 2V \cos \theta / \lambda$ ) places the following requirement upon the bandwidth  $W$  of the narrowband filter:  $W = 2V/L$  where  $L$  is the aircraft size [7].

Narrowband filtering need be only in a single antenna element channel in the system. Fig. 6 shows the minimal circuitry. The filtered output from one antenna element serves as a reference wave for measuring in that figure involves phaselock loops. The efficiency of operation is improved if narrowband filters are added to each channel, as shown dashed.

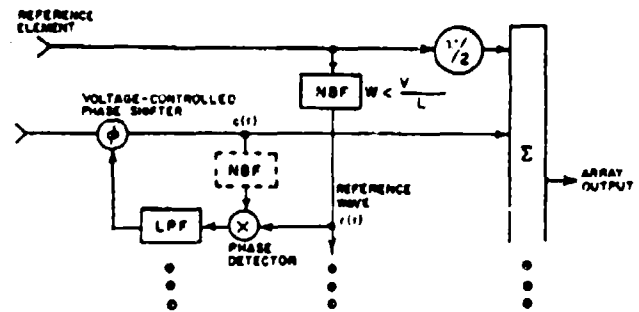


Fig. 6. Reference element and one other element in airborne radio camera. All signals phaselocked by clutter-derived reference wave obtained from narrowband filter.

#### IV. MIXTURE OF I AND II

Using Method II, echoes from every range bin will have a suitably low amplitude variance across the array to be useful for adaptive beamforming. However, the integration time  $T \sim W^{-1}$  may be excessive for certain missions. In this case, a shorter integration time followed by the minimum echo amplitude variance test I may be used. Let the integration time  $T = kW^{-1}$ , where  $k$  is, say,  $1/2$  or  $1/3$  or  $1/4$ . Then the Doppler-reduced patch is two or three or four times too large to insure a planar wavefront across the array but is still many times smaller than  $R\Delta\theta$ , the cross range dimension of the path illuminated by the transmitter. Although it is not small enough to insure planar reradiation, the likelihood that the radiation is planar has materially increased. In other words, by integrating as long as is practical, the probability is maximized for achieving the excellent results demonstrated with the first algorithm.

#### V. MINIMUM CLUTTER BANDWIDTH CRITERION

Method II is appropriate when the terrain is "frozen." If the scatterers are wind driven or if the backscatter is from the sea surface, the Doppler shift associated with each scattering center is related not only to its bearing angle from the radar, but also the radial component of its motion. This smearing of the Doppler signature by scatterer motion effectively spreads or enlarges the size of the clutter patch whose echoes pass through the Doppler filter. Calculations show that the Doppler spread associated with backscatter from the sea surface at wavelengths shorter than 0.3 m is too great to depend on Method II [8].

A more complicated signal processor which accommodates the additional Doppler spread due to scatterer motion is described in this section. Conceptually, an adaptive array of the kind used to solve adaptive nulling problems is introduced. A least mean square (LMS) closed loop circuit including a band reject filter (BRF) is designed to set the complex weights of the antenna elements in such a fashion as to minimize the spectral spread of the clutter echoes as they pass through the filter. Provided that the clutter is statistically homogeneous,

clutter, this condition is equivalent to forming a beam with minimum beamwidth. The technique is described below.

Fig. 7 demonstrates the relationship between spatial and spectral properties. Since scatterers are tagged in an

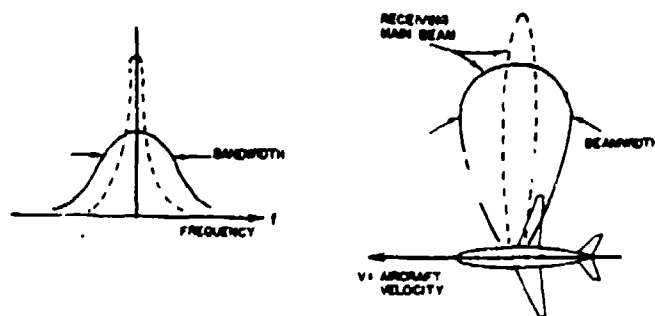


Fig. 7. Array beam pattern and clutter spectrum. ---: After array is cohered. —: Before array is cohered.

gle by their Doppler shifts, the spectral bandwidth of clutter echoes measured at the output of the array is monotonic with the beamwidth of the radiation pattern. Any circuit that minimizes the bandwidth of the clutter also minimizes the array beamwidth.

One such circuit is shown in Fig. 8. This circuit is an adaptive subsystem for determining the weights. Following the adaptive weight setting, the weights are frozen and the band reject filters are bypassed by the target echoes. The discussion below relates only to the self-cohering mode where inputs are sea clutter echoes. The outcome of the process is a proper weighting vector. The input vector  $X^T = (X_1, X_2, \dots, X_n)$  is applied to a bank of reject filters. The weighted sum  $Y'(t)$  is applied to an LMS constrained subsystem that constantly changes the weighting vector  $W$  so as to minimize the mean output power  $E\{|Y'(t)|^2\}$  while maintaining the system gain  $\sum_{i=1}^n |W_i|^2$  constant.<sup>1</sup>

The operation of the system can be understood by considering the following. The beamforming direction is determined by the notch frequency of the band reject filters. The system is constrained not to shut itself off. Hence, in order to minimize the output power  $E\{|Y'|^2\}$ , the system must form nulls toward the directions from which signals are coming. Signals arrive, however, from

<sup>1</sup> $W_i$  is the complex weight  $W_{i1} + jW_{i2}$ .  $X_i$  is phase shifted by  $\pi/2$  to produce quadratic components. Weighting the quadrature components by two real weights ( $W_{i1}, W_{i2}$ ) is equivalent to weighting  $X_i$  by the complex weight  $W_i$ .

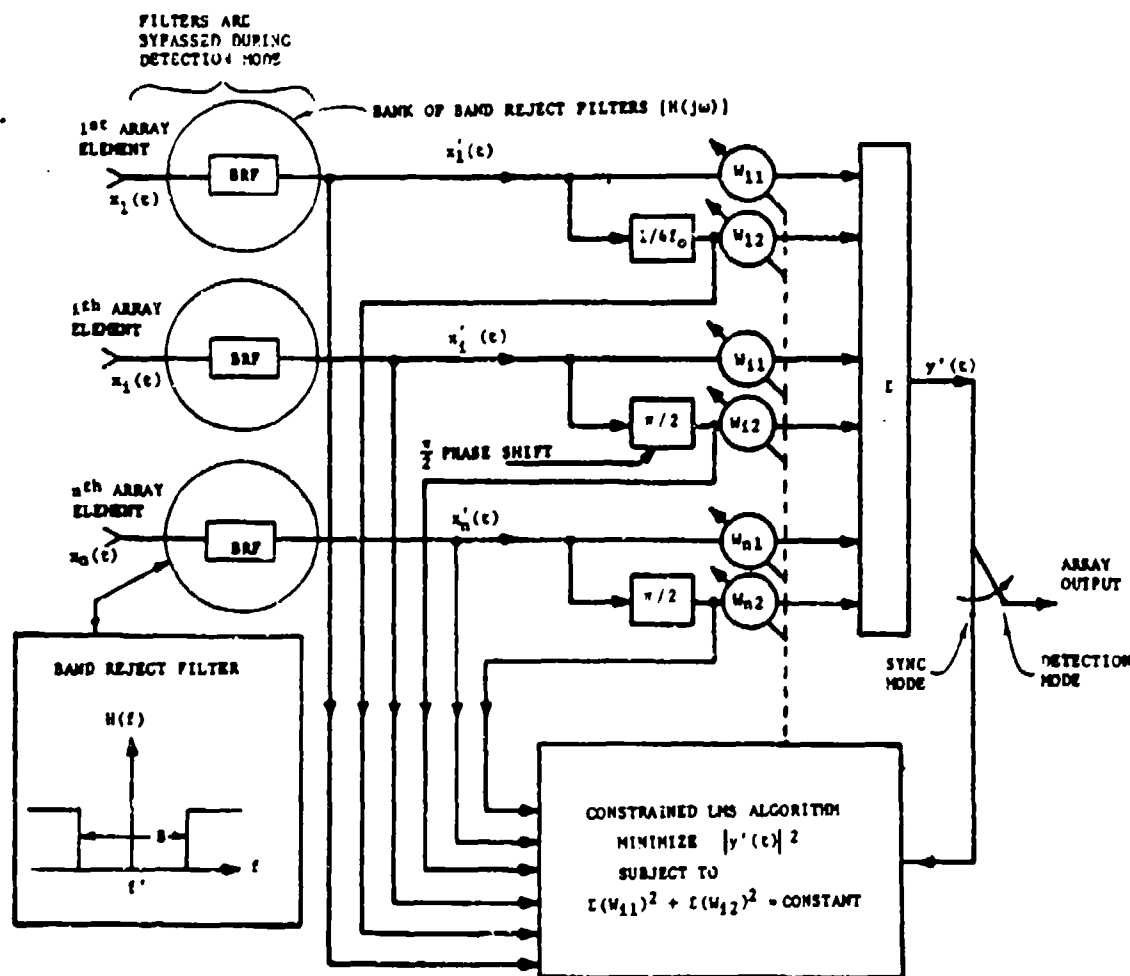


Fig. 8. Adaptive subsystem controls weights during self-cohering.

all directions within the azimuthal sector illuminated by the transmitter. The nulls, therefore, are deployed in those directions from which the clutter power is greatest. Fig. 9 shows that the clutter power passing through a BRF is smallest for echoes arriving from the desired look

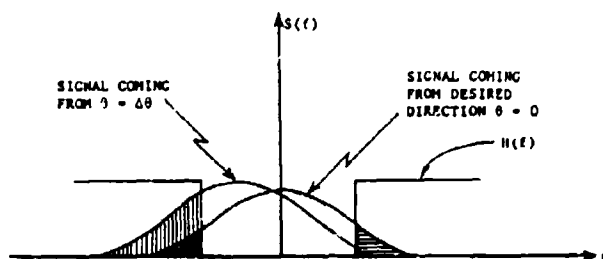


Fig. 9. Ideal band reject filter and two echo spectra.  $\equiv$ : Clutter coming from desired direction.  $\equiv$ : Clutter coming from other direction.

direction, and the output power increases as the angle of arrival (relative to the desired look direction) increases. Since the clutter power passing through the BRF from the desired direction is smaller than from any other direction, no null is placed in that direction. Thus the process results in the formation of a main beam. A detailed analysis is given in [8].

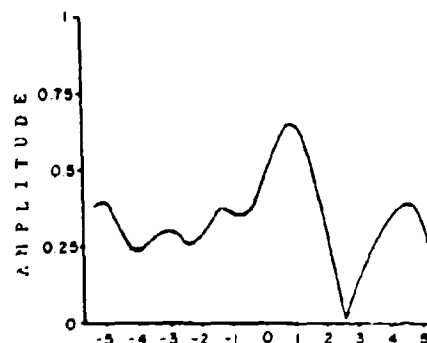
This adaptive beamforming technique was successfully computer-tested with simulated sea clutter echoes. The experiments involved a 7-element array 2.9 wavelengths long, and a variety of system parameters. Uncertainties in element locations are accounted for by assuming that initially the array is weighted with random complex weights  $W_1(0), W_2(0), \dots, W_n(0)$  which are independent of the element positions. The outcome of the self-cohering process is a set of weights  $W_1, W_2, \dots, W_n$ . This set defines the radiation pattern of the array. During the synchronization process, the sea clutter echoes are received by the different array elements. Clutter echoes are modeled as a sum of several independent Gaussian processes  $g_1(t), g_2(t), \dots, g_s(t)$ , each process representing echoes reradiated from a different direction. The processes have the same spectral shapes, but each is shifted in frequency due to its assumed direction of arrival ( $f_d = 2V \cos \theta / \lambda$ ). Coherent demodulation at the front end is assumed. Thus clutter echoes arrive at the different elements with different phases due to the different geometrical locations of the elements and the directions of arrival of the different clutter components. The simulated inputs are time samples of the sum of the Gaussian processes. A gradient search technique based on the Widrow LMS algorithm [8-10] is used to find the optimum weighting vector  $W$  which minimizes the mean output power  $E\{|Y'(t)|^2\}$  subject to a constant gain constraint ( $\sum |W_i|^2 = 1$ ). The process is iterative in  $W$  as given by [8]:

$$W(j+1) = W(j) - \mu Y'(j) * [X'(j) - W(j)Y'(j)] \quad (1)$$

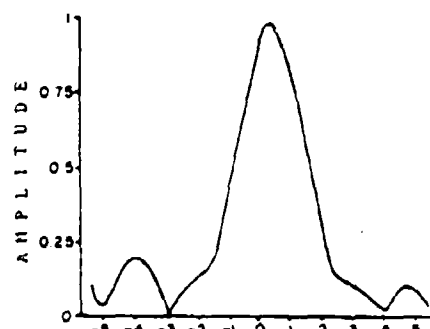
where  $j$  represents the iteration number and  $\mu$  is a constant gain. It is shown in [8] that the iterative process

converges to the desired solution in  $W$  for  $0 < \mu < 2/p$  where  $p$  is the expected output power  $E\{|Y'(t)|^2\}$ .

Fig. 10 shows the results of one of the simulated experiments in which an ideal BRF, as shown in Fig. 10,



(units of  $\lambda/2L$ )  $u = \sin \theta$   
(a)



(units of  $\lambda/2L$ )  $u = \sin \theta$   
(b)

Fig. 10. Broadside adaptive beamforming; no noise injected; ideal filtering assumed. (a) No adaptation (initial pattern). (b) After 70 iterations.

was used. Fig. 10(a) is the pattern associated with the initial random weights  $W(0)$ . Fig. 10(b) is the pattern achieved after 70 iterations of the adaptive process (1). The 3 dB beamwidth is  $0.9 \lambda/L$  and the main-beam gain toward the desired look direction is  $-0.2$  dB;  $0.76 \lambda/L$  and  $0$  dB represent ideal coherent summation. Similar results were obtained with realistic, 5-pole band reject filters.

Fig. 11 shows the same problem with noise added. The upper figure shows successful convergence with  $\text{SNR} = 10$  dB at the input to the BRFs. The lower figure shows significant gain-loss and rising sidelobes at  $\text{SNR} = 5$  dB, notwithstanding a quadrupling of the allowed time for convergence. In many such simulation experiments, 10 dB SNR was found to be a safe threshold for successful operation.

## VI. SUMMARY

By distributing antenna elements or small subarrays throughout the skin of an aircraft, a large portion of the

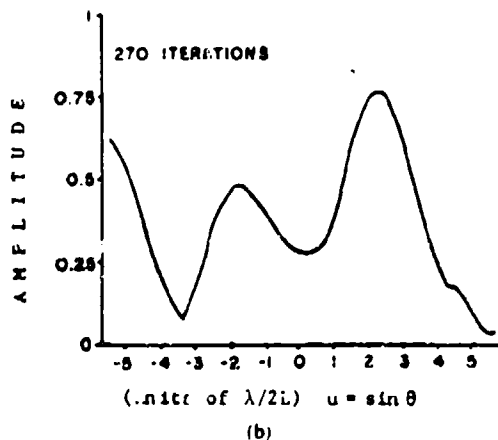
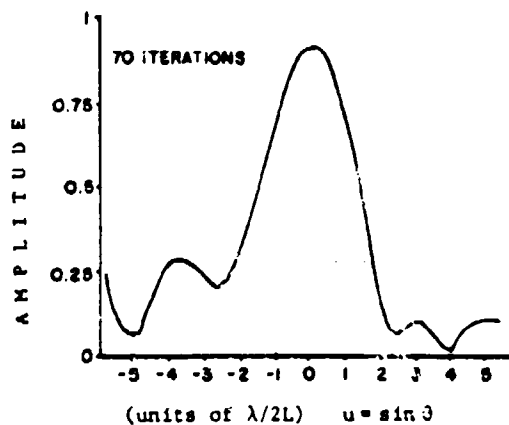


Fig. 11. Noise added to simulation of Fig. 10. (a) SNR = 10 dB. (b) SNR = 5 dB.

airframe can act as an electromagnetic transducer. The basic problem associated with such a design is that uncertainty in element locations due to the nonrigidness of the airframe induces phase errors. Self-cohering techniques are required to compensate for those errors. Four such techniques are presented in this paper. The first technique searches in range for a good phase synchronizing source. It uses a minimum echo-amplitude variance test to select the "best" range bin, after which it uses echoes reradiated from the selected range bin in a self-cohering process. This technique was tested successfully with airborne radar data of land clutter echoes obtained from an NRL experiment. The major advantage of this technique is its simplicity. There is, however, an inherent problem, which is the dependence on the existence of targets of opportunity that can act as good phase synchronizing sources.

The other techniques use Doppler filtering to extract the desired phase synchronizing signal. They are more complicated but they do not depend upon proper targets of opportunity. Technique II can adaptively beamform on echoes reradiated from a frozen terrain. Technique III is a mixture of I and II and is also suitable for frozen terrain. The fourth algorithm, which is the most complicated one, can operate upon wind-driven clutter echoes such as sea clutter, as well as land clutter echoes. This technique uses a constrained LMS algorithm to adaptively adjust the element weights of the phased array so as to minimize the output clutter spectral bandwidth. Its validity is demonstrated through computer simulations.

# REFERENCES

- [1] Steinberg, B.D. (1981)  
Radar imaging from a distorted array: The radio camera algorithm and experiments.  
*IEEE Transactions on Antennas and Propagation*, Sept. 1981.
- [2] Steinberg, B.D., and Luthra, A.K. (1982)  
A simple theory of the effects of medium turbulence upon scanning with an adaptive phased array.  
*Journal of the Acoustical Society*, Mar. 1982.
- [3] Steinberg, B.D. (1973)  
Design approach for a high-resolution microwave imaging radio camera.  
*Journal of the Franklin Institute*, vol. 296, Dec. 1973.
- [4] Dorny, C.N. (1978)  
A self-survey technique for self-cohering of antenna systems.  
*IEEE Transactions on Antennas and Propagation*, Nov. 1978, pp. 877-881.
- [5] Steinberg, B.D.  
Properties of phase synchronizing sources for a radio camera.  
Submitted to the *IEEE Transactions on Antennas and Propagation*.
- [6] Steinberg, B.D. and Yadin-Jadlovker, E. (1982)  
Radio camera experiment with airborne radar data.  
*Proceedings of the IEEE (Letters)*, Jan. 1982, pp. 96-98.
- [7] Steinberg, B.D. (1976)  
*Principles of Aperture and Array System Design*.  
New York: Wiley, 1976.
- [8] Jadlovker, E. (1981)  
Phase synchronizing distributed, adaptive airborne antenna arrays.  
Ph.D. Dissertation, 1981.
- [9] Widrow, B., et al. (1967)  
Adaptive antenna systems.  
*Proceedings of the IEEE*, vol. 55, Dec. 1967, pp. 2143-2159.
- [10] Owsley, N.L. (1971)  
Source location with an adaptive antenna array.  
Technical Document NL-3015, U.S. Naval Underwater and Systems Center, 1971.



**Bernard D. Steinberg** (S'48—A'50—SM'64—F'66) was born in Brooklyn, N.Y., in 1924. He received the B.S. and M.S. degrees in electrical engineering from the Massachusetts Institute of Technology, Cambridge, in 1949 and the Ph.D. degree from the University of Pennsylvania, Philadelphia, in 1971.

He worked in the Research Division of Philco in the 1950s, specializing in radar backscatter and radar signal processing. He was one of the founders of General Atronics Corporation in Philadelphia in 1956 and served as its Vice President and Technical Director for 15 years. His work there was in signal processing techniques and their applications to radar, HF communications, hydroacoustics, and seismology. His most recent work is in self-adaptive signal processors, particularly in large antenna arrays. Since 1971 he has been a Professor with the Moore School of Electrical Engineering at the University of Pennsylvania, Philadelphia, and Director of its Valley Forge Research Center, where he is engaged in development of a large self-adaptive microwave imaging system called the Radio Camera. He is the author of *Principles of Aperture and Array System Design* (Wiley, 1976), in which early radio camera concepts are described, and currently is preparing a detailed book on the subject. He also is a consultant in the Airborne Radar Branch of the Naval Research Laboratory.

Dr. Steinberg is a member of U.S. Commissions B and C of the International Scientific Radio Union (URSI).



**Eli Yadin** (S'79) was born in Haifa, Israel, in 1950. He received the B.S. degree in electrical engineering from the Technion—Israel Institute of Technology, Haifa, in 1972 and the M.S. degree in electrical engineering from Tel Aviv University in 1978. He is a candidate for the Ph.D. degree at the University of Pennsylvania, Philadelphia.

From 1972 through 1977 he was a military and electronic systems engineer in the Israeli Air Force where he was involved in areas of radar and fire control systems. From 1978 through 1981 he was a graduate student and held a research fellowship at the University of Pennsylvania, where his recent research work has been in the area of large self-adaptive antenna arrays. He is now employed by Interspec Inc., Philadelphia, where he is leading a system design for a high resolution radar system.

### Radio Camera Experiment with Airborne Radar Data

BERNARD D. STEINBERG AND ELI YADIN

**Abstract**—The radio camera signal processing algorithm for retrodirective adaptive beamforming and scanning is demonstrated to work successfully on radar clutter echoes. The experiment was conducted with airborne radar data obtained from the Naval Research Laboratory.

A radio camera is an imaging radar with too large an aperture to ensure that the aperture is mechanically stable. Retrodirective adaptive beamforming techniques are used to cohere or phase-synchronize the array. The receiving beam, after it is self-cohered upon the reradiation from some target outside of the array, can be scanned in angle by conventional, open-loop phased array techniques.

The first experimental radio camera demonstration of high angular resolution imaging appeared in 1979 [1]. In that experiment, a highly distorted, 27-m array, consisting of 100 randomly located sample points, self-cohered on the backscatter from a corner reflector at 210 m. The experiment was conducted at X-band. Thirty meters more

Manuscript received July 29, 1981. This work was supported by the Naval Research Laboratory and the Air Force Office of Scientific Research.

The authors are with the Valley Forge Research Center, Moore School of Electrical Engineering, University of Pennsylvania, Philadelphia, PA 19104.

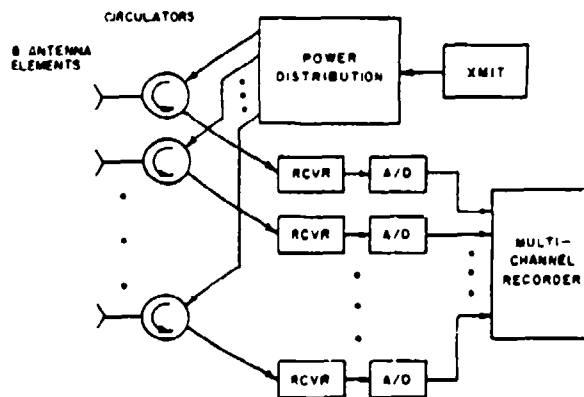


Fig. 1. NRL experimental equipment.

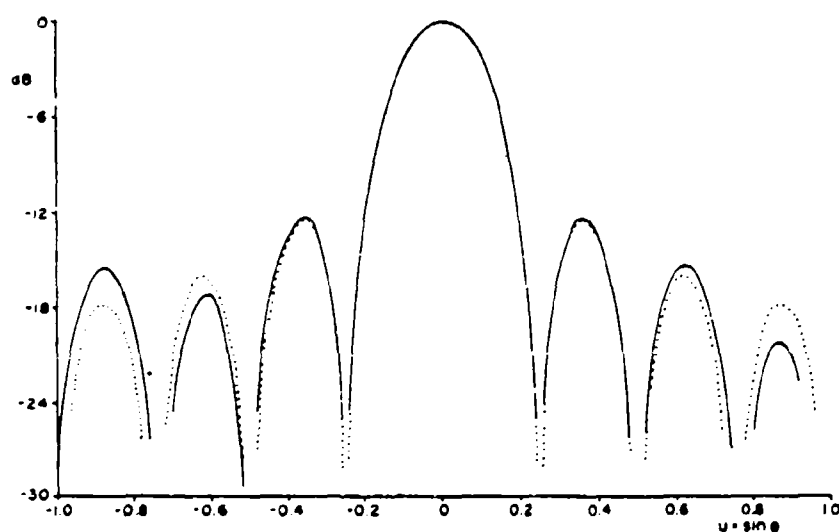


Fig. 2. Comparison of patterns formed adaptively (solid) and non-adaptively. Beam direction is near ground track of aircraft.

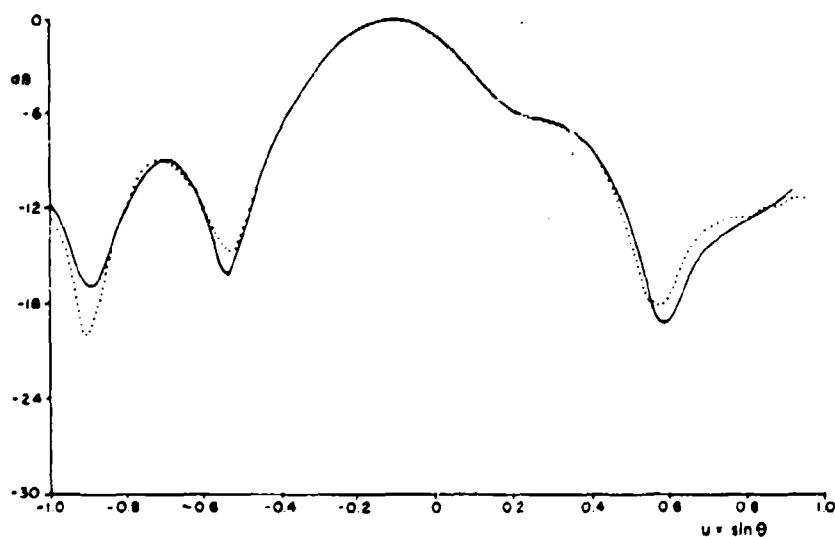


Fig. 3. Comparison of scanned outputs of adaptively (solid) and non-adaptively formed beams.

distant was a target group consisting of two corner reflectors. The beamforming reflector and the target reflectors both were in the near field of the array. In the experiment the adaptively formed beam was refocused to the target range and scanned in angle across the target. The resulting image was indistinguishable from the calculated response of the system when operating in free space.

The experiment reported in this letter used airborne radar data obtained from F. Staudaher of the Naval Research Laboratory. An 8-element UHF phased array was flown at 200 knots at an altitude of 15 000–20 000 ft over the southeastern portion of the U.S. The transmitting pattern was Dolph-Chebyshev-weighted for -24 dB side-lobes. The received radar echoes were separately recorded on each of the 8 channels in a specially designed, high quality digital recording system. Demodulation was coherent and the in-phase and quadrature video channels were recorded with 10 bit precision. A functional sketch is shown in Fig. 1.

One object of the experiment was to test whether the radio camera algorithm would operate successfully upon ground clutter. Since the array was rigid, its proper performance could be predicted and, hence, compared to the performance of the adaptive system.

The radio camera algorithm used in the experiment is described in [2]. The algorithm consists of three parts. First, the variance of the amplitudes of the group of echoes from each range bin is measured. The range bin having the lowest echo variance, when normalized to the average echo power in that range bin, is selected as the reference range for the system. Next, the processor either multiplies the complex sample at each array element from each range trace by the complex conjugate of the echo at the reference range or, more simply, merely phases rotates the received echoes by the phases of the complex conjugates of the signals at the reference range. This is the adaptive part of the process. Lastly, the processor applies linear phase weighting across the array to electronically scan the adaptively formed beam in angle.

The object of the first step is to find a target or a clutter patch whose reradiation most closely approximates that of the point source. The object of the second step is to self-cohere the array upon that target. The object of the third step is to scan the beam in angle to the left and right of that target.

The solid curve of Fig. 2 shows the pattern which resulted from the adaptive process. As is explained in [3], the beam which is formed by the adaptive procedure is directed toward the dominant scattering center in the illuminated ground patch in the range bin selected by the signal processor for adaptive beamforming. Hence, the origin will usually differ from the bearing of the transmitting array. In this experiment the difference turned out to be 0.07 rad or  $\sim 0.3 \lambda/L$  ( $\lambda$  = wavelength,  $L$  = antenna length). The bearing of the transmitting array was fixed at  $0.6^\circ$  from the flight direction. The dashed curve shows the receiving pattern of a uniformly weighted 8-element array associated with conventional nonadaptive beamforming. The origin of that pattern which is the bearing of the transmitting array has been shifted by 0.07 rad so that the adaptive and nonadaptive patterns can be compared. The results are very similar, indicating that the adaptive process worked well. The smallest echo variance observed was 0.0026.

Satisfactory results have been obtained when the normalized echo amplitude variance is 0.025 or smaller. The largest echo variance observed was 0.77. Adaptive beamforming on such a range bin is not fruitful. On the other hand, it is possible to self-cohere the array on the echoes from a low-variance bin and scan the adaptively formed beam at all other ranges. Fig. 3 is an example. There the beam is self-cohered at the range bin used in Fig. 2 and then scanned at the range bin having the 0.77 variance (solid curve). The response of the rigid, electronically scanned phased array is shown dashed. Again the agreement is excellent.

While this experiment has shown that the algorithm works on ground clutter having the proper statistical properties, it has not disclosed the frequency of occurrence of such clutter cells. This knowledge is necessary for system design purposes but unfortunately is not available from the experiment because the transmitting beam of the rigid array was the same width as the receiving beam of the self-cohered array. In contrast, the contemplated airborne radio camera designs use a small, broad-beam transmitter in conjunction with a large, receive-only self-cohered aperture having a very narrow beamwidth [4]. This matter remains to be studied.

#### REFERENCES

- [1] B. D. Steinberg, E. N. Powers, D. Carlson, B. Meagher, Jr., R. S. Berkowitz, C. N. Dorny and S. Seeleman, "First experimental results from the Valley Forge radio camera program," *Proc. IEEE*, vol. 67, no. 9, pp. 1370–1371, Sept. 1979.
- [2] B. D. Steinberg, "Radar imaging from a distorted array: The radio camera algorithm and experiments," to be published in *IEEE Trans. on Ant. & Prop.*, Sept. 1981.
- [3] —, *Principles of Aperture & Array System Design*. New York: Wiley, 1976.
- [4] B. D. Steinberg and E. Jadlovker, "Distributed airborne array concepts," to be published in *IEEE Trans. Aerospace Electron. Syst.*

October 1981

## Appendix C: Space Based Large Array Radar

## HIGH RESOLUTION SURVEILLANCE FROM SPACE

## INTRODUCTION

This unsolicited proposal addresses the critical problem of a high resolution space surveillance system, that of making an antenna array sufficiently large so as to provide the required resolving power. For example, a receiving array in geosynchronous orbit has to be on the order of 100 km in size to have a spot size on the earth of 40 meters. Such a size cannot be achieved with a rigid structure. The antenna array, therefore, will be inherently nonrigid. It may be a flexible aperture or it may be an aperture consisting of a very large number of separate platforms, which may or may not be loosely tethered. A normal antenna array, on the other hand, must be quite rigid, the permitted motions or distortions in its surface being no more than about one-tenth wavelength. Thus the problem of the essential nonrigidity of a huge spaceborne array large enough to provide useful resolving power for surveillance purposes is the critical problem. Without a solution to this problem, no amount of sophisticated designs and light-weight hardware will suffice.

The general problem of the nonrigid antenna array has been studied for the last ten years at the Valley Forge Research Center of the University of Pennsylvania, during which time successful ground-based designs have been made. During the last three years, work has been extended to the airborne platform. Under Air Force Office of Scientific Research support (Grant #78-3688) a study has been conducted to find ways of designing a nonrigid or flexible array to be as large as the aircraft it is carried by. In this work it was assumed that the array was at least as nonrigid as the air frame and the skin of the aircraft. Techniques were created for accomplishing this task, one such technique being successfully demonstrated on airborne radar ground clutter data obtained from the Naval Research Laboratory.

The objective of the proposed program is to study the applicability of these and further advanced techniques to space radar.

The research work done under the AFOSR grant was performed by Dr. Eli Yadin, then a graduate student supervised by Professor Bernard D. Steinberg. Dr. Yadin is now with Interspec Inc., a Philadelphia company located at the edge of the campus of the University of Pennsylvania. The proposed program is for a collaborative effort by Professor Steinberg and Dr. Yadin. Other members of the staffs of both Interspec and Valley Forge Research Center will support the effort, as needed.

#### BACKGROUND

The Valley Forge Research Center has developed procedures during the last decade for designing phased antenna arrays with remarkably fine resolving power. Two such designs under way for the U.S. Army are illustrative. In one, a ground based imaging radar is being designed to provide one-third meter azimuthal resolution at a distance of four kilometers. The second is an airborne (helicopter) array designed to provide three-meter resolving power at a distance of about 60 kilometers. Although the scales are vastly different from what would be relevant for space radar, the techniques developed would be identical.

There are several critical problems facing the designer of a super-resolution system. The size of the array must be huge to achieve the desired resolving power; yet array systems become mechanically unstable or nonrigid when they exceed some limiting size. Some built-in self-adaptive controls are needed to preserve the desired resolution and radiation pattern of the array.

A second basic problem deals with cost. Most phased arrays have antenna elements that are separated by one-half wave length. For an array as large as that required for surveillance from space, the number of components and, therefore, the cost become astronomical.

We have developed solutions to both problems. We use self-cohering, adaptive beamforming procedures for continuously self-organizing the array

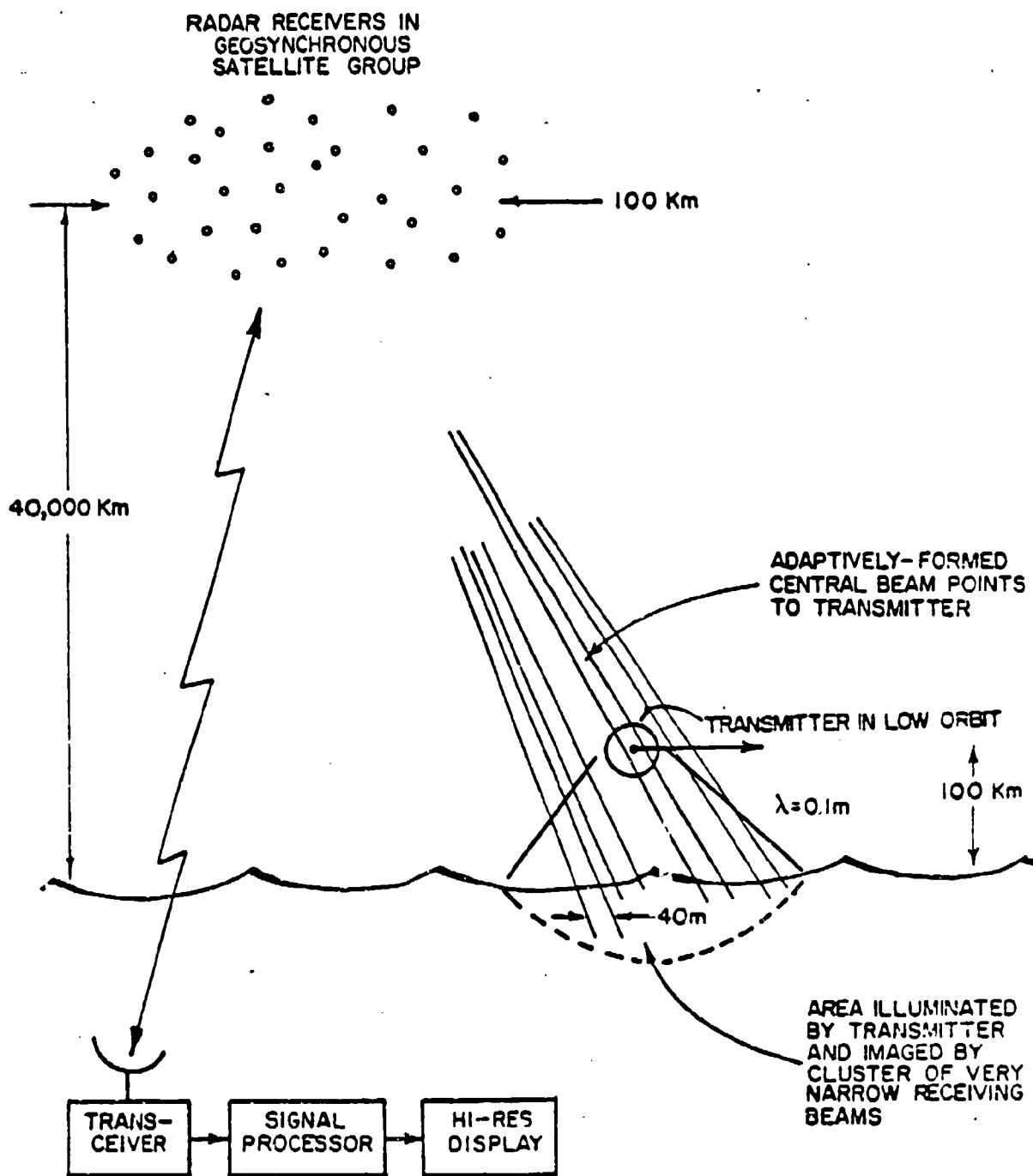
irrespective of deformations in its geometry. We have also learned the rules for drastically thinning the array so that no more than the order of 1000 parts typically are required.

While the method is sufficiently developed to be applied to ground-based problems, as for example, the two Army projects indicated above, a more basic study is required for exploration of the applicability of the techniques to untended and unmaintained space vehicles. This is a proposal for such a study.

We have carried our studies beyond the ground based system stage. Recently, we have completed a three-year examination of the applicability of the radio camera (which is our name for instruments based upon this technology) to aircraft, with emphasis upon designs for airborne early warning (AEW) aircraft.

#### CONCEPT

There are many possible system concepts that we have contemplated, one of which is sketched in Figure 1. The extremely fine resolution is obtained from a space-borne array, which is a distribution of microwave receivers aboard a large group of geosynchronous satellites. The satellites are clustered, covering a region the order of 10 to 100 kilometers. They are in radio contact with the earth, which provides supervisory instructions by the uplink and which receives the radar signals transmitted to the ground via the down link. The receivers, in geosynchronous orbit, detect echoes from the earth, which is illuminated by a microwave transmitter in a low-orbiting trajectory. The transmitter uses a one-meter dish to illuminate the ground and the sea surface underneath the orbiting satellite. The back radiation toward the receiving array is used by the receiving system to adaptively form a high resolution beam in the direction of the transmitter. Thus the movement of the transmitter scans the receiving radiation pattern.



## Appendix D

### 6. FORWARD LOOKING SYNTHETIC APERTURE RADAR<sup>\*</sup>

C. Nelson Dorny

A conventional synthetic aperture radar is side looking. The platform flies in a carefully controlled straight line perpendicular to the direction in which imaging is desired. An adaptive beamforming scheme is proposed in [1] for loosening the tolerance on the flight path in order to obtain high resolution images with a helicopter-borne synthetic aperture radar (SAR).

There is no theoretical reason why an arbitrarily shaped flight path could not be used to form the synthetic aperture if the motion were known adequately. Adaptive techniques such as those used in [1] may provide sufficiently loose tolerances on flight path knowledge to permit considerable flexibility in the SAR flight path. This article describes forward-looking SAR concepts which may be applicable for terrain-follower imaging at microwaves.

Figure 6.1 shows the top view of a vehicle flight path which provides a significant forward-looking synthetic aperture. The beamwidth of the forward-looking SAR is 2 to 3 orders of magnitude smaller than the beamwidth associated with the real aperture. The actual usable synthetic aperture is a function of the vehicle velocity and the distance to the target region. According to Figure 6.2, if  $V$  is the vehicle velocity,  $T$  is the time permitted for cross-range motion, and  $\theta$  is the angle of flight relative to the target direction, then the aperture size is  $D = VT \sin\theta$ . Assume that the cross-range travel time must be limited to  $VT \leq 0.1R$ , where  $R$  is the range to the target, in order that the vehicle have time to maneuver before it reaches the target. This restriction limits the synthetic aperture

---

<sup>\*</sup>This work is principally supported by the Air Force Office of Scientific Research under Grant No. AFOSR-78-3688.

[1] Earl N. Powers, et al., "System Design Considerations for a High Resolution Airborne Imaging Radar," Valley Forge Research Center Quarterly Progress Report No. 24, February 1978, pp. 40-58.

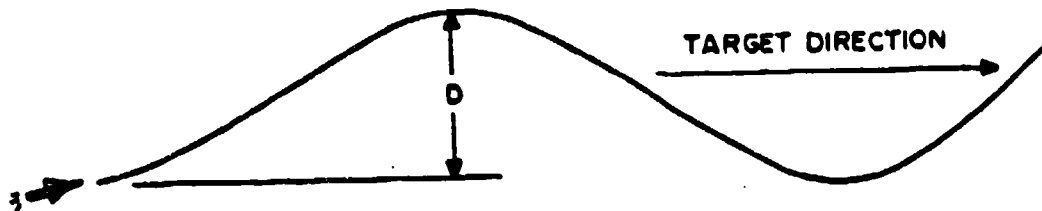


FIGURE 6.1 VEHICLE FLIGHT PATH FOR FORWARD LOOKING SYNTHETIC APERTURE (D = aperture size).

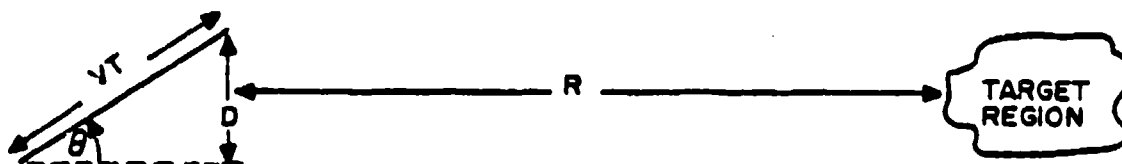


FIGURE 6.2 GEOMETRY FOR SYNTHETIC APERTURE CALCULATION

size. The beamwidth associated with the synthetic aperture is  $\lambda/2D$ , where  $\lambda$  is the radiated wavelength. Thus, the minimum beamwidth  $\theta_B$  is

$$\theta_B = \frac{\lambda}{2(0.1R)\sin\theta} = \frac{5\lambda}{R\sin\theta} \quad (1)$$

Suppose  $V = 300$  meters per second (583 nautical miles per hour),  $R = 10$  km,  $\theta = 10^\circ$ , and  $\lambda = 0.03$  m (X-band). Then  $T = 3.3$  sec and  $\theta_B = 8.6 \times 10^{-5}$  rad. The corresponding cross-range resolution at the target is  $R\theta_B = 0.86$  meters.

An inertial platform can provide an approximate indication of the flight path. However, the accuracy will probably not be within the  $\lambda/10$  tolerance required for beamforming. For imaging purposes, however, the return from strong, isolated scatterers can be used to assist the focusing,

thereby loosening the required tolerances. According to [2, p. 249] (see Figure 6.3), the relationship between  $\sigma_x$ , the cross-range position tolerance of the platform, and  $\theta_m$ , the maximum angle of scan from the point of adaptive beam formation, is  $\sigma_x = \frac{\lambda}{4\pi\theta_m}$ . If  $L$  is the cross-range dimension of the target region to be imaged, then  $\theta_m = L/2R$ , and

$$\sigma_x = \lambda R / 2\pi L \quad (2)$$

Suppose  $L = 250$  m,  $\lambda = 0.03$  m and  $R = 10$  km. Then  $\sigma_x = 0.2$  m, a reasonable tolerance on relative position location using an inertial platform.

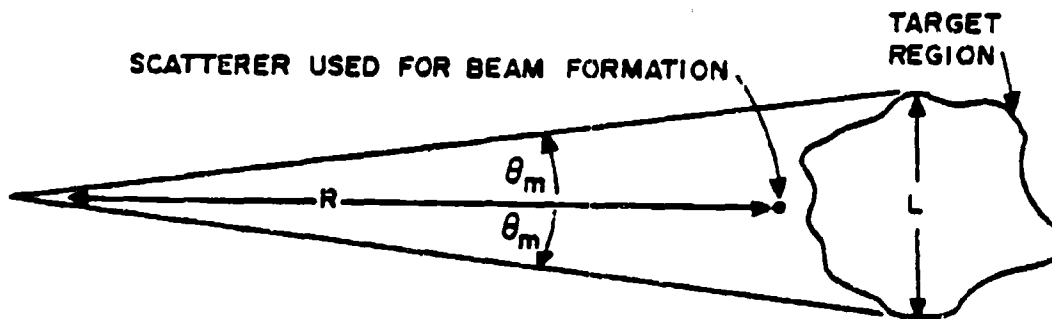


FIGURE 6.3 GEOMETRY ASSOCIATED WITH TARGET IMAGING.

If a strong isolated scatterer is not available in the neighborhood of the target, it may be possible to use range (time of arrival) and doppler (angle of arrival) to isolate the signal reflected from a small clutter patch to achieve the same purpose. Another alternative is to fly a weak beacon or reflector ahead of the imaging receiver for the purpose of providing help in beamforming.

The amount of processing which is required to form synthetic aperture images by conventional means is excessive for real-time on-board processing. However, the data can be thinned drastically without affecting the

[2] Bernard D. Steinberg, Principles of Aperture and Array System Design, John Wiley and Sons, New York, 1976.

beam properties significantly [1]. The primary effect of data thinning (thin spatial sampling of the target reflection across the aperture) is an increase in the sidelobe level of the synthetic beam. Grating lobes are suppressed by randomizing the positions of the spatial samples. The expected average sidelobe power level is  $1/N$ , where  $N$  is the number of samples in the sampled aperture. The peak sidelobe level should be no more than 10 dB higher than the average level. Consequently, 1000 samples are expected to provide a -30 dB average sidelobe level and a -20 dB peak sidelobe level;  $10^4$  samples will reduce both numbers by 10 dB. For the example described above (an aperture flight time of 3.3 sec and an aperture size  $D = 174$  m) the average sample spacing would be 3.3 msec (in time) and 0.174 m (in space). The average spatial spacing across the aperture is 5.8 wavelengths, 10 times the spacing of conventional SAR samples.

Research areas relating to the forward-looking SAR include:

1. First order system design and tolerance theory related to specific applications.
2. Development of adaptive focusing techniques compatible with the applications;
3. Development of computational algorithms which are fast enough for real-time imaging;
4. Experimental demonstration of the adaptive focusing and imaging concepts. In this regard it may be possible to make use of equipment that is presently being developed at the Valley Forge Research Center for demonstration of a helicopter-borne sidelooking high resolution SAR.

It should be possible to extend the forward-looking SAR to a larger, multi-platform SAR. Figure 6.4 shows several "weaving" vehicles of the type described above. They could be coordinated to form a single forward-looking aperture which is larger by an order of magnitude (using 10 vehicles) than the aperture provided by one of the vehicles alone. Thus, resolution should be improved by another order of magnitude. Some of the vehicles might be used only for the purpose of enlarging the aperture.

In the multi-element SAR it may be desirable to relay all data to a central or command platform for image formation and analysis. The inter-

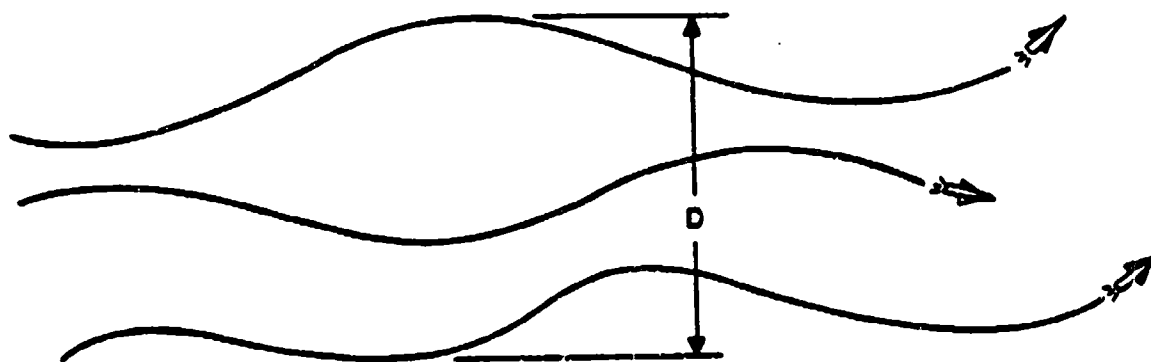


FIGURE 6.4 MULTI-ELEMENT SYNTHETIC APERTURE RADAR.

element communication system becomes a major concern because of the need for close physical and electrical synchronization. The total amount of data needed for imaging does not rise, relative to the single SAR case, however. If each platform takes only 100 samples, then 10 platforms together can provide the 1000 samples needed to reduce the expected average sidelobe level to -30 dB.

In some applications the multi-platform aperture may be so large relative to the target range that extreme near-field focusing is required. Thus, the very near field properties of arrays must be examined. Figure 6.5 shows a final-approach configuration in which the target lies within the synthetic aperture array. In this example, the concept of beamwidth must be changed to the concept of focal region in analyzing the focusing properties of the system.

C. Nelson Dorny

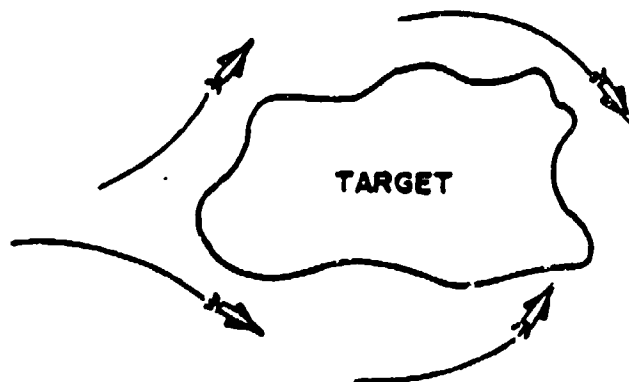


FIGURE 6.5 TARGET WITHIN THE SYNTHETIC APERTURE.

## Radar Imaging from a Distorted Array: The Radio Camera Algorithm and Experiments

BERNARD D. STEINBERG, FELLOW, IEEE

**Abstract**—High angular resolution radar imaging may be achieved with a large-aperture antenna even if the aperture is distorted, provided that adaptive signal processing compensates for the distortion. The radio camera is an instrument designed for this purpose. Its algorithm for imaging ground-based targets is described and experimental results are given for a 3 cm wavelength demonstration system using a distorted 27-m random sparse array. The measured beamwidth of 1 mrad conformed to theory, confirming the validity of the technique. Extension of the algorithm to accommodate isolated targets such as aircraft and ships also is discussed.

### INTRODUCTION

A MICROWAVE array may be distorted for many reasons. It may be too large to be surveyed properly. It may suffer from windloading. Its installation may be faulty. Or its distortion may be electrical rather than geometric: medium turbulence can cause the integral of the dielectric constant over a path from a source or a target to the array to vary randomly with position in the array. Also, electromagnetic coupling from the antenna elements to the local environment may vary randomly with position in the array, causing random errors in the driving point impedances of the antenna elements. The tolerance on the random variation is about 30° root-mean-square (rms) or somewhat less than one-tenth wavelength [1].

That a microwave array designed for high angular resolution imaging is likely to suffer from one or more of these difficulties is evident from an examination of (1)

$$j(u) = \int_L l(x) \left[ \int s(u) e^{ikxu} du \right] e^{-ikxu} dx \quad (1)$$

which is the simplest form of the integral equation relating a source function or scene  $s$  and its image or estimate  $j$  when the radiation field due to the source is measured by a line aperture of extent  $L$  having aperture weighting  $l$ . The source is assumed to be in the far field of the aperture, which permits its description in terms of the one-dimensional reduced angular variable  $u = \sin \theta$ ,  $\theta$  being measured from the normal to the aperture. The aperture also is assumed to be one-dimensional. The exponential kernels are Fourier kernels and both integrals are Fourier integrals. The inner integral is the radiation field  $S$  at the aperture. Equation (1) can be written in terms of  $S$ :

$$j(u) = \int_L l(x) S(x) e^{-ikxu} dx \\ = F\{l(x)S(x)\} \quad (2)$$

Manuscript received January 11, 1980; revised April 15, 1981. This work was supported in part by the Air Force Office of Scientific Research under Contract AFOSR-78-3688 and the Office of Naval Research under Contract N00014-79-C-0505.

The author is with the Valley Forge Research Center, Moore School of Electrical Engineering, University of Pennsylvania, Philadelphia, PA 19104, and the Airborne Radar Branch, Naval Research Laboratory, Washington, DC 20375.

where  $F\{\cdot\}$  means Fourier transform. By the multiplication-convolution property of the Fourier transform

$$j(u) = F\{l(x)\} * F\{S(x)\} \\ = I(u) * s(u) \quad (3)$$

where the asterisk indicates convolution.  $I(u)$  is the radiation or diffraction pattern of the aperture. Since convolution broadens or spreads a function, the closer that  $I(u)$  approximates a  $\delta$ -function, the better the estimate  $j(u)$  is of  $s(u)$ . Since the width of  $I(u)$  is always the order of  $\lambda/L$ , it is evident that the larger the aperture size  $L$  the more closely  $s$  will be represented by  $j$ . The same conclusion pertains to a target or scene in the near field.

To achieve a resolving power of  $10^{-4}$  to  $10^{-5}$  rad, which is typical of common optical instruments such as cameras and small telescopes, a microwave antenna must be hundreds of meters to tens of kilometers in size. Such antennas are too large to be constructed as single structures such as the parabolic dish. Instead they must be phased arrays. They must be highly thinned (mean interelement spacing  $\gg \lambda/2$ ) to limit cost, and the element distribution must be aperiodic to eliminate grating lobes [1]. It is most likely that the large size will preclude accurate knowledge of element location; hence, the array properties will tend to degenerate to those of the random array and the system design must accommodate the poor sidelobe performance expected from such an array [2]. As a consequence, array distortion is a highly likely property of a huge array designed for microwave imaging. However its effect can be neutralized to a considerable extent by introducing adaptively controlled phase corrections within the system based upon measurements at the array of the radiation field from a point source [3], [4]. Adaptive retrodirective beam-forming techniques then focus the distorted array upon the source [5], [6, ch. 5].

The paper describes an algorithm for phase synchronizing or self-cohering a distorted array upon such a source, moving the focused beam in range and angle to a target area, and scanning it across the target to image it. An instrument embodying this procedure is called a radio camera. Experimental evidence of the validity of the technique is given. The experiments were conducted with an X-band ( $\lambda = 3$  cm) radar, using a distorted quasi-linear random antenna array 27-m long.

### THE RADIO CAMERA

Fig. 1 shows a badly distorted receiving array and a point source of radiation in its near field. It also shows a pulsed transmitter. The near-field source may be active, such as a beacon, or passive, such as a large cross-section reflector echoing the radiation from the transmitter. This source or reflector is called the adaptive beam former; it also is called the phase synchronizer. The array is shown measuring the phase of the signal received at each element relative to the

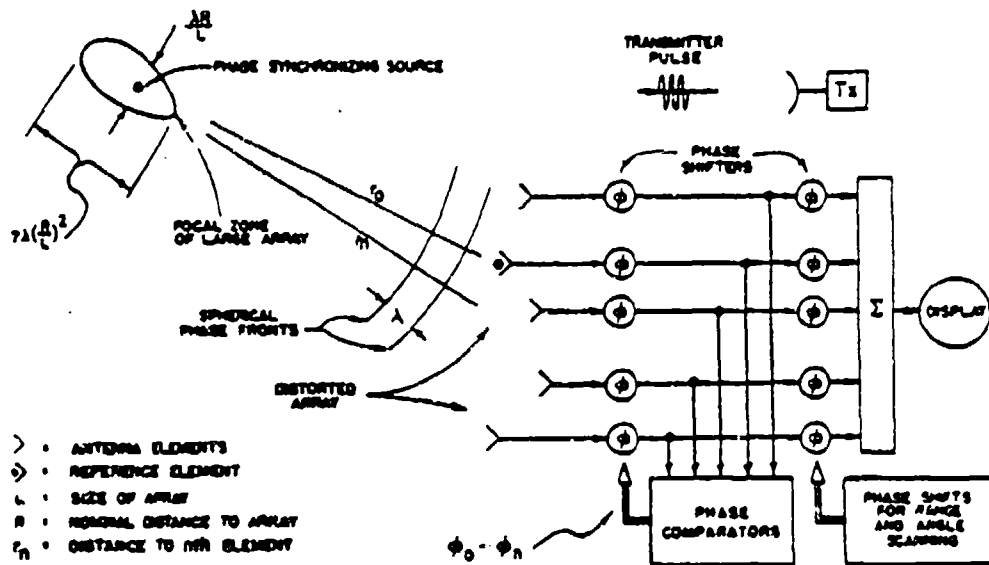


Fig. 1. Distorted array self-coheres on phase synchronizing source.

phase at some reference element within the array. In the absence of multipath the phase  $\phi_n$  of the received signal at the  $n$ th element is  $(\omega r_n/c_n) + \xi_n$ , where  $\omega$  is the radiation frequency,  $r_n$  is the path length,  $c_n$  is the average speed of propagation over the path, and  $\xi_n$  is the phase shift due to electromagnetic coupling of the element to its environment as well as through the receiving element and associated circuits.  $\phi_n$  may be rewritten as

$$\phi_n = \frac{\omega(r_{0n} + \delta r_n)}{c_0 + \delta c_n} + \xi_n \quad (4)$$

to explicitly show the displacement  $\delta r_n$  of the element in the direction toward the adaptive beam former from its correct distance  $r_{0n}$ , and the deviation  $\delta c_n$  of the mean propagation speed over the  $n$ th path from the average speed  $c_0$  in the medium. Since  $\delta c_n \ll c_0$ ,

$$\begin{aligned} \phi_n &\approx \frac{\omega(r_{0n} + \delta r_n)(1 - \delta c_n/c_0)}{c_0} + \xi_n \\ &\approx kr_{0n} + k\delta r_n - \frac{kr_{0n}\delta c_n}{c_0} + \xi_n, \quad k = \frac{\omega}{c_0} \end{aligned} \quad (5)$$

The phase differences from element to element are seen to have four components. The primary component  $kr_{0n}$  is due to source location relative to the undistorted array and is the same as in any phased array. The residuals are due to the distorted geometry of the array, to variations in propagation conditions from the source to different parts of the array due to its large size, and to variations in the phase shifts through the elements and in electromagnetic coupling between them and their surroundings. By phase shifting each receiver channel by the negative of these phase differences, all signals from the adaptive beam former become cophased. The output, following summation, is that of an array focused upon the beam-forming source. The spot size of the focal zone in the near field, calculated from diffraction theory, is shown in the figure. It is nominally  $\lambda R/L$  in the cross-range dimension and  $7\lambda(R/L)^2$  in range.  $\lambda/L$  is the beamwidth of a focused diffraction-limited

aperture of length  $L$ ; it also is the beamwidth of the distorted array following the adaptive beam-forming procedure.  $7\lambda(R/L)^2$  is the approximate value of the 3 dB range beamwidth due to the limited depth of field of an aperture focused on a near-field target [1].  $\lambda R/L$  also is the far-field cross-range dimension.

Also shown schematically in the figure is a second set of phase shifters located prior to the summer. Unlike the first phase shifting operation, the second operation is open loop and nonadaptive. After the array is phase synchronized the focused beam is scanned in range and angle by open-loop corrections calculated from the geometry. The calculations are made exactly as in a conventional phased array. During near-field scanning the spot size and shape remain as indicated in the figure. In the very near field the resolution of the two-dimensional image that results from the scanning operation is about equal to the spot size. When the target is in the far field of the large array the depth of field becomes infinite and the resolution in range is determined by the pulse duration of the transmitter. At intermediate distances the range resolution is the smaller of the depth of field and the radar pulse length.

Both phase shift operations can be analog or digital. The phase-lock loop is the natural analog circuit for adaptive beam forming. The experimental equipment described later uses digital phase shifting. Fig. 2 shows the procedure more explicitly. A transmitted pulse illuminates both a target area to be imaged and a passive phase synchronizing target, which is sketched as a corner reflector. The echo trace consists of their echoes plus clutter. The signals received at the several antenna elements are sampled in range and stored in the format shown. The range trace delivered by each antenna element is stored as a row of complex numbers. Successive rows correspond to successive elements in the array. The position of a sample in a row is proportional to range and designates the range bin. The position of a sample in a column designates the array element number and is monotonic with but not necessarily proportional to element position since the array is distorted.

For simplicity it is assumed that  $|r_n - r_m| \ll \Delta R$ , all  $n, m$ , where  $\Delta R$  is the length of a range cell. Thus all echoes from a common target will appear in a single range bin in the format shown in Fig. 2. Actually, target echoes can appear in dif-



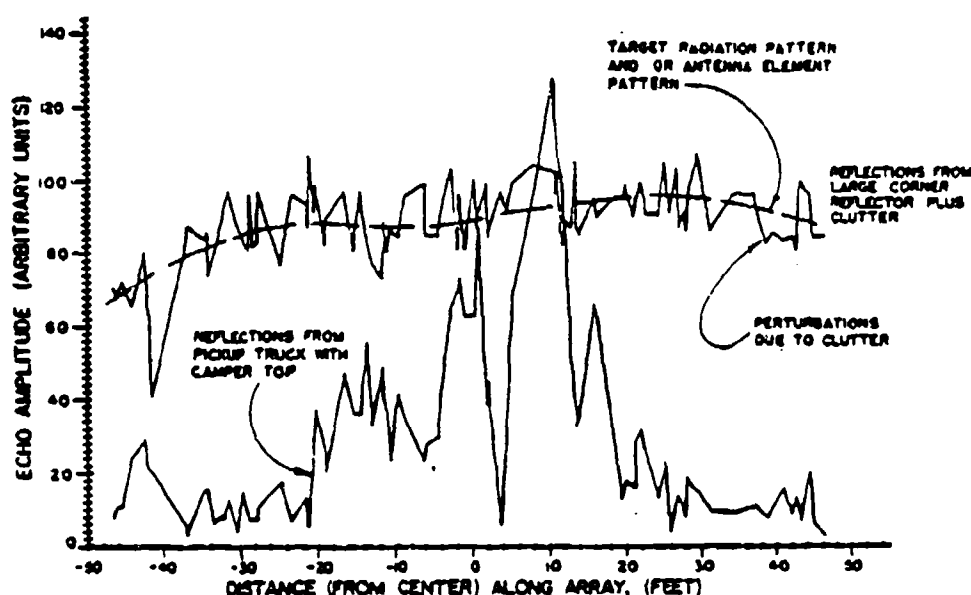


Fig. 3. Echo strength from two range bins versus element position in array. Corner reflector approximates a point source.

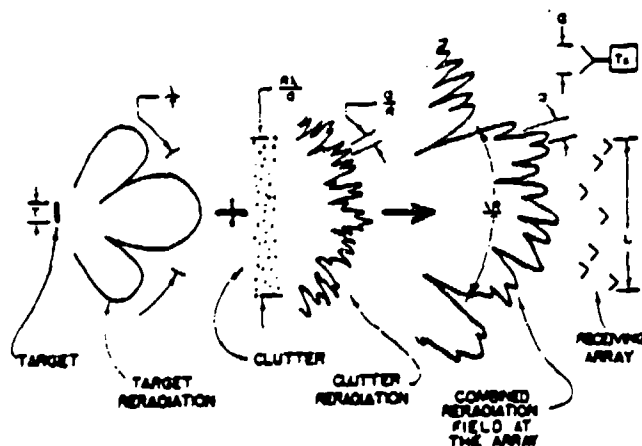


Fig. 4. Target size and clutter contribute to echo amplitude variations across array.

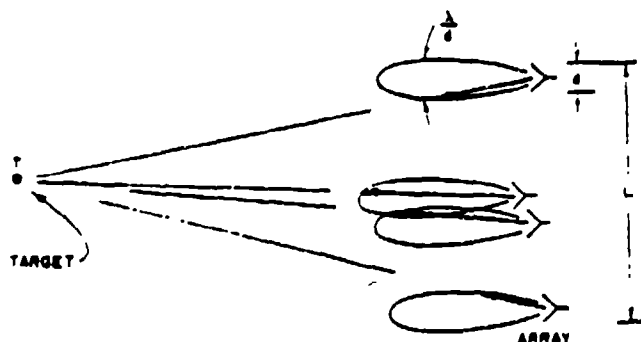


Fig. 5. Element pattern also contributes to amplitude variation.

target strength and range from the calculations. The normalized variance is  $1 - \bar{A}_i^2/A_i^2$ , which is a minimum at that range element for which  $\bar{A}_i^2/A_i^2$  is the largest value. The rule for finding  $R_0$ , then, is to calculate  $\bar{A}_i^2/A_i^2$  for all range elements and search for the largest value. The signal sequence from that range bin becomes the reference signal.

#### ADAPTIVE BEAM FORMING

Table I shows all the steps in the procedure. Step 1 initiates the process.  $V_{in} \exp(j\psi_{in})$  is the complex envelope of the echo from the  $i$ th range bin received by the  $n$ th element. Steps 2 and 3 are the search for  $R_0$  discussed above. Step 4 is the adaptive beam-forming step. The measured phases  $\psi_{in}$  can be broken into the sum of two terms  $\psi_{in}' + \psi_{in}''$ . The first term contains the conventional target and array geometry and is all that would be expected in the absence of array distortion, medium turbulence, multipath, and scattering. The second term represents the errors which the phase synchronization process must overcome. In the absence of such errors the image of the target or clutter from the  $i$ th range element would be obtained from the integral of the phase-weighted signals received across the array from the  $i$ th range bin. As in any phased array the phase weighting is the conjugate of the kernel of the diffraction integral. For ease of discussion the diffraction integral can be approximated by the Fresnel integral, which reduces to the Fourier integral when the target is in the far field. That integral in turn is best represented by a sum as in (6) because the array is discrete. The sum

$$j_i(u) = \sum_{n=1}^N A_{in} e^{j\psi_{in}'} e^{-jk(x_n u - x_n^2/2R_i)} \quad (6)$$

is the image  $j_i$  of the scattering sources in the  $i$ th range bin provided that  $\psi'' = 0$ . As in (1),  $u = \sin \theta$  and  $\theta =$  scan angle from the normal to the array. The discrete variables  $x_n$  and  $R_i$  are, respectively, the  $x$  coordinate in the array (transverse to the array normal) of the  $n$ th element and the distance to the  $i$ th range bin. Although  $j_i(u)$  is written as a one-dimensional image (in the reduced angular variable  $u$ ) of the echoes from the  $i$ th bin, it is, in reality, a two-dimensional image in  $u$  and  $R$  when the targets are in the near field of the array. Properties of the two-dimensional image are described in [12].

The function of the adaptive processor is to compensate for  $\psi_{in}''$  so that the operation described by (6) may be accomplished. In the earlier steps of the process the data were searched to find the range bin in which the echo amplitude across the

TABLE I  
STEPS IN RADIO CAMERA IMAGING

Step	
1 Measure and store complex envelopes of echo samples	$V_{in} e^{j\psi_{in}}$ range bin $\xrightarrow{\quad}$ element number
2 Correct amplitudes by dividing by element pattern estimate $f_n$	$A_{in} e^{j\psi_{in}}$
3 Find $R_0$ such that $A_{0n} \approx A$ , all $n$	$A e^{j\psi_{0n}}$
4 Phase conjugate at $R_0$	$A e^{j\psi_{00}}$
5 Phase rotate at all range elements	$A_{in} e^{j(\psi_{in} - \psi_{0n} + \psi_{00})}$
6 Focus at each range $R_i$	$A_{in} e^{j(\psi_{in} - \psi_{0n} + \psi_{00} - \frac{kx_n^2}{2} (\frac{1}{R_i} - \frac{1}{R_0}))} \triangleq B_{in}$
7 Phase shift linearly with angle	$B_{in} e^{-jkx_n u}$
8 Sum at each range element	$i(u) = \sum_{n=1}^N B_{in} e^{-jkx_n u}$

array had the smallest variation. That range bin became the reference range and the signal from that range bin became the synchronizing signal. Its complex envelope following normalization to  $f$  is  $A_{0n} \exp(j\psi_{0n})$  where the amplitudes are all nearly the same. The phases of the echoes are random, however, due to the perturbed geometry of the array or the spatial variations of the refractive index or the impedance variations from element to element of any combination of these factors. If the reference source were an ideal source the phase differences would be due entirely to them. In addition the phases are perturbed by multipath and scattering and by the finite lobe width of the reradiation from the synchronizing source. However, because it is generally impossible for the system designer to obtain *a priori* information about these latter conditions, the signal processor must necessarily ignore them.

The fourth step in the process is to compensate for the phase variations, which are assumed to be due to the first set of factors. Correction is accomplished by phase rotating the complex envelopes of the signals from  $R_0$  received by the different array elements. The proper phase shift for the  $n$ th element is the negative of the phase difference  $\Delta\psi_{0n} = \psi_{0n} - \psi_{00}$ . The complex signal envelope at the  $n$ th element becomes  $A_{0n} \exp(j\psi_{0n}) \exp[-j(\psi_{0n} - \psi_{00})] \approx A \exp(j\psi_{00})$ . This correction, or phase conjugation, is exactly what a phased array or lens would do when focusing upon the reference source. The output signal from the array when it is so focused is the sum of these phase-corrected echoes from  $R_0$ .

#### SCANNING

The fifth step (performed simultaneously with Step 4) is to phase rotate all the signal samples from each antenna element by  $\psi_{0n} - \psi_{00}$ . The samples of the complex envelope from the  $i$ th range bin now become  $A_{in} \exp[j(\psi_{in} - \psi_{0n} + \psi_{00})]$ . The sum of such a set of complex samples represents the output of a misfocused phased array or lens since  $\psi_{in} \neq \psi_{0n}$  except at the range  $R_0$  of the reference reflector.

The sixth step is to focus the array at all ranges simultaneously. This task is accomplished for an arbitrary range  $R_i$  by refocusing the array from the reference range  $R_0$  to  $R_i$ . The

phase correction is approximately quadratic, as given by (6). Assuming that the earlier steps were performed properly, the self-cohering process forced the quadratic component of the phase shift of the signal in the  $n$ th channel to become  $-kx_n^2/2R_i + kx_n^2/2R_0$ . To focus the array to range  $R_i$  this term must be set to zero, which requires a further phase addition of  $(kx_n^2/2)(1/R_i - 1/R_0)$ . This step requires a knowledge of the range  $R_0$  of the reference reflector. Fortunately, the value of  $R_0$  is available in the system for it is measured, as in conventional radar, by the round-trip travel time of the pulse to the phase synchronizing source and it is read directly into the signal processor from the radar receiver. The accuracy of measurement is determined by the range resolution of the system, which is the order of the reciprocal of the signal bandwidth (in distance units), or the near-field range beamwidth, whichever is smaller.

Step 7 imparts a linear phase rotation to the range-focused complex envelope (designated  $B_{in}$  in Table I) for each scan angle  $u$ . The phase shift is  $-kx_n u$ .

The last step forms the sum of the linearly phase-weighted, range-focused samples to obtain the image  $i(u)$  for the  $i$ th range bin:

$$i(u) = \sum_{n=1}^N B_{in} e^{-jkx_n u} \quad (7)$$

#### ELEMENT POSITION TOLERANCE

Steps 3, 4, and 5 require no knowledge whatsoever of element position. The phase synchronization process is purely retrodirective. Steps 6 (refocusing in range) and 7 (scanning in angle) do require coordinate information. The tolerances on element position error have been worked out [7], [8], [1, ch. 13]. The most stringent tolerance is invoked by Step 7. Briefly, the theory consists of the following points. First, the loss in main-lobe gain, in decibels, due to all the random phase errors across the array is  $\Delta G \approx 4.3\sigma_\phi^2$  where  $\sigma_\phi^2$  is the variance of the phase errors in square radians. Second, the phase variance due to random position errors is approximately  $\sigma_\phi^2 \approx$

$k^2 \sigma_x^2 \theta^2$  where  $\sigma_x^2$  is the position error variance in the array in the direction perpendicular to the beam-forming direction and  $\theta$  (rad) is the scan angle measured from the direction of beam-forming. Combining these expressions, and allowing 1-dB loss in array gain as an acceptable gain-loss tolerance, the rms element tolerance becomes  $\sigma_x \approx (\lambda/4\pi)\theta_{\max}^{-1}$ .

The factor  $\lambda/4\pi$  is the conventional tolerance in phased array, mirror, or lens design.  $\theta_{\max}$  is the maximum scan angle from the direction of the reference source and is half the field of view. Since an individual radar target always subtends a very small angle at the radar,  $\theta_{\max} \ll 1$  and the allowed element position error is exceedingly large. For example, if the system were designed to image a target as large (in angle) as the moon,  $\theta_{\max}$  would be approximately  $10^{-2}$  rad; in this case the position accuracy tolerance increases by two orders of magnitude to about  $10\lambda$ . It is precisely this extraordinary liberty in position tolerance, following adaptive phase synchronization, that permits radio camera imaging with a nonrigid or ill-surveyed array.

### EXPERIMENTS

Fig. 6 shows the result of an X-band radio camera imaging experiment using a low power (5 W) radar transmitter and a corner reflector for the phase synchronizer. The size of the reflector was 0.46 m and its radar cross-section was calculated to be  $56 \text{ m}^2$ . The estimated clutter cross-section was  $2 \text{ m}^2$ . The receiving array was the one used in the experiment for Fig. 3: it was 27-m long and 1.2-m wide. The 100 element positions were randomly located within it. Uniform probability density functions of element position were chosen for both the length and width dimensions of the array. The experiment was conducted on a time-shared basis in which a single radar receiver was successively moved from position to position, delivering a radar echo trace to a microprocessor from each receiver position, after which the operations described earlier were performed. The image is one-dimensional deflection modulated. The target consisted of two additional reflectors, each 0.61 m, drawn to scale below the image. The target was 240 m from the array and subtended an angle of 14 mrad. The reference reflector was 41 m closer. Drawn also in Fig. 6 is the calculated response of the array in free space had it self-organized perfectly. It is evident that the experiment was exceedingly successful.

The theoretical beamwidth for this experiment, based upon diffraction theory, was  $0.88\lambda/L \cos \theta$ . The coefficient corresponds to the particular probability density function of element location used [1].  $\theta$ , the target angle from the array normal, was  $25^\circ$ . This expression evaluates to 1.1 mrad, which is indistinguishable from the measured beamwidth.

Fig. 7 is the image of the same reflectors when the equipment was operated in the synthetic aperture mode [9]: the low power transmitter and receiver both were moved from position to position for each radar transmission and reception. (The experimental setup and procedure were illustrated and described in [3].) Because of the doubling of the wavenumber due to the synthetic aperture operation, the beam cross-section in Fig. 7 is halved. Again, the comparison with the calculated free space response is excellent. The separation of the corner reflectors was increased to 16 mrad in this experiment.

In both experiments the sidelobe properties conform to the theory of the random array [1], [2], which predicts that the contribution to the average sidelobe power level is  $V^{-1}$  times the main-lobe power response of a target. Thus, the

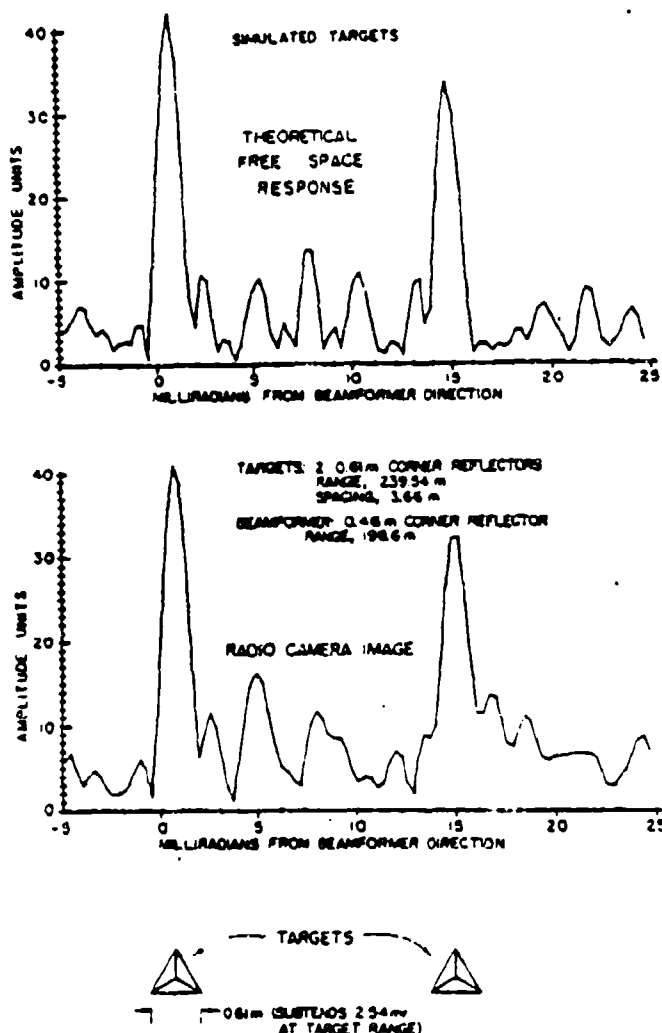


Fig. 6. One-dimensional image of two corner-reflector targets using another corner reflector for adaptive beam forming. Theoretical response in free space shown for comparison.

theoretical average sidelobe level for the two nearly equal strength targets in Figs. 6 and 7 is  $-17 \text{ dB}$ ; the measured levels are within a few tenths of a decibel of this value.

### ISOLATED TARGET

The situation is somewhat different for an isolated target such as an aircraft or a ship in which the reference source is on the target. One difference is that no range refocusing (Step 6 of Table I) is required since the size of the aircraft usually will be small compared to the depth of field of the array. A more significant difference lies in the fact that target echoes are used both for adaptive phase synchronization as well as for imaging. The requirements upon the echo characteristics are opposed for these two processes. Phase synchronization requires a dominant point source, whereas the objective of picture taking is to reproduce the angular backscatter profile of a complicated target so that the target may be classified or characterized.

The conflict resolves itself when the target is moving relative to the observer. Fig. 8 shows an aircraft at distance  $R$  with its velocity vector  $V$  making an angle  $\alpha$  with the direction to the array. The aspect angle  $\alpha$  changes with time at the rate

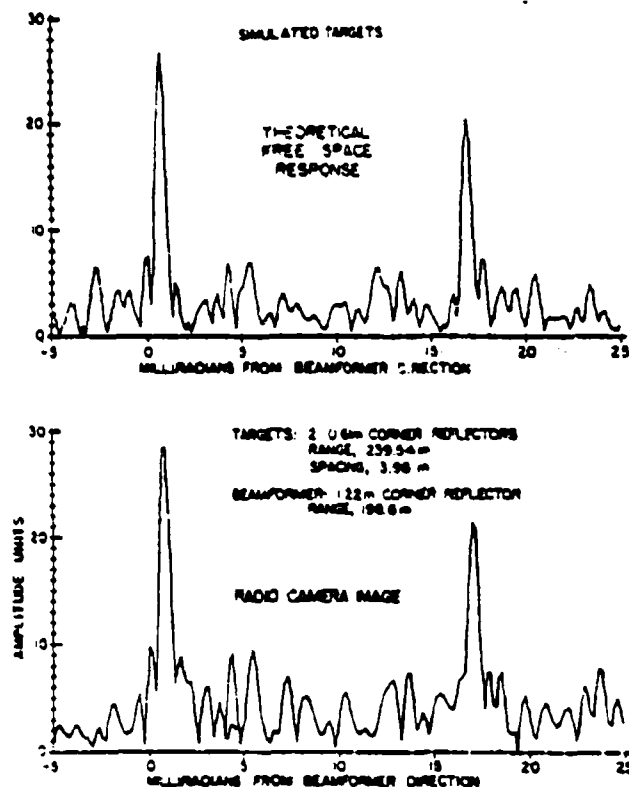


Fig. 7. Radio camera image of same two targets in synthetic aperture mode.

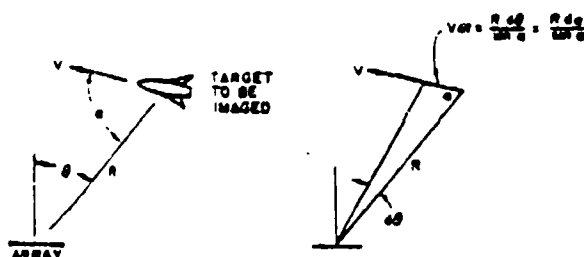


Fig. 8. Aspect angle  $\theta$  changes with time.

$da/dt = V \sin \alpha / R$ . Because of this turning motion, the radar echo changes with time, sometimes having the desirable properties for phase synchronization while at other times the return signal is good for imaging purposes. From time to time a strong highlight appears due, say, to a broadside specular return from the fuselage, or a two-plane corner reflector formed by wing and fuselage or in the tail assembly. The highlights are severely aspect-angle dependent, as is demonstrated in Fig. 9. There a small flat-plate reflector of length  $T$  is shown momentarily oriented broadside to the direction to the array. As the line-of-sight angle  $\theta$  changes due to platform motion the reradiation pattern moves through twice that angle. Consequently, the time that the main lobe dwells upon the array is

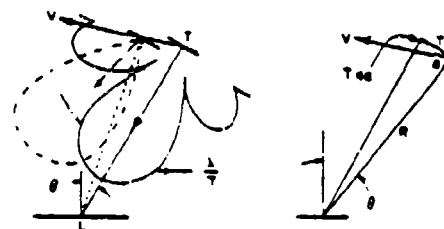


Fig. 9. Reradiation pattern rotates with platform motion.

determined by the turning rate  $da/dt$  and the reradiation beamwidth ( $\approx \lambda/T$ ). The duration or correlation time can be estimated as the time required for the differential phase of the echoes from two scatterers separated a distance equal to the target size  $T$  to change about  $\pi/2$ . The right of Fig. 9 shows the geometry. The change in the differential distance  $\delta R$  from two such scatterers is approximately  $Td\alpha$ . The rate of change is  $d(\delta R)/dt \approx Tda/dt \approx TV \sin \alpha / R$  and the phase difference between their echoes changes at a rate  $d(\delta \phi)/dt = 2kd(\delta R)/dt \approx 4\pi TV \sin \alpha / \lambda R$ . Hence, the correlation time is the order of

$$T_c \approx \lambda R / 8TV \sin \alpha. \quad (8)$$

Consider a Mach 1 aircraft with a reflecting region 1 m in size oriented normal to the radar line-of-sight. When observed with 3-cm radiation from a distance of 20 km and at a  $30^\circ$  angle the correlation time is about 1/2 s. During this time the large array on the ground may be synchronized, forming a narrow beam focused on the specular reflector. Rather than determining at what range to phase conjugate or focus, as in the earlier discussion (Step 3 of Table I), the signal processor now determines when to perform this operation. Its criterion is exactly the same, i.e., reasonable uniformity of echo strength across the array. Furthermore, it can apply an additional and highly sensitive measure: the correlation time, which is the reciprocal of the echo modulation bandwidth, varies inversely with target size. When the highlight disappears the "target" in (8) becomes the size of the aircraft. If the 1-m flat plate reflector were on a 30-m aircraft the modulation rate would jump by a factor of 30 following the 1/2 s phase-synchronizing period. Similar, the echo modulation bandwidth would drop by this factor when a stable echo appears, thereby permitting the signal processor to readily determine when to phase synchronize.

Observation of the drop in echo modulation bandwidth can be made in the low-frequency control branch of the phase-lock loop, if such a circuit is used for adaptive beam forming, or in the data store of a real-time digital processor. In the latter case the data may be organized in the same format shown in the lower part of Fig. 2 except that the horizontal coordinate is no longer range, but time. All the data come from the same range bin and the columns are spaced by one interpulse period. Successive columns are successive range-gated samples of the echoes at each antenna element. The processor observes the data bandwidth and the amplitude stability to determine when to phase synchronize (Step 3). During the dwell time of a highlight the signal processor ceases the imaging process and phase conjugates instead (Step 4). Next it observes when the modulation bandwidth returns to normal, at which time it begins again the imaging process (Steps 7 and 8). Following the high-resolution angle scan it

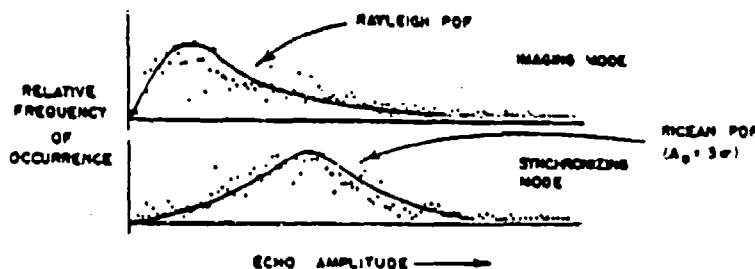


Fig. 10. Histograms of aircraft echo sequences.

awaits the next synchronizing interval to repeat the process. The cycle time is the order of one second. During several such seconds the aircraft has moved and rotated insignificantly insofar as the observer is concerned, but has altered its orientation sufficiently to cause successive images to be statistically independent. Hence, the logical next step is to form "multiple exposures," i.e., sums of intensities of several successive images. Doing so builds up the information content in the image and fills in the speckles or glint resulting from the narrow-band (near monochromatic) radiation. In addition, it reduces the sidelobe peaks of the random array by several decibels [1].

An experiment has been conducted to measure highlight dwell times and the percentages of time that aircraft targets are in the so-called "synchronizing" and "imaging" modes [10]. The basis for the measurement is the expected change in the probability density function (pdf) of the echo amplitude when a highlight occurs. Without it the echo is the vector sum of a large number of small, randomly phased echoes. The sum is a two-dimensional, zero mean, random Gaussian variate, the amplitude of which is Rayleigh distributed, i.e., if  $A$  is the echo amplitude and  $2\sigma^2$  is its mean square value, the pdf of  $A$  is  $f(A) = (A/\sigma^2) \exp(-A^2/2\sigma^2)$ . When a strong scatterer of strength  $A_0$  is added, the pdf changes to the Ricean distribution  $f(A) = (A/\sigma^2) \exp[-(A^2 + A_0^2)/2\sigma^2] I_0(AA_0/\sigma^2)$ , where  $I_0$  is the modified Bessel function of the first kind and zeroth order.  $f(A)$  reduces to the Rayleigh pdf when  $A_0 = 0$  [1].

The experiment was designed to gather simple statistics on the short-time pdf of radar echoes from aircraft. The radar was an L-band AN/TPS-1D. It is located at the Valley Forge Research Center of the Moore School of Electrical Engineering, University of Pennsylvania, at Valley Forge, Pennsylvania, 40-km west of Philadelphia. Commercial aircraft flying in the Philadelphia-New York-Scranton triangle were observed and tracked. Distances varied from 15 to 100 km. Echo sequences of varying numbers of pulses were sorted by amplitude in real time in a histogram generator and the nature of the pdf was judged to be Rayleigh, Ricean, or nondescript.

The results are shown in the tables for broadside, nose, and tail aspect. Sample histograms are shown in Fig. 10. As expected, Rayleigh and Ricean pdfs did occur, the former with about three times the frequency of the latter (Table II). About 20 percent of the sample runs showed no preference for either, exhibiting instead tendencies toward uniformity or bimodality, for example. The average correlation time in each mode also was measured (Table III). Note that the 1/2-s dwell time estimated earlier for the sync mode is within the range shown. The measurements confirmed the expectation that aircraft will alternately permit array synchronizing and imaging.

TABLE II  
RELATIVE FREQUENCIES OF OCCURRENCE OF IMAGING AND PHASE SYNCHRONIZING MODES

View	Number of Aircraft	Imaging Mode (Rayleigh pdf)	Synchronizing Mode (Ricean pdf)	Neither
Broadside	3	0.594	0.286	0.120
Nose	2	0.501	0.363	0.136
Tail	4	0.668	0.048	0.284
All	9	0.606	0.193	0.201

TABLE III  
APPROXIMATE CORRELATION TIMES FOR AIRCRAFT ECHOES

View	Number of Aircraft Observed	Average Correlation Time (s)	Average Deviation (s)
Broadside	16	1.66	0.68
Nose	7	0.30	0.04
Tail	4	0.17	0.11

## SUMMARY

A radar antenna array distorted beyond the normal tolerance of about one-tenth wavelength can be made to function as a diffraction-limited imaging aperture by adaptively phase-compensating for the distortion. An external point source of radiation, called the phase synchronizer or adaptive beam former, illuminates the array. The source may be an active beacon or a passive reflector echoing the radiation from a radar transmitter. The phase of the radiation field is measured at each array element. Phase shifts are added to each element channel to eliminate the phase differences. An array focused at the beam-forming source results. Open loop scanning in range and angle follows adaptive focusing of the array.

An algorithm suitable for digital signal processing is given. It describes 1) a search procedure for locating the target most favorable for adaptive beam forming, 2) the adaptive beam-forming process, and 3) range and angle scanning of the focused beam. Experimental evidence of the validity of the technique is given, based upon experiments with a 27-m X-band random sparse array.

A modification to the basic algorithm is described to accommodate an isolated target such as an aircraft or ship. A radar experiment with aircraft of opportunity disclosed that the fluctuating properties of airborne target echoes satisfy the requirements of the search procedure for a suitable adaptive beam-forming source.

## ACKNOWLEDGMENT

The experimental staff of the Valley Forge Research Center developed the equipment and conducted experiments that produced the data given in Figs. 6 and 7. The principal members of the group, led by Donald Carlson, were Bernard S. Mesgher, Jr. and William T. Whustler.

## REFERENCES

- [1] B. D. Steinberg, *Principles of Aperture and Array System Design*. New York: Wiley, 1976.
- [2] Y. T. Lo, "A mathematical theory of antenna arrays with randomly spaced elements," *IRE Trans. Antennas Propag.*, vol. AP-12, pp. 257-268, May 1964.
- [3] B. D. Steinberg et al., "First experimental results from the Valley Forge Radio Camera Program," *Proc. IEEE Lett.*, vol. 67, no. 9, pp. 1370-1371, Sept. 1979.
- [4] B. D. Steinberg, "High angular microwave resolution from distorted arrays," in *Proc. 1980 Int. Computing Conf.*, vol. 231, pp. 150-156, Apr. 1980.
- [5] Special Issue on Active and Adaptive Antennas, *IEEE Trans. Antennas Propag.*, vol. AP-12, no. 2, Mar. 1964.
- [6] R. C. Hansen, Ed., *Microwave Scanning Antennas*. New York: Academic, 1964, vol. 3.
- [7] B. D. Steinberg, "Design approach for a high-resolution microwave imaging radio camera," *J. Franklin Institute*, vol. 296, no. 6, pp. 415-432, Dec. 1973.
- [8] S. H. Taheri and B. D. Steinberg, "Tolerances in self-cohering antenna arrays of arbitrary geometry," *IEEE Trans. Antennas Propag.*, vol. AP-24, no. 5, pp. 733-739, Sept. 1976.
- [9] R. S. Berkowitz and E. N. Powers, "Tasar, A thinned adaptive synthetic aperture radar," *IEEE EASCON '78 Record*, Arlington, VA, IEEE Publication 78 CH 1354-4 AES, pp. 133-142.
- [10] D. L. Carlson, "The phase synchronization of large random arrays using specular aircraft radar return signals," M.S. thesis, Univ. Pennsylvania, Philadelphia, PA, 1975.

- [11] S. O. Rice, "Mathematical analysis of random noise," *Bell System Tech. J.*, no. 23, pp. 282-332, July 1944.
- [12] —, "Mathematical analysis of random noise," *Bell System Tech. J.*, no. 24, pp. 46-156, Jan. 1945.
- [13] B. D. Steinberg and A. K. Luthra, "Asymmetries in the diffraction pattern of an asymmetrical aperture," *IEEE Trans. Antennas Propag.*, to be published.



Bernard D. Steinberg (S'48-A'50-SM'64-F'66) was born in Brooklyn, New York in 1924. He received the B.S. and M.S. degrees in electrical engineering from the Massachusetts Institute of Technology, Cambridge, in 1949, and the Ph.D. degree from the University of Pennsylvania, Philadelphia, in 1971.

He worked in the Research Division of Philco through the middle 1950's, specializing in radar backscatter and radar signal processing. He was one of the founders of General Atomics Corporation in Philadelphia in 1956 and served as its Vice President and Technical Director for 15 years. His work there was in signal processing techniques and their applications to radar, HF communications, hydro-acoustics, and seismology. His most recent work is in self-adaptive signal processors, particularly in large antenna arrays. Since 1971, he has been a Professor in the Moore School of Electrical Engineering at the University of Pennsylvania, Philadelphia, and Director of its Valley Forge Research Center, where he is engaged in development of a large self-adaptive microwave imaging system called the Radio Camera. He is the author of *Principles of Aperture and Array System Design* (Wiley, 1976) in which early radio camera concepts are described, and currently is preparing a detailed book on the subject. He also is a consultant in the Airborne Radar Branch of the Naval Research Laboratory.

Dr. Steinberg is a member of U.S. Commissions B and C of the International Scientific Radio Union (URSI).

# Properties of Phase Synchronizing Sources for a Radio Camera

BERNARD D. STEINBERG, FELLOW, IEEE

**Abstract**—A distorted phased array can be made to operate as a diffraction-limited aperture if a compensating time delay and/or phase shift is added in each antenna element channel. When the distortion is not known *a priori* the correction must be based upon phasefront measurements of the radiation from a source external to the array. The ideal adaptive synchronizing source is a point source radiating in free space. The phasefronts of realistic sources are perturbed, however. Three types of practical sources and calculations of the conditions under which their radiation fields are acceptable for adaptive beamforming are discussed. The sources are the passive reflector, the active beacon, and radar ground clutter.

## I. INTRODUCTION

A RETRODIRECTIVE array samples the radiation field from a point source at a distance and adjusts the phase of the radiated wave at each element to be the complement of the measured signal phase [1]–[3]. The radio camera (distorted array plus self-adaptive beamforming) requires retrodirective procedures [4]–[8]. The function of the radio camera is very much angular resolution imaging. The aperture size required at microwaves to achieve the resolving power of common optical instruments, which is  $10^{-5}$  to  $10^{-4}$  rad, is hundreds of meters to tens of kilometers, as is evident from the relation  $\Delta\theta \approx \lambda/L$ , where  $\Delta\theta$  is the beamwidth,  $\lambda$  is the wavelength, and  $L$  is the size of the aperture. Apertures so large will be very difficult if not impossible to survey to the one-tenth wavelength or smaller tolerance required for diffraction-limited operation [5]. Some apertures will flex and may even be time-varying. Earlier papers describe various aspects of the radio camera. The overall system concept is given in [4] and [5]. The details of the algorithm for searching for the retrodirective beamformer, focusing upon it, and scanning the focused beam in range and angle are given in [7]. Early experimental results were published in that paper and in [6] and [8].

This paper examines the retrodirective beamforming source and determines the required properties for satisfactory operation of a radio camera. The principle of operation with a distorted array, the radiation pattern that results from retrodirective beamforming, and the losses that can develop in array gain are discussed in the next two sections. In the following section bounds are calculated on the necessary physical properties of retrodirective synchronizing sources. The sources discussed include the passive reflector such as the corner reflector, the active beacon and radar ground clutter. Experimental one-dimensional radio camera images show how array gain can be degraded by an imperfect retrodirective source.

Manuscript received June 30, 1981; revised October 16, 1981. This work was principally supported by the Office of Naval Research and the Air Force Office of Scientific Research.

The author is with the Valley Forge Research Center, Moore School of Electrical Engineering, University of Pennsylvania, Philadelphia, PA 19104 and the Airborne Radar Branch, Naval Research Laboratory, Washington, DC 20375.

## THE RADIO CAMERA

Fig. 1 shows a pulsed transmitter illuminating a point reflector which reradiates to a distorted receiving array. The array system measures time and/or phase differences between the echoes at each antenna element and assumes that they are due entirely to differential distances from the source to the antenna elements and to variations in the index of refraction of the propagation medium along the ray paths. Following envelope time-delay correction, an automatic phase correction  $\phi_0 - \phi_n$  is made, which is the difference between the echo phases received at some arbitrary reference element and the  $n$ th element. The second term  $-\phi_n$  is the key to the corrective process. It is the complement of the phase of the received signal relative to some reference phase which is constant across the array. In practice, the reference signal need not be the signal from another element in the array; instead, it can be the local oscillator wave from a central source in the system delivered to each element with the same phase. Either procedure is satisfactory.

Automatic phase conjugation also is called adaptive beamforming or self-cohering or phase synchronizing. After the beam is formed it may be scanned by geometrically calculated phase corrections applied open loop to the second bank of phase shifters. Analog or digital circuits can be used to implement both banks of phase shifters and the phase controllers.

The result of adaptive beamforming is a receiving array self-focused upon the synchronizing source. The dimensions of the focal zone of the array when focused upon a near-field source at a distance  $R$  are shown in Fig. 1. The nominal cross-range beamwidth is  $\lambda R/L$ . The beamwidth in range is the depth of field of the aperture, which is approximately  $7\lambda(R/L)^2$  [5]. The focal zone when the source is in the far field is an angular sector of width  $\lambda/L$  rad. Thus, the angular resolution in the scanned image of the radio camera is essentially the same in the near field as in the far field. The far-field range resolution is determined by the pulse duration of the transmitter (expressed in distance units) and in the near field it is the pulse duration or the depth of field, whichever is smaller.

Fig. 2 shows two one-dimensional radio camera images which illustrate the importance of a high quality beamforming source. These one-dimensional angle scans were obtained with a modified AN/APQ-102 radar operating in the synthetic aperture radio camera mode described in [6], [7], and [9]. The array was approximately linear. Its length was 40 m, consisted of 200 sample points located at random. The radar was an X-band ( $\lambda = 3$  cm) set with 50 kw peak power and a range cell of 9 m. The adaptive beam-forming source in the experiment of Fig. 2(a) was a 4 ft corner reflector 5.6 km from the radar. 31 m more distant was a 2 ft corner reflector. The radio camera first self-focused upon the 4 ft reflector, then scanned in angle and range to the location of the smaller reflector, following which it scanned in angle across it to produce the image shown in Fig. 2(a). The ordinate is in ampli-

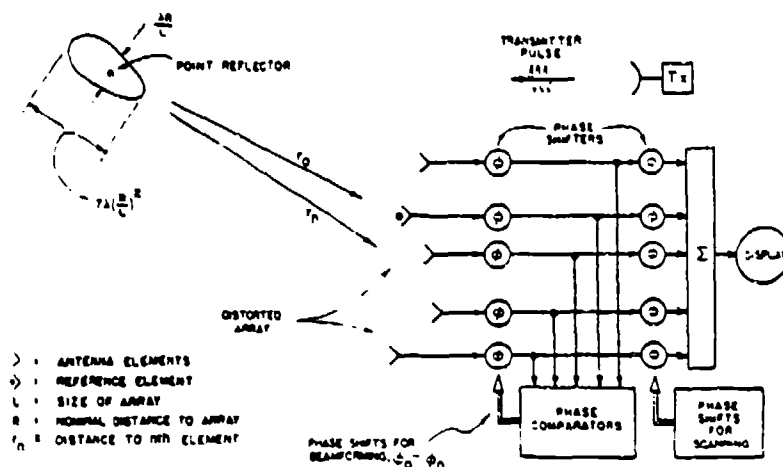


Fig. 1. Phase synchronizing a badly distorted radio camera array on echoes from a point reflector.

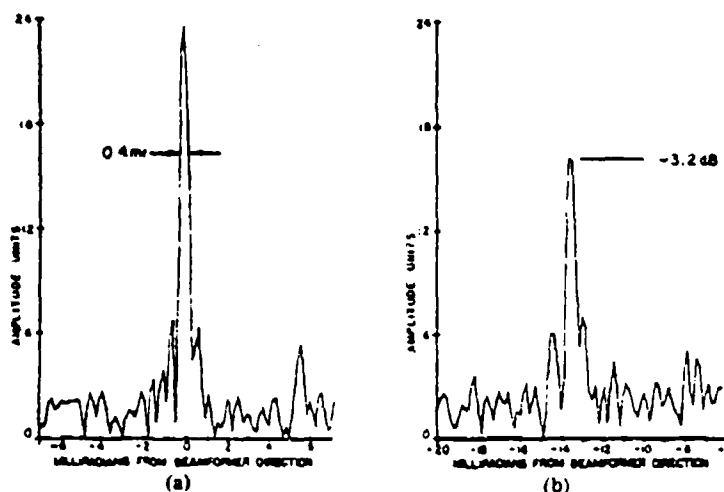


Fig. 2. One-dimensional radio camera images of a two-ft corner reflector at 5.6 km. Beamforming target in (a) is another corner reflector; in (b) it is a house. Loss in array gain is 3.2 dB.

tude units, and the abscissa is in milliradians from the direction to the 4 ft reflector. The cross section of the imaged 2 ft reflector is 0.4 mrad which is 2.2 m at the target range. The expected values based upon diffraction theory, synthetic array theory, and random array theory are the same.

Fig. 2(b) shows the same target imaged by the same equipment using exactly the same array and imaging algorithm. The only difference is the beamforming source. The source in Fig. 2(b) is a house located 15.5 mrad to the left of the target and 45 m from it in range. The resolving power of the instrument is not significantly altered but the array gain is reduced by 3.2 dB.

That the array gain is seriously affected by the properties of the synchronizing source, while the array beamwidth is not, is predictable from random array theory [5]. Array gain is sensitive to random phase errors across the array according to  $E\{G/G_0\} = \exp[-\sigma_\phi^2]$  where  $E\{\cdot\}$  means expectation,  $G$  is the array power gain,  $G_0$  is the gain in the absence of errors, and  $\sigma_\phi^2$  is the phase-error variance across the array. Expressed in decibels the loss in gain is  $\Delta G(\text{dB}) = 4.3 \sigma_\phi^2$ . Based on these equations it may be deduced that the phase variance across the array after phase synchronization on the echoes from the

house was  $0.74 \text{ rad}^2$  or  $0.86 \text{ rad rms}$ . The nominal widths of all lobes (main lobe and sidelobes) of a random array remain unchanged irrespective of the phase errors. Thus, phase errors during the adaptive beamforming process reduce array gain but have no first-order effect upon array beamwidth.

It is evident that the house was not a satisfactory target of opportunity for adaptive phase synchronization of the distorted array. In the following sections the conditions under which targets are satisfactory sources are examined and bounds are derived for their use.

#### LOSS IN ARRAY GAIN

The radiation power pattern formed by the adaptive retro-directive process is approximately a replica of the source function or scene that produces the incident radiation field. Let the source or scene be at distance  $R$  from the distorted array (Fig. 3). Let  $y$  be an axis through the scene perpendicular to the direction of phase synchronization of the array, which will be called the  $z$ -axis. Define the reduced angular variable  $u = \sin \theta = y/R$  where the angle  $\theta$  is measured from the  $z$ -axis.  $\theta$  is called the scan angle. The source or scene  $s(u)$  produces a radiation field along the  $x$ -axis in the array (Fresnel approxi-

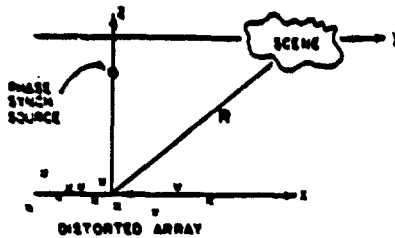


Fig. 3. The scene to be imaged is at distance  $R$  from the array. The  $z$ -axis is in the direction of the synchronizing source. The  $x$ - and  $y$ -axes are perpendicular to the  $z$ -axis and are in the same plane.

mation)

$$S(x; R) = \int s(u) e^{jk(xu - x^2/2R)} du \quad (1)$$

where the  $x$ -axis also is perpendicular to the  $z$ -axis. Now assume a phase conjugation operation such that the current excitation in the array along the  $x$ -axis is the complex conjugate  $S^*(x)$  of (1). The radiation pattern of the array in the source region becomes

$$f(u; R) = \int S^*(x; R) e^{jk(xu - x^2/2R)} dx \quad (2)$$

which implies

$$S^*(x; R) e^{-jkx^2/2R} = \int f(u; R) e^{-jkxu} du \quad (3)$$

by the properties of the Fourier transform. Equation (3) may be rewritten

$$S(x; R) = e^{-jkx^2/2R} \int f^*(u; R) e^{jkxu} du \quad (4)$$

from which, by comparison with (1), it is evident that the radiation pattern  $f = s^*$  or  $|f| = |s|$ , thus validating the opening statement of this section. Now introduce a discrete sampling of the radiation field in the  $x$ -axis at locations  $x_i$  and let the adaptive circuits weight the  $N$  elements by  $w_i = S^*(x_i; R)$ . The radiation pattern

$$f_a(u; R) = \int_L \sum_{i=1}^N S^*(x_i; R) \delta(x - x_i) e^{jk(xu - x^2/2R)} dx \quad (5)$$

is an approximation to (2), the approximation being due to the discrete sampling in the aperture and to its finite extent  $L$ . In (5)  $\delta(\cdot)$  is the Dirac-delta function. Since the array is not solely in the  $x$ -axis (5) is not an exact expression of the radiation pattern but is a close approximation in the angular neighborhood of the adaptive beamforming source.

A further approximation is made in the radio camera: since the amplitude of the radiation field must be nearly constant for the source to approximate a point source, it is sufficient merely to phase-weight the elements in the array by the conjugate of the incident field and to ignore its amplitude variation.

Based on this reasoning, it is seen that when various scattering centers exist in the source region the gain of the adaptively formed beam will be reduced from its maximum possible value due to the gain of the radiation pattern in the directions of those scatterers. The scatterers may be part of the synchronizing target, as in the case of the house (Fig. 2(b)), or they may be clutter scatterers in the patch illuminated by the trans-

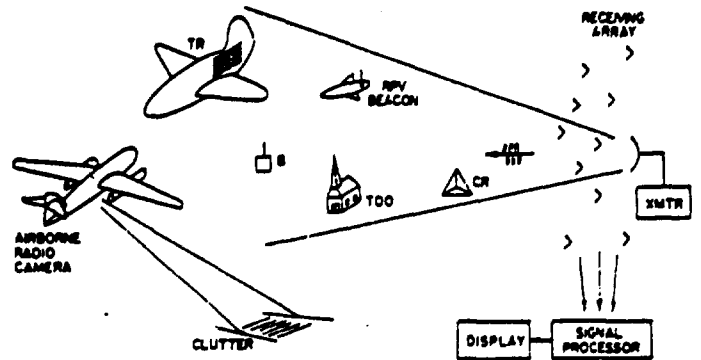


Fig. 4. Types of synchronizing sources: passive reflectors, active beacons, and distributed clutter.

mitter. To calculate the loss in gain it is necessary only to relate the phasefront distribution to the scatterer distribution and then deduce the gain loss from the phase-front distortion.

First, the scatterer distribution, whether on the beamforming target or in the illuminated clutter patch, may be presumed to be random, which is a sufficient condition to ensure that the phase perturbations in the phasefront of the reradiation also are random. Given this condition the loss in gain, in decibels, is  $4.3 \sigma_\phi^2$ . Next, assume that a tolerable loss in gain is 1 dB. The phase variance allowed in the phasefront is  $\sigma_\phi^2 = 1/4.3 \text{ rad}^2$ . Now assume that the target having radar cross section  $\sigma_T$  radiates as a point source and that the clutter cross section  $\sigma_C < \sigma_T$ . Their echoes received at some arbitrary antenna element in the array arrive with arbitrary phase  $\alpha$  and amplitude ratio  $a = \sigma_C^{1/2}/\sigma_T^{1/2} < 1$ . The phase error  $\delta\phi = \tan^{-1} [a \sin \alpha / (1 + a \cos \alpha)]$  is a zero mean random variable. Equating its variance to  $1/4.3$  leads to the condition  $\sigma_T \geq 2.5 \sigma_C$ , which guarantees that the loss in gain will not exceed tolerance.

## TYPES OF SYNCHRONIZING SOURCES

Fig. 4 illustrates several types of synchronizing sources. Shown on the ground are a corner reflector (CR), which is a near-ideal beamforming source, and a large, prominent target of opportunity (TOO). Both are passive reflectors. Also shown is an active beacon (B). The beacon can be airborne as well, as illustrated by the one carried in the remotely piloted vehicle (RPV). The beamforming target also may be a reflecting surface on the target to be imaged (called a target reference (TR)), as is illustrated by the large specular reflecting surface of the airplane target. Lastly, the beamforming source can be distributed clutter echoes as is illustrated for the airborne radio camera. These three types of sources (passive reflector, active beacon and distributed clutter) are discussed separately in the subsections below.

### Passive Reflector

Not only must the passive reflector have a large enough radar cross section so that its echo dominates the phasefront of the radiation field illuminating the array, but its physical size must be small enough so that its reradiation is nearly planar or spherical. These two conditions place bounds on the acceptable size of a passive target.

The nominal lobe spacing of the radiation from a target of size  $T$  is  $\lambda/T$ . That this is so may be seen by considering structures of simple or known characteristics. For example, a flat-plate reflector of length  $T$  radiates a pattern having the angu-

lar characteristic  $\sin(\pi Tu/\lambda)/(\pi Tu/\lambda)$ , where  $u = \sin(\theta - \theta_0)$ ,  $\theta$  is the angle measured from the normal to the surface, and  $\theta_0$  is the direction of maximum reradiation. The width of the main lobe is approximately  $\lambda/T$ , as is the spacing between zero crossings in the remainder of the reradiation pattern. Similarly, if the target contains two prominent scatterers of equal strength spaced by  $T$  the reradiation pattern has the form  $\cos(\pi Tu/\lambda)$ . The zero-crossing interval is  $\lambda/T$ . If the scatterers are of unequal strength the radiation pattern develops an additive constant but the angular modulation period remains the same. Lastly, if a target consists of many scatterers of random amplitudes and locations within the interval  $T$  the results will be similar. Let the scatterer distribution be a sample function of a random process characterized by  $\sum a_i \delta(y - y_i)$ , where  $a_i$  are the scattering amplitudes and  $y_i$  are their locations on the reflector. The radiation pattern is

$$g(u) = \int_{-\frac{T}{2}}^{\frac{T}{2}} \sum a_i \delta(y - y_i) e^{ik_y u} dy$$

$$= \frac{\sin(\pi Tu/\lambda)}{\pi Tu/\lambda} * \sum a_i e^{jk_y y_i} \quad (6)$$

where the asterisk means convolution. The second term is the underlying radiation pattern of the collection of scatterers. The first term is due to the truncation of the random process; it is the Fourier transform of the window function representing the extent of the target. The lobe spacing of  $g(u)$  can be no smaller than that of the sinc function, which is  $\lambda/T$ . All three examples indicate  $\lambda/T$  to be a typical value of the lobe spacing. A lobe width is about half this value, and its cross section at the array a distance  $R$  from the target is  $\lambda R/2T$ . Unless the central portion of such a lobe encompasses the entire array the second condition above is not satisfied. Hence, a minimum condition for satisfactory beamforming is

$$\frac{\lambda R}{2T} > L \text{ or } T < \frac{\lambda R}{2L} \quad (7)$$

To satisfy the first condition the radar cross section of the adaptive beamformer must exceed the combined cross sections of all the scatterers in the illuminated patch so as to dominate the phasefront. The clutter cross section  $\sigma_C = A_C \sigma_0$ , where  $A_C = R \Delta R \Delta \theta$  is the area of the patch illuminated by the transmitter,  $\Delta \theta$  is the nominal beamwidth,  $\Delta R$  is the pulse length, and  $R$  is the distance from the transmitter.  $\sigma_0$  is the normalized backscatter coefficient of the terrain. The radar cross section of the target  $\sigma_T = A_T G$ , where  $A_T$  is the projected target area illuminated by the transmitter, and  $G$  is the gain or directivity of the target reradiation in the direction of the receiver. The peak gain of a flat plate reflector is  $4\pi A_T/\lambda^2$  and its maximum radar cross section is  $\sigma_T = 4\pi A_T^2/\lambda^2$  which equals  $4\pi T^4/\lambda^2$  for a square reflector of side  $T$ . Since the effective area of a corner reflector is that of the inscribed equilateral hexagon, its area is  $T^2/2\sqrt{3}$  and its radar cross section is approximately  $T^4/\lambda^2$ . Radar cross sections of other standard shapes are well documented [10].

By using the condition  $\sigma_T \geq 2.5 \sigma_C$  derived earlier, and expressing  $\sigma_T$  and  $\sigma_C$  in terms of radar and target parameters, the lower bound on target size is easily calculated for any shape. For example, by using the last expression above for target cross section the inequality  $T^4/\lambda^2 < 2.5 \sigma_0 R \Delta R \Delta \theta$  expresses a lower bound upon corner reflector target size. Com-

TABLE I  
MAXIMUM AND MINIMUM SIZES OF CORNER REFLECTORS  
FOR USE AS SOURCES FOR X-BAND AND L-BAND  
ILLUSTRATIONS

Band	$\lambda$ (m)	$\sigma_0$	$\Delta R$ (m)	$\Delta \theta$ (rad)	$\lambda/L$	$T_{\min}$ (m)	$T_{\max}$ (m)
X	0.03	$10^{-2}$	5	1/20	1/2000	0.25	5
L	0.3	$10^{-3}$	20	1/20	1/2000	0.61	5

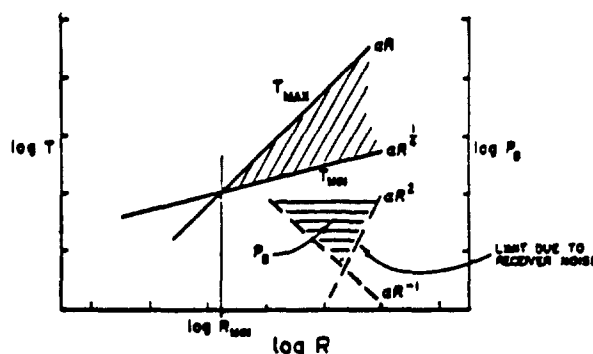


Fig. 5. Range dependencies on size of passive reflector  $T$  and beacon power  $P_B$ .

binning it with (7) yields

$$(2.5 \lambda^2 \sigma_0 R \Delta R \Delta \theta)^{1/4} < T < \frac{\lambda R}{2L} \quad (8)$$

Table I illustrates two cases of radars with beamwidths of 1/20 rad or approximately  $3^\circ$ . One has a 3 cm wavelength and a 5 m range resolution. The other has a 30 cm wavelength and a 20 m range resolution. In each case the design problem is to make the azimuthal resolution 100 times finer through the use of a large, distributed, receiving phased array. The adaptive beamformer is at a distance of 10 km in both cases. Values of  $\sigma_0 = 10^{-2}$  and  $10^{-3}$  are assumed for the two wavelengths. The right side of the table shows the maximum and minimum sizes of corner reflectors that satisfy the requirements described above.

Fig. 5 expresses the bounds as a function of range  $R$ . It is evident that at short ranges the minimum allowed size exceeds the maximum allowed size, which means that adaptive beamforming cannot be accomplished with a passive reflector at distances less than some minimum range. The minimum range is found by equating the bounds:

$$R_{\min} = (40 L^4 \lambda^{-2} \sigma_0 \Delta R \Delta \theta)^{1/3} \quad (9)$$

#### Active Beacon

The second phase synchronizing source is an active beacon triggered by the radar transmitter radiating a pulse sequence of power  $P_B$  at a distance  $R$  from the array. Isotropic radiation is assumed. The beacon power density at the array is  $P_B/4\pi R^2$ . The clutter power density at the array is  $P_T G_T \sigma_C / (4\pi R^2)^2$  where  $P_T$  is the radar transmitter power and  $G_T$  is the antenna gain [11]. The clutter cross section  $\sigma_C$  was given in the subsection above. Combining these terms and requiring that the beacon signal exceed the clutter echo by a factor of 2.5 or more results in the following condition on the beacon power:

$$P_B > \frac{P_T G_T \sigma_0 \Delta R \Delta \theta}{1.6 \pi R} \quad (10)$$

Whereas the required size of the passive target grows with range (see (8)), the minimum required beacon power is inversely proportional to distance. This surprising result is due to the fact that the beacon power density at the receiver suffers an inverse square propagation loss while the clutter power decreases with the cube of range.  $P_B$  cannot decrease indefinitely with range because the beacon signal always must exceed receiver noise. Based on the assumption that receiver noise is independent from antenna-element channel to channel the received signal must exceed the noise by the same factor of 2.5 as it must exceed the clutter. The received beacon signal power is  $P_B A_R / 4\pi R^2$ , where  $A_R$  is the effective area of the entire receiving array. Receiver noise power is  $kTBF$  where  $k$  is Boltzmann's constant,  $T$  is receiver temperature,  $B$  is receiver bandwidth, and  $F$  is the system noise figure. Combining these expressions leads to the second requirement upon beacon power:

$$P_B > \frac{10\pi R^2 kTBF}{A_R} \quad (11)$$

These equations also are plotted in Fig. 5. If the beacon is self-triggered (radar transmitter turned off) the weak demand upon beacon power given by (10) vanishes.

Due to the different range dependencies of the passive target and the active beacon, the following general observations may be made:

- A TOO, which is required for synchronizing a mobile radio camera, is most likely to be found at a short distance from the radar.
- A fixed installation can use an implanted source. The choice of active beacon triggered by the radar transmitter versus passive reflector will be influenced by the distance from source to radar (short range favors a passive source and long range favors the beacon).

#### Clutter as a Synchronizing Source

Earlier it was shown that the beam pattern, following self-cohering, approximates the source function that produces the incident radiation field. If the echoes are primarily from clutter the pattern will approximate the angular clutter distribution weighted by the pattern of the illuminating beam. Its width, therefore, will be the same as that of the transmitter, and no resolution improvement will result. When the radar system is airborne, however, echoes from scatterers within the ground patch may be distinguished from each other by their Doppler shifts; hence, narrow-band filtering of the received clutter echoes can extract the reflections from scatterers within a subpatch of the desired width. The output of such a filter can be used as a phase-synchronizing reference [5].

Fig. 6 shows an airborne radar moving with speed  $V$  illuminating a clutter patch with beamwidth  $\Delta\theta$  at distance  $R$  and at angle  $\theta$  from the ground track. The receiving array of length  $L$  is assumed to be distributed on the airframe. The width of the clutter patch  $R\Delta\theta = R\lambda/a$ ,  $a \ll L$  is the aperture of the radar transmitter, whereas the proper width cannot exceed  $\lambda R/2L$ , as derived in (7). Assuming that the aircraft altitude is much smaller than the range, the Doppler shift of an echo from a scatterer at angle  $\theta$  is

$$f_d \approx 2V \cos \theta / \lambda. \quad (12)$$

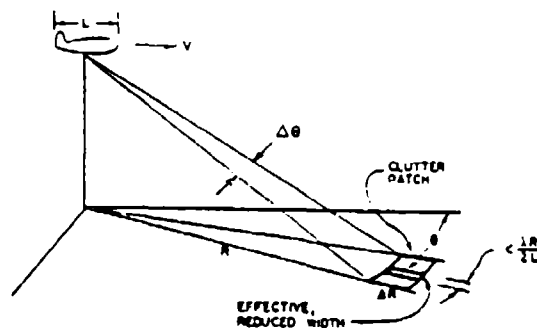


Fig. 6. The clutter patch is too wide to be a synchronizing source. Narrow-band filtering in the receiver reduces effective patch width to  $\lambda R/2L$ .

To confine the response of the filter to echoes from the desired subpatch its bandwidth

$$W < \frac{2V}{\lambda} \left[ \cos \left( \theta - \frac{\lambda}{4L} \right) - \cos \left( \theta + \frac{\lambda}{4L} \right) \right] \\ = \frac{4V}{\lambda} \sin \frac{\lambda}{4L} \sin \theta \approx \frac{V}{L} \sin \theta. \quad (13)$$

Fig. 7 shows how the reference signal would be used.<sup>1</sup> One element is chosen as the reference element. A narrow-band filter (NBF) of bandwidth  $W$  centered at the mean Doppler shift delivers the reference signal to a bank of phase detectors, each associated with one antenna element. The clutter echoes received at each antenna element pass through a voltage-controlled phase shifter to the summer of the phased array. The signal also passes to the other input of the phase detector. The beat product is smoothed in a low pass filter and applied as the control voltage to the phase shifter. The circuit is a phaselock loop which drives the two inputs to the phase detector into a quadrature relationship. The loop responds to those components of the element signal which correlate with the narrow-band reference signal.

Fig. 8 shows the clutter spectrum at an arbitrary element and after passage through the NBF. The clutter signal may be represented by the sum of  $M$  sinusoidal echoes of amplitudes  $a_i$ , Doppler shifts  $f_d + f_i$  where  $f_d = 2V \cos \theta / \lambda$  is the mean shift, and phases  $\phi_i$ . The  $a_i$ ,  $f_i$  and  $\phi_i$  are independent random variables. In addition, there is a phase shift  $\Phi$  due to the position of the element in the distorted array;  $\Phi$  is the quantity to be corrected by the adaptive process. Calling the clutter signal  $c(t)$ , its equation is

$$c(t) = \sum_{i=1}^M a_i \cos [(\omega_0 + \omega_d + \omega_i)t + \phi_i + \Phi] \quad (14)$$

where  $\omega = 2\pi f$ . The reference wave is the sum of  $K < M$  echoes from the central portion of the ground patch. Its waveform is

$$r(t) = \sum_{j=1}^K a_j \cos [(\omega_0 + \omega_d + \omega_j)t + \phi_j]. \quad (15)$$

<sup>1</sup> A receiver chain containing the usual circuits such as amplifiers, mixer, and local oscillator is implicit in each channel. Coherent detection also is implicit. The NBF is assumed to be preceded by a range gate so that the NBF responds only to scatterers in the range interval  $[R, R + \Delta R]$ . Similarly, a range gate is assumed at the signal-input port of the phase detector. The analysis which follows also pertains to wide-band delay-line filters having narrow passbands at intervals of the pulse repetition frequency and to optical correlators [11].

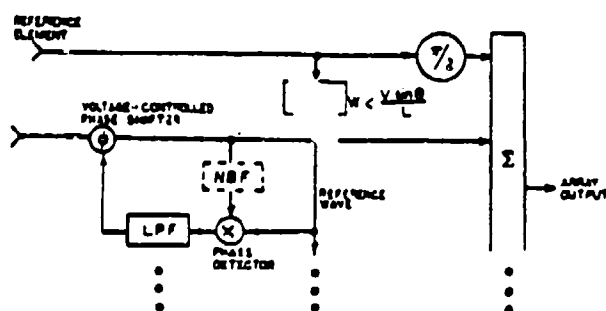


Fig. 7. Reference element and one other element in airborne radio camera. All signals phaselocked by clutter-derived reference wave obtained from narrow-band filter.

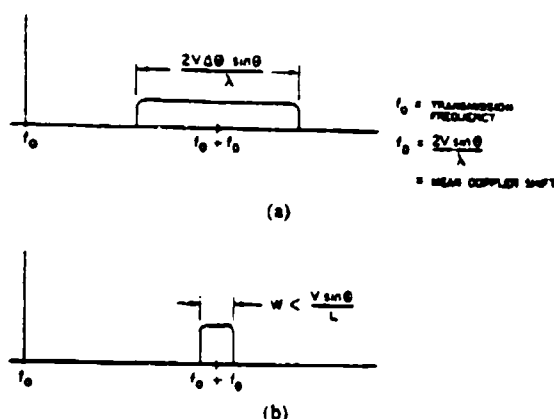


Fig. 8. (a) Input clutter spectrum. (b) After narrow-band filter in reference channel.

The mixer output is the product  $e(t) = c(t)r(t)$ , only the low frequency terms of which pass through the low pass filter. Its output voltage is

$$u(t) = \frac{1}{2} \sum_{i=1}^{M>K} \sum_j a_i a_j \cos [(\omega_i - \omega_j)t + \phi_i - \phi_j + \Phi] \\ = \frac{1}{2} \cos \Phi \sum_{i=1}^K a_i^2 + \frac{1}{2} \sum_{i=1}^{M>K} \sum_{j=1}^K a_i a_j \\ \cdot \cos [(\omega_i - \omega_j)t + \phi_i - \phi_j + \Phi]. \quad (16)$$

The dc output is  $\bar{u}(t) = K\bar{a}^2 (\cos \Phi)/2$  where  $\bar{a}^2$  is the mean square echo strength of the scatterers. Thus, the dc control voltage for the phase shifter is proportional to  $\cos \Phi$ . Since the loop drives this voltage to zero, the portion of the phase-shifted element signal within the passband of the NBF is brought into phase quadrature with the reference signal independent of the array distortion-induced phase error  $\Phi$ . This procedure is performed in all array-element channels, resulting in the cophasing of their signals. The reference signal channel may be added provided that it is shifted in phase by  $\pi/2$ . The sum is the array output. Adding the NBF (shown dashed) in the PLL improves both its acquisition and tracking characteristics by reducing the phase noise in the loop. The steady state phase-error variance in the loop is proportional to the variance of (16) which is the power in the second term. That term consists of  $K(M-1)$  sinusoids of average amplitude

$1/2\bar{a}_i\bar{a}_j = 1/2\bar{a}_i\bar{a}_j = 1/2\bar{a}^2$ , assuming that the scatterers are statistically independent and have common statistics. Since the Doppler shifts and scatterer phases are independent from scatterer to scatterer the average power in the second term is the sum of the component powers, each of which contributes  $1/2(1/2\bar{a}^2)^2 = \bar{a}^4/8$ . Hence, the variance of (16) is  $\sigma_u^2 = K(M-1)\bar{a}^4/8$ .

By adding the dashed NBF's in the element channels the number of scatterers in the clutter signal (13) drops from  $M$  to  $K$ , which reduces the variance to  $\sigma_{u,NBF}^2 = K(K-1)\bar{a}^4/8$ . The reduction in phase-noise power is the factor  $(M-1)/(K-1) \approx M/K$  since the number of scatterers is large. This ratio is  $2L\Delta\theta/\lambda$ , which is approximately the ratio of the clutter bandwidth to the filter bandwidth because random ground and sea clutter typically exhibit uniform angular distributions and the transformation (12) from angle to frequency shift is, for small angles, nearly constant. This phase-noise power reduction factor is exactly the angular resolution improvement ratio, which can be very large. For example, consider an S-band radar ( $\lambda = 10$  cm) with a  $3^\circ$  beamwidth ( $\Delta\theta \approx 1/20$  rad) aboard a 30 m aircraft. The resolution improvement factor is 30, which means that the reduction in the phase-noise power in the PLL can be as large as 15 dB when the NBF is added in the loop.

In addition to the proper filter bandwidth (13) the frequency selectivity of the filter must ensure that the clutter power of the echoes passing through the central region of the filter exceeds the remainder by at least a factor of 2.5, or 4 dB. Let the clutter power density spectrum be represented by  $C(f)$  and the filter transfer function by  $H(f)$ , where the origin of the frequency variable  $f$  is taken at the mean Doppler shift  $f_d$ . Based on (12) and the assumption at  $e$  of a uniform angular distribution of scatterers,  $C(f)$  is proportional to the probability density function of the frequency variable in (12) and the weighting due to the antenna pattern. The former can be shown to be proportional to  $[(2V/\lambda)^2 - f^2]^{-1/2}$ . The latter is the two-way antenna pattern transformed from the angle variable  $\theta$  to the frequency variable  $f$  using (12). The required condition on  $H(f)$  is given by

$$\frac{\int_0^{W/2} C(f)|H(f)|^2 df}{\int_{W/2}^W C(f)|H(f)|^2 df} > 2.5. \quad (17)$$

## SUMMARY

A distorted phased array can be made to operate as a diffraction-limited aperture if a compensating phase shift is added in each antenna element channel. When the distortion is not known *a priori* the phase correction must be based upon phasefront measurements of the radiation from a source external to the array. The ideal phase synchronizing source is a point source radiating in free space. The phasefronts of realistic sources are perturbed, however. This paper discusses three types of practical sources and calculates the conditions under which their radiation fields are acceptable for adaptive beamforming.

The most important source is a passive reflector such as a corner reflector or a large target of opportunity. It is shown

that bounds exist on the minimum and maximum sizes of such reflectors and that there is some minimum distance below which the conditions cannot be met. The bounds on size  $T$  when the synchronizing source is a corner reflector and the minimum range  $R_{\min}$  are

$$(2.5\lambda^2\sigma_0 R \Delta R \Delta\theta)^{1/4} < T < \frac{\lambda R}{2L} \quad (8)$$

$$R_{\min} = (40L^4\lambda^{-2}\sigma_0 \Delta R \Delta\theta)^{1/3} \quad (9)$$

An active beacon is an excellent adaptive beamforming source. The required beacon power decreases with range according to the relation

$$P_B > \frac{P_T G_T \sigma_0 \Delta R \Delta\theta}{1.6\pi R} \quad (10)$$

until such a range is reached at which receiver noise competes with the beacon signal. Beyond that range the beacon power must increase with distance according to

$$P_B > \frac{10\pi R^2 k T B F}{A_R} \quad (11)$$

It is also possible to use clutter echoes to phase synchronize a distorted array provided that the radiation from scatterers located at different angular positions in the ground patch can be distinguished in the receiver. This condition can be met if the radar is on a moving platform, for then the scatterer echoes are Doppler shifted in proportion to  $\cos \theta$ . Narrow-band filters in each antenna element channel respond only to echoes from scatterers in a narrow angular or cross-range swath no larger than  $T_{\max}$ , given above. The procedure permits the extraction from the clutter echoes of a reference signal to phase synchronize the array, thereby permitting the technique to be applied to an airborne distributed antenna array aboard a nonrigid aircraft. The first condition on the filter bandwidth is

$$W < \frac{V \sin \theta}{L} \quad (13)$$

and on the frequency selectivity of its transfer function  $H(f)$  it is

$$\int_0^{W/2} C(f) |H(f)|^2 df > 2.5 \int_{W/2}^{\infty} C(f) |H(f)|^2 df \quad (17)$$

$C(f)$  in (17) is the clutter power density spectrum.

## REFERENCES

- [1] *IEEE Trans. Antennas Propagat.*, vol. AP-12, no. 2, Mar. 1964, Special Issue on Active and Adaptive Antennas (contains 13 papers on retrodirectivity).
- [2] R. C. Hansen, Ed., *Microwave Scanning Antennas*, vol. 3, New York: Academic, 1964. (See ch. 5 by D. L. Margerum.)
- [3] R. C. Chermoff, "Large active retrodirective arrays for space applications," *IEEE Trans. Antennas Propagat.*, vol. AP-27, no. 4, pp. 489-495, July 1979.
- [4] B. D. Steinberg, "Design approach for a high-resolution microwave imaging radio camera," *J. Franklin Inst.*, vol. 296, no. 6, pp. 415-432, Dec. 1973.
- [5] —, *Principles of Aperture and Array System Design*, New York: Wiley, 1976.
- [6] B. D. Steinberg, E. N. Powers, D. Carlson, B. Meagher, Jr., R. S. Berkowitz, C. N. Dorn, and S. H. Seeleman, "First experimental results from the Valley Forge radio camera program," *Proc. IEEE*, pp. 1370-1371, Sept. 1979.
- [7] B. D. Steinberg, "Radar imaging from a distorted array: The radio camera algorithm and experiments," *IEEE Trans. Antennas Propagat.*, pp. 740-748, Sept. 1981.
- [8] —, "High angular microwave resolution from a distorted array," *Proc. 1980 Int. Comput. Conf.*, vol. 231, pp. 150-156, Apr. 1980.
- [9] R. S. Berkowitz and E. N. Powers, "TASAR, a thinned adaptive synthetic aperture radar," *IEEE EASCON '78 Rec.*, Arlington, VA, IEEE Pub. 78 CH 1354-4 AES, pp. 135-142.
- [10] G. T. Ruck, Ed., *Radar Cross Section Handbook*, New York: Plenum, 1970.
- [11] R. S. Berkowitz, Ed., *Modern Radar Systems*, New York: Wiley, 1965.

Bernard D. Steinberg (S'48-A'50-SM'64-F'66), for a photograph and biography please see page 748 of the September 1981 issue of this TRANSACTIONS.

EFFECT OF MULTIPATH AND SCATTERING  
ON ARRAY GAIN OF A LARGE ADAP-  
TIVE BEAMFORMING PHASED ARRAY\*

Bernard D. Steinberg  
Valley Forge Research Center  
Moore School of Electrical Engineering  
University of Pennsylvania  
Philadelphia, Pennsylvania

and

Eli Yadin  
Interspec Inc.  
101 N. 33rd Street  
Philadelphia, Pennsylvania

ABSTRACT

An adaptive antenna array system large enough to obtain angular resolving power comparable to common optical systems is called a radio camera. Following an adaptive beamforming procedure the beam is open-loop scanned to get the desired images. Multipath and scattering of the energy reradiated from the target induce phasefront distortions. A theory has been developed showing that the loss in array gain due to the scattered field can be described by a simple relationship involving only two quantities: the strength  $S$  of the scattered field relative to the direct field and a spatial correlation function  $\rho(\theta)$  associated with the scattering process. The argument  $\theta$  is the scanning angle. The array gain is  $G(\theta) = G(0)S[1 - \rho(\theta)]$ .

A series of experiments has been conducted to test the assumptions underlying the development of the theory, which appears to vindicate them. The theory and experiments are described. The theory is then used to determine the degradation in radio camera scanning performance for several important cases of interference caused by reflections.

\*This work was principally supported by the Office of Naval Research, the Air Force Office of Scientific Research and the Army Research Office.

Submitted for publication to the IEEE Transactions on Antennas and Propagation.

EFFECT OF MULTIPATH AND SCATTERING  
ON ARRAY GAIN OF A LARGE ADAP-  
TIVE BEAMFORMING PHASED ARRAY\*

Bernard D. Steinberg & Eli Yadin

1. INTRODUCTION

An earlier paper described a procedure for self-cohering a distorted or time varying phased array so as to obtain diffraction-limited imaging from it [1]. Beamforming was accomplished by measuring the radiation field at each point in the array due to a point source or reflector. Conjugate phases were added at each antenna element to form a focused, retrodirective beam, which was scanned in angle and range for imaging. The beamwidth (in radians) was approximately the reciprocal of the size of the array in units of wavelength and the sidelobe properties were those of the random array. A high angular resolution imaging system incorporating this procedure is called a radio camera.

While beamforming requires no knowledge of antenna element positions, scanning does require such knowledge. The self-cohering beamforming process eases the tolerance on element position errors [2], [3], [4]. A nominal rms surface tolerance of  $\lambda/4\pi$ , which normally reduces array gain by 1 dB, can be increased by the reciprocal of the angle (in radians) through which the system is scanned. Given a field of view as large as the moon, the element position error tolerance can be increased by two orders of magnitude.

This paper addresses the effects on array gain of a radio camera when propagation conditions differ from free-space propagation. Multipath and scattering distort the radiation field at the array, the measurements of which are used to retrodirectively focus a beam on the source. It is shown that two relatively simple descriptors of the scattering process describe the loss in array gain. These are the ratio of the scattered-to-direct field intensities and a correlation function of phase errors induced in the measurements of the radiation field due to

the scattering. Experimental evidence lends support to the theory.

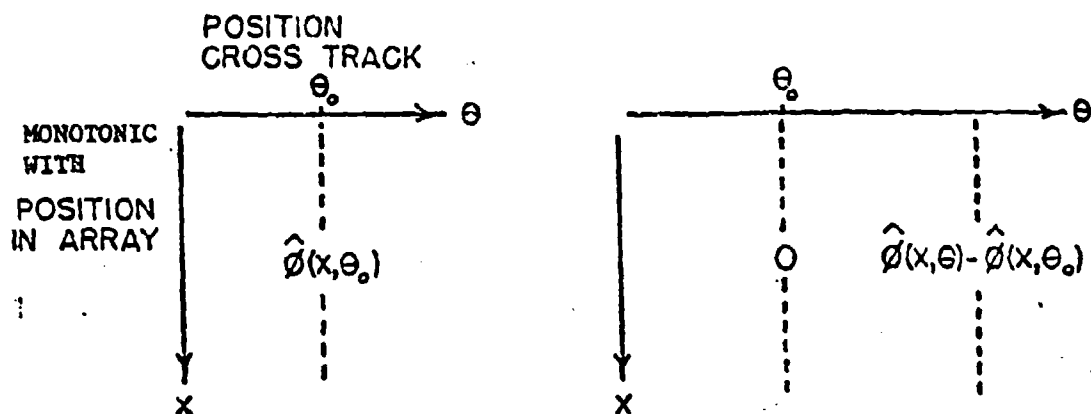
Two types of scattering and three cases for each type are analyzed: The fixed point reflector and the specular reflector located close to the target area, roughly mid-path between target and array, and within the array.

## 2. ADAPTIVE BEAMFORMING

No loss of average array gain is incurred at the beamforming angle, when adaptive beamforming is employed, even in the presence of phase errors in the beamforming signals. Loss develops when scanning the radio camera away from  $\theta_0$ , the direction of beamforming. Although different methods of adaptive beamforming exhibit detailed differences, the following discussion illustrates the general distinction between the closed-loop (adaptive) beamforming and the open-loop (nonadaptive) scanning functions.

Figure 1 illustrates how phase errors degrade array gain during scanning. The symbol  $\hat{\phi}$  is used to distinguish between the measured phase with error and the proper phase  $\phi$ . Let  $x$  represent position in the array and let the  $x$ -axis be approximately perpendicular to the target direction. Let  $\theta$  represent target angular position and let the  $\theta$ -axis be an arc of constant distance from the array. Next let the measured phase at point  $x$  due to a target or source at angle  $\theta$  in the field be  $\hat{\phi}(x, \theta) = \phi(x, \theta) + \delta\phi(x, \theta)$ . The first term is the "geometric" phase (modulo  $2\pi$ ) equal to  $2\pi/\lambda$  times the distance between point  $x$  and the target. The second term is an error due to noise, multipath, element position error, and other sources of phase error. The amplitude of the received signal is  $a(x, \theta)$ .

Now assume a strong synchronizing source at  $\theta = \theta_0$  radiating energy to the array. The retrodirective process focuses the array on the source.  $\hat{\phi}(x, \theta_0)$  (Figure 1a) is a column vector in a matrix  $\hat{\phi}(x, \theta)$ . To form a beam at  $\theta = \theta_0$  it is necessary to phase rotate the received signal  $a(x, \theta_0) \exp[j\hat{\phi}(x, \theta_0)]$  by the negative of  $\hat{\phi}(x, \theta_0)$  (Figure 1b), and to sum the phase-rotated vectors. All signals from the direction  $\theta = \theta_0$  become cophased and may be added. This is what the phase shifters in a phased array do.



(a)  $\hat{\phi}(x, \theta)$  MATRIX.  $\hat{\phi}(x, \theta_0)$  IS THE PHASE OF THE SYNCHRONIZING SIGNAL RECEIVED AT POINT X IN THE ARRAY FROM A SOURCE AT  $\theta_0$ .

(b) PHASE MATRIX AFTER BEAMFORMATION AT  $\theta = \theta_0$ .

FIGURE 1. BEAMFORMING PROCEDURE

In adaptive beamforming, closed-loop self-phasing procedures do the phase rotation. Signals arriving from any other direction  $\theta$  are similarly phase shifted by  $\hat{\phi}(x, \theta_0)$ . The general entry in Figure 1b becomes  $\hat{\phi}(x, \theta) - \hat{\phi}(x, \theta_0)$ . Designating discrete element locations as  $x_1$ , the complex sum

$$f(\theta) = \sum_{i=1}^N a(x_i, \theta) \exp[j\{\hat{\phi}(x_i, \theta) - \hat{\phi}(x_i, \theta_0)\}] \quad (1)$$

is the complex gain of the array in the direction  $\theta$ . Of course at  $\theta = \theta_0$  the phase-rotated signals are all cophased and (1) becomes

$$f(\theta_0) = \sum_{i=1}^N a(x_i, \theta_0) \exp[j\{\hat{\phi}(x_i, \theta_0) - \hat{\phi}(x_i, \theta_0)\}] = \sum_{i=1}^N a(x_i, \theta_0) \quad (2)$$

In the absence of phase errors the radiation pattern (1) would have been

$$f_0(\theta) = \sum_{i=1}^N a(x_i, \theta) \exp[j\{\phi(x_i, \theta) - \phi(x_i, \theta)\}] \quad (3)$$

and its peak value

$$f_0(\theta_0) = \sum_{i=1}^N a(x_i, \theta_0) = f(\theta_0) \quad (4)$$

is the same as in (2), showing that loss does not develop at the beamforming angle even in the presence of phase errors in the beamforming signals.

The effects upon scanning are different, however. The objective of the scanning operation is to make some other column vector in the matrix, say  $\phi(x, \theta_1)$ , equal to zero. Signals arriving from  $\theta = \theta_1$  should, after processing become cophased, and their vector sum should add to the sum of the amplitudes, as in (2). Errors in phase measurement, however, reduce the vector sum, implying a loss in main-lobe gain.

This loss in gain is the dominant effect of phase measurement errors provided that (a) the errors in phase measurement are random and independent and (b) the element placements are random. Beamwidth, beam shape and pointing error effects then become nil. The sidelobe properties are already those of a random process; further random phase perturbations change the details of the side radiation pattern but not its statistics. Hence the effect of phase measurement errors is to reduce the contrast in the scanned image (main lobe to average sidelobe ratio) but not the resolution (proportional to beamwidth).

Equation (1) illustrates adaptive beamforming: the second term in the argument of the exponential zeros the phases at  $\theta = \theta_0$ . Scanning the beam to  $\theta_1$  after adaptive focus at  $\theta_0$  requires a further phase correction.  $\hat{\phi}(x, \theta_0)$  must be sub-

tracted from the phase of the signal. This is an open-loop process. The signal processor can only estimate the required phase correction from the geometry:  $\phi(x, \theta_1) - \phi(x, \theta_0)$ . The difference between the desired phase shift and the actual open-loop phase shift is the residual phase error introduced by the scanning process (dropping the subscript on beam direction  $\theta$ ):

$$\hat{\phi}(x, \theta) - \hat{\phi}(x, \theta_0) - [\phi(x, \theta) - \phi(x, \theta_0)] = \delta\phi(x, \theta) - \delta\phi(x, \theta_0) \neq 0 \quad (5)$$

The mean residual phase error across the array may be assumed to be zero. The residual phase-error variance is the mean square error.

$$\begin{aligned} \sigma_{\phi}^2 &= E[\delta\phi(x, \theta) - \delta\phi(x, \theta_0)]^2 \\ &= E[\delta\phi(\theta)]^2 - 2E[\delta\phi(\theta)\delta\phi(\theta_0)] + E[\delta\phi(\theta_0)]^2 \end{aligned} \quad (6)$$

It was shown in [4] that phase errors in the signals received across a receiving array decrease the expected value of the main-beam power gain  $G$ , under fairly general conditions, according to

$$E[G] = G_0 \exp(-\sigma_{\phi}^2) \quad (7)$$

where  $G_0$  is the gain in the absence of errors. Given  $K$  independent sources of phase error their variances add to form the total phase-error variance. The expected change in gain in decibels is

$$10 \log E[G/G_0] = -4.3 \sum_{i=1}^K \sigma_{\phi i}^2 \text{ dB} \quad (8)$$

The loss in gain, in decibels, called  $\Delta G$ , is the negative of (18).

$$\Delta G = 4.3 \sum \sigma_{\phi i}^2 \text{ dB}$$

### 3. PHASEFRONT DISTORTION DUE TO MULTIPATH AND SCATTERING

One source of phase error is multipath and scattering. Energy from the target may be scattered by reflectors located outside the direct path to the array and some of the scattered energy may arrive at the array. The phase of the sum of the direct and scattered energy across the array differs from the signal phases which would exist without scattering. Because the signal processor of the adaptive

array has no a priori means for calculating the phase changes due to the scattering, such phase alterations constitute phase errors which increase the phase error variance  $\sigma_\phi^2$ . From (6), the contribution to  $\sigma_\phi^2$  due to multipath and scattering is

$$\begin{aligned}\sigma_\phi^2 &= E[\delta\phi(x, \theta) - \delta\phi(x, \theta_0)]^2 = E[\delta\phi(x, \theta)]^2 - 2E[\delta\phi(x, \theta)\delta\phi(x, \theta_0)] + E[\delta\phi(x, \theta_0)]^2 \\ &= 2E[\delta\phi(x)]^2 [1 - \rho(x, \Delta\theta)] = 2\sigma_S^2 [1 - \rho(\Delta\theta)]\end{aligned}\quad (9)$$

where  $\sigma_S^2$  is the initial phase-error variance across the array due to the scattered energy, and  $\rho(\Delta\theta)$  is the autocorrelation function of the phase error as a function of the beamsteering displacement  $\Delta\theta = \theta - \theta_0$ . The residual phase-error variance is doubled because the residual phase error is the difference between two phase errors, and is reduced according to the correlation between them.

Four assumptions are implicit in (9), the first three of which are weak for arbitrary terrain. However, the excellent agreement is the theory with experimental data from the Valley Forge field site (shown later) lends confidence to the theory. The first assumption is that the statistics of  $\delta\phi(x, \theta)$  at any position  $x$  in the array is independent of  $\theta$ : thus

$$E[\delta\phi(x, \theta_1)]^2 = E[\delta\phi(x, \theta_j)]^2 \triangleq E[\delta\phi(x)]^2, \text{ all } i, j. \quad (10)$$

The second is that the covariance of the phase error is independent of  $\theta$  and is dependent only in the spacing  $\Delta\theta$ . This condition is the equivalent of "stationarity" in time series analysis. The third assumption is that the phase-error statistics are independent of  $x$ ; therefore

$$E[\delta\phi(x_1)]^2 = E[\delta\phi(x_j)]^2 \triangleq E[(\delta\phi)^2], \text{ all i.i.} \quad (11)$$

Lastly, it is assumed that the phase error is unbiased (zero mean) such that  $E[(\delta\phi)^2]$  is also the variance  $\sigma_S^2$ .

$\sigma_S^2$  is related to the power ratio  $S$  of the scattered signal received at the array to the direct signal.  $S^{1/2}$  is the amplitude of the scattered "signal" in Figure 2;  $\psi$  is a random phase variable uniformly distributed in  $[0, 2\pi]$ . The variance of  $\delta\phi$  is

$$\sigma_S^2 = E\left[\tan^{-1} \frac{S^{1/2} \sin\psi}{1 + S^{1/2} \cos\psi}\right]^2 \quad (12)$$

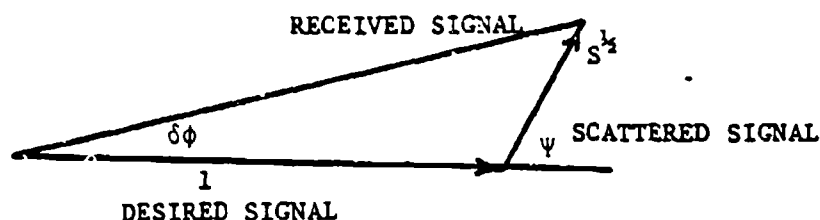


FIGURE 2. PHASE MEASUREMENT ERROR DUE TO SCATTERING

Equation (12) is approximately equal to  $S/2$  when  $S$  is small, the error being less than 7% for  $S \leq 0.25$ . Making this substitution in (7), and redefining the angle  $\theta$  to represent the scan angle from the direction of phase synchronization, the loss in gain due to scattering becomes

$$\Delta G_S(\text{dB}) = 4.3 \sigma_\phi^2 = 4.3S[1 - \rho(\theta)] \quad (13)$$

Equation (13) gives the loss as a function of only two properties of the scattering process, the scatter strength and the correlation between phase errors induced by the scattering. Being an autocorrelation function,  $\rho(\theta)$  is unity when  $\theta = 0$  and it should drop asymptotically to zero as  $\theta$  gets large. The dB loss in gain should be zero at the origin and should grow asymptotically toward 4.3 dB.  $S = 1/4 = -6$  dB corresponds to  $\Delta G_S = -1$  dB. Thus the intensity of the scattered field, at the array, can be as large as 1/4 the direct field intensity without causing more than

a 1 dB loss in image contrast.

Data taken at the Valley Forge field site tend to validate the theory. In one experiment involving strong forward scattering from the ground midway between the array and the beamforming source, it was possible to estimate the value of  $S$  [7]. In that experiment the amplitude of the wave received from a source in the field was plotted as a function of element number (monotonic with distance) within the array. This was done with the 27 m rooftop array at a wavelength of 30 cm. 20 elements were used. The source-to-array distance was 240 m. The simple, undulatory variation of amplitude shown in Figure 3 suggests a direct ray plus a single scattered or multipath ray. The average peak-to-valley ratio, observed to be  $2\frac{1}{2}:1$ , equals  $(1 + S^{\frac{1}{2}})/(1 - S^{\frac{1}{2}})$ . From these data the forward scatter coefficient  $S^{\frac{1}{2}} \approx 0.43$  and the asymptotic loss should be less than 1 dB. Measurements of the type shown in Figure 3 were made from two different sources in the field at two different locations and the results were almost identical. Based on these observations, it is assumed that  $S \sim 1/5$  typifies the scattering strength for this portion of the field site at the wavelength used.

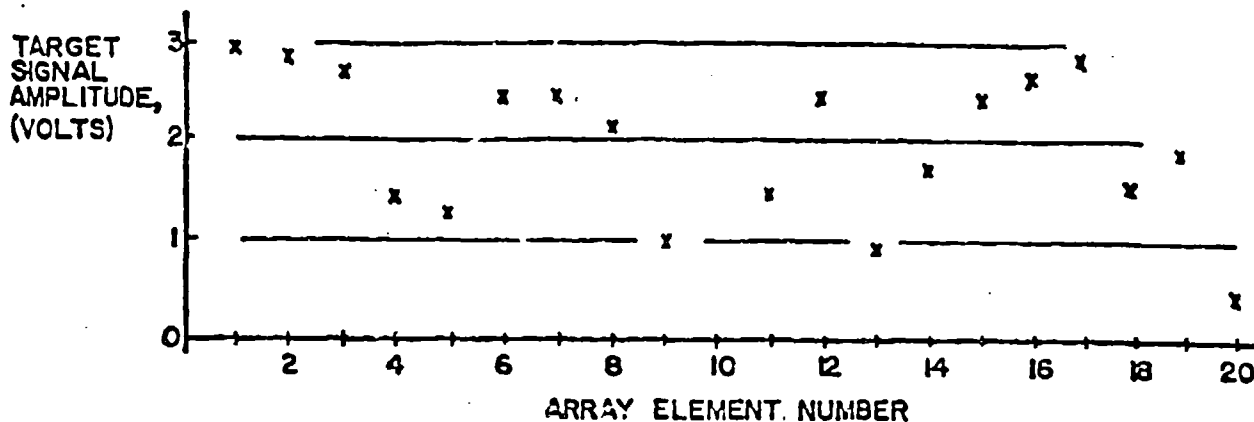


FIGURE 3. SIGNAL AMPLITUDE vs. ELEMENT NUMBER. DATA FROM [36].

A later experiment was conducted at the same site which completed the testing of the theory. Phase was measured at each element of a 16-element L-band random array when a source was moved through an angle of approximately  $6^\circ$  [8]. The source was at distance of 240 m and the 16 elements were distributed over the same 27 m portion of the laboratory roof. Also, the same portion of the field site was used for which the forward scattering coefficient estimated above was obtained. Four such experiments were conducted. A typical result showing the region in which the gain dropped with scan angle is shown in the curve labeled "experimental" in Figure 4. The direction of adaptive beamforming is at the left edge of the figure. The abscissa is the scan angle in degrees measured at the array. The general decrease in gain toward an asymptotic value of about 1 dB, as predicted by the theory, is observed. The undulations in the experimental results can be shown to be due to discrete forward-scattering from the terrain [6]. The dashed curve is calculated from the theory. The agreement is excellent. Three additional experiments yielded similar results.

The dashed curve was obtained in the following manner. The scattering process at the field site was modeled as that of a single fixed point reflector. The correlation function  $\rho(\theta)$  was calculated for this case (see Section 5). Using the expression for the correlation function derived in that section and the theory represented by (13), the loss in array gain was calculated as a function of angle. Parameters of that expression are the reflection or the forward scattering coefficient of the terrain  $S^h$  and the coordinates of the dominant reflecting portion of the terrain. A computer search was made for the set of three coordinates (scattering strength and location) for which the loss in gain with scan angle would most closely approximate the measured function of Figure 4. The computer search yielded best fit scattering strength of 0.42 which is in agreement with the measurements of Figure 3.

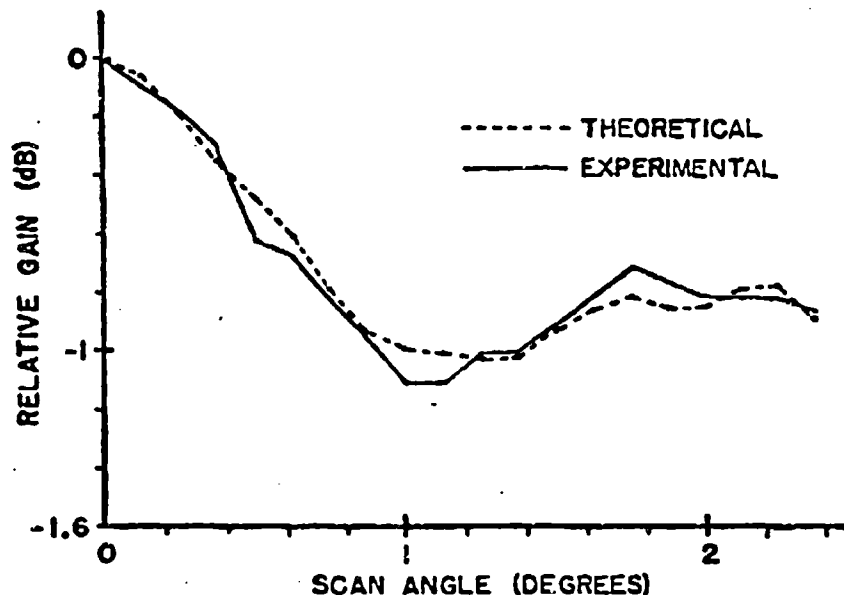


FIGURE 4. MAINBEAM GAIN vs. SCAN ANGLE FOLLOWING SELF-COHERING BEAMFORMING AT ZERO DEGREES. EXPERIMENTAL DATA FROM [8]. THEORETICAL CURVE FROM [6].

#### 4. MULTIPATH MODELS

Equation (13) gives the loss of gain as a function of the autocorrelation function of phase error in the array. In this section the autocorrelation function is calculated for two scattering models and for three scattering situations for each model.

Both models are single-scatterer models. Realistically, many scatterers contribute to the reradiation. The scattered field in general is the linear, vector superposition of the reflected energy from the several scatterers, plus the secondary reflections among them. However, a single-scatterer model sometimes suffices if one of the scatterers is larger than the vector sum of the remainder. This is because the phase of the field at any point is a nonlinear function of the scattered components, even though the field itself is a linear sum:

$$\phi = \tan^{-1} \frac{\sum a_i \sin \psi_i}{\sum a_i \cos \psi_i} \quad (14)$$

In (14)  $a_i$  is the amplitude of the  $i$ th scattered component and  $\psi_i$  is  $2\pi/\lambda$  times the distance to that scatterer. Because of the nonlinear operations  $\phi$  can be dominated by the phase of a single, large scatterer. This nonlinear phase-capture effect is assumed in the discussion which follows. The amplitude of the dominant scatterer is  $S^{1/2}$ .

The models are sketched in Figure 5. The first model is a single, fixed-point reflector. Such a scatterer would be a large rock or a prominent mound on the scattering surface. It also may be a shed or a small building. The second model is a specular surface in which the reflection point moves with target position and also with element position within the array. The three cases for each model are:

1) Scatterer close to or within the target area. Multiple scattering from a complex target in which energy reflected from one part of the target is reflected from another surface nearby the first surface before returning to the array.

2) Midpath scattering: is forward-scatter surface reflections from horizontal or near-horizontal surfaces, typified by low angle forward surface scattering in ground-to-ground radar as well as forward scattering from the sea surface in air-to-air radar.

3) Scatterers that are local to the array: within the radome structure, or by floors, walls and ceilings upon which antenna modules are located.

##### 5. THE FIXED POINT REFLECTOR MODEL

The geometry is sketched in Figure 6. Beamforming source  $T_0$  and target  $T$  subtend an angle  $\theta$  at the array. Let the direct ray from  $T$  to array point  $E$  have unit amplitude, and let the amplitude of the reflected ray be  $S^{1/2}$ . The phase of the sum of the direct and the reflected energies differ from the phase of the direct ray by

$$\delta\phi = \tan^{-1} \left\{ \frac{S^{1/2} \sin \left[ \frac{2\pi}{\lambda} (\overline{TP} + \overline{EP} - \overline{TE}) \right]}{1 + S^{1/2} \cos \left[ \frac{2\pi}{\lambda} (\overline{TP} + \overline{EP} - \overline{TE}) \right]} \right\} \quad (15)$$

where  $\overline{TP}$  is the length of the line segment connecting points T and P.

the phase error that affects the scanning performance is the difference between (15) and the phase error  $\delta\phi_0$  in the direction of adaptive beamforming. The latter has the same form as (16) with  $T_0$  replacing T in that equation. T and  $T_0$  are assumed to be at common altitudes. Their coordinates are related by  $x' = x'_0 - y'_0 \theta$ ,  $y' = y'_0 + x'_0 \theta$ ,  $z' = z'_0$ . The correlation function  $\rho(\theta)$  in (13) is given by

$$\rho(\theta) = \frac{E[\delta\phi_1 \delta\phi_0] - E[\delta\phi_1]E[\delta\phi_0]}{\sqrt{E[\delta\phi_1^2] - (E[\delta\phi_1])^2} \sqrt{E[\delta\phi_0^2] - (E[\delta\phi_0])^2}} \quad (16)$$

where E means expected value.

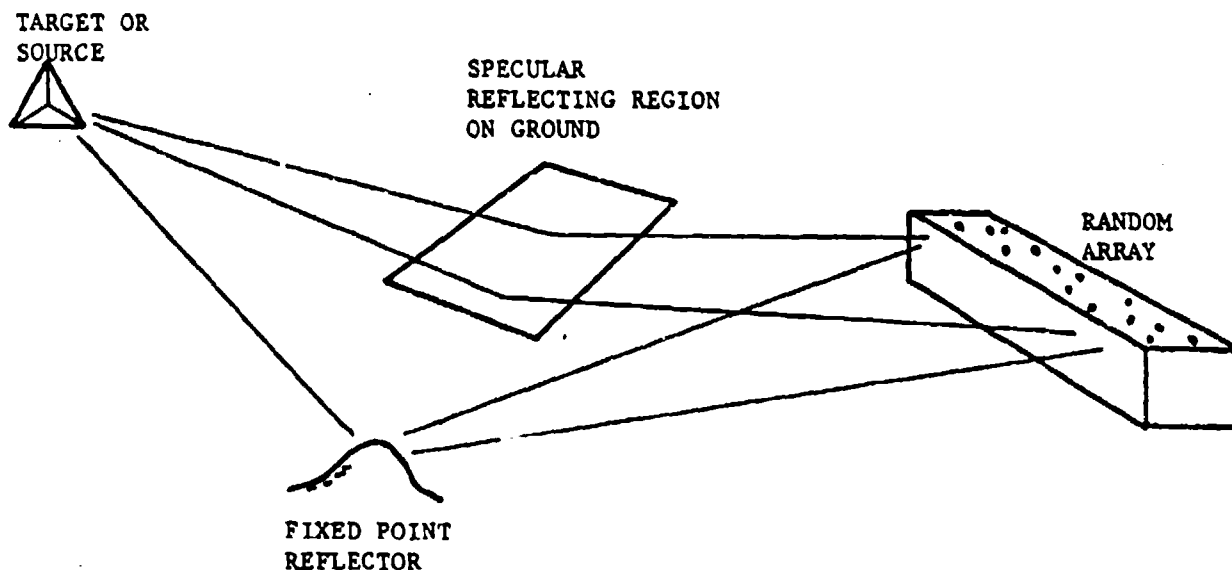


FIGURE 5. TWO FORWARD-SCATTERING MODELS

$\rho(\theta)$  was computer simulated using (16). Expected values were estimated by averaging over the actual locations of the 16 elements in the array described in Section 3. The known locations of target, beamformer and array elements were used in evaluating  $\delta\phi_0$  and  $\delta\phi_1$ , using the formulation given by (15). The scatter coordinates (strength, position) used in (15) were found from a computer search for the best fit between the predicted losses and the measured losses. One such result was shown in Figure 5. The model accurately predicted the lengths of the correlation intervals and the general character of the loss vs. scan angle in each of the four experiments.

Table 1 shows the best-fit scatter coordinates as well as the rms difference ( $\sigma_d$ ) in dB between measured and predicted losses. The reflection point is located approximately midway between array and target area.

Experiment	1	2	3	4
$S^{\frac{1}{2}}$	0.38	0.36	0.42	0.4
$x''$ (ft)	328.5	337.5	301.5	381
$y''$ (ft)	-47.5	-69.5	-45.5	-63
$\sigma_d$ (dB)	0.130	0.065	0.060	0.075

TABLE 1. BEST-FIT SCATTER COORDINATES AND RMS LOSS DIFFERENCES (dB)

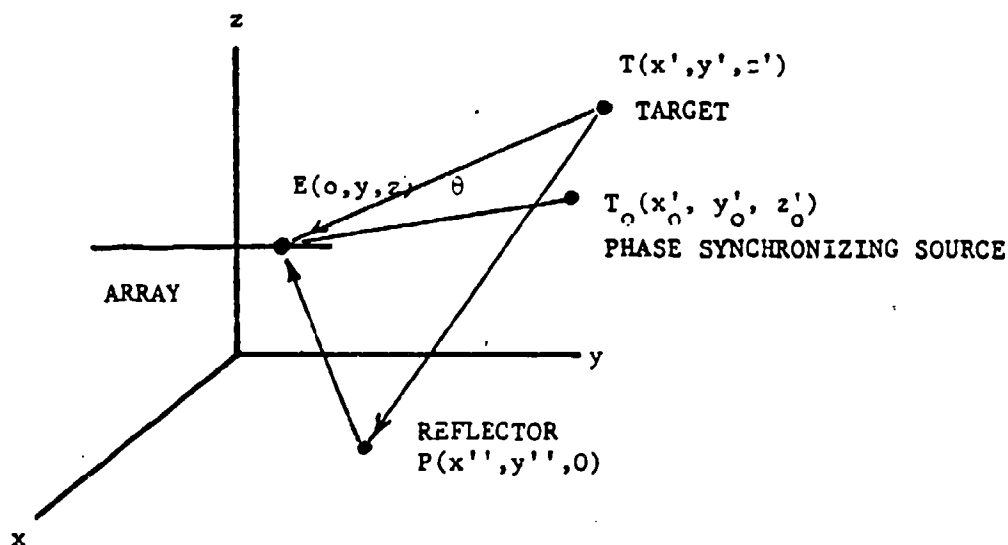


FIGURE 6. FIXED POINT REFLECTOR (FPR) SCATTERING MODEL

The reflector strength is reasonably consistent from experiment to experiment and is close to the approximate value (0.43) inferred from amplitude measurements across the array reported earlier. Thus it is evident that the scattering process at this field site can be modeled by a FPR for beam scanning experiments following adaptive beamforming.

A closed form approximation for  $\rho(\theta)$  which closely matches the accurate expression given in (16) is developed in Appendix A.

## 6. THE SPECULAR REFLECTOR

The geometry for this case is shown in Figure 7. The phase error is given by

$$\delta\phi = \tan^{-1} \left\{ \frac{S^h \sin(\frac{4\pi}{\lambda} zz' / \overline{TE})}{1 + S^h \cos(\frac{4\pi}{\lambda} zz' / \overline{TE})} \right\} \quad (17)$$

A closed form approximation for the correlation function  $\rho(\theta)$  is derived in [6].

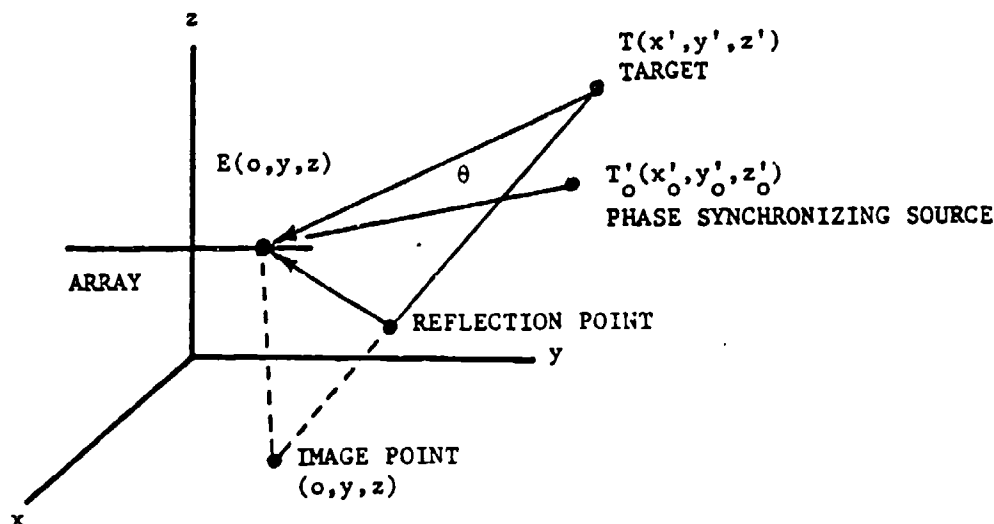


FIGURE 7. SPECULAR REFLECTOR (SR) SCATTERING MODEL

## 7. EXTENSIONS TO OTHER CASES

Since a single point reflector model, when applied to the gain-loss theory, satisfactorily predicted the scanning loss for the field site, it is with some confidence that the theory can be applied to three common and important cases. The first is typified by ground or sea surface reflections. The scattering region generally is somewhere between target and array, the exact location depending upon their heights above the ground plane and, for the SR, the slope of the ground plane. The second case involves a reflecting object near the target or a large target structure having parts separated by more than a beamwidth. It can be above or below the target and can have arbitrary orientation and location. The third case involves reflectors in or near the array. A different reflector is assumed for each antenna element; that is, each element is influenced only by its immediate physical surroundings. This last case pertains to a large array having widely spaced elements in which the reflections may arise from the walls or floors or supports for the antenna modules. In each case the correlation function, which is the necessary ingredient for the calculation of the gain-loss, can be developed [6]. They are listed in Table 2.

SCATTERING MODEL	CORRELATION FUNCTION $\rho(\theta)$	CORRELATION INTERVAL $\Delta\theta$
Many SRs near array	$\frac{\sin(\frac{\pi x' B \theta}{\lambda R})}{\frac{\pi x' B \theta}{\lambda}} \frac{\sin(\frac{\pi y' A \theta}{\lambda R})}{(\frac{\pi y' A \theta}{\lambda})}$	$> N \Delta \theta \quad \text{for } z' > \gamma$ $> \frac{x'}{y'} N \Delta \theta \quad \text{for } x' < \gamma'$
Many FPRs near array	same as above	same as above
Single specular ground plane approximately midpath	$\frac{\sin(\frac{2\pi z' z}{R^2} \frac{\theta}{\Delta \theta})}{\frac{2\pi z' z}{R^2} \frac{\theta}{\Delta \theta}} \cos(\frac{2\pi z' z}{\lambda R} \theta^2)$	$\sqrt{\frac{\lambda R}{4z' z}}$
Single FPR approximately midpath	$\frac{\sin(\frac{\pi \theta}{\Delta \theta})}{\frac{\pi \theta}{\Delta \theta}} \cos(\frac{\pi R}{\lambda} \theta^2)$	$\leq \Delta \theta$
Single vertical specular plane in target region	$\frac{\sin[\pi(1 + \frac{\Delta x}{\Delta R}) \frac{\theta}{\Delta \theta}]}{\pi(1 + \frac{\Delta x}{\Delta R}) \frac{\theta}{\Delta \theta}} \cos[\frac{2\pi}{\lambda} \frac{R}{\Delta R} \Delta y \theta]$	$\leq \Delta \theta$
Single FPR in target region	$\frac{\sin(\frac{\pi \theta}{\Delta \theta})}{\frac{\pi \theta}{\Delta \theta}} \cos \frac{2\pi}{\lambda} [\frac{R^2}{2\Delta R} \theta^2 + (\frac{x' \Delta y - y' \Delta x}{\Delta R}) \theta]$	$\leq \Delta \theta$

TABLE 2. CORRELATION FUNCTION AND CORRELATION INTERVAL FOR FIXED POINT AND SPECULAR REFLECTORS.

It is evident from (13) that the loss in main-beam gain is small when the correlation function is nearly unity (small scan angle) and is asymptotically large when the correlation drops toward zero. The scan angle interval in which the loss grows from zero to nearly the maximum value (4.35 dB) may be called the correlation interval. This quantity,  $\theta_c$ , and not the shape of  $\rho(\theta)$ , is the pertinent characteristic of the correlation function. It is given in Table 2 for the six cases studied.

The symbols used in Table 2 are the following:  $z$  is the elevation of the array.  $x'$ ,  $y'$  and  $z'$  are the target coordinates.  $N$  is the number of antenna elements.  $R$  is the distance from array center to target.  $\Delta R$  is the distance between the reference target and the reflection point.  $\Delta x$ ,  $\Delta y$  and  $\Delta z$  are the components of  $\Delta R$  in the  $x$ ,  $y$  and  $z$  directions, respectively.  $\Delta\theta = \lambda R/Lx'$  is the beamwidth of the array in the direction of the target.  $\theta$  is the scan angle following adaptive beamforming.  $A$  and  $B$  are statistical parameters relating to the distribution of many reflectors near the array. It is assumed that each element receives scattered energy only from a single reflector and that that reflector is different for each element. The latter assumption follows from the large size of the array and large spacing between elements implicit in [1]. The distance between each element and its reflection point is a random variable uniformly distributed between  $-A/2$  to  $A/2$  in the  $x$  direction and between  $-B/2$  and  $B/2$  in the  $y$  direction.

#### 8. OBSERVATIONS

A useful scalefactor for the correlation interval is the beamwidth of the array. A correlation interval of  $n$  beamwidths means that the radio camera can scan approximately  $n$  beamwidths to the left and  $n$  beamwidth to the right without significant scattering losses.

The first line in the correlation interval column of Table 2 pertains to the forward scanning sector of the array while the second line pertains to the end-fire region. The former region is the one of dominant interest. In this region, the correlation interval is more than  $N$  beamwidths. This means that scanning is essentially lossless in an angular sector  $\pm N\Delta\theta$  when the multipath sources are located within or very close to the array. This is true for both scattering models.

The mid-path specular model is more complicated. The correlation interval is very sensitive to array and target heights. The correlation interval nearly vanishes when the array and target both are airborne, while it can extend over the entire forward scanning sector for low angle scattering.

In the last three cases, decorrelation occurs within one beamwidth of the array; hence, the asymptotic loss 4.35 dB, may be presumed to pertain everywhere for these cases.

## 9. SUMMARY

A theory has been developed to predict the effect of phasefront distortion due to multipath and scattering on the quality of the imaging process with the radio camera. The measure used is the loss in array gain due to the scattered field, as a function of scan angle from the direction of adaptive beamforming. The loss can be described by a simple relationship involving only two quantities: the strength  $S$  of the scattered field relative to the direct field and a spatial correlation function  $\rho(\theta)$  associated with the scattering process. The argument  $\theta$  is the scanning angle away from the beamforming direction. The loss in array gain due to scattering is given by

$$\Delta G_s(\text{dB}) = 4.3S (1-\rho(\theta)) \quad (18)$$

A series of experiments conducted to test the assumptions underlying the development of the theory appear to vindicate them.

The theory is applied to several important cases of interference caused by reflections. Those cases relate to scatterers in the array region, somewhere between the target and the array, and in the target region. For each case two reflector models, a specular reflector and a fixed point reflector, were considered. Predicted degradations in beam quality for each case were calculated. These models correspond to such scatterers as a horizontal smooth ground plane, a mound or other prominent ground reflector, a building in the target region, or walls and antenna support structures in the neighborhood of the array.

The most important parameter associated with the correlation function  $\rho(\theta)$  is the correlation interval. The correlation interval is the angular scanning distance from the direction of adaptive beamforming relatively free from scattering losses.

The correlation interval was studied for the several cases of reflection. It was found that for reflections due to one fixed point reflector or due to a building in the target region the correlation interval is less than a beamwidth. For those cases the theory (13) requires only one parameter  $S$  in order to predict the effect

of the scattered field on the quality of the imaging process. When the reflectors are located in the immediate vicinity of the array and when each element is exposed to a different reflector, then a minimum of about  $N$  (number of elements) beamwidths can be scanned without significant scattering loss, provided that the typical distance between element and its reflector is smaller than half the average distance between two elements.

When the reflection is due to a specular earth or sea surface, the correlation interval is very large provided that the grazing angle is small. In that case the radio camera can perform nearly unlimited scanning without significant loss due to scattering.

#### APPENDIX A

##### FIXED POINT REFLECTOR (FPR) SCATTERING MODEL

In this section, a closed form approximation for  $\rho(\theta)$  associated with this case is developed. Accepting the assumptions inherent in the theory which leads to (13), i.e.,  $E(\delta\phi_1) = E(\delta\phi_0)$  and

$$E(\delta\phi_1)^2 = E(\delta\phi_0)^2 = \sigma_S^2 = S/2; \rho(\theta) \text{ reduces to}$$

$$\rho(\theta) = E[\delta\phi_1 \delta\phi_0] / \frac{S}{2} \quad (A1)$$

Referring to Figure 3, for  $S \leq 0.5 \delta\phi_1$ ,  $\delta\phi_0$  can be expressed as

$$\delta\phi_1 = S^{1/2} \sin\psi_1, \delta\phi_0 = S^{1/2} \sin\psi_0 \quad (A2)$$

where  $\psi_0, \psi_1$  are the respective phases of the scattered signal associated with the beamforming look direction and with the direction  $\theta$ .  $\delta\phi_1 \delta\phi_0 = S \sin\psi_1 \sin\psi_0 =$

$$\frac{S}{2} [\cos(\psi_1 - \psi_0) - \cos(\psi_1 + \psi_0)].$$

Since  $\psi_1, \psi_0$  are arbitrary values in the interval  $[0, 2\pi]$  we can assume that  $E[\cos(\psi_1 + \psi_0)] = 0$ . Therefore,  $\rho(\theta) = E[\cos(\psi_1 - \psi_0)]$ . (A3)

From the geometry of Figure 6,  $\psi_1, \psi_0$  and, therefore,  $\psi_1 - \psi_0$ , are given by

$$\psi_1 = \frac{2\pi}{\lambda} (\overline{TP} + \overline{EP} - \overline{TE}), \quad \psi_0 = \frac{2\pi}{\lambda} (\overline{T_0P} + \overline{EP} - \overline{T_0E})$$

$$\psi_1 - \psi_0 = \frac{2\pi}{\lambda} [(\overline{TP} - \overline{T_0P}) - (\overline{TE} - \overline{T_0E})] \quad (A4)$$

Let  $R_o$  be the distance between the center point of the array and the phase synchronizing source  $T_o$ , and let  $R_s$  be the distance from  $T_o$  to the reflector P. Evaluation of the terms in (A4) and substitution into (A3) yields

$$\rho(\theta) = E\{\cos(k_1 + k_2 y)\} \quad (A5)$$

$$\text{where } k_1 = \frac{2\pi}{\lambda R_s} (y_o' x'' - x_o' y'') \theta + \frac{\pi(x_o'^2 + y_o'^2)}{2\lambda} \left(\frac{1}{R_s} - \frac{1}{R_o}\right) \theta^2$$

$$k_2 = \frac{2\pi x_o'}{\lambda R_o} \theta \quad (A6)$$

and the expectation is with respect to element location  $y$ . Assuming that  $y$  is uniformly distributed between  $-L/2$  and  $L/2$ ,  $\rho(\theta)$  is given by

$$\begin{aligned} \rho(\theta) &= \frac{1}{L} \int_{-L/2}^{L/2} \cos(k_1 + k_2 y) \delta y = \frac{\sin k_2 L/2}{k_2 L/2} \cos(k_1) \\ &= \left[ \frac{\sin(\pi x_o' L \theta / \lambda R_o)}{\pi x_o' L \theta / \lambda R_o} \right] \cos \left\{ \frac{\pi \theta}{\lambda R_s} \left[ \left(1 - \frac{R_s}{R_o}\right) (x_o'^2 + y_o'^2) \theta + 2(x_o' y_o' - y_o' x_o') \right] \right\} \quad (A7) \end{aligned}$$

This closed form approximation was compared to the accurate expression for  $\rho(\theta)$  given by (16) in several computer simulations. Using various parameters the two curves obtained in each case looked almost indistinguishable [6].

#### REFERENCES

- [1] B.D. Steinberg, "Radar Imaging from a Distorted Array: The Radio Camera Algorithm and Experiments," IEEE Trans. Antennas & Prop., September 1981, pp. 740-748.
- [2] B.D. Steinberg, "Design Approach for a High Resolution Microwave Imaging Radio Camera," Journal of the Franklin Institute, December 1973.
- [3] S. Hassan Taheri and B.D. Steinberg, "Tolerances in Self-Cohering Antenna Arrays of Arbitrary Geometry," IEEE Trans. on Antennas & Prop., Vol. AP-24, No. 5, September 1976.
- [4] B.D. Steinberg, Principles of Aperture and Array System Design, John Wiley & Sons, New York, 1976.
- [5] B.D. Steinberg, "Properties of Phase Synchronizing Sources for a Radio Camera," to be published in IEEE Trans. on Antennas & Prop., November 1982.
- [6] E. Yadin-Jadlovker, "A Study of the Effect of Multipath and Scattering upon Scanning with a Radio Camera," M.S. Thesis, School of Engineering, Department of Electronics, Tel-Aviv University, 1978.
- [7] E.N. Powers, "Adaptive Arrays for Microwave Imaging," Ph.D. Dissertation, University of Pennsylvania, Philadelphia, 1974.
- [8] C.N. Dorny and B.Meagher Jr., "Experimental Beamforming and Scanning of an 80 ft Random Antenna Array Operating at 1 GHz," VF #107, Valley Forge Research Center, University of Pennsylvania, Philadelphia, March 1977.

than other samples? No justification for such windowing is clear. Perhaps a similar approach to that of the overlapped weighted periodogram technique proposed in [4], which treats all data samples more nearly equal, should be considered if weighting is to be used for least squares estimates.

As a counterexample to the claim that weighting the data improves the least squares estimate, consider the results of the least squares sinusoidal fit, performed without weighting, as shown in [1, Table V]. Sinusoids 1-3 in the table correspond to the three true sinusoids in the 64-point data epoch. The amplitude, phase, and frequency estimates are closer to the true values than those values estimated with the weighted technique proposed above. The true initial phases were  $126^\circ$ ,  $162^\circ$ , and  $166^\circ$ .

#### REFERENCES

- [1] S. M. Kay and S. L. Marple, Jr., "Spectrum analysis—A modern perspective," *Proc. IEEE*, vol. 69, pp. 1380-1419, Nov. 1981.
- [2] C. Bingham, M. D. Godfrey, and J. W. Tukey, "Modern techniques of power spectrum estimation," *IEEE Trans. Audio Electroacoust.*, vol. AU-15, pp. 55-66, June 1967.
- [3] C. van Schooneveld and D. J. Frijling, "Spectral analysis: On the usefulness of linear tapering for leakage suppression," *IEEE Trans. Acoust., Speech, Signal Processing*, vol. ASSP-29, pp. 323-329, Apr. 1981.
- [4] G. C. Carter and A. H. Nuttall, "On the weighted overlapped segment averaging method for power spectral estimation," *Proc. IEEE*, vol. 68, pp. 1352-1354, Oct. 1980.

## Two-Dimensional Imaging with a Radio Camera

BERNARD D. STEINBERG, WILLIAM WHISTLER, AND  
DONALD CARLSON

**Abstract**—In the radio camera, adaptive control techniques self-cohere the antenna elements of a phased array, thereby permitting the system to be distorted and even time varying. By doing so, enormous antenna arrays can be constructed.

A two-dimensional (range-angle) radio camera imaging experiment is reported. A 39-m, X-band (3-cm wavelength) array was formed on a cable strung between two towers, each 10 m high, on a hilltop. A pulsed microwave transmitter on the hilltop illuminated the vicinity of Phoenixville, PA, some 7 km distant. As the receiver was moved along the cable, echoes were recorded at random positions. The time-shared receiving array was highly distorted as well as time-varying, yet the radio camera processing produced nearly diffraction-limited images of three city blocks at a distance of 6.5 km in the town, and details of a power plant at a distance of 8.2 km.

The use of two different pilot signals or beamforming sources for the self-synchronization process is demonstrated. One source is a corner reflector located in the town; the other is a target of opportunity located in the vicinity.

The radio camera technique, first described in [1], permits an antenna array to be arbitrarily large notwithstanding distortions in its surface resulting from structural nonrigidity, or variations in the medium's refractive index. Steinberg *et al.* [2] showed the first experimental results of early radio camera experimentation, and demonstrated a one-dimensional (angle only) diffraction-limited capability of a radio camera under conditions of severe aperture distortion. Algorithm and general procedures are described in [3]. Steinberg and Yadin [4] demonstrated use of the algorithm in airborne radar. This letter reports on the first two-dimensional (range-angle) radio camera experiment.

The experiment employed a 39-m-length antenna operating at 3-cm

Manuscript received June 20, 1983. This work was primarily supported by The U.S. Army Research Office under Contract DAAC 29-81-K-0105, the Office of Naval Research under Contract N00014-79-C-0505, and the Air Force office of Scientific Research under Grant AFOSR-82-0012.

The authors are with the Valley Forge Research Center, University of Pennsylvania, The Moore School of Electrical Engineering, Philadelphia, PA 19104.

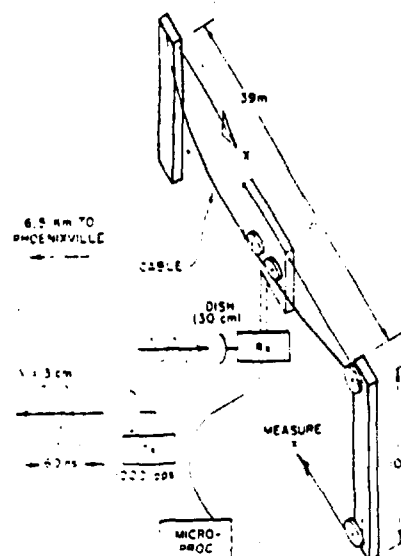


Fig. 1. Schematic of radar-imaging experiment.

wavelength. The antenna consisted of a random array having 200 sample points uniformly distributed over the length. Direction of view was  $32^\circ$  from array normal. The theoretical diffraction-limited beamwidth of a proper, rigid structure having these parameters is  $\Delta\theta = 0.88\lambda/L \cos\theta = 0.83$  mrad.

Fig. 1 is a schematic of the experiment. A 3-cm transmitter having a 60-ns pulse radiated 1000 pps in the direction of Phoenixville. A single microwave receiver having a 1-ft dish was mounted on a trolley which was positioned along the cable by a clothesline and pulley arrangement. The experiment was bistatic and time-shared. As the receiver was pulled along the 39-m cable, a read command was given to it 200 times at predetermined but randomly distributed locations of the receiver. Because the clothesline was nonrigid, antenna positions along the cable at instants of pulse transmission were uncertain to at least the order of a wavelength. The antenna elevation was also varied with receiver position along the cable because of progressive cable deformation as the receiver was moved along it. In addition, the receiving system, swaying with the breeze, was uncertain in position in the direction of the target by several wavelengths. With such uncertainties in receiver position at times of pulse transmission, the expected image in the absence of adaptive self-cohering of the system would be a noise field.

One target area was a few city blocks in Phoenixville, a distance of 6.5 km from the Valley Forge Research Center of the University of Pennsylvania. An optical telephoto image of the target area, taken from the array, is shown in Fig. 2(a). The central portion shows houses and street patterns in the region imaged by the system. The lower left- and right-hand portions are obscured by trees. In the upper central region is a park in which a 1.2-m corner reflector was placed. The park is about 0.5 km beyond the target area. Echoes from the corner reflector provided the reference signal for phase synchronizing or self-calibrating the distorted array.

Received signals were delivered to a processor which searched in range for an echo sequence across the array that appeared to originate from a point source. The processor inevitably found the corner reflector echo. Echoes from the corner reflector range bin were co-phased by the algorithm (see [3]) and the beam that was formed was scanned to the target area. A one-dimensional angle scan was made at each range bin. The sequence of angle scans formed the two-dimensional image shown in Fig. 2(b). The longitudinal dimension is range and transverse direction is azimuth or cross range. This figure is a 1-bit photograph of a color display and therefore contains no gray level. Street lines and names were scribed onto the image (white dotted lines on Fig. 2(a) identify mapped streets on the telephoto).

Range resolution measurable in the data is 9 m, exactly as expected from the 60-ns pulse transmission. Measured cross-range beamwidth is  $0.85$  mrad, corresponding to a cross-range dimension of 5.5 m at a target distance of 6.5 km. Angular or cross-range beamwidth was measured using a deflection-modulated, one-dimensional angle scan from some arbitrary range in the image. Width of the narrowest response was taken to be the system's cross-range beamwidth.

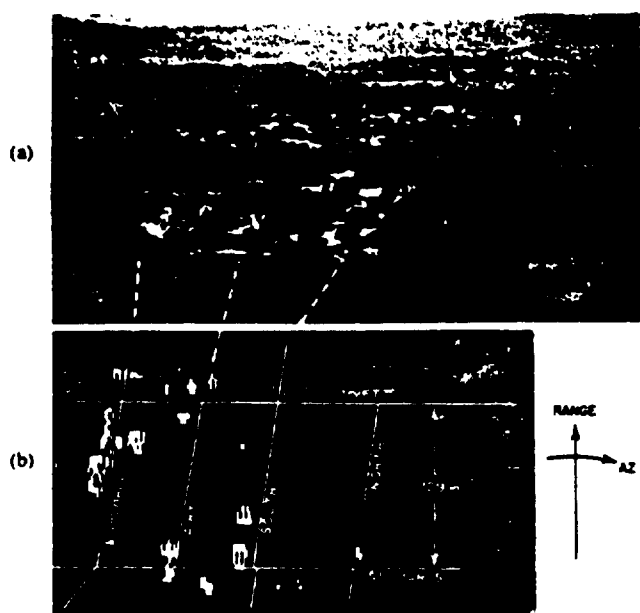


Fig. 2. Radar targets in Phoenixville, PA (houses, streets). (a) Optical telephoto from antenna site. (b) Radar image.

The large target on the right-hand side of Marshall Street in Fig. 2(b) is believed to be a truck, because that target did not appear in subsequent images.

Fig. 3 shows images of another target, a power plant some 8.2 km distant from the array. Fig. 3(a) is an optical telephoto (from the antenna site) of the radar-visible features of the plant (portion inside the delineated area); Fig. 3(b) and (c) are radar images of these features. The 1.2-m corner reflector, located at the same place as for Fig. 2(b), was used for Fig. 3(b); however, a radar target of opportunity was used for adaptive beamforming for the image in Fig. 3(c). The target of opportunity was the northernmost smokestack of the power plant, and is indicated by the arrows on Fig. 3(a) and (c). Fig. 3(b) and (c) show the same targets and are of essentially equal quality indicating that man-made structures may be adequate for phase synchronizing the array. Outlines of the power plant's major buildings, stacks, and structures, have been added manually to the images to indicate the related positions of the plant's radar-visible features (i.e., radar visible only above the masking trees and ground elevations near the plant, as observed from the antenna site).

**Summary:** Radio camera microwave images of portions of Phoenixville, PA, are shown. They are obtained from a highly distorted and nonrigid

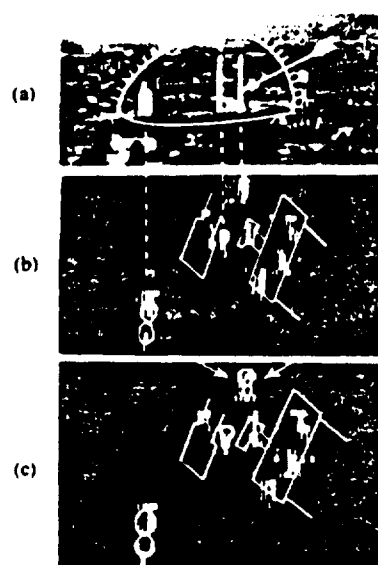


Fig. 3. Optical and radar images of portions of a power plant. The distance is 8.2 km. (a) Optical telephoto from the radio camera array. (b) Radar image. Beamformer was a 1.2-m corner reflector (same one and in same place as for Fig. 2). (c) Radar image. Beamformer was a target of opportunity. The arrows here and in (a) indicate the image and photo of the smokestack target used as a beamformer.

39-m-length phased array operating at 3-cm wavelength. The images are diffraction-limited, notwithstanding the severe distortion. Electrical phase compensation is made for the distortion based upon echoes from a corner reflector in one experiment, and from the corner reflector and an unknown target of opportunity in the second one.

#### REFERENCES

- [1] B. D. Steinberg, "Design approach for a high-resolution microwave imaging radio camera," *J. Franklin Institute*, vol. 296, no. 6, pp. 415-432, Dec. 1973.
- [2] B. D. Steinberg, E. N. Powers, D. Carlson, B. Meagher, Jr., R. S. Berkowitz, C. N. Dorny, and S. H. Seeleman, "First experimental results from the Valley Forge Radio Camera Program," *Proc. IEEE*, vol. 67, no. 9, p. 370, Sept. 1979.
- [3] B. D. Steinberg, "Radar imaging from a distorted array: The radio camera algorithm and experiments," *IEEE Trans. Antennas Propagat.*, vol. AP-29, no. 5, pp. 740-748, Sept. 1981.
- [4] B. D. Steinberg and E. Yadin, "Radio camera experiment with airborne radar data," *Proc. IEEE*, vol. 70, no. 1, pp. 96-98, Jan. 1982.

# Phase Synchronizing a Nonrigid, Distributed, Transmit-Receive Radar Antenna Array

BERNARD D. STEINBERG, Fellow, IEEE  
University of Pennsylvania

A means is described for self-organizing a nonrigid, distributed, transmit-receive antenna array for use in airborne radar. The techniques are applicable to ground-based or shipborne radar as well. Methods are described for initializing the array using various primary microwave illuminators. The description of phase conjugation technique and means for distributing phase reference to all elements in the array are the central parts of the paper.

## I. INTRODUCTION

An airborne radar with a phased array the size of the aircraft would have many desirable attributes [1]: (1) for fixed transmitter power, the large aperture would provide unusually large detection range; (2) for a given desired performance, the transmitter power could be reduced dramatically; (3) the small horizontal beamwidth would offer a resolving power approaching human vision, which is a few milliradians; (4) adaptive interference cancellation circuits [2-4] operating from the large aperture would suppress jamming very close to the beam axis.

An aircraft-size array would consist of flush-mounted antenna elements distributed throughout the skin of the aircraft. Structural members, doors, windows, etc., would preclude a regular distribution of element locations. Furthermore, the nonrigidity of the airframe and skin would displace the elements from their design positions when in flight. Thus the design principles must be based upon the properties of the random array [5, 6] and self-cohering or adaptive beamforming techniques must be used to compensate for the time-varying positions of the array elements [7-9]. Such a system is called a "radio camera."

Adaptive beamforming is a retrodirective process in which a beam is focused upon a synchronizing source external to the array [10, 11]. The synchronizing source for an airborne radio camera must be another aircraft, a surface target, or clutter [12].

An airborne radio camera can use a conventionally designed transmitter and a distributed receiving array. Alternatively, transmission as well as reception can take place through the self-cohered array. The latter is a much more formidable problem. Means for accomplishing it is the subject of this paper.

The main reason for accepting the increased complexity of the transmit-receive system is because of the poor sidelobe properties of the one-way pattern. The sidelobes of the random array are high because of the random locations of the elements: the average sidelobe level is  $N^{-1}$  ( $N$  = number of elements) [5] and the peak sidelobe level is 10 dB higher or more [6]. By transmitting through the same array the side radiation pattern is squared, average sidelobe power level (ASL) drops to  $N^{-2}$ , and PSL  $\approx 100 N^{-2}$ .

Symbols and abbreviations used in this paper are

ASL	average sidelobe power level
BPF	bandpass filter
$N$	number of elements
PCC	phase conjugating circuit
PLL	phaselock loop
PSL	peak sidelobe power level
VCO	voltage controlled oscillator
VCPS	voltage controlled phase shifter.

Manuscript received October 20, 1981; revised March 15 and April 12, 1982

Author's address: Valley Forge Research Center, The Moore School of Electrical Engineering, University of Pennsylvania, Philadelphia, PA 19104

This work was supported in part by the Air Force Office of Scientific Research and in part by the Office of Naval Research.

0018-9251/82/0900-0609 \$00.75 © 1982 IEEE

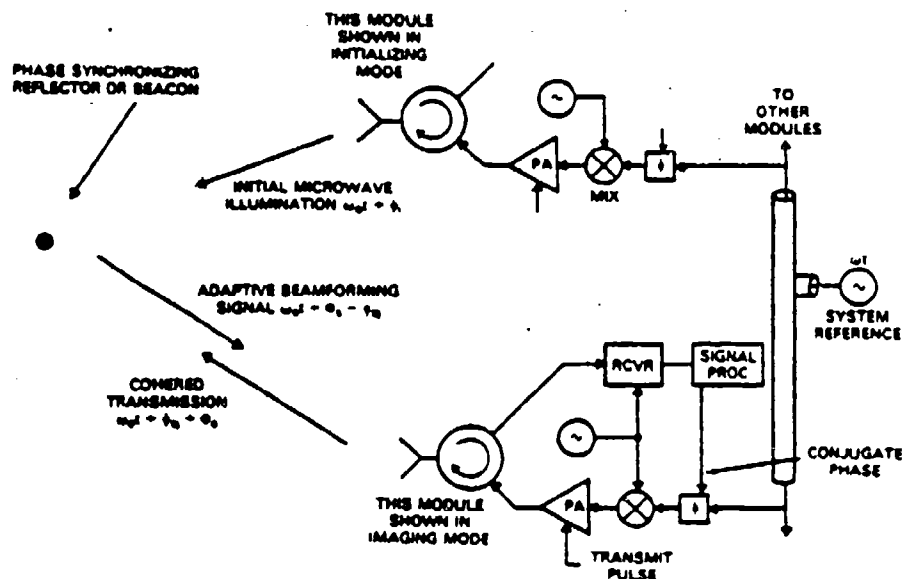


Fig. 1. Adaptive beamforming transmit-receive array without auxiliary transmitter.

## II. INITIALIZATION OF THE ARRAY

Synchronization or self-cohering of a random, distorted receiving array has been amply demonstrated [9, 27]. An external reference field is required, as in holography. Measurements of the field disclose the phase corrections to be made at each antenna element. The array is then scanned as a phased array. When transmitting through the same array, however, a logical difficulty is encountered. The external reference field needed to cohere the array must first be set up by the transmitter before the array can be used for transmission.

A variety of techniques can be used to break this conundrum.

(1) The first is to overdesign the transmitter by the necessary margin of  $N$ , the number of antenna elements, which is the relative gain of the synchronized array to the nonsynchronized array. This is a costly choice.

(2) Use a separate high gain illuminator for initial synchronization and transfer power to the array afterwards. This is a sound approach when an auxiliary transmitter is available.

The auxiliary radar transmitter could be a nearby radar operating in the same frequency band but not at the same frequency. Target reflections at that frequency can successfully phase synchronize the receiving system. Phase conjugation of the received waveforms results in a receiving beam focused at the source [7-9]. However, since the transmission of the phase-conjugated waves from the antenna elements is at a slightly different frequency, the transmitting beam is offset somewhat, an effect which must be prevented by special phase conjugation circuits of the type described by Chernoff in [13]. An important advantage is obtained in using a

lower frequency for initial synchronization on a target reflection, for then the lobes of the reradiation pattern are widened by the frequency ratio, thereby easing a size-limitation tolerance on the synchronizing source [8]. Instead of a passive source the auxiliary radar could actuate an active beacon which would radiate to the array at the design frequency to self-cohere the array. This avoids the angular offset or "squint."

(3) A rigid subarray of the full system can be used for coherent transmission of a broad beam to establish the reference field.

(4) The entire array can be driven noncoherently prior to self-phasing, in which case the average power density is  $N^{-1}$  times the full power density of the system after the array is synchronized. Although this loss is large, it can be compensated through use of a beacon or by initializing on the reflected signal from a nearby target. The squint problem is avoided since synchronization is at the system frequency. The method is effective when synchronizing upon target reflections because of the  $R^{-2}$  dependence of received signal power on target distance. To overcome a 30 dB initializing disadvantage ( $N = 1000$ ) the reference reflection must be located no further than 18 percent of the maximum distance at which it could be placed if the transmitters were cohered. This distance reduces to 10 percent when  $N = 10^4$ . This technique, appropriate for an airborne system using ground or sea clutter for the reference target [12, 28], is illustrated in Fig. 1. Two modules of the array are shown. Each consists of an antenna element, circulator (or other diplexer), receiver, phase-stable reference oscillation common to the entire array, transmitter phase shifter, mixer, local oscillator cohered in frequency to the reference wave, and pulsed power amplifier.

To initialize the system each module radiates an RF pulse having common system frequency  $\omega_0$  and random phase. The instantaneous transmission phase of the

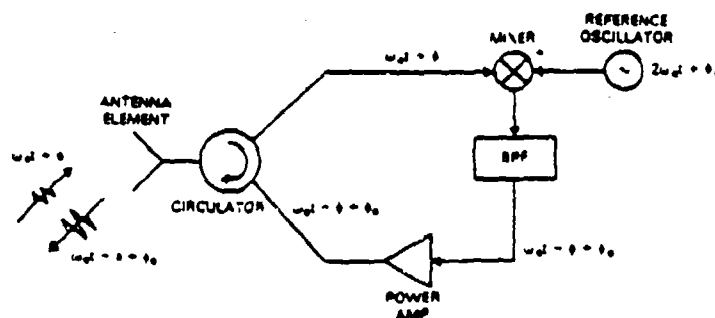


Fig. 2. Phase conjugation schematic.

wave from the  $i$ th module may be designated  $\omega_0 t + \phi_i$ . This wave arrives at the synchronizing source with delay  $\omega_0 t + \phi_i - \phi_0$ , where  $\phi_0$  is the phase delay from the module. The combined illumination at the reflector or beacon is  $\sum_{i=1}^N a_i \exp j(\omega_0 t + \phi_i - \phi_0)$ , the instantaneous

phase of which is  $\omega_0 t + \Phi$ , the subscript meaning source. The source wave is returned to the array with a different phase delay  $\phi_j$  at each module. Thus the signal phase received by the  $j$ th module is  $\omega_0 t + \Phi - \phi_j$ .

To focus the transmitting beam upon the source the radiation from the  $j$ th module must be changed from  $\omega_0 t + \Phi - \phi_j$  to  $\omega_0 t + \phi_j + \Phi_0$  where  $\Phi_0$  is an arbitrary phase constant across the array. This is the phase conjugation step needed to achieve retrodirectivity, which is the heart of the process.

### III. PHASE CONJUGATION TECHNIQUES

Retrodirectivity requires phase conjugation at each element, which in turn demands symmetry with respect to some reference. If  $\phi_r(x; \theta_0)$  is the phase of the received wave at position  $x$  in the array due to a synchronizing source at angle  $\theta_0$ , and  $\phi_t(x; \theta_0)$  is the transmitted phase variation needed to achieve retrodirectivity, the required relation is  $\phi_t(x; \theta_0) = -\phi_r(x; \theta_0)$  plus an arbitrary constant. This equation implies the existence of some reference phase from which  $\phi_r$  and  $\phi_t$  may be measured. The symmetry can exist in more than one domain. Spatial symmetry is utilized in one of the oldest forms of retrodirective array, the Van Atta array [14, 15]. Symmetrical sidebands in the frequency domain is another. A third is paired, symmetrical phase shifters.

Dependence upon spatial symmetry is inappropriate for an airborne array distributed about the airframe. Here the array is assumed to be distorted, random, and highly thinned.

The other two techniques are practical. The use of symmetrical sidebands is illustrated in Fig. 2. Let a signal characterized by the real (or imaginary) part of  $\exp[j(\omega_0 t + \phi)]$  be received and heterodyned (mixed) with a local oscillator at frequency  $\omega_{LO}$ . The mixer products are  $\exp[j(\omega_{LO} + \omega_0)t + \phi]$  and  $\exp[j(\omega_{LO} - \omega_0)t$

$-\phi]$ . The sidebands are symmetrically displaced about the local oscillator frequency and the lower sideband has the desired phase. Further, if the local oscillator frequency is made exactly twice the frequency of the received signal, the lower sideband is  $\exp[j(\omega_0 t - \phi)]$ .

In Fig. 2, the input signal at frequency  $\omega_0$  and phase  $\phi$  (indicated by the instantaneous phase  $\omega_0 t + \phi$ ) is passed through a circulator where it mixes with the second harmonic at an arbitrary phase  $\phi_0$ . The difference frequency output of the mixer, at  $\omega_0$ , is passed by the bandpass filter to the amplifier. The phase of this signal is  $\omega_0 t + \phi_0 - \phi$ . This signal is amplified and radiated. Provided that  $\phi_0$  is constant across the array, the radiation is retrodirective.

This circuit is useful for illustration but has two limitations which keep it from being a practical circuit. First, the down-converting mixer is a source of trouble because of the harmonic relation between the signals at its inputs. Being a nonlinear circuit the second harmonic of its fundamental frequency input will be generated. A current due to the second harmonic will flow in the source impedance of the second-harmonic input circuit, thereby altering the phase of the reference signal at  $2\omega_0$ . Also direct feedthrough of the input signal to the output will alter the phase of the output signal. Either the frequency of the reference signal must be different from  $2\omega_0$  to avoid these troubles or the mixer must be carefully balanced so that neither second harmonic generation nor input-output leakage will affect the phase of the radiated wave.

The second problem is that this circuit transmits an amplified replica (with conjugated phase) of the received radar trace concurrent in time with the received signal. However, the desired transmission is an RF pulse (with conjugated phase) occurring at a later time. This means that the echo received from the synchronizing source must be sampled, its phase extracted, conjugated and applied to an oscillation at the echo frequency, which is gated at the appropriate time, amplified, and radiated.

Figs. 3-7 show several circuits for accomplishing this task. They differ in their means of storage of the phase information (as the phase of a coherent oscillator, e.g.,

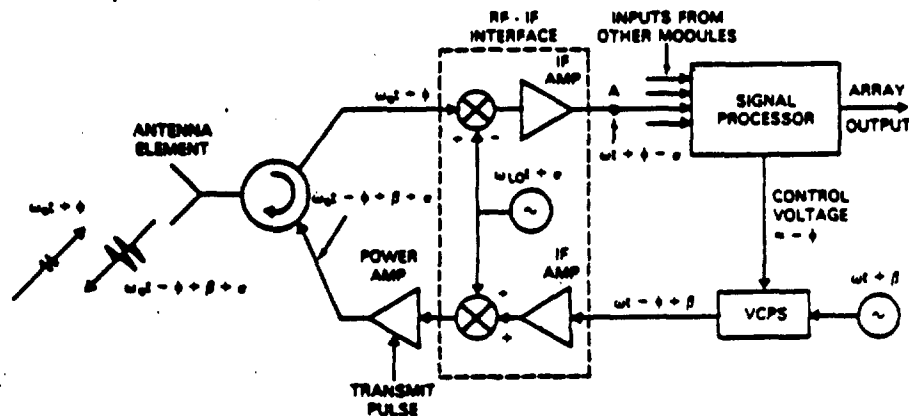


Fig. 3. Phase conjugation circuit.

as in a phaselock loop (PLL) [16-21], or as a digital number is the signal processor of the system), according to whether control of the phase shifter through which the signal to be transmitted is passed is open loop or closed loop, and according to the choices of components, e.g., analog versus digital phase shifters.

Fig. 3 shows a means of phase conjugating when a digital signal processor is used to combine the signals received from the distributed array elements. The received signal is shown as an echo pulse having instantaneous phase  $\omega_0 t + \phi$ . It is heterodyned to IF by a local oscillator at frequency  $\omega_{LO}$  having some arbitrary phase  $\alpha$ . The LO is assumed to be coherent to the reference wave at the intermediate frequency  $\omega$ . The phase  $\beta$  of the reference is assumed to be constant across the array. The IF pulse, with instantaneous phase  $\omega t + \phi - \alpha$ , is delivered to the signal processor. The signal processor measures the phase relative to the phase of some reference element in the array, whose phase is arbitrarily identified as zero phase. Since all signals entering the signal processor experience the same phase offset  $\alpha$ , the local oscillator phase cancels out. The negative of the measured signal phase  $\phi$  is delivered as a control voltage to a voltage controlled phase shifter (VCPS) in the reference signal path. The output, having instantaneous phase  $\omega t - \phi + \beta$ , is up converted to form the transmitted wave. The transmitted phase is  $\omega_0 t - \phi + \beta + \alpha$ . Provided that  $\beta$  and  $\alpha$  are constants across the array, the transmitted wave is the phase conjugate of the input signal.

The accuracy to which the signal processor measures  $\phi$  (or  $-\phi$ ) is influenced by noise and multipath. However, the precision with which this measurement is made and held for delivery to the phase conjugation circuit can be made arbitrarily fine; it is determined by how many significant figures or bits are used in the measurement. Thus the quality of the delivered value  $-\phi$  need be no poorer than that of the measured  $+\phi$ .

Errors develop when the phase shifts through the system are not tuned out. Let the phase shift be  $\delta$  from the antenna to the VCPS through the circulator, receiver, and signal processor. The output of the phase

shifter then becomes  $\omega t - \phi - \delta + \beta$ . Let the phase shift be  $\eta$  in the transmitting chain from VCPS to the antenna through the transmitter and circulator. The radiated wave becomes  $\omega_0 t - \phi - \delta + \beta + \alpha + \eta$ . Its phase is in error by  $-\delta + \eta$ . The variance of this error (in square radians) across the array, multiplied by  $10 \log e$ , is the expected loss in array gain in decibels [12]. For example,  $1/4 \text{ rad}^2$  phase error variance leads to a loss in mainlobe gain of 1 dB. Thus each module must be carefully tuned to balance the phase shifts in the receiving and transmitting chains.

The circuit of Fig. 3 stores the signal phase in the signal processor and uses open-loop phase control. The next circuit (Fig. 4) retains open-loop phase control but remembers the signal phase in a PLL. This circuit also demonstrates the use of paired, symmetrical phase shifters. The receiver chain is the same as in Fig. 3 to point A, at which point the circuit branches. The received signal continues to the signal processor as before. It also is applied to the input port of the phase detector in a PLL in which the controlled element is a VCPS rather than the more common voltage-controlled oscillator (VCO). The control voltage in the loop drives the phase of the signal at the VCPS to be in quadrature with the input IF signal. As in the earlier system the signal through the VCPS is the reference oscillation at  $\omega$  with arbitrary phase  $\beta$ . Hence the loop drives the VCPS to a phase shift  $\phi - \alpha - \beta - \pi/2$ . Ganged to the VCPS is a matched phase shifter with opposite phase. Its phase is  $-\phi + \alpha + \beta + \pi/2$ . While the phase of the VCPS is set in a closed loop, the paired phase shifter is set open loop. Carefully matched analog phase shifters are required; otherwise digital phase shifters must be used.

Digital phase shifters generally are preferable. The number of discrete phase-shift components required is easily calculated. If  $m$  is the number of quantization bits and  $M$  is the number of levels of quantization, the relation between them is given by  $M = 2^m$ . The loss in gain as a function of the number of quantization bits is [12]

$$\text{loss in gain (dB)} = 20 \log [\sin(\pi/2^m)/(\pi/2^m)]. \quad (1)$$

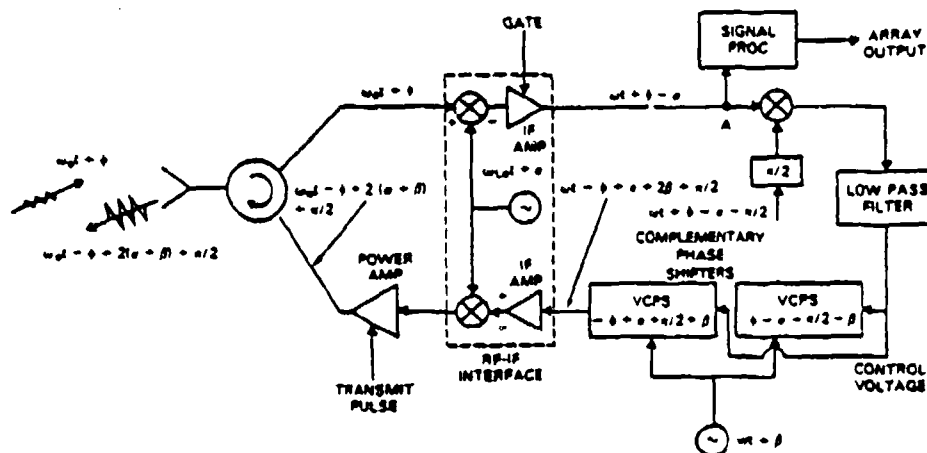


Fig. 4. Phase conjugation circuit.

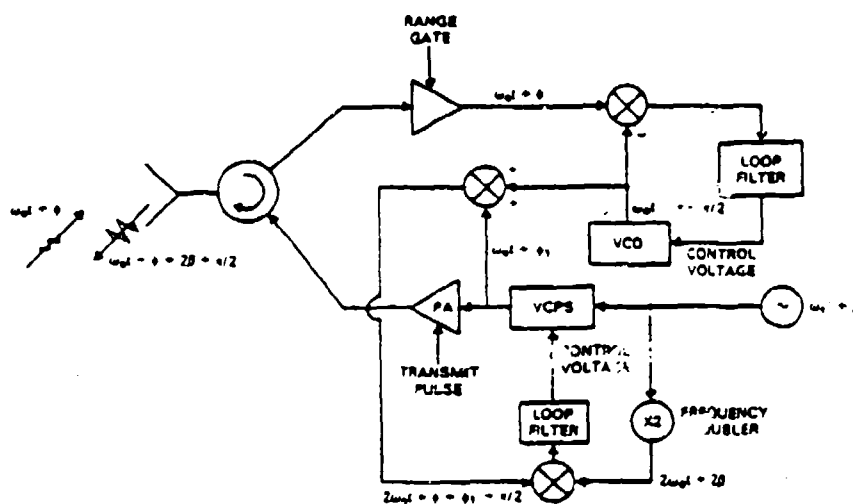


Fig. 5. Phase conjugation circuit.

A quantization value of two bits limits the loss to less than 1 dB, a value of three bits to less than 1/4 dB, and a value of four bits to 0.06 dB. The side radiation pattern also is affected by phase quantization errors, although the statistics in the sidelobe region are not. This is because the element positions are randomized, leading to Rayleigh sidelobe statistics. Further phase errors do not noticeably increase the sidelobe levels; they only reduce the mainlobe gain.

Returning to the figure, it is seen that the input to the paired phase shifter is  $\omega t + \beta$ ; its output, therefore, is  $\omega t - \phi + \alpha + 2\beta + \pi/2$ . This IF signal is heterodyned to RF via the mixer and the local oscillator at  $\omega_{LO}t + \alpha$ . The upper sideband at  $\omega_0$  is selected by the power amplifier, providing a signal at the desired frequency having a phase  $\omega_0 t - \phi + 2(\alpha + \beta) + \pi/2$ . This signal is gated in the power amplifier by the transmit-pulse waveform from the radar synchronizer, and radiated. Provided that  $\alpha + \beta$  is a constant across the array the high power transmitted pulse has the desired phase.

Fig. 5 shows a phase conjugating circuit (RF-IF heterodyning circuits not shown) which replaces the open-loop ganged phase shifter of Fig. 4 by a phase shift circuit under closed-loop control.<sup>1</sup> The circuit is PLL. The received target echo at  $\omega_0 t + \phi$  is applied to the PLL. The VCO phase after the loop is locked is  $\omega_0 t + \phi - \pi/2$ . It is applied as one input to an up converter. The other input, also at  $\omega_0$ , is delivered by a voltage controlled phase shifter driven by the reference oscillation. Call its phase  $\phi_1$ . The up converter output is at the second harmonic frequency  $2\omega_0$ . Its instantaneous phase is  $2\omega_0 t + \phi + \phi_1 - \pi/2$ . Assume that adequate balance is achieved in the up converter to avoid second harmonic feed through. This signal is compared in a phase detector with the second harmonic of the reference. The beat product is integrated in the loop filter and applied as the

<sup>1</sup>This circuit and the next two were suggested by Prof. Y. Bar-Ness of Tel Aviv University while a Visiting Professor at the University of Pennsylvania.

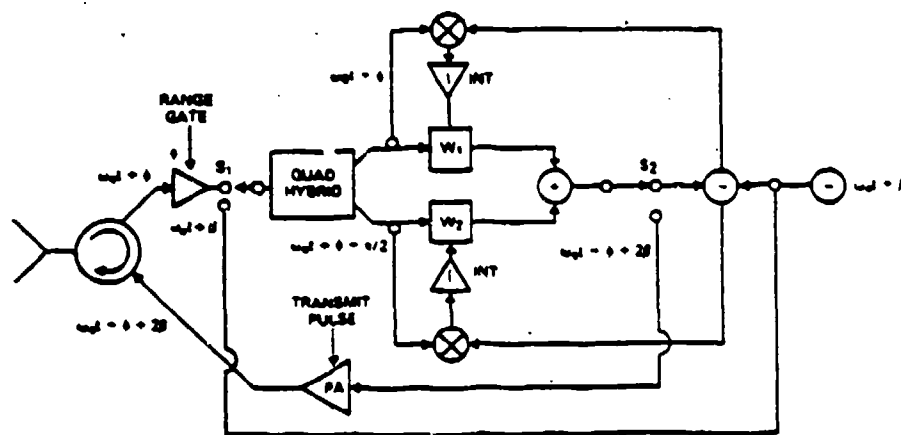


Fig. 6. Phase conjugation (another method).

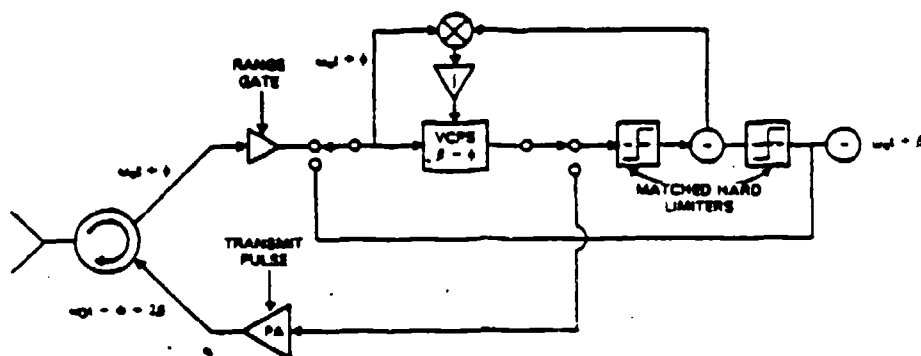


Fig. 7. Hard-limited version of Fig. 6.

control voltage to the VCPS. Convergence requires that  $\phi + \phi_1 = 2\beta$  or  $\phi_1 = -\phi + 2\beta$ . Thus the instantaneous phase of the CW output of the VCPS is  $\omega_0 t - \phi + 2\beta$ , which is the correct frequency and phase provided that  $\beta$  is constant across the array. Hence the drive for the gated power amplifier is taken from this point.

The circuit of Fig. 6 introduces another method of phase conjugation. The received echo pulse from the reference target is gated as before. The input to the phase conjugating network is switch  $S_1$ , connected as shown. The echo at  $\omega_0 t + \phi$  passes through a quadrature hybrid which delivers pulses at  $\omega_0 t + \phi$  and  $\omega_0 t + \phi - \pi/2$ . These signals are weighted by real gain controls  $w_1$  and  $w_2$  and added. This sum,  $w_1 \cos(\omega_0 t + \phi) + w_2 \cos(\omega_0 t + \phi - \pi/2)$ , passes through switch  $S_2$  to the comparator where it is subtracted from the reference wave  $\cos(\omega_0 t + \beta)$ . The difference is fed back to the mixers of two correlators, the other inputs of which are driven by the quadrature outputs of the hybrid. The integrated mixer products drive the real weights  $w_1$  and  $w_2$  to those values that cause the sum waveform to equal  $\cos(\omega_0 t + \beta)$ .

The portion of the circuit between the switches is used extensively in adaptive nulling and interference

cancellation problems. The closed loops set the weights  $w_1$  and  $w_2$  so as to solve the equation

$$w_1 \cos(\omega_0 t + \phi) + w_2 \cos(\omega_0 t + \phi - \pi/2) = \cos(\omega_0 t + \beta). \quad (2)$$

The solution is

$$\tan(\phi - \beta) = w_2/w_1, \quad w_1^2 + w_2^2 = 1. \quad (3)$$

When the loops have converged, the circuit between the two switches has transformed the input  $\omega_0 t + \phi$  to the output  $\omega_0 t + \beta$ . In short, the transfer function of the circuit at  $\omega_0$  is  $H(\omega_0) = \exp[j(\beta - \phi)]$  which means that the circuit is a phase shifter having phase shift  $\beta - \phi$ . Following loop convergence the weights are frozen and both switches are thrown to their lower positions. The reference wave having phase  $\omega_0 t + \beta$  then passes through the circuit and emerges with phase  $\omega_0 t - \phi + 2\beta$ . It is amplified, gated, and radiated.

Fig. 7 shows another version of the previous circuit in which the signals entering the comparator are hard limited in carefully matched limiters. Given that their amplitudes are matched it is only necessary to shift the

phase of the input echo by  $\beta - \phi$  to zero the comparator output. Only a single cancellation loop is needed as there is only a single parameter to be varied. A latching phase shifter, such as the digital phase shifter discussed earlier, is required. After loop convergence is completed the phase shift is frozen, the switches are thrown and  $\omega_0 t - \phi + 2\beta$  is radiated.

#### IV. ERRORS IN PHASE CONJUGATION

Two types predominate. The first is a random phase shift due to mistunings in open-loop portions of phase conjugating networks. The second is a linear phase shift due to a frequency offset. The former constitutes a random variation in phase across the array, the effect of which is loss in mainlobe gain as described earlier. Assuming a 1-dB total loss budget for the entire system, the allowed phase error is about 1/2 rad rms. It is evident that the allowed random error in phase conjugation is smaller still. Frequency offset, which has been ignored in the preceding section, may occur in two ways. First, the initializing microwave illuminator may be at a somewhat different frequency from the transmitting array. Second, the need for isolation between low-level incoming signals and high-level outgoing signals may force a frequency offset. The effects are the same in both cases.

The magnitude of the frequency offset is determined by the manner in which the phase is conjugated. The simplest way is to adjust the phase shift at the initial frequency and accept the error which results. Let the reflecting source be at angle  $\theta_0 = \sin^{-1} u_0$  from the array normal and the initializing (self-cohering on reception) frequency be  $\omega' = k'c$ . The phase of the wave across the array is  $\phi_R = k'xu$ . Let  $i_0(x)$  be the excitation across the transmitting array. Let the conjugated phase be  $-k'xu_0$  and let the wave-number of the signal transmitted by the array be  $k$ . The radiation pattern becomes

$$f(u; u_0) = \int i_0(x) \exp(-jk'xu_0) \exp(jkxu) dx \\ = \int i_0(x) \exp(jkx\{u - [(k'/k)u_0]\}) dx. \quad (4)$$

Note that the beam no longer points to  $u_0$  but to  $k'u_0/k$ . The error or displacement

$$\Delta u_0 = u_0[1 - (k'/k)] = u_0[1 - (\omega'/\omega)] \quad (5)$$

is called the squint angle. Equation (5) can be rewritten

$$|\Delta u_0/u_0| = |\Delta\omega/\omega| \quad (6)$$

indicating that the magnitude of the fractional change in the beamsteering angle equals the magnitude of the fractional change in the frequency. The largest typical value of  $\Delta\omega$  is the receiver bandwidth. Rarely will the angular displacement exceed one or a few percent of the scan angle. Such scale distortion will be unimportant unless

the beam displacement exceeds the beamwidth of the large array and no synchronizing source resides within the transmitting beam. A phase conjugating circuit devoid of squint is required if this problem is anticipated [13].

The reason why the angle distortion arises is that the phase is measured and conjugated at one frequency but radiation takes place at another frequency. The error is eliminated if the phase shift resulting from the conjugation process is correct at the new frequency. Then the radiation pattern of the retrodirective array is

$$f(u, u_0) = \int i_0(x) \exp[jk'x(u - u_0)] dx f[k'(u - u_0)] \quad (7)$$

The argument of the function is  $k'(u - u_0)$ . The beamsteering angle, therefore, is  $u_0$ . Hence the frequency change is no longer reflected in an angular displacement. The sole effect is a change in the angular scale, measured from  $u_0$ , by a factor  $k'/k$ . This scale change is of no consequence in adaptive beamforming.

#### V. PHASE REFERENCE

A reference oscillation with constant phase  $\omega t + \beta$  is required in every module in the array. This signal must be derived from an oscillator arbitrarily located in the array and delivered to each module by a circuit or subsystem. A frequency-stable and phase-stable oscillator is assumed as well as a frequency synthesizer capable of generating the local oscillator waveform.

Cables of equal and constant lengths can deliver the reference wave from the source to each module. This is a practical technique when the array is compact and the modules are contiguous. It becomes impractical when the array is large and distributed. Furthermore, being an open-loop system, differential phase changes between cables due, for example, to temperature differences or mismatches at connections are passed directly as phase errors to the modules.

Circuits have been devised to deliver the phase reference from source to module, or from module to module. The major impetus to date has been design work for the Solar Power Satellite [22, 23]. Fig. 8 illustrates a method due to Lindsey [24]. It consists of two distinct circuits separated by a cable having arbitrary phase delay  $\Delta$ . The reference signal passes between circuits via this cable at frequency  $\omega$ . It is provided to each phase conjugating circuit at twice that frequency and at the common reference phase  $\beta$ . Thus in the left circuit of Fig. 8 is a reference source of frequency  $2\omega$  and phase  $\beta$ .

The upper left circuit is a PLL. Its VCO phase is  $\omega t + \phi_0$  where, for the moment,  $\phi_0$  is an arbitrary value. Oscillator output is taken from the loop and passed, via the first diplexer (shown as a circulator), to the cable, which delivers  $\omega t + \phi_0 - \Delta$  to the right-hand circuit.

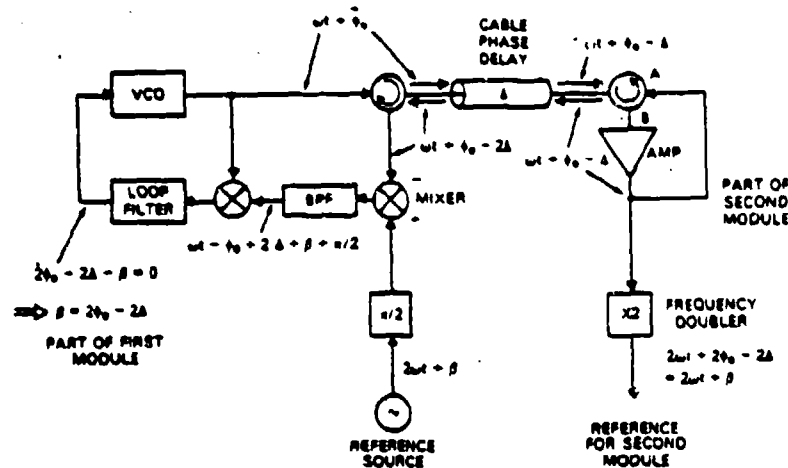


Fig. 8. Frequency and phase-reference delivery circuit (from [24]).

There the cable-delivered signal is doubled in frequency to provide the reference  $2\omega + 2\phi_0 - 2\Delta$  for the second module. In this way both modules are driven by the same reference frequency. It is shown below that they are also driven to the same phase.

Prior to frequency doubling in the second module, the amplified wave at  $\omega t + \phi_0 - \Delta$  is fed back to the second diplexer and returned to the first module. Its phase is further retarded by the cable delay  $\Delta$ . It is passed by the circulator to the mixer where it is heterodyned by the  $90^\circ$  phase shifted reference wave. The lower sideband is selected by the bandpass filter (BPF). Its output is the input to the phase detector of the PLL. The instantaneous phase of this wave is  $\omega t - \phi_0 + 2\Delta + \beta + \pi/2$ . The other input is  $\omega t + \phi_0$ , delivered by the VCO. The low-pass filtered output of the phase detector is zero when the loop drives the phase difference between the inputs to  $90^\circ$ . Hence  $2\phi_0 - 2\Delta - \beta = 0$  or  $\beta = 2\phi_0 - 2\Delta$ , which is the condition sought. Thus both modules have the same reference phase  $2\omega t + \beta$  independent of the cable length between them. Other modules are fed in the same manner.

The circuit as drawn in Fig. 8 is subject to several phase error sources. First, the nonlinear mixer will generate harmonics of the input signal. The second harmonic will add to the reference source at  $2\omega$  to produce a net reference signal with altered phase. In addition, feed through the mixer at the fundamental frequency will alter the net phase of the signal delivered by the bandpass filter to the phase detector of the PLL.

The second source of phase errors is the phase shifts through all the nonclosed-loop controlled portions of the circuit. The circulators, the bandpass filter, and the signal return loop are examples. This is a tuning-type problem common to all the preceding circuits as well.

Last, the signal-return loop has a special problem.

Unless there is sufficient isolation in the circulator from ports A and B, the loop will oscillate. The amplifier is needed to overcome the signal losses to the cable in both directions. Hence the signal level delivered back to the circulator as port A is larger by the gain of the amplifier than the signal delivered by the circulator at port B. The ideal circulator (or other diplexer) provides zero coupling between ports A and B; the practical circulator has limited isolation. To avoid the danger of oscillation the isolation must exceed the amplifier gain which, in turn, must at least equal the two-way cable loss. Hence the maximum allowed cable loss is limited by the isolation available in practical circulators.

A small modification to the circuit avoids the more serious of these problems. Fig. 9 shows the reference source frequency to be  $m$  times the VCO frequency and the frequency of the return signal to be  $n\omega$ . The VCO signal  $\omega t + \phi_0$  again is delivered by cable to the next module, amplified, and returned. The return signal is frequency multiplied by the factor  $n$ , delayed by the cable, and mixed with the reference in the down converter. The phase of the output of the BPF is  $(m - n)\omega t + \beta - n\phi_0 + (n + 1)\Delta + \pi/2$ .

The VCO output is multiplied in frequency by  $(m - n)$  to equate the frequencies of the phase detector inputs. The loop drives these signals into quadrature, resulting in the phase equation  $m\phi_0 - \beta - (n + 1)\Delta = 0$ , which implies that the instantaneous phase of the reference source  $m\omega t + \beta = m\omega t + m\phi_0 - (n + 1)\Delta$ .

The output to the next module is derived from a frequency multiplication, by the factor  $m$ , of the signal delivered by the cable; its phase is  $m\omega t + m\phi_0 - m\Delta$ . The only condition required to equate the last two expressions is  $m = n + 1$ . When this condition is met the desired phase reference is transferred from the first to the second module. In addition, the need for the frequency multiplier (shown dashed) which follows the VCO and drives the phase detector is eliminated; instead a direct connection may be made.

System frequencies are determined by the choice of a



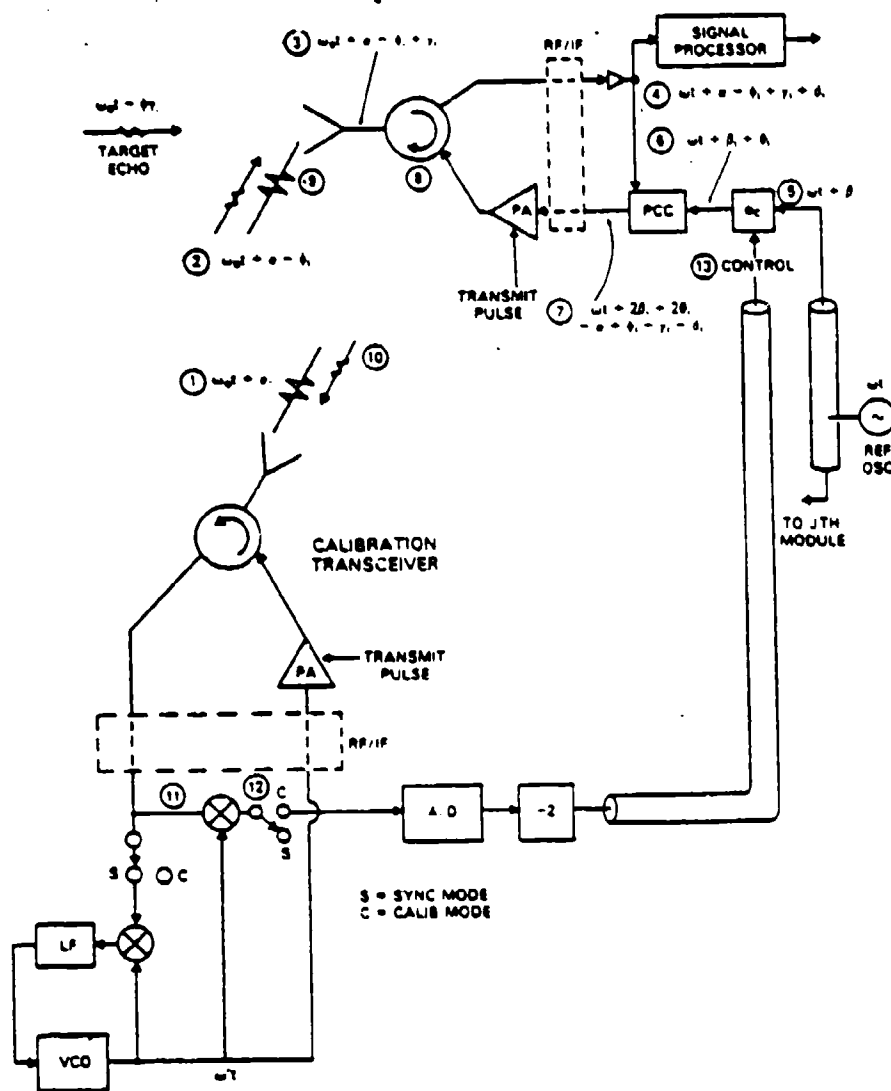


Fig. 10.  $i$ th module of distorted array.

delay  $\phi_i$  is contributed upon arrival at the calibration system (10). There the instantaneous phase is  $\omega t + 2\beta_i + 2\theta_i - \alpha - \delta_i + \eta_i$ . It is evident that both the propagation delay and the antenna element phase shifts have dropped out.

This wave is received with the switches thrown to C, which places the calibration transceiver in the CALIB mode. The phase shift from antenna to phase detector (11) is  $\mu$ . Hence the phase detector output (12) is a video voltage proportional to  $-2\beta_i - 2\theta_i + \alpha + \delta_i - \eta_i - \mu$ . This voltage is converted to a digital number, divided by two, and delivered (13) to the digital phase shifter in the module where it changes the phase through that component by  $\Delta\phi_i = -\beta_i - \theta_i + (\frac{1}{2})(\alpha + \delta_i - \eta_i - \mu)$ . The signal reentering the PCC as a phase reference is, therefore,  $\omega t + (\frac{1}{2})(\alpha + \delta_i - \eta_i - \mu)$ .

This is the desired reference phase: the random initial phase  $\theta_i$  of the phase shifter and the random reference oscillation phase  $\beta_i$  have been removed, the circuit phase shifters  $\delta_i$  and  $\eta_i$  cancel out during system

operation (see below), and the remainder is a constant across the array.

Now let a target echo  $\omega t - \phi_T$  arrive at the  $i$ th antenna element. The IF signal delivered to the PCC is  $\omega t - \phi_T + \gamma_T + \delta_i$ . The phase-conjugated output is  $\omega t + (\frac{1}{2})(\alpha + \delta_i - \eta_i - \mu) - [(-\phi_T + \gamma_T + \delta_i) - (\frac{1}{2})(\alpha + \delta_i - \eta_i - \mu)] = \omega t + \alpha - \eta_i - \mu + \phi_T - \gamma_T$ , and the signal radiated in the direction of the target is  $\omega t + \alpha - \mu + \phi_T$ , which is exactly the conjugated phase plus an arbitrary constant.

The only circuit in the system not under closed-loop control is the phase measuring and phase control branch (12) to (13) from calibrator to module. Gain and bias errors can develop in this circuit. Let the phase detector gain be in error by the factor  $K$  and let a bias  $M$  develop in its output circuit. Then the phase shift in the digital phase shifter is changed by  $\Delta\phi_i = K[-\beta_i - \theta_i + (\frac{1}{2})(\alpha + \delta_i - \eta_i - \mu)] + M$ . The reference for the PCC becomes  $\omega t + \beta_i + \theta_i + \Delta\phi_i \triangleq \omega t + \psi$ . The PCC output is  $\omega t + 2\psi + \phi_T - \gamma_T \delta_i$ . After passage through the transmitter and antenna the radiated wave toward the target is

$$\begin{aligned}
& \omega_0 t + 2\psi + \phi_{Ti} - \delta_i + \eta_i \\
& = \omega_0 t + 2M + K(\alpha - \mu) + \phi_{Ti} \\
& + (1 - K)(2\beta_i + 2\theta_i + \eta_i + \delta_i). \quad (8)
\end{aligned}$$

The first four terms are the conjugated phase ( $\phi_{Ti}$ ) plus an arbitrary constant ( $2M + K(\alpha - \mu)$ ). The last term represents a phase error in transmission from the  $i$ th module, which goes to zero when the gain error goes to zero. The maximum effect is easily calculated.  $\beta$ ,  $\theta$ ,  $\eta$ , and  $\delta$  may be assumed to be random variables independent of the errors in the other modules. Their sum is a random phase error. The magnitude of the net phase error  $\phi_i$  is a function of the fractional gain error  $K$  of the phase detector. Note that the phase error is not a function of the bias error of the phase detector.

Using the theory of mainlobe gain-loss referenced in Section III [12], a tolerance can be calculated for the phase detector gain error. The random phase error is, at worst, uniformly distributed to the interval  $[-\pi, \pi]$ .<sup>2</sup> The variance of a uniform distribution is one-twelfth the square of the length of the interval.<sup>3</sup> Hence

$$\sigma_\phi^2 \leq (1 - K)^2 (2)^2 / 12 \quad (9)$$

which must not exceed  $1/4 \text{ rad}^2$  if the loss in mainlobe gain is to be limited to 1 dB. Taking this value as the tolerance in gain loss, the allowed fractional gain error  $K$  in the phase detector is found by equating (9) to 0.25, which yields  $K = 0.724$ . In other words the gain can change by 27 percent without causing more than 1 dB loss in system performance. This is a relatively easy tolerance to maintain.

## VII. SUMMARY

The logical requirements for a self-adaptive, non-rigid, distributed radar antenna array are discussed. A transmitter is required to illuminate a target, the reflections from which are received by the elements in the array. The target must reradiate a nearly spherical wavefront. The phases of the received echoes are used to set the phase shifts in the antenna elements so that a receiving beam is focused on the target. The same phase information permits setting the transmission phase shifts as well.

<sup>2</sup>For example, the probability density function of the modulo- $2\pi$  sum of two random variables, each uniformly distributed in a  $2\pi$  interval, also is uniform in the interval. This case corresponds to the equality condition in (9). If the pdfs are clustered near the center of the interval, the pdf of the sum also is clustered, leading to the strict inequality in (9). The random variables in (8) will generally correspond to this case. If the pdfs are lower in the central region than at the edges, the inequality could reverse. There is no physical basis for assuming that this situation will occur in this system.

<sup>3</sup>Let  $w(x) = 1/L$ ,  $|x| \leq L/2$  and  $= 0$ , elsewhere. Then  $\sigma_x^2 = (1/L) \int_{-L/2}^{L/2} x^2 dx = L^2/12$ .

Once the transmitting beam is formed and focused on the target the initializing illumination no longer is required. The beam is scanned by modifying the phase shifts in the same manner that is used in a conventional phased array.

Phase conjugation of the received wave at every element is necessary to achieve focused transmission. There are two primary circuit and system choices to make in the design of phase conjugating networks. The first choice is between analog and digital circuits. The second choice is between open-loop and closed-loop control of the phase shift. The bases for these choices are discussed and several circuits are given. The phase conjugating circuit at each antenna element requires a reference wave of constant frequency and fixed phase. Methods for distributing the phase reference across the array are described.

## REFERENCES

- [1] Steinberg, B.D., and Yadin, E. (1982) Distributed airborne array concepts. *IEEE Transactions on Aerospace and Electronic Systems*, Mar. 1982, AES-18, 219-227.
- [2] Applebaum, S.P. (1966) Adaptive arrays. Syracuse University Research Corp., Report STLSPL TR 66-1, Aug. 1966.
- [3] Widrow, B., et al. (1967) Adaptive antenna systems. *Proceedings of the IEEE*, Dec. 1967, 55, 2143-2159.
- [4] Brennan, L.E., and Reed, I.S. (1973) Theory of adaptive radar. *IEEE Transactions on Aerospace and Electronic Systems*, Mar. 1973, AES-9, 237-252.
- [5] Lo, Y.T. (1964) A mathematical theory of antenna arrays with randomly spaced elements. *IRE Transactions on Antennas and Propagation*, May 1964, AP-12, 257-268.
- [6] Steinberg, B.D. (1972) The peak sidelobe of the phased array having randomly located elements. *IEEE Transactions on Antennas and Propagation*, Mar. 1972, AP-20.
- [7] Steinberg, B.D. (1973) On the design of a radio camera for high resolution in microwave imaging. *Journal of the Franklin Institute*, Dec. 1973.
- [8] Steinberg, B.D. (1980) High angular microwave resolution from distorted arrays. *Proceedings of the Symposium of the Society of Photo-Optical Instrumentation Engineers*, Apr. 1980.
- [9] Steinberg, B.D. (1981) Radar imaging from a distorted array: The radio camera algorithm and experiments. *IEEE Transactions on Antennas and Propagation*, Sept. 1981.
- [10] *IEEE Transactions on Antennas and Propagation*, (Special Issue on Active and Adaptive Antennas), Mar. 1964, AP-12, 140-246.
- [11] Hansen, R.C. (Ed.) (1964) *Microwave Scanning Antennas*, vol. 3. New York: Academic Press, 1964, ch. 5.

- [12] Steinberg, B.D. (1976)  
*Principles of Aperture and Array System Design*.  
New York: Wiley, 1976.
- [13] Chernoff, R. (1979)  
Large active arrays for space applications.  
*IEEE Transactions on Antennas and Propagation*, July 1979, AP-27, 489-496.
- [14] Sharp, E.D., and Diab, M.A. (1960)  
Van Atta reflector array.  
*IRE Transactions on Antennas and Propagation*, July 1960, AP-8, 436-438.
- [15] Hansen, R.C. (1961)  
Communications satellites using arrays.  
*Proceedings of the IRE*, June 1961, 49, 1066-1074.
- [16] Gardner, F.M. (1979)  
*Phaselock Techniques*, 2nd ed.  
New York: Wiley, 1979.
- [17] Viterbi, A.J. (1966)  
*Principles of Coherent Communication*.  
New York: McGraw-Hill, 1966.
- [18] Lindsey, W.C. (1972)  
*Synchronization Systems in Communications and Control*.  
Englewood Cliffs, N.J.: Prentice-Hall, 1972.
- [19] Klapper, J., and Frankle, J.T. (1972)  
*Phase-Locked and Frequency Feedback Systems: Principles and Techniques*.  
New York: Academic Press, 1972.
- [20] Lindsey, W.C., and Tansworth, R.C. (1973)  
Bibliography of the theory and application of the phase-lock principle.  
Technical Report 32-1581, Jet Propulsion Laboratory, California Institute of Technology, Pasadena, Apr. 1973.
- [21] Grimberg, E., and Bar-Ness, Y. (1979)  
Acquisition behavior of pulse tracking phase-locked loop.  
*International Journal of Electronics*, July 1979, 47, 1-15.
- [22] Glazer, P. (1968)  
Power from the sun: Its future.  
*Science*, Nov. 1968, 162, 857-861.
- [23] Satellite power systems — Concept development and evaluation program.  
USDOE and NASA Report DOE/ER-0023.  
Available from *National Technical Information Services*, U.S. Department of Commerce, Jan. 1979.
- [24] Lindsey, W.C., and Kanek, A.V. (1978)  
Automatic phase control in solar power satellite systems.  
Technical Report TR-7802-0977, LinCom Corp., P.O. Box 2793D, Pasadena, Calif., Feb. 1978.
- [25] Steinberg, B.D., and Powers, E.N. (1975)  
High angular resolution radar.  
*Proceedings of the IEEE International Radar Symposium*, Arlington, Va., Apr. 1975.
- [26] Godlove, T.F., and Granatstein, V.L. (1977)  
Relativistic electron beam sources.  
*Society of Photo-Optical Instrumentation Engineers*, 105, Far Infrared/Submillimeter Wave Technology/Applications, 1977.
- [27] Steinberg, B.D. (1982)  
Adaptive microwave holography.  
*Optica Acta*, Apr. 1982.
- [28] Steinberg, B.D., and Yadia, E. (1982)  
Radio camera experiment with airborne radar data.  
*Proceedings of the IEEE (Letters)*, Jan. 1982, 70, 96-98.



Bernard D. Steinberg (S'48—A'50—SM'64—F'66) was born in Brooklyn, N.Y., in 1924. He received the B.S. and M.S. degrees in electrical engineering from the Massachusetts Institute of Technology, Cambridge, in 1949, and the Ph.D. degree from the University of Pennsylvania, Philadelphia, in 1971.

He worked in the Research Division of Philco through the middle 1950's, specializing in radar backscatter and radar signal processing. He was one of the founders of General Atronics Corporation in Philadelphia in 1956 and served as its Vice President and Technical Director for 15 years. His work there was in signal processing techniques and their applications to radar, HF communications, hydroacoustics, and seismology. His most recent work is in self-adaptive signal processors, particularly in large antenna arrays. Since 1971, he has been a Professor with the Moore School of Electrical Engineering at the University of Pennsylvania, Philadelphia, and Director of its Valley Forge Research Center, where he is engaged in development of a large self-adaptive microwave imaging system called the "radio camera." He is the author of *Principles of Aperture and Array System Design* (Wiley, 1976) in which early radio camera concepts are described and currently is preparing a detailed book on the subject. He also is a consultant in the Airborne Radar Branch of the Naval Research Laboratory.

Dr. Steinberg is a member of U.S. Commissions B and C of the International Scientific Radio Union (URSI).

# ABSTRACT

## AMBIGUITY RESOLUTION IN SELF-COHERING ARRAYS\*

Chung H. Lu, RCA Laboratories, Princeton, NJ

C. Nelson Dorn, Valley Forge Research Center, Moore School of Electrical Engineering, University of Pennsylvania, Philadelphia, Pennsylvania

Two approaches to resolving the phase ambiguity associated with phase multilateration of self-cohering antenna arrays are described and the probability of ambiguity error is derived for each approach. For the minimum least-square error method an efficient computational technique is introduced which permits element position uncertainties as large as one wavelength in the presence of phase measurement errors in the order of one radian. The multiple frequency method permits element position uncertainties significantly larger than one wavelength, at some increase in bandwidth. The probability of ambiguity error is shown to be acceptably small if the rms phase measurement errors are in the order of 0.5 radian or smaller.

\*Submitted to IEEE Transactions on Antennas and Propagation, July 1983.

AMBIGUITY RESOLUTION IN SELF-COHERING ARRAYS<sup>\*</sup>

Chung H. Lu, RCA Laboratories, Princeton, NJ

C. Nelson Dorny, Valley Forge Research Center, Moore School of Electrical Engineering, University of Pennsylvania, Philadelphia, Pennsylvania

A number of self-cohering random arrays, up to 1000 wavelengths in length, with average element spacings in the order of 10 wavelengths, have been constructed at the Valley Forge Research Center. An extensive theory for design of such large, sparse, random arrays has been developed [1,2]. A self-survey technique for self-cohering of such an array is described in [3]; experimental testing of the technique is described in [4]. The technique determines each element position in the array from phase measurements made at the element for signals transmitted from beacons at known (measured) locations. The technique also calibrates the phase reference at each element. Use of this technique considerably loosens the mechanical tolerances required to obtain acceptable array performance, and thereby permits operation of very large, loosely-surveyed, or non-rigid arrays. The self-survey is basically a phase multilateration technique, in which ranges are inferred from phase measurements. There is a phase ambiguity inherent in each phase comparison. High-precision element location requires accurate ambiguity resolution. This article describes two approaches to resolving this phase ambiguity, a minimum least square (MLS) method and a multifrequency method.

The self-survey works as follows. A few beacons of known location are blinked consecutively. (In some applications those beacons would be replaced by passive reflectors.) At the  $i^{\text{th}}$  element of the array, the phases of the signals received from each beacon are compared to the phases of the corresponding signals received at a reference element and delivered by cable to the  $i^{\text{th}}$  element (see Fig. 1). Except for the ambiguity caused by the mod  $2\pi$  nature of the phase measurement process, these phase measurements are indicators of the differential beacon-to-element time delays.

<sup>\*</sup>This work was supported primarily by the Air Force Office of Scientific Research under Grant No. AFOSR-78-3688.

These delays are used to estimate the element position  $(x_1, y_1)$  relative to the reference and the phase delay  $\phi_1^c$  in the reference cable. These computed values of  $x_1, y_1, \phi_1^c$  are used to cohere the array.

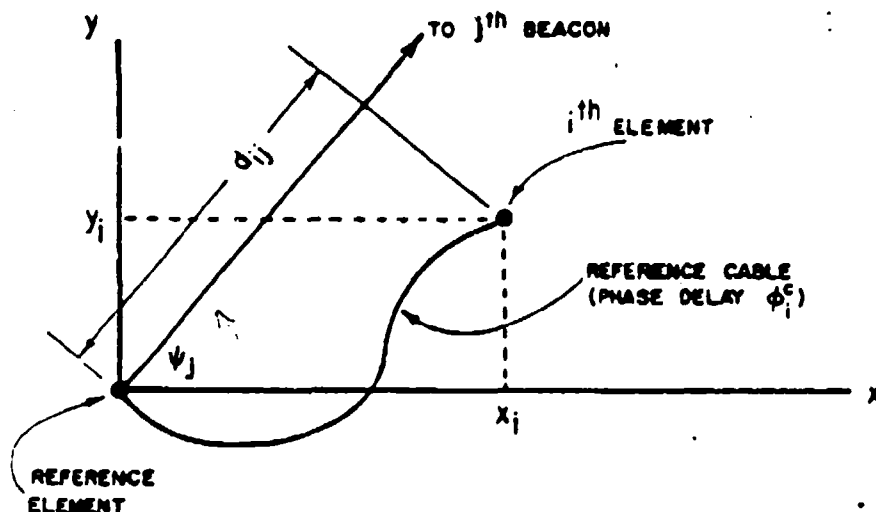


FIGURE 1 Differential Phase Delay

Let the origin of the coordinate system be placed at the reference element of Fig. 1. According to free-space theory, if we broadcast from the  $j^{\text{th}}$  beacon, which is in the far-field of the array at angle  $\psi_j$  from the x axis, the phase  $\phi_{ij}$  of the beacon signal received at element  $i$  relative to the corresponding beacon signal received at the reference element and delivered by cable to element  $i$  is

$$\begin{aligned}\phi_{ij} &= kd_{ij} + \phi_1^c - 2\pi n_{ij} \\ &= k(d_{ij} + d_c) - 2\pi n_{ij}\end{aligned}\tag{1}$$

where  $d_{ij} = x_i \cos \psi_j + y_i \sin \psi_j$ , the differential distance to the beacon,  $k = 2\pi/\lambda$ ,  $\lambda$  is the wavelength,  $(x_i, y_i)$  is the element position,  $\phi_1^c$  is the phase delay in the cable plus the differential delay in the electronics,  $d_c$  is the electrical length of the cable and electronics delay, and  $n_{ij}$  is the number of multiples of  $2\pi$  removed by the mod  $2\pi$  phase measurement process. Thus we assume  $\phi_{ij}$  lies in the interval  $[0, 2\pi]$ . Lee[5, p.11] shows

$$(2)$$

that use of a broadcast reference rather than the cable does not change the mathematical form of (1). Measurement of  $\phi_{1j}$ ,  $n_{1j}$ , and  $\psi_j$  determines a single equation in the three unknowns  $x_1$ ,  $y_1$ ,  $\phi_1^c$ . The measurements are taken for N different beacons ( $N \geq 3$ ) resulting in a set of N equations in the three unknowns associated with element 1:

$$BX = \phi \quad (2)$$

where  $X = (x_1, y_1, \phi_1^c)^T$ ,  $\phi = (\phi_{11}^d, \dots, \phi_{1N}^d)^T$ ,  $\phi_{1j}^d = \phi_{1j} + 2\pi n_{1j}$ , and B is an  $N \times 3$  matrix of known quantities. It is shown in [3] that use of the least-square phase error solution

$$X = (B^T B)^{-1} B^T \phi \quad (3)$$

in beam formation usually leads to acceptable expected gain loss for beam pointing directions within the spread of the beacons.

#### MLS Ambiguity Resolution

Since  $\phi_{1j}^d$  depends on  $n_{1j}$ , equation (3) specifies a unique solution for each choice of the ambiguity integers  $\{n_{1j}\}$  used in the "demod" process to obtain  $\{\phi_{1j}^d\}$ . We determine the possible values of  $n_{1j}$  from the region of uncertainty of the position of element 1 and from the direction of beacon j. The MLS (minimum least square) method of ambiguity resolution consists of computing the least-square phase error solution X for each combination of the possible values of  $n_{11}, \dots, n_{1N}$ , then selecting as the correct solution that X which yields the minimum value of least-square phase error.

If the array is not extremely large, and if the structure on which the elements are mounted is fairly rigid (as in an airborne array), the element positions may be known to within approximately one wavelength, and each ambiguity integer will have only a few possible values. On the other hand, if the array elements are widely separated (perhaps on separate aircraft), and if a priori relative positions are obtained by time delay measurements, the position uncertainties will be somewhat larger, and  $n_{1j}$  may have many possible values. In either case uncertainty in the cable delay  $\phi_1^c$  in (1) increases the uncertainty in  $n_{1j}$ . Therefore, in determining the possible values of  $n_{1j}$ , uncertainty in  $\phi_1^c$  must be considered. We refer to the set of possible values of  $n_{1j}$  as the "integer set" associated with  $n_{1j}$ . The next section describes a technique which permits testing of the possible combinations of ambiguity integers without excessive computation.

If the integer sets are correctly determined, (that is, if the correct integers are included), then comparison of the least-square errors associated with the various ambiguity integer combinations will pinpoint which choice of ambiguity integers and corresponding self-survey solution is correct. On the other hand, if the correct ambiguity integer is excluded from an integer set, the correct combination will not be among the candidates which are checked, and an ambiguity error will occur.

We wish the  $N$  integer sets to be as small as possible in order to minimize the computation required to test the combinations. If tight bounds on each ambiguity integer can be determined, then each integer set will include the correct integer. Let  $P_j$  be the probability that the correct ambiguity integer associated with beacon  $j$  is excluded from the corresponding integer set, and let  $P$  be the resulting probability that the correct combination of integers is not found. Then, the probability of correct ambiguity resolution is  $1 - P = \prod_{j=1}^N (1 - P_j)$ , where  $N$  is the number of beacons (typically four or more). In order that  $P$  be reasonably small, say 0.01, it is necessary that  $P_j$  be very much smaller (say, 0.0025, for  $N = 4$ ).

In most applications coarse estimates of the differential distance  $d_{ij}$  and the electrical length  $d_c$  and some knowledge of the accuracy of the estimates will be available prior to self-survey. For example, if the array is distributed over the surface of an aircraft, nominal element positions and cable lengths will be known, and the range of relative element position deviations from the nominal values (which result from flexing of the airframe in flight) can be described in terms of random variables. For normally distributed errors in a priori estimation of  $d_{ij} + d_c$ , Fig. 2 shows the probability  $P_j$  of the correct ambiguity integer being excluded from the integer set associated with a particular beacon, as a function of the size of the uncertainty region (as measured by the standard deviation  $\sigma$  in the estimate of  $d_{ij} + d_c$ ) and the size  $n$  selected for the integer set. This figure can be used to select the size of the integer set in such a way as to obtain sufficiently low probability of ambiguity error in the self-survey.

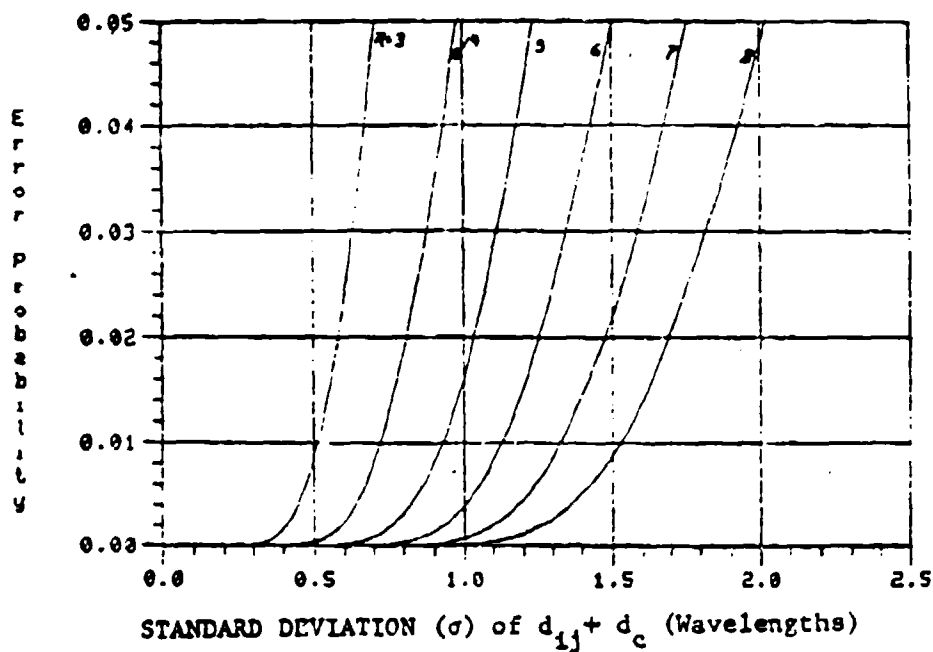


FIGURE 2 Effect of Integer Set Size  $n$  on Error Probability  $P$   
(assuming normally distributed estimate of  $d_{ij} + d_c$ )

It can be observed from Figure 2 that if the standard deviation  $\sigma$  is one wavelength, it is necessary that  $n \geq 6$  to obtain a reasonably small probability of ambiguity error. That is, the integer set size  $n$  must be large enough to include the correct ambiguity integer in all but very low probability instances. It is shown in [7] that the MLS method of selecting  $n_{ij}$  is equivalent to the maximum likelihood method if the estimation errors are independent identically distributed Gaussian random variables as assumed in Figure 2.

(5)

### Reduction in Computation

This section describes a technique for reducing the computation associated with testing each combination of ambiguity integers. For a system with  $N$  beacons, the technique reduces the amount of computation by at least a factor of  $n^{N-3}$ , where  $n$  is the integer set size. Thus, the computation grows by no more than  $n^3$ . This section also shows that the least-square phase error associated with each combination can be determined directly from the measured data without explicitly computing the self-survey solution associated with that combination.

The square phase error associated with the least-square error solution (3) is

$$\epsilon = ||BX - \phi||^2 = ||G\phi||^2 \quad (4)$$

where

$$G = I_N - B(B^T B)^{-1} B^T, \quad (5)$$

$I_N$  is an  $N^{\text{th}}$  order identity matrix, and  $\phi$  is a linear function of the  $N$  ambiguity integers  $(n_{11}, \dots, n_{1N})$  as shown in (2);  $\epsilon$  is computed for each candidate combination of ambiguity integers, and the combination which gives minimum  $\epsilon$  is selected.

Consider  $(n_{11}, \dots, n_{1N})$  as an  $N$ -tuple of real numbers. Then, since  $\phi$  is linear in  $\{n_{1j}\}$  and  $G^T G = G$ , the  $N$ -tuple which minimizes  $\epsilon$  satisfies

$$G\phi(n_{11}, \dots, n_{1N}) = 0 \quad (6)$$

Equation (6) can be viewed as a constraint on the possible ambiguity integer combinations. In other words, only those combinations which satisfy (6) need be tested for minimum  $\epsilon$ . Because of quantization noise and measurement errors however, an  $N$ -tuple which satisfies (6) will not consist of integers. Therefore, we select as the possible ambiguity integer combinations, the ones which nearly satisfy (6) in the sense described below.

Because  $G$  is idempotent,  $\text{rank}(G) = \text{trace}(G)$ . But  $\text{trace}(I_N) = N$  and  $\text{trace}[B(B^T B)^{-1} B^T] = \text{trace}[(B^T B)^{-1} B^T B] = \text{trace}(I_3) = 3$ . Therefore,  $\text{rank}(G) = N - 3$ , and nullity( $G$ ) = 3. (This result is intuitively reasonable, since  $B$  is a rank 3 matrix.) Thus the equation (6), which is linear in the integer variables  $\{n_{ij}\}$ , constitutes  $N - 3$  linearly independent constraints on the combination of ambiguity integers, and only three of the integers (say, the first three) can be chosen arbitrarily. Once the three arbitrarily designated integers are specified, the other integers can be obtained from (6) by a single matrix multiplication using a conventional linear system algorithm. (Such a procedure is described in [7]). Because of quantization noise and measurement errors,  $G\phi(n_{11}, \dots, n_{1N})$  is not precisely the zero vector for the allowed combination of ambiguity integers. Therefore, the computed values for the  $N - 3$  integers must be rounded to the closest integers. If any of the integers in the resulting solution does not lie in its corresponding integer set, the ambiguity combination is not the correct one and can be dropped. Otherwise, the corresponding square error  $\epsilon$  in (4) is computed. Note that the matrix  $G$  need only be computed once. In general, if we were to try all combinations of  $N$  integer sets of size  $n$ , we would have to test  $n^N$  cases. However, by pretesting via the constraints (6), we test at most  $n^3$  cases, a reduction by the factor  $n^{N-3}$ . If the system has no redundancy ( $N = 3$ ),  $G$  is the zero matrix and  $\epsilon$  is zero for any integer combination. Therefore data redundancy is necessary for ambiguity resolution by the MLS method.

If each ambiguity integer in the solution to (6) is increased by one, the resulting phase vector  $\phi$  is affected in the same fashion as it would be by a  $2\pi$  increase in the cable phase-shift. Since the cable phase-shift need only be known mod  $2\pi$  in order to form beams, such ambiguity integer combinations are redundant and need not be tested. This fact may permit some further reduction in the number of combinations to be tested.

The MLS ambiguity resolution technique was applied to self-survey of paired elements in [7]. Simulation of the element-pair system without errors in the phase measurements  $\phi_{ij}$  showed a clear-cut difference between the minimum-least-square phase error for correct and incorrect integer combinations. Simulation with phase errors showed that the average allowable phase-measurement error for correct integer-combination selection is  $39^\circ$ . The phase-measurement error tolerance for the non-paired system described in this article should be looser by a factor of 2, that is  $78^\circ$ .

This resistance of the MLS ambiguity resolution technique to phase measurement errors is in agreement with the observation in [5, p. 79] that the effect on the least-square phase error of an error in one of the ambiguity integers is typically at least 40 times larger than the effect of an error in one of the phase measurements.

### Multiple Frequency Ambiguity Resolution

In this section a sequence of frequencies is used to progressively resolve the ambiguity in the self-survey phase measurements. The technique extends [6] by taking advantage of prior estimates of element and beacon positions, and by including the effect of cable and electronics delays; it provides, in addition, a prediction of probability of ambiguity error. The technique makes use of the relatively long beat wavelength between close frequencies. Although the use of the beat wavelength magnifies phase errors, accuracy can be maintained by using a succession of progressively reduced beat wavelengths. Thus accuracy of the computed element positions can be increased by increasing the number of beat wavelengths (bandwidth). Throughout this section, reference is made only to element  $i$  and beacon  $j$ . Thus, the subscripts  $i$  and  $j$  are dropped.

Let  $\lambda_0$  denote the nominal wavelength, and assume the sequence of auxiliary wavelengths  $\{\lambda_p\}$  satisfies

$$\lambda_0 < \lambda_m < \dots < \lambda_2 < \lambda_1 \quad (7)$$

The beat wavelength between  $\lambda_0$  and  $\lambda_p$  is

$$\lambda_{op} = \frac{\lambda_0 \lambda_p}{\lambda_p - \lambda_0}, \quad p = 1, \dots, m \quad (8)$$

where  $\lambda_0 < \lambda_{01} < \lambda_{02} < \dots < \lambda_{0m}$ . The sequence of beat wavelengths will determine a sequence of ambiguity integers  $n_p$  terminating with the desired ambiguity integer,  $n_0 = n_{1j}$ , of (1).

Assume the cable is nondispersive. Then the cable phase delay is proportional to frequency, and we can rewrite (1) as

$$\phi_p = k_p d - 2\pi n_p, \quad p = 0, 1, \dots, m \quad (9)$$

where  $\phi_p$  is the phase measurement at the element corresponding to the  $p^{\text{th}}$  frequency transmitted from the beacon,  $k_p = 2\pi/\lambda_p$ ,  $\lambda_p$  is the  $p^{\text{th}}$  wavelength,  $d = d_{1j} + d_c$ ,  $d_c$  is the electrical length of the cable, and  $n_p$  is the ambiguity integer associated with  $\lambda_p$ . We subtract the  $p^{\text{th}}$  equation from the  $0^{\text{th}}$  equation of (9) to obtain

$$\phi_o - \phi_p = 2\pi d/\lambda_{op} - 2\pi(n_o - n_p), \quad p = 1, \dots, m \quad (10)$$

Because  $\phi_o$  and  $\phi_p$  are both in  $[0, 2\pi)$ ,  $\phi_o - \phi_p$  must lie in  $(-2\pi, 2\pi)$ . We define

$$\phi_{op} = \phi_o - \phi_p \quad (11)$$

and

$$n_{op} = n_o - n_p \quad (12)$$

Thus  $\phi_{op}$  is a measured quantity and  $n_{op}$  is an unknown integer. Suppose that

$$d = d_e + \delta d \quad (13)$$

where  $d_e$  is an estimate of  $d$  and  $\delta d$  is the remaining uncertainty in  $d$ . We divide (10) by  $2\pi/\lambda_{op}$ , substitute from (11)-(13), and rearrange terms to yield

$$\delta d - n_{op}\lambda_{op} = \frac{\phi_{op}}{2\pi} \lambda_{op} - d_e, \quad p = 1, \dots, m \quad (14)$$

The  $0^{\text{th}}$  equation of (9) can be rewritten as

$$\delta d - n_o\lambda_o = \frac{\phi_o}{2\pi} \lambda_o - d_e \quad (15)$$

We rearrange the  $m^{\text{th}}$  equation of (14) to obtain

$$n_{om} = \left( \frac{d_e}{\lambda_{om}} - \frac{\phi_{om}}{2\pi} \right) + \frac{\delta d}{\lambda_{om}} \quad (16)$$

We design the auxiliary wavelength  $\lambda_m$  so that the beat wavelength  $\lambda_{om}$  satisfies  $|\delta d|/\lambda_{om} < 0.5$ . That is, the uncertainty in  $d$  is less than one half of the beat wavelength. Then  $n_{om}$  can be computed unambiguously as

$$n_{om} = \text{Round} \left[ \frac{d_e}{\lambda_{om}} - \frac{\phi_{om}}{2\pi} \right] \quad (17)$$

where Round [ ] means rounding to the nearest integer. In an ideal noise-free situation, the right hand side of (16) would be identically equal to an integer. Equation (17) would in effect restore the unknown portion represented by  $\delta d / \lambda_{om}$ . Therefore, we refer to  $\lambda_{om}$  as the maximum resolvable element position uncertainty. Note that in [6],  $\lambda_{om}$  determines the maximum resolvable element spacing. The procedure described in this article therefore provides a much higher resolving power.

Once  $n_{om}$  is determined, equations (14)-(15) constitute  $m+1$  linear equations in the  $m+1$  unknowns  $\delta d$ ,  $n_o$ ,  $n_{o1}$ , ...,  $n_{o,m-1}$ . However, all of the variables except  $\delta d$  are integers. These equations can be solved sequentially to obtain  $n_o$ , thereby resolving the ambiguity in the phase measurements used for phase multilateration. Specifically, insert  $n_{om}$  from (17) into the  $m^{th}$  equation of (14) and solve for  $(\delta d)_m$ , the " $m^{th}$ " estimate of  $\delta d$ . Insert  $(\delta d)_m$  into the  $(m-1)^{st}$  equation of (14), solve for  $n_{o,m-1}$  and round to the nearest integer. Use that integer in the  $(m-1)^{st}$  equation of (14) to compute  $(\delta d)_{m-1}$ . Repeat with each of equations (14) until  $(\delta d)_1$  is obtained, then use (15) to obtain  $n_o$  (and if desired,  $d \triangleq d_e + \delta d$ ).

The following example illustrates the computation process. Suppose that  $d = 107.84 \lambda_o$ , that  $d_e = 100 \lambda_o$ , and thus  $\delta d = 7.84 \lambda_o$ . The correct ambiguity integer is  $n_o = 107$ , and  $\phi_o = 1.68\pi$ . Assume we use three ( $m=3$ ) auxiliary wavelengths,  $\lambda_1 = 1.4 \lambda_o$ ,  $\lambda_2 = 1.15 \lambda_o$ , and  $\lambda_3 = 1.06 \lambda_o$ . The beat wavelengths are respectively  $\lambda_{o1} = 3.5 \lambda_o$ ,  $\lambda_{o2} = 7.67 \lambda_o$ , and  $\lambda_{o3} = 17.67 \lambda_o$ . The free-space, error-free values of the difference phases (denoted by superscript "o") are  $\phi_{o1}^o = 1.62\pi$ ,  $\phi_{o2}^o = 0.13\pi$ , and  $\phi_{o3}^o = 0.21\pi$ . We add simulated phase errors to these quantities to obtain  $\phi_o = 1.87\pi$ ,  $\phi_{o1} = 1.73\pi$ ,  $\phi_{o2} = 0.19\pi$ , and  $\phi_{o3} = 0.12\pi$ .

From (17), we compute  $n_{o3} = 6$  (rounded from 5.63). The third equation of (14) is used with  $n_{o3}$  to yield  $(\delta d)_3 = 7.08 \lambda_o$ . This quantity is substituted into the second equation of (14) to obtain  $n_{o2} = 14$  (rounded from 13.87). The second equation of (14) is again used with this integer value of  $n_{o2}$  to obtain  $(\delta d)_2 = 8.11 \lambda_o$ . The process is repeated to

obtain  $n_{o1} = 30$  (rounded from 30.02),  $(\delta d)_1 = 8.03 \lambda_o$ , and finally, from (15),  $n_o = 107$  (rounded from 107.10) and  $\delta d = 7.94 \lambda_o$ .

If  $n_o$  were computed in one step using only (15) and the third equation of (14), we would have obtained  $n_o = 106$  (rounded from 106.15). A sequence of computational stages is needed to prevent phase errors from corrupting the computations. The rounding operation prevents the errors from accumulating.

At the  $(p-1)^{st}$  (or last) stage of the process  $n_{o,p-1}$  (or  $n_o$ ) is determined from  $n_{op}$  (or  $n_{o1}$ ) by

$$n_{o,p-1} = \text{Round}[(n_{op} + \frac{\phi_{op}}{2\pi})(\frac{\lambda_{op}}{\lambda_{o,p-1}}) - \frac{\phi_{o,p-1}}{2\pi}] \quad p = m, \dots, 2, \quad (18)$$

or

$$n_o = \text{Round}[(n_{o1} + \frac{\phi_{o1}}{2\pi})(\frac{\lambda_{o1}}{\lambda_o}) - \frac{\phi_o}{2\pi}]$$

Thus the error in the difference phase  $\phi_{op}$  (or  $\phi_{o1}$ ) is magnified by the wavelength ratio  $\lambda_{op}/\lambda_{o,p-1}$  (or  $\lambda_{o1}/\lambda_o$ ). The beat wavelengths can be selected to minimize the probability of an ambiguity error. If the errors in the right hand side of (16) and in the bracketed quantity in (18) prior to the Round operation are less than 0.5 at each stage, then the final value of  $n_o$  will be correct. Let  $\epsilon$  be a bound on the error in the phase measurements  $\phi_p$ . Then it can be determined from (16) and (18) that  $n_o$  will be error free if

$$\left. \begin{aligned} \frac{|\delta d|}{\lambda_{om}} + \frac{\epsilon}{\pi} &< \frac{1}{2} \\ \lambda_{op}/\lambda_{o,p-1} &< \pi/2\epsilon, \quad p = m, \dots, 2 \\ \lambda_{o1}/\lambda_o &< (\pi/2\epsilon + 0.5) \end{aligned} \right\} \quad (19)$$

It follows from these inequalities that

$$\lambda_{om} < (\pi/2\epsilon + 0.5)(\pi/2\epsilon)^{m-1} \lambda_o \quad (20)$$

For a given error bound and a given maximum size  $|\delta d|$  of element position uncertainty, the minimum number of auxiliary wavelengths required for error-free ambiguity resolution can also be determined from (20); namely,

$$m > 1 + \frac{\log\{2|\delta d|/[\lambda_0(1 - 2\epsilon/\pi)(\pi/2\epsilon + 0.5)]\}}{\log(\pi/2\epsilon)} \quad (21)$$

For the earlier example we assumed that the maximum expected phase error was  $\epsilon = 0.5$  radian and that  $|\delta d| = 7.64 \lambda_0$ . Then (21) required use of three frequencies; (19) and (20) required that  $\lambda_1 > 1.38 \lambda_0$ ,  $\lambda_2 > 1.11 \lambda_0$ , and  $\lambda_3 > 1.03 \lambda_0$ .

In general, more auxiliary frequencies (and thus wider bandwidth) provides higher immunity of the ambiguity resolution process to phase measurement errors. The minimum fractional bandwidth, derived from (8) and (19), is

$$\text{Fractional BW} \triangleq \left| \frac{f_1 - f_0}{f_0} \right| = \frac{\lambda_1 - \lambda_0}{\lambda_1} \geq \frac{2\epsilon}{\pi + \epsilon} \quad (22)$$

It is obvious from (22) that the required bandwidth increases as phase error increases. The minimum bandwidth for the previous example is 27.5%. The actual bandwidth is 28.6%. It should be pointed out that the operating frequency  $f_0$  in the denominator of (22) is at the top of the frequency band rather than at the band center.

#### Ambiguity Error Probability

Equations (19)-(21) describe the process for selecting auxiliary frequencies for unambiguous determination of the ambiguity integer  $n_0$  under the assumption that phase errors will be no larger than some number  $\epsilon$ . In practice it will probably not be possible to bound the phase errors tightly enough to avoid excessively large bandwidth. The following analysis determines the probability of ambiguity error -- an error in the computed value of the ambiguity integer  $n_0$  -- for normally distributed phase errors.

Phase errors occur because of anomalous transmission and noise in the phase-measuring devices. They typically have a bell-shaped probability density function, but are always limited to an interval of length  $2\pi$ . For ease of computation we assume the phase error in  $\phi_p$ , denoted by  $\epsilon_p$ , is independent, identically and normally distributed, with zero mean and variance  $\sigma_o^2$ . This assumption of unbounded phase error will produce a slightly pessimistic error probability, but the effect will be negligible if the standard deviation  $\sigma_o$  is small.

The quantity in brackets in (17) differs from the correct integer  $n_{om}$  by the amount

$$X_m \triangleq \frac{-\delta d}{\lambda_{om}} - \frac{(\epsilon_o - \epsilon_m)}{2\pi} \quad (23)$$

For correct determination of  $n_{om}$ ,  $X_m$  must be in the range  $(-0.5, 0.5)$ . Note that if  $|\delta d|$  were nearly equal to  $\lambda_{om}/2$ , then correct determination of  $n_{om}$  would be guaranteed only if the phase measurement error  $(\epsilon_o - \epsilon_m)$  were negligible. Practical ambiguity resolution requires selection of a beat frequency  $\lambda_{om}$  which is somewhat larger than  $2|\delta d|$ . We treat the quantity  $\delta d$  as a zero mean random variable which is uniformly distributed over an interval of size somewhat smaller than  $\lambda_{om}$ .

Let  $P_p^l$  denote the probability that the computed value of  $n_{op}$  is larger than the correct value by the integer  $l$ . Then

$$P_m^l = P\{l - 0.5 < X_m < l + 0.5\} \quad (24)$$

Define  $\alpha_{p-1} \triangleq \lambda_{op}/\lambda_{o,p-1}$  and  $\alpha_o \triangleq \lambda_{o1}/\lambda_o$ . Note that the quantity in brackets in the first equation of (18) includes the error component  $\alpha_{p-1}$  if  $n_{op}$  is in error by 1. Consequently

$$P_{p-1}^l = \sum_{k \in I} P_p^k P\{(l - k\alpha_{p-1} - .5) < X_{p-1} < (l - k\alpha_{p-1} + 0.5)\} \quad (25)$$

$p = 2, 3, \dots, m$

where  $I$  refers to the integers and the composite phase error  $2\pi X_{p-1} \triangleq (\alpha_{p-1}(\epsilon_o - \epsilon_p) - (\epsilon_o - \epsilon_{p-1}))$  is  $N(0, 2(\alpha_{p-1}^2 - \alpha_{p-1} + 1)\sigma_o^2)$ . Using the symmetry of uniform and normal random variables, it can be shown that  $P_p^l = P_p^{-l}$  for  $p = 1, 2, \dots, m$ .

Finally, from the second equation of (18), the probability that there is no error in  $n_o$  is

$$P_o^0 = \sum_{k \in I} P_1^k P\{(-k\alpha_o - .5) < X_o < (-k\alpha_o + .5)\} \quad (26)$$

where the composite phase error  $2\pi X_o \triangleq \alpha_o(\epsilon_o - \epsilon_1) - \epsilon_o$  is  $N(0, (2\alpha_o^2 - 2\alpha_o + 1)\sigma_o^2)$ . The probability of ambiguity error is then given by

$$P_e \triangleq 1 - P_o^0 \quad (27)$$

Equations (24) - (27) define a recursive relation for the ambiguity error probability  $P_e$  which can be plotted against the standard deviation  $\sigma_0$  for different combinations of auxiliary wavelengths. Figure 3 and Table 1 show some example combinations under the assumption that  $\lambda_{om} > 2.5|\delta d|$ .

For each set of auxiliary wavelengths, the ambiguity error probability  $P_e$  decreases toward zero as  $\sigma_0$  decreases.  $P_e$  is determined by the element position uncertainty  $|\delta d|$ , the number of auxiliary wavelengths  $m$ , and the phase error magnification factors  $\alpha_0, \alpha_1, \dots, \alpha_{m-1}$ . Curve 2 of Figure 3 shows the error probability of the suboptimal example system of the previous section. The plots shown in Figure 3 suggest a lower bound on the error probability. For a given element position uncertainty, it is always possible to select a proper combination of  $m, \alpha_0, \alpha_1, \dots, \alpha_{m-1}$ , and therefore the auxiliary wavelengths, to approach this lower bound. This lower bound will be further reduced if  $|\delta d|$  is restricted to a smaller fraction of  $\lambda_{om}$ . Equations (19)-(21) provide a good starting point for determining  $m$  and selecting  $\alpha_0, \alpha_1, \dots, \alpha_{m-1}$  for minimum  $P_e$ . Some empirical design rules can be derived from Figure 3. In general, to reduce  $P_e$  it is best to arrange the values of  $\alpha_0, \alpha_1, \dots, \alpha_{m-1}$  in the order of increasing magnitude. For  $\sigma_0$  less than  $20^\circ$ , the lower bound is approached if  $\alpha_0$  and  $\alpha_1$  are not larger than 2. Further reduction in the magnification factors reduces the error probability only for larger  $\sigma_0$ . Furthermore,  $\alpha_0$  is the reciprocal of the fractional bandwidth (see (8) and (22)). Therefore, a small  $\alpha_0$  results in a large bandwidth.

In summary, with a reasonable number and proper arrangement of auxiliary wavelengths, the ambiguity error probabilities in the multi-frequency method can be made negligible for  $\sigma_0 < 10^\circ$  and can be maintained below 1% if  $\sigma_0$  is not larger than  $20^\circ$ .

### Conclusion

A multifrequency method and an MLS method for ambiguity resolution in phase multilateration systems for array self-cohering have been described. The multi-frequency method has the capability of minimizing the effect of phase measurement errors and achieves negligible ambiguity error by utilizing a set of auxiliary frequencies at the expense of wider bandwidth. The ambiguity error is reduced as the bandwidth is increased. For Gaussian phase errors, the ambiguity error probability is negligible for a phase error standard deviation smaller than  $10^\circ$ . The error probability in-

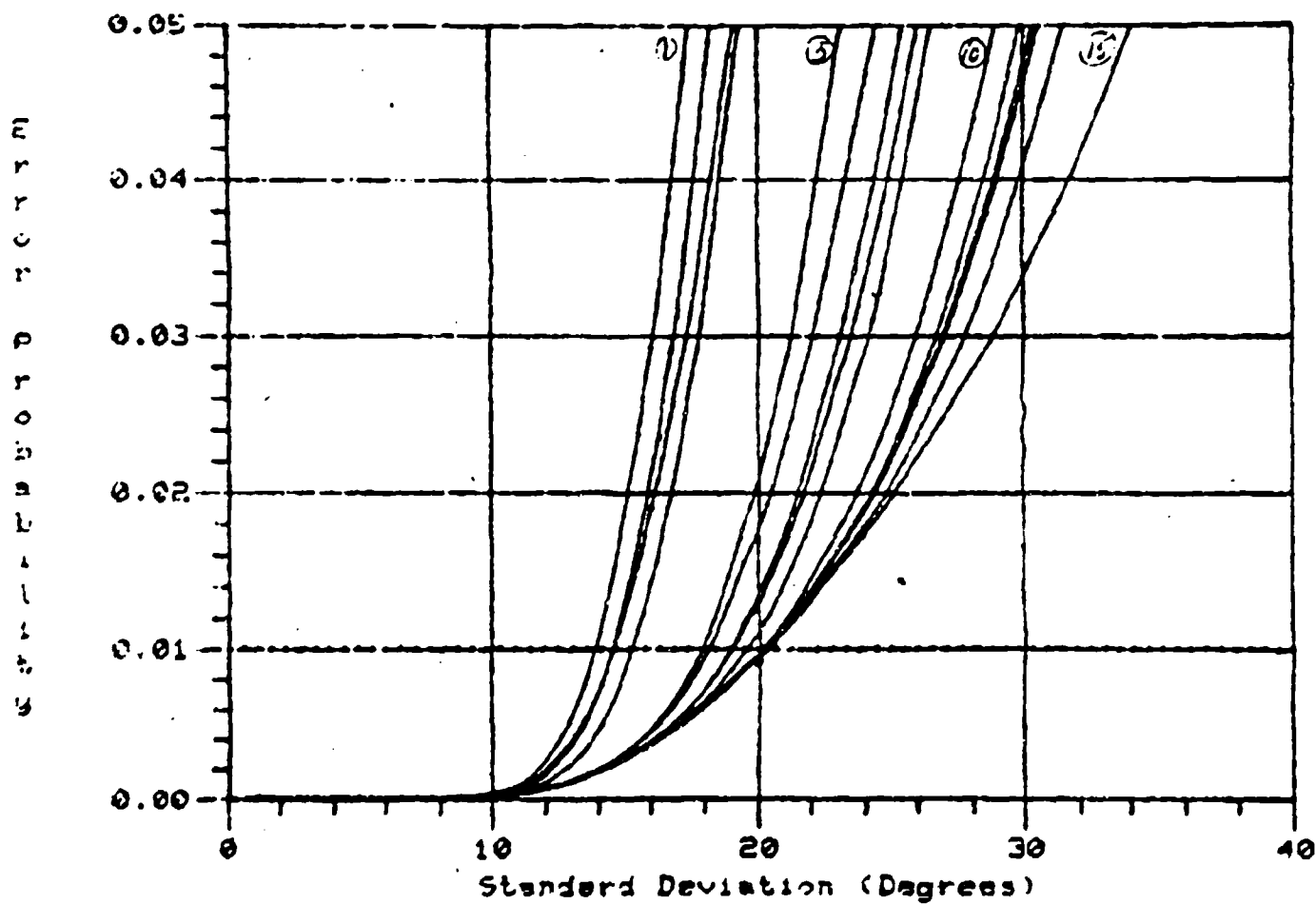


FIGURE 3 Probability  $P_e$  of Ambiguity Error vs Standard Deviation  $\sigma_o$  of Phase Error  
 (Assumes  $\delta d$  uniformly distributed on  $[-0.4 \lambda_{om}, 0.4 \lambda_{om}]$ ,  
 and normal, zero mean phase errors with variance  $\sigma_o^2$ .)

TABLE 1

Auxiliary Wavelength Selections For Figure 3  
(In order of decreasing error probability)

<u>Curve Number</u>	<u>Number of Frequencies</u>	<u><math>\lambda_{om}</math></u>	<u>Wavelength ratios, <math>\alpha_i, i = 0, \dots, m-1</math></u>			
1	3	11	3.67	1.5	2.0	
2	3	17.67	3.5	2.19	2.30	
3	3	11	1.5	3.67	2.0	
4	2	11	3.317	3.317		
5	3	11	2.75	2.0	2.0	
6	3	11	2.0	2.75	2.0	
7	2	5	2.5	2.0		
8	3	11	2.0	2.5	2.2	
9	3	11	2.224	2.224	2.224	
10	3	11	2.0	2.0	2.75	
11	4	11	1.821	1.821	1.821	1.821
12	3	11	2.0	1.5	3.67	
13	2	5	2.0	2.5		
14	5	11	1.615	1.615	1.615	1.615
15	3	5	1.5	1.5	2.22	

creases from zero to 1% as the standard deviation increase from  $10^\circ$  to  $20^\circ$ .

The MLS method is based on the special properties of the over-determined self-survey equations and on limited a priori knowledge of directional interelement spacings. In particular, it makes use of the property that the least-square phase error due to an ambiguity integer error is an order of magnitude larger than that due to phase measurement errors. The ambiguity error probability is dependent on the accuracy of estimation of the interelement spacings and the number of possible integers associated with each beacon. Advantage of the periodic property of ambiguity integers and of the singularity of the system matrices is taken to reduce the amount of computation by at least a factor of  $n^{N-3}$  for a system of  $N$  beacons each of which has a possible integer set of size  $n$ . If the phase errors are independent, identically distributed Gaussian random variables, it is pointed out that the MLS method reduces to a maximum likelihood method.

#### REFERENCES

- [1] B. D. Steinberg, Principles of Aperture and Array System Design, Wiley, New York, 1976.
- [2] B. D. Steinberg, Microwave Imaging With Large Antenna Arrays: Radio Camera Principles and Techniques, Wiley, New York, 1983.
- [3] C. Nelson Dorn, "A Self-survey Technique for Self-cohering of Antenna Systems", IEEE Transactions on Antennas and Propagation, Vol. AP-26, No. 6, Nov. 1978, pp. 877-881.
- [4] C. Nelson Dorn and Bernard S. Meagher, Jr., "Cohering of an Experimental Non-rigid Array by Self-survey", IEEE Transactions on Antennas and Propagation, Vol. AP-28, No. 6, Nov. 1980, pp. 902-904.
- [5] Eu-Anne Lee, "Self-cohering of a Large Array", (Doctoral Dissertation), Report No. UP-VFRC-30-81, Moore School of Elec. Engr., Univ. of Pennsylvania, Philadelphia, PA 19104, Aug. 1981.
- [6] Dzekov, Tomislav, "Self-cohering by Self-survey of Large, Conformal Antenna Arrays", Zbornik Radova Jurema 24 (1979), 6 svezak, pp. 59-62.
- [7] Lu, Chung H., "Interference Cancellation in Self-cohering Arrays", (Doctoral Dissertation), Report No. UP-VFRC-19-80, Moore School of Elec. Engr., Univ. of Pennsylvania, Philadelphia, PA 19104, Aug. 1980.

August 1983

A GENERALIZED SELF-SURVEY TECHNIQUE

FOR SELF-COHERING OF LARGE ARRAYS\*

Eu-Anne Lee  
Ford Aerospace and  
Communications Corporation

and

C. Nelson Dornay  
Moore School of Elec. Engr.  
University of Pennsylvania

ABSTRACT

A technique is proposed for locating the elements of a flexible phased array sufficiently accurately to form high quality beams. The technique requires beacon signal phase measurements and baseline measurements, but does not require the accurate beacon-location knowledge which is characteristic of radio navigation schemes. The effects of phase measurement errors and baseline measurement errors on array beam gain and pointing error are predicted.

\*This work has been supported primarily by the Air Force Office of Scientific Research under grant AFOSR-78-3688.

## INTRODUCTION

A very large phased array can produce a very narrow beam which is useful for such functions as tracking, imaging, and direction finding. Self-cohering of such an array can be difficult because most large structures flex with time, and the array cannot be made rigid without excessive weight [1]. For example, the Valley Forge Research Center has constructed an X-band (3 cm wavelength) synthetic-aperture receive-only array consisting of 200 sample points distributed randomly over a 40 meter aperture on a suspended cable [2]. The elements are spaced randomly along the dimension perpendicular to the line of sight, with average sample-to-sample spacing of seven wavelengths, and the sample positions vary randomly from their design values by a wavelength or more in all three dimensions. A low frequency (75 MHz) signal is cabled to a stationary transmitter and to the receiving element. This signal is multiplied to X-band to provide the phase reference for both transmitter and receiver. A 300 m x 300 m target region on the ground at a range of seven kilometers is illuminated by narrow pulses from the transmitter with a beamwidth of 5°. Quadrature detection is used to measure the relative amplitude and phase of the target reflections at each element position as the receiver is transported along the cable. These measured phasors are processed digitally to form a high resolution image of the target region.

A new array is under construction, consisting of up to 256 real antenna elements placed randomly over a 100 meter diameter hillside region for imaging of airborne targets. This array will be approximately planar. In this array the low frequency reference signal will be passed through an

impedance-matched power divider, distributed by cable to the elements, then multiplied to X-band to provide the element phase references.

The motivation for this article is self-cohering of a large, very sparse, random conformal, receive-only phased array. A self-survey technique for self-cohering of a large array is introduced in [3] and demonstrated experimentally in [4]. That technique requires knowledge of the positions of a set of beacons. This article focuses on a generalized self-survey technique which does not require knowledge of the beacon positions. Although the technique is designed for sparse arrays in which mutual coupling can be ignored, it may prove to be useful in self-cohering of conventional phased arrays.

A two-dimensional radar image with high cross-range resolution requires a large aperture only in the cross-range dimension. Thus, a one-dimensional (or linear) array with a fan beam is appropriate. If the array is very large, the element positions cannot be controlled accurately. Such an array is illustrated in Figure 1. Since element position deviations perpendicular to the x-y plane have little effect on the beam, they can be ignored. Thus the array is essentially a two-dimensional array which forms beams in the plane of the array. It is such two-dimensional arrays which are the focus of the analysis in this article. It may be desirable in some applications to adjust the element positions in order to conform to some surface significantly different from a straight line. If most of the elements deviate from a straight line by less than 0.1 radian (as seen from the reference element) we refer to the array as an approximately linear array.

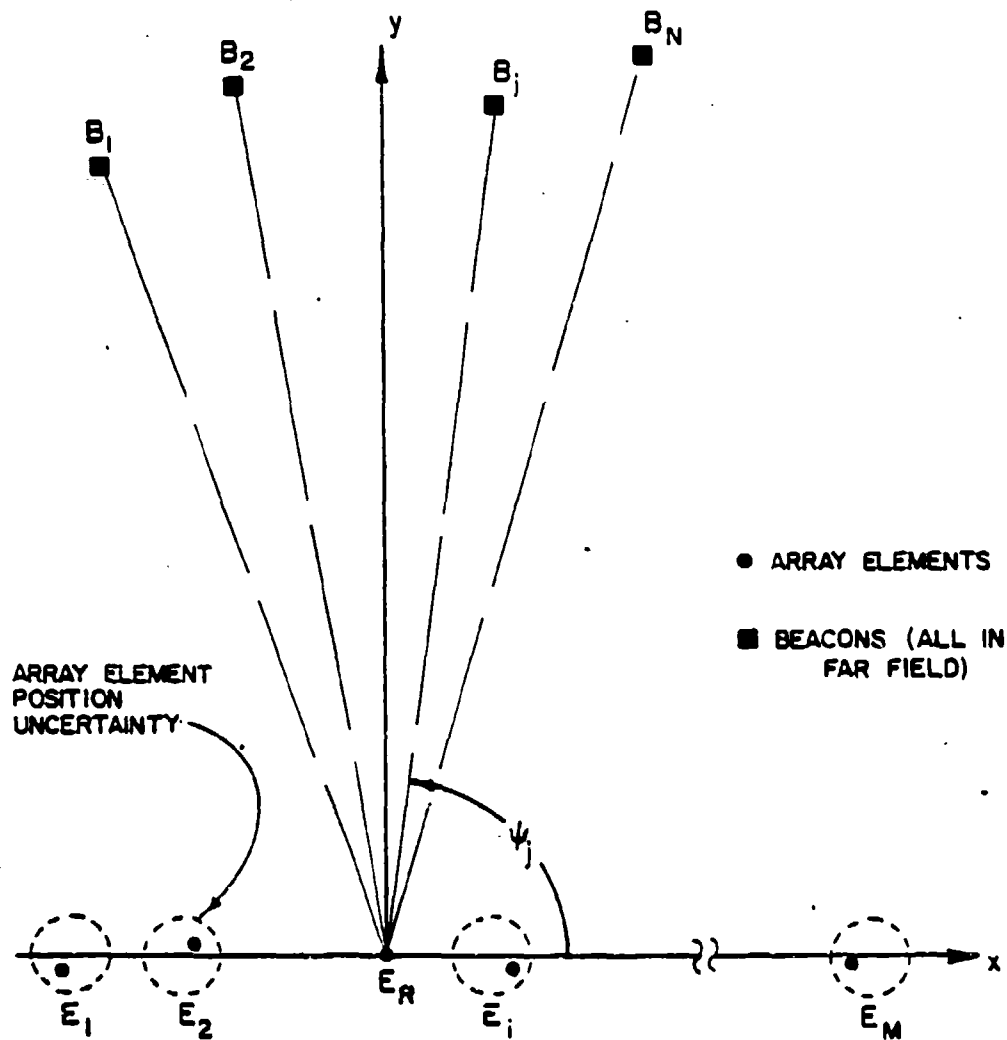


FIGURE 1 Array Geometry  
(Phase Reference Cables Not Shown)

Figure 1 shows a two-dimensional receive-only array which forms beams in the plane of the array. The system includes several microwave beacons in the far-field of the array. (These beacons can be passive point reflectors such as corner reflectors.) One of the array elements is selected as a phase reference element and as the origin of the coordinate system. Signals received at the reference element are transmitted by cable to each of the other elements of the array. We

measure the signal phase (relative to the cabled reference) at each array element, then phase shift and sum the measured phasors in order to compute the array output. The amount of phase shift required at each element in order to focus the beam is determined from the desired focal point, the array element positions, and the delays in the cables. The generalized self-survey technique uses simultaneously the phase measurements of the beacon signals at a subset of the array elements to determine the required array element positions and the cable delays. It also provides, as a byproduct, the beacon locations. The computed element positions and cable delays are then used to focus the array for tracking, imaging, or other purposes.

#### PHASE MULTILATERATION

The self-survey is basically a phase multilateration technique. It works as follows. The beacons are blinked consecutively. (If the beacons are passive, they must be at different ranges so the corresponding returns can be separated.) At each element of the array, the signals received from each beacon are compared in phase to the corresponding signals received at the reference element (see Fig. 1). The relations between the phase measurements and the geometry are identical with those described in [3]. That is, the phase  $P_{ij}$  of the  $j^{\text{th}}$  beacon signal received at element  $i$  relative to the corresponding beacon signal received at the reference element and delivered by cable to element  $i$  is

$$P_{ij} = k(x_j \cos \psi_j + y_j \sin \psi_j) + \phi_1 \quad (1)$$

where  $(x_i, y_i)$  represents the coordinates of the  $i^{\text{th}}$  element,  $\phi_i$  is the cable delay at the  $i^{\text{th}}$  element, and  $\psi_j$  is the angle of the  $j^{\text{th}}$  far-field beacon relative to the coordinate system;  $k = 2\pi/\lambda$ , where  $\lambda$  is the wavelength of the beacon signal. The measured phase difference corresponding to transmission from the  $j^{\text{th}}$  beacon is

$$\phi_{ij}^m = k(x_i^o \cos \psi_j^o + y_i^o \sin \psi_j^o) + \phi_i^o + \phi_{ij} - 2\pi n_{ij}^o \quad (2)$$

where  $\phi_{ij}$  is the phase deviation relative to free-space theory (owing to multipath, receiver noise, etc.) and  $n_{ij}$  is the number of multiples of  $2\pi$  removed by the mod- $2\pi$  measurement process. The superscript "o" denotes exact values of  $x_i$ ,  $y_i$ ,  $\psi_j$ ,  $\phi_i$ , and  $n_{ij}$ .

Two methods for determining the correct ambiguity integers  $\{n_{ij}^o\}$  are introduced in [5]. The first method tries each possible combination of integers  $\{n_{ij}\}$  which is consistent with the region of uncertainty, computes the least-square error of the self-survey solution corresponding to each set, and picks as the correct combination of integers the one with the smallest least-square error. The second method uses a sequence of increasing frequencies to progressively reduce the region of uncertainty until there is no ambiguity.

Suppose the phase ambiguity in each measurement (the uncertainty in  $n_{ij}$ ) has been removed. Define  $\phi_{ij}^{md} = \phi_{ij}^m + 2\pi n_{ij}^o$ . Then  $\phi_{ij}^{md}$  and  $P_{ij}$  are comparable quantities. Measurements of the form (2) for  $M$  beacons and  $N$  elements (not including the reference element) produce the equations

$$P_{ij}(x_i, y_i, \phi_i, \psi_j) = \phi_{ij}^{md} \quad i = 1, \dots, M, \quad j = 1, \dots, N \quad (3)$$

We solve these equations simultaneously in a least-square error sense.

That is, we pick the variables  $x_i$ ,  $y_i$ ,  $\phi_i$ , and  $\psi_j$  to minimize

$$V = \sum_{i=1}^M \sum_{j=1}^N [\phi_{ij}^{md} - p_{ij}]^2 \quad (4)$$

The minimum of  $V$  can be found by equating to zero the partial derivatives of  $V$  relative to  $x_i$ ,  $y_i$ ,  $\phi_i$ , and  $\psi_j$  for  $i = 1, \dots, M$ ,  $j = 1, \dots, N$ . It is shown in the next section that the resulting  $3M + N$  simultaneous nonlinear equations are not independent, but have a continuum of solutions. In order to remove the dependencies (or degrees of freedom) from the equations, a baseline element is defined (denoted the  $M^{\text{th}}$  element) and its coordinates  $x_M, y_M$  are measured separately from the self-survey process. The remaining  $(3M+N-2)$  equations are shown in (A-1) of the Appendix.

We can solve the equations simultaneously or we can process only a subset of the elements and beacons at one time. For  $M$  elements and  $N$  beacons treated simultaneously, we have  $(3M + N - 2)$  variables and  $MN$  measured values. The number of measurements must at least equal the number of unknowns in order that the equations adequately define the solution. Thus  $MN \geq 3M + N - 2$ , or  $M \geq (N - 2)/(N - 3)$ . It is apparent that the smallest number of beacons that can be included in the processing group is  $N = 4$ . The corresponding minimum number of elements is  $M = 2$ .

#### BASELINE VARIABLES

In this section we show that the equations for a two-dimensional array have two degrees of freedom--electrical freedom and rotational

freedom. Then we designate a pair of "baseline variables" which must be measured separately from the self-survey process in order to eliminate that freedom and produce a unique solution. Equation (1) can be written

$$P_{ij} = kr_1 \cos(\theta_1 - \psi_j) + \phi_1 \quad (5)$$

where  $(r_1, \theta_1)$  is the element position in polar coordinates. In this polar form it is easier to recognize special features associated with linear (or nearly linear) arrays. The freedom in the solution to the self-survey equations can be thought of as changes in the variables  $r_1, \theta_1, \phi_1, \psi_j$  which do not effect the phase measurements  $P_{ij}$ . If we rotate the whole system (array and beacons) around the origin of the coordinate system, the element positions and beacon directions change but the phase measurements  $P_{ij}$  remain the same. Thus, the solution to the equations has one degree of rotational freedom. We explore the degrees of freedom further for the case of a linear array ( $\theta_1 = \text{constant}$ ). Without loss of generality, we treat the case  $\theta_1 = 0$ . If we increment the variables in (5) by the arbitrary amounts  $\delta r_1$ ,  $\delta \theta_1$ ,  $\delta \psi_j$ , and  $\delta \phi_1$  and let  $\theta_1 = 0$ , the resulting change in  $P_{ij}$  satisfies

$$\begin{aligned} \frac{\delta P_{ij}}{kr_1} &= \cos \psi_j [\cos(\delta \psi_j - \delta \theta_1) - 1] - \sin \psi_j \sin(\delta \psi_j - \delta \theta_1) + \frac{\delta \phi_1}{kr_1} \\ &+ \frac{\delta r_1}{r_1} [\cos \psi_j \cos(\delta \psi_j - \delta \theta_1) - \sin \psi_j \sin(\delta \psi_j - \delta \theta_1)] \end{aligned} \quad (6)$$

Let  $\delta r_1 = 0$ ,  $\delta \phi_1 = 0$ , and  $\delta \theta_1 = \delta \psi_j$  for all  $i$  and  $j$ . This set of variable changes, which constitutes the above-mentioned geometric rotation, maintains  $\delta P_{ij} = 0$ . In order to remove the rotational freedom, we fix one of the variables; for example,  $\delta \theta_1 = 0$ .

The linearity of the array introduces a second degree of freedom. We now assume that  $\delta\theta_1 = 0$ , and  $\delta\phi_1 = 0$  for all  $i$ , and let  $\frac{\delta r_1}{r_1} = \frac{\delta r_1}{r_1}$  for all elements of the array (a pure stretch). According to (6) the array can be stretched without changing  $P_{1j}$  if

$$\begin{aligned} \frac{\delta P_{1j}}{kr_1} &= \cos\psi_j [\cos\delta\psi_j - 1] - \sin\psi_j \sin\delta\psi_j \\ &+ \frac{\delta r_1}{r_1} [\cos\psi_j \cos\delta\psi_j - \sin\psi_j \sin\delta\psi_j] = 0 \end{aligned}$$

or

$$\cos\psi_j \cos\delta\psi_j - \sin\psi_j \sin\delta\psi_j = \frac{\cos\psi_j}{1 + \delta r_1/r_1} \quad (7)$$

The nonlinear equation (7) can be solved, for each value of  $j$ , to yield a set of beacon position changes  $\{\delta\psi_j\}$  which will compensate for the array stretch. For small values of the stretch ratio  $\delta r_1/r_1$ , equation (7) is approximately linear in  $\delta\psi_j$  and can be solved in closed form:  $\delta\psi_j = (\delta r_1/r_1) \cot\psi_j$ . Computer simulations demonstrate that this stretch freedom is a degeneracy freedom which arises only if the array is exactly linear.

The existence of the unknown cable delay adds a third degree of freedom. Suppose that the array is linear ( $\theta_1=0$ ), that  $\delta\theta_1 = 0$  and  $\delta r_1 = 0$  (no rotation or stretch), and introduce a phase tilt into the cable delays:  $\delta\phi_1/kr_1 = \delta\phi_1/kr_1$  for all  $i$ . This phase tilt can be compensated for by beacon position changes  $\{\delta\psi_j\}$  which satisfy

$$\frac{\delta P_{1j}}{kr_1} = \cos\psi_j [\cos\delta\psi_j - 1] - \sin\psi_j \sin\delta\psi_j + \delta\phi_1/kr_1 = 0 \quad (8)$$

For small tilt factors  $\delta\phi_1/kr_1$ , (8) is approximately linear in  $\delta\psi_j$ , and  $\delta\psi_j = \delta\phi_1/kr_1 \sin\psi_j$ . Computer simulations show that this electrical freedom

also exists for arrays which are not linear, although the resulting freedom is then more complicated than a pure phase tilt.

In summary, the self-survey equations for a two-dimensional array have two degrees of freedom, rotational freedom (inherent in the geometry) and electrical freedom (introduced by the cable delay). If the array is exactly linear, the geometry introduces a third (stretch) freedom.

Computer simulations demonstrate that, except for a perfectly linear array, fixing two appropriate variables in the equations will produce a unique solution. It is probably most convenient to designate one element of the array as the baseline element and measure its coordinates relative to the reference element. In this article we assume such a baseline has been defined and that its coordinates  $(x_M, y_M)$  have been measured separately from the self-survey process.

#### CONVERGENCE PROPERTIES

The nonlinear equations (A-1) of the Appendix have been solved by Newton's iterative method for a variety of geometries, using 50 different sets of initial estimates for each geometry [6]. Each set of initial estimates consisted of element coordinates which deviated 1 to 6 wavelengths from the true values, beacon angles which deviated 1 to 4 array beamwidths from the true values, and arbitrarily chosen values for cable delays. The Newton iteration consistently converged to within 4 significant digits of the correct solution within 3 or 4 iterations for initial estimates which consisted of element coordinates within 3 wavelengths of the true values, beacon angles within 3 beamwidths of the true values, and arbitrary values for cable delays [7]. Since the mod- $2\pi$  ambiguities are assumed

to be been resolved, the remaining uncertainty in each element location is less than one wavelength. Consequently, the initial estimate associated with each element location lies well within the 3 wavelength convergence radius.

The good convergence properties described above assume adequate accuracy in the computations. For a given array size, if the beacons are too closely spaced the equations will be ill-conditioned. The beacon separation, expressed in array beamwidths, is a measure of the equation conditioning. The more ill-conditioned the equations, the more precision is needed for accurate computation. Thus, if the target field of view is very narrow, the array must be very large (the beamwidth small) in order to permit accurate computation with limited computer precision. For example, computer simulations of four-beacon geometries with a sixteen-digit computer showed that a minimum interbeacon spacing of twenty-eight beamwidths was required to guarantee that the round-off errors would not affect convergence.

#### TOLERANCE TO MEASUREMENT ERRORS

The estimates of element position  $(x_1, y_1)$  and cable delay  $\phi_1$  provided by the generalized self-survey technique described above will be in error because of the errors in the beacon signal phase measurements and the errors in the baseline measurements. These errors in the self-survey, in turn, cause errors in beam formation. The self-survey is carried out primarily to achieve beamforming. Therefore we focus on the beamforming phase errors rather than the errors in the element positions and cable delays.

The vector of unknowns is

$$X = [x_1, y_1, \phi_1, \dots, x_{M-1}, y_{M-1}, \phi_{M-1}, \phi_M, \psi_1, \dots, \psi_N]^T \quad (9)$$

Note that  $x_M, y_M$  are missing in (9) because the coordinates of a baseline element, denoted by  $(x_M, y_M)$ , are measured separately from the self-survey in order that the algorithm produce a unique solution.

Let  $X_M$  denote the baseline column vector  $[x_M, y_M]^T$  and  $\phi$  the vector of phase measurements  $\phi_{ij}^{md}$  in (3).

In order to find the relationship between the errors  $dX$  in the solution and the measurement errors  $\phi$  and  $dX_M$  which cause them, under the assumption that the errors are small, we take the total differentials of the nonlinear equations  $\{g_p(X) = 0\}$  in (A-1) of the Appendix. Specifically, we take the differentials of  $\{g_p(X)\}$  with respect to the variables  $x_1, y_1, \psi_j, \phi_1$  and  $\phi_{ij}^{md}$  and evaluate all the variables at their error-free values. The resulting equations, which are linear in the error variables, can be expressed in the matrix form

$$dX = -H^{-1}F\phi - H^{-1}LdX_M \quad (10)$$

where  $dX = [dx_1, dy_1, d\phi_1, \dots, d\psi_N]^T$ ,  $dX_M = [dx_M, dy_M]^T$ ,  $\phi = [\phi_{11}, \phi_{12}, \dots, \phi_{MN}]^T$  and  $\phi_{ij}$  is the error in  $\phi_{ij}^{md}$ .

The elements of the matrix  $H$  are partial derivatives of the functions  $\{g_p(X)\}$  relative to the unknown parameters in  $X$ .  $F$  consists of the partial derivatives of the functions  $\{g_p\}$  relative to the phase measurement errors  $\{\phi_{ij}\}$ .  $L$  consists of the partial derivatives of the functions  $\{g_p\}$  relative to the baseline coordinates  $(x_M, y_M)$ . The detailed expressions for  $H$ ,  $F$ , and  $L$  are given in the Appendix.

In order to steer the beam formed by the array to the angle  $\psi$ , the signal received at element  $i$  must be phase-shifted by an amount  $P_i = k(x_i \cos \psi + y_i \sin \psi) + \phi_i$ . The error  $\delta P_i$  in this phase shift owing to those self-survey errors which are associated with element  $i$  can be represented by

$$\delta P_i = R dX_i \quad i = 1, \dots, M \quad (11)$$

where  $R = [k \cos \psi, k \sin \psi, 1]$  and  $dX_i = [dx_i, dy_i, d\phi_i]^T$ . In the Appendix we derive the following structural form for  $\delta P_i$ , the beamforming phase error at element  $i$ :

$$\delta P_i = [\alpha_1, \dots, \alpha_N] \begin{bmatrix} \phi_{i1} \\ \vdots \\ \phi_{iN} \end{bmatrix} + kr_i [\beta_{i1p}, \dots, \beta_{iMN}] \begin{bmatrix} \phi_{11} \\ \vdots \\ \phi_{MN} \end{bmatrix} + kr_i [\gamma_{i1}, \gamma_{i2}] \begin{bmatrix} dx_M \\ dy_M \end{bmatrix} \quad (12)$$

where the variable  $r_i$  is the distance of the  $i^{\text{th}}$  element from the origin of the coordinate system, and  $k$  is the wave number;  $\alpha_j$ ,  $\beta_{iqj}$ , and  $\gamma_{ip}$  are complicated functions of the variables. The subscript  $i$  refers to the element at which the phase error  $\delta P_i$  occurs during beamforming. The subscript  $q$  refers to the element at which the phase measurement error  $\phi_{qj}$  occurs during the self survey phase measurement process. The subscript  $j$  refers to the beacon associated with the phase measurement error  $\phi_{qj}$ . The subscript  $p$  refers to the error in the  $p^{\text{th}}$  coordinate of the baseline element.

In most applications intended for two-dimensional radar imaging the array will be linear or approximately linear, as discussed in the introduction. It can be shown that for a linear array  $\beta_{iqj}$  and  $\gamma_{ip}$  are independent of  $i$  [7]. In the succeeding tolerance analysis we focus on the linear array and drop the subscript  $i$  from these coefficients. In the

case of the linear array, equation (12) can be written in the form

$$\delta P_1 = \delta P_{1G} + kr_1 \delta P_P + kr_1 \delta P_B \quad (13)$$

where the subscripts G, P, and B are used to imply that the three terms of (13) lead to reduced gain, pointing error, and baseline-induced pointing error, respectively, as described below. The error phenomena are determined primarily by the  $k$  and  $r_1$  structure of (12). This structure is derived in the Appendix.

#### PHASE-INDUCED GAIN REDUCTION

Detailed examination of the matrices involved in (10) and (11) shows that the coefficients  $\alpha_j$  depend only on the beacon distribution  $\{\psi_j\}$  and the beamforming angle  $\psi$ , and are independent of the array geometry and the wave number  $k$  (Appendix). The first term of (12) involves the phase measurement errors associated only with element 1. Since the coefficients  $\{\alpha_j\}$  are identical for all array elements and the phase errors  $\phi_{1j}$  which multiply the  $\alpha_j$  vary randomly from element to element,  $\delta P_{1G}$  represents a beamforming phase error which is random across the array. According to [8], such beamforming phase errors result primarily in reduction in the expected gain of the main beam. Assume the phase measurement errors  $\{\phi_{1j}\}$  are independent, zero mean, and identically distributed, with variance  $\sigma_\phi^2$ . Then  $\delta P_{1G}$  is zero mean with variance  $\sigma_G^2 = \alpha^2 \sigma_\phi^2$ , where  $\alpha^2 \triangleq \sum_{j=1}^N \alpha_j^2$ . The expected reduction in gain is  $\exp(-\sigma_G^2)$ ; if  $\sigma_G < 0.5$  radian, the expected reduction in gain owing to the phase errors will be less than 1 dB [8]. A typical curve of  $\alpha$  as a function of beamforming angle is given in Figure 2. It can be shown that for most distributions of the beacons,

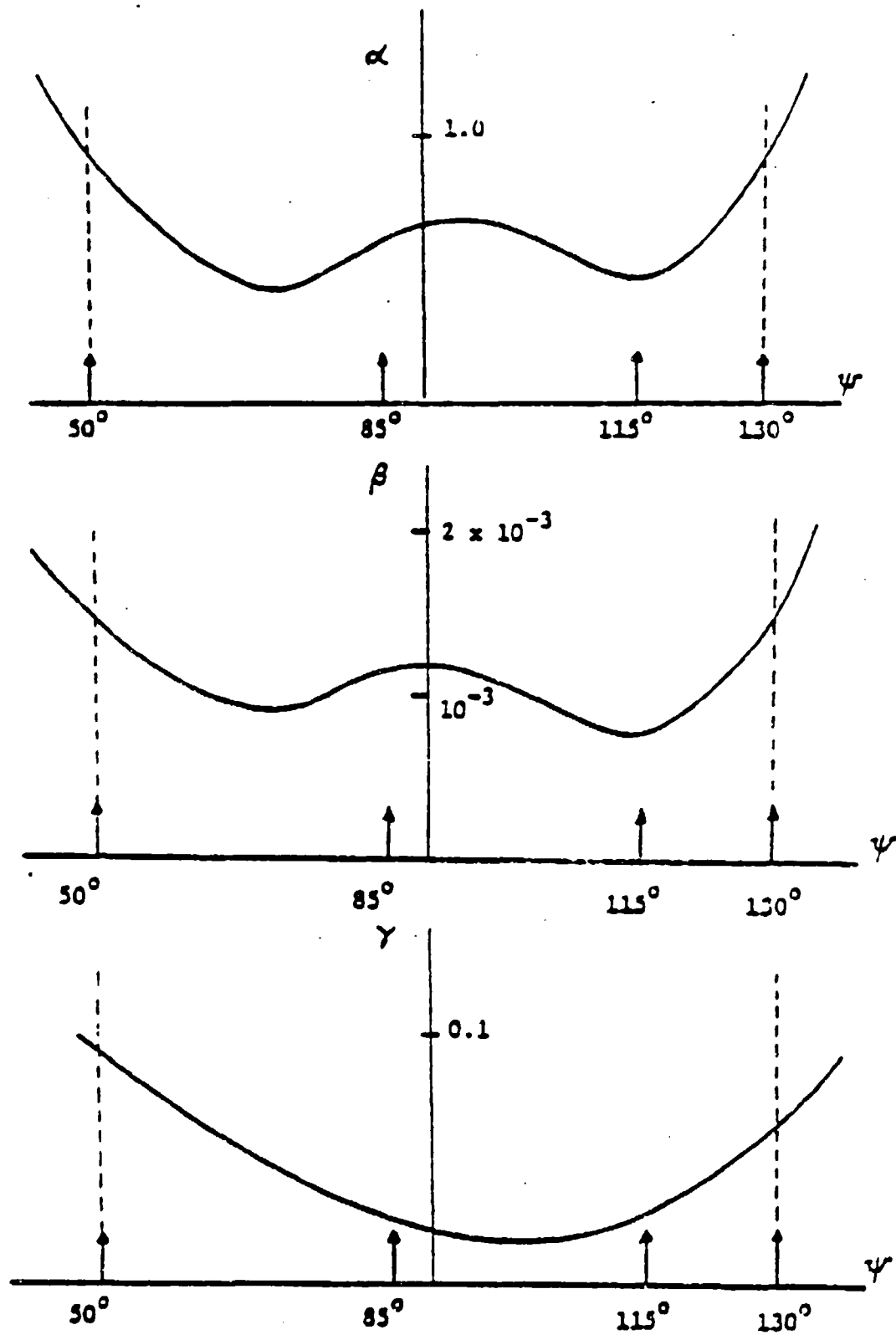


FIGURE 2 Sensitivity Factors  $\alpha$ ,  $\beta$ , and  $\gamma$   
 "↑" indicates beacon location

$\alpha \leq 1$  for beam pointing directions within the spread of the beacons [3,7]. Consequently  $\sigma_G \leq \sigma_\phi$ . For certain poor distributions of the beacons, such as those for which beacons are bunched into two regions, the value of  $\alpha$  can grow large for all pointing angles except those in the angular spread of each bunch. We refer to this magnification of measurement errors owing to poor beacon geometry as geometric dilution of precision (GDOP).

#### PHASE-INDUCED POINTING ERROR

The Appendix shows that the second term of (12) is proportional to  $r_1$  and independent of  $k$ . The factor  $kr_1$  is removed in (12), leaving  $\beta_{iqj}$  proportional to  $\lambda$ ;  $\beta_{iqj}$  also depends on the beacon distribution, the beam-forming angle, and the array geometry. Each coefficient  $\beta_{iqj}$  includes a factor of the form  $r_q U$ , where  $r_q$  is the radius to the  $q^{\text{th}}$  element and  $U$  is shown in (A-13). Consequently,  $\beta_{iqj}$  is inversely proportional to the array size. That is, if all dimensions of the array are doubled, each  $\beta_{iqj}$  will be halved. If the array is linear, it can be shown that  $\beta_{iqj} \propto \beta_{qj}$ . Under the previously mentioned assumptions concerning the random phase errors  $\{\phi_{qj}\}$ , the pointing error  $\delta P_p$  is zero mean with variance  $\sigma_p^2 = \beta^2 \sigma_\phi^2$ , where  $\beta^2 = \sum_{q=1}^{MN} \beta_q^2$ . A typical curve of  $\beta$  versus beam pointing angle  $\psi$  is shown in Figure 2. We computed  $\beta(\psi)$  for 50 randomly selected geometries, each consisting of 4 beacon positions and 6 element positions; the elements in each geometry formed a linear array. The simulations consistently showed that for pointing directions  $\psi$  within the spread of the beacons,  $\beta \leq 0.3 \lambda/L$ , where  $L$  is the length of the array. Thus, we expect  $\beta$  to be significantly smaller than the array beamwidth. It follows that the standard deviation in pointing error owing to phase measurement error can be expected to satisfy  $\sigma_p \leq 0.3 \frac{\lambda}{L} \sigma_\phi$ . In practice, the array elements would be surveyed in groups of 6, each group forming a subarray of about the same length ( $L$ ) and using the same baseline.

## BASELINE-INDUCED POINTING ERROR

The third term of (12) pertains to baseline measurement errors. The Appendix shows that the third term of (12) is proportional to  $kr_1$ . The coefficient  $\gamma_{ip}$  depends on the beacon distribution, the beamforming angle, and the array geometry, but is independent of wavelength;  $\gamma_{ip}$  includes a factor of the form  $r_M U$ , where  $r_M$  is the length of the baseline and  $U$  is shown in (A-13). Therefore,  $\gamma_{ip}$  is inversely proportional to array size  $L$ . If the array is linear, it can be shown that  $\gamma_{ip} \rightarrow \gamma_P$ . The baseline errors  $\{dx_M, dy_M\}$  are also independent of  $i$ . Therefore, if the array is linear the third term of (12) produces a phase tilt across the array, and thus a pure pointing error in the beam. It is interesting that even a pure stretch error in the baseline ( $\delta y_M = 0$ ) causes a pure pointing error in the linear array.

Assume the baseline measurement errors  $dx_M$  and  $dy_M$  are independent, zero mean, and identically distributed with variance  $\sigma_x^2$ . The resulting baseline-induced pointing error  $\delta P_B$  is then zero mean with variance  $\sigma_B^2 = \gamma^2 \sigma_x^2$ , where  $\gamma^2 = \sum_{j=1}^2 \gamma_P^2$ . We computed  $\gamma(\psi)$  for the 50 randomly selected linear array geometries described earlier. A typical result is shown in Figure 2. The simulations show that for pointing directions within the spread of the beacons,  $\gamma \leq \sqrt{2}/L$ , consequently,  $\sigma_B \leq \sqrt{2} \sigma_x / L$ .

If the same baseline is used in self-survey of each subset of elements of the array, and if the length of each subset is approximately the baseline length, then the resulting pointing error in the full array will be essentially the one predicted by  $\delta P_B$  (with variance  $\sigma_B^2$ ). The pointing error does not apply randomly to each pointing direction. Rather, the pointing error will typically exhibit a smooth unimodal change as the beam is scanned across the target [4]. Thus a target will be stretched or shrunk according to its position within the spread of

the beacons. The total stretch (or shrinking) of the whole beacon spread is in the order of  $\sigma_B$ . Similar comments can be made concerning phase-induced pointing error; in the imaging process, after the self-survey has been completed, it typically exhibits a smooth unimodal variation across the array.

#### ERROR TOLERANCE SUMMARY

In sum, we make the following conclusions concerning an array which is self-cohered by the generalized self-survey technique described in this article. Only four beacons are required. We assume the self-cohered array is used for beamforming or imaging only within the spread of the beacons. For any reasonably uniform distribution of these beacons, the errors in beacon phase measurements and in baseline measurements cause limited gain reduction and pointing error during imaging. The gain reduction and pointing error vary smoothly and unimodally across the imaged region. Consequently, the image of a target of somewhat limited extent is slightly stretched or shrunk, and the intensity relative to sidelobe artifacts is slightly reduced. If the array is linear (or approximately linear) the gain reduction is due primarily to the beacon phase measurement errors. The expected gain reduction factor is  $\exp(-\sigma_\phi^2)$ , where  $\sigma_\phi^2$  is the variance of the beacon phase measurement errors. For the linear (or approximately linear) array the pointing error has two statistically independent components, caused by the beacon phase measurement errors and baseline measurement errors, respectively. The standard deviations of these two components are

$$\sigma_p = 0.3 \frac{\lambda}{L} \sigma_\phi \quad \text{and} \quad \sigma_B = \sqrt{2} \frac{\sigma_x}{L} \quad (14)$$

where  $L$  is the array size,  $\lambda$  is the wavelength, and  $\sigma_x$  is the standard deviation in each component of the baseline measurement error. Suppose  $\sigma_\phi = 0.5$  radian,  $L = 1000\lambda$ , and  $\sigma_x = \lambda$ . Then the expected reduction in gain owing to self-survey errors would be 1 dB and the corresponding standard deviation in pointing error would be 1.4 mrad (1.4 beamwidths).

The phase errors in the target data used for imaging are not included in this analysis. These additional phase errors, if random across the array, would lead to additional gain reduction. If the array were not approximately linear, the second and third terms of (12) would also lead to some beam defocusing and gain reduction in addition to the pointing error.

#### EXTENSIONS

Reference [7] shows that the standard deviation  $\sigma_\psi$  of the errors in the computed values of the beacon angles, owing to the measurement errors, satisfies

$$\sigma_\psi^2 \leq \left(0.3 \frac{\lambda}{L} \sigma_\phi\right)^2 + \left(\sqrt{2} \frac{\sigma_x}{L}\right)^2 \quad (15)$$

This result may be useful in certain direction-finding applications. Reference [7] also describes the extension of the self-survey process to a three-dimensional geometry. The three-dimensional equations result in more degrees of freedom (baseline variables) than the two associated with the two-dimensional equations. The convergence properties and the tolerance relationships for the three-dimensional system have not been thoroughly analyzed, but are expected to be similar to those of the two-dimensional system.

#### EXPERIMENTAL SELF-SURVEY

The self-survey algorithm has been extended to near-field, synthetic aperture-systems and used to successfully cohere experimental X-band (3 cm) synthetic aperture radar data [9]. The experiment used seven randomly selected synthetic aperture element positions spread over a linear 27 m aperture. Reflections from four corner reflectors in different range bins at a range of approximately 250 m were used as beacon signals. The element positions were measured to within about  $1/3$  wavelength. The beacon (corner reflector) positions were measured to within about 1.3 wavelengths. One of the element positions was selected as the reference element and for each beacon its round trip phase delay was subtracted from the round trip phase delays at six other elements in order to obtain phase delays relative to the reference element. These differential phase delays were used in the self-survey algorithm to compute the six-element positions. The six-element array (plus reference) was used to image the neighborhood of one of the corner reflectors using only the measured element positions, resulting in a poor image with sidelobes higher than the main lobe. The imaging process was repeated using the element positions computed by the self-survey process. The latter image was essentially the image expected from a perfectly surveyed seven-element random array. The direction of the image was shifted from the measured target direction by an amount essentially equal to that predicted by (14).

## SUMMARY

A phase multilateration scheme is used to locate the elements of a very large, very sparse, poorly surveyed array with sufficient accuracy to permit formation of high quality beams. The scheme requires phase measurement, at each element, of the signals from each of four point targets or beacons. These target signals must be separable in time (or range). The scheme also requires measurement of the location of a baseline element. Errors in these self survey phase measurements and baseline measurements lead to gain loss and pointing error during beam formation. The expected loss and pointing error are derived for the typical case of an approximately linear array. These errors do not cause serious image distortions for beam pointing directions within the spread of the beacons. These conclusions have been verified experimentally with synthetic aperture radar data.

## REFERENCES

- [1] Steinberg, Bernard D., "Design Approach for a High-Resolution Microwave Imaging Radio Camera," J. Franklin Institute, Vol. 296, No. 6, December 1973, pp. 415-432.
- [2] Steinberg, B. D., Microwave Imaging With Large Antenna Arrays: Radio Camera Principles and Techniques, Wiley, New York, 1983.
- [3] Dorny, C. Nelson, "A Self-Survey Technique for Self-Cohering of Antenna Systems," IEEE Transactions on Antennas and Propagation, November 1978, pp. 877-881.
- [4] Dorny, C. Nelson and Bernard S. Meagher, Jr., "Cohering of an Experimental Nonrigid Array by Self-Survey," IEEE Transactions on Antennas and Propagation, November 1980, pp. 902-904.
- [5] Lu, Chung H. and C. Nelson Dorny, "Ambiguity Resolution in Self-Cohering Arrays," Report UP-VFRC-4-83, Valley Forge Research Center, University of Pennsylvania, Philadelphia, Pennsylvania, 1983. (Submitted to IEEE Trans. AP-S)
- [6] Dorny, C. Nelson, A Vector Space Approach to Models and Optimization, New York, 1975, pp. 474-483.
- [7] Lee, Eu-Anne, "A Generalized Self-Survey Technique for Self-Cohering of a Large Array," Doctoral Dissertation, (also a Report UP-VFRC-30-81, Valley Forge Research Center), The Moore School of Electrical Engineering, University of Pennsylvania, Philadelphia, Pennsylvania, 1981.
- [8] Steinberg, Bernard D., Principles of Aperture and Array System Design, Wiley, New York, 1976, pp. 305-309.
- [9] Lei, TianHu and C. Nelson Dorny, "Synthetic Aperture Near-Field Self-Survey", Valley Forge Research Center QPR No. 42, University of Pennsylvania, Philadelphia, Pennsylvania, March 1983.

# APPENDIX - STRUCTURE OF EQUATION (12)

The self-survey equations are obtained by equating to zero the partial derivatives of (4) with respect to  $x_i, y_i (i=1, \dots, M-1); \phi_i (i=1, \dots, M);$  and  $\psi_j (j=1, \dots, N)$ . These four sets of equations are:

$$g_i = \sum_{j=1}^N (\phi_{ij}^{md} - kx_i \cos \psi_j - ky_i \sin \psi_j - \phi_i) (k \cos \psi_j) = 0, \quad i=1, \dots, (M-1)$$

$$g_{(i+M-1)} = \sum_{j=1}^N (\phi_{ij}^{md} - kx_i \cos \psi_j - ky_i \sin \psi_j - \phi_i) (k \sin \psi_j) = 0, \quad i=1, \dots, (M-1)$$

$$g_{(i+2M-2)} = \sum_{j=1}^N (\phi_{ij}^{md} - kx_i \cos \psi_j - ky_i \sin \psi_j - \phi_i) = 0, \quad i=1, \dots, M \quad (A-1)$$

$$g_{(j+3M-2)} = \sum_{i=1}^M (\phi_{ij}^{md} - kx_i \cos \psi_j - ky_i \sin \psi_j - \phi_i) (kx_i \sin \psi_j - ky_i \cos \psi_j) = 0, \\ j=1, \dots, N$$

The tolerance equations consist in the total differentials of the equations (A-1) subject to the conditions  $\phi_{ij}^{md} = k(x_i \cos \psi_j + y_i \sin \psi_j) + \phi_i$ . They can be written in the matrix form

$$H dX + F \phi + L dX_M = 0 \quad (A-2)$$

where  $dX = (dx_1, dy_1, d\phi_1, \dots, dx_{M-1}, dy_{M-1}, d\phi_{M-1}, d\phi_M, d\psi_1, \dots, d\psi_N), dX_M = (dx_M, dy_M),$  and  $\phi = (\phi_{11}, \dots, \phi_{MN})$ . The tolerance results in this paper require determination of the  $k$  and  $r_1$  structure of (10) where  $r_1$  is the radial coordinate of element 1. This Appendix presents the  $k$  and  $r_1$  structure of  $H^{-1}, F,$  and  $L$ .  $H$  can be partitioned in the form

$$H = \begin{bmatrix} A & B \\ C & D \end{bmatrix} \quad (A-3)$$

where A and D are square and invertible. Then

$$H^{-1} = \begin{bmatrix} A^{-1} + A^{-1}B(D-CA^{-1}B)^{-1}CA^{-1} & A^{-1}B(D-CA^{-1}B)^{-1} \\ -(D-CA^{-1}B)^{-1}CA^{-1} & (D-CA^{-1}B)^{-1} \end{bmatrix} \quad (A-4)$$

We show only the structure of  $k$  and  $r_1$  in each of the following matrices. Blank entries are zero. Each non-zero element includes an additional trigonometric factor which depends on beacon angles and element position angles. Signs of entries are ignored. Equality of two entries does not imply equality of the corresponding undisplayed trigonometric factors. The detailed derivation of the matrix structures is given in [6]. The derivation makes use of the relation  $x_1 \sin \psi_j - y_1 \cos \psi_j = r_1 \sin(\psi_j - \theta_1)$ .

$$A = \begin{bmatrix} \begin{array}{ccc|ccc} k^2 & k^2 & k & & & \\ & & & k^2 & k^2 & k \\ & & & & & \\ & & & & & \\ & & & & & \\ & & & & & \end{array} & \begin{array}{ccc} k^2 & k^2 & k \\ k^2 & k^2 & k \\ & & \\ & & \\ & & \\ & & \end{array} \\ \hline \begin{array}{ccc|ccc} k & k & 1 & & & \\ & & & k & k & 1 \\ & & & & & \\ & & & & & \\ & & & & & \\ & & & & & \end{array} & \begin{array}{ccc} k & k & 1 \\ k & k & 1 \\ & & \\ & & \\ & & \\ & & \end{array} \\ \hline & 1 \end{bmatrix} \quad \begin{array}{l} M-1 \\ \\ M-1 \\ \\ M-1 \end{array} \quad (A-5)$$

$$A^{-1} = \begin{bmatrix} 1/k^2 & & 1/k^2 & & 1/k & & \\ 1/k^2 & & 1/k^2 & & 1/k & & \\ 1/k & & 1/k & & 1 & & \\ \hline & 1/k^2 & & 1/k^2 & & 1/k & \\ & 1/k^2 & & 1/k^2 & & 1/k & \\ & 1/k & & 1/k & & 1 & \\ & \vdots & & \vdots & & \vdots & \\ & \vdots & & \vdots & & \vdots & \\ \hline & \underbrace{\hspace{2cm}}_{M-1} & & \underbrace{\hspace{2cm}}_{M-1} & & \underbrace{\hspace{2cm}}_{M-1} & 1 \end{bmatrix} \quad \begin{matrix} M-1 \\ \text{sets} \end{matrix} \quad (A-6)$$

$$B = \begin{bmatrix} k^2 r_1 & \dots & k^2 r_1 & & \\ \vdots & & & & \\ \vdots & & & & \\ \hline k^2 r_{M-1} & \dots & k^2 r_{M-1} & & \\ \hline k^2 r_1 & \dots & k^2 r_1 & & \\ \vdots & & & & \\ \vdots & & & & \\ \hline k^2 r_{M-1} & \dots & k^2 r_{M-1} & & \\ \hline kr_1 & \dots & kr_1 & & \\ \vdots & & & & \\ \vdots & & & & \\ \hline kr_{M-1} & \dots & kr_{M-1} & & \\ \hline kr_M & & & & kr_M \end{bmatrix} \quad \begin{matrix} M-1 \\ \\ M-1 \\ \\ M-1 \\ 1 \end{matrix} \quad (A-7)$$

N

$$C = \left[ \begin{array}{ccc|c|ccc|c} k^2_{r_1} & k^2_{r_1} & kr_1 & & k^2_{r_{M-1}} & k^2_{r_{M-1}} & kr_{M-1} & kr_M \\ \vdots & \vdots & \vdots & \dots & \vdots & \vdots & \vdots & \vdots \\ k^2_{r_1} & k^2_{r_1} & kr_1 & & k^2_{r_{M-1}} & k^2_{r_{M-1}} & kr_{M-1} & kr_M \end{array} \right] \quad \left. \vphantom{\begin{array}{c} \\ \\ \end{array}} \right\} N \quad (A-8)$$

$\underbrace{\hspace{15em}}_{M-1 \text{ sets}} \quad \underbrace{\hspace{2em}}_1$

$$D = \left[ \begin{array}{c} \sum_{i=1}^M k^2_{r_1} \\ \vdots \\ \sum_{i=1}^M k^2_{r_1} \end{array} \right] \quad \left. \vphantom{\begin{array}{c} \\ \\ \end{array}} \right\} N \quad (A-9)$$

$$\begin{array}{c}
 \begin{array}{c}
 \text{N} \\
 \underbrace{\hspace{1.5cm}} \\
 \begin{array}{|c|c|c|c|}
 \hline
 k \dots k & & & \\
 \hline
 & k \dots k & & \\
 \hline
 & & \ddots & \\
 \hline
 & & & k \dots k \\
 \hline
 k \dots k & & & \\
 \hline
 & k \dots k & & \\
 \hline
 & & \ddots & \\
 \hline
 & & & k \dots k \\
 \hline
 1 \dots 1 & & & \\
 \hline
 & 1 \dots 1 & & \\
 \hline
 & & \ddots & \\
 \hline
 & & & 1 \dots 1 \\
 \hline
 & & & & 1 \dots 1 \\
 \hline
 kr_1 & & & kr_{M-1} & kr_M \\
 \hline
 & & & \ddots & \ddots \\
 \hline
 & & & kr_{M-1} & kr_M \\
 \hline
 \end{array}
 \end{array}
 \end{array}
 \begin{array}{c}
 \left. \begin{array}{c} \\ \\ \\ \\ \\ \end{array} \right\} \begin{array}{c} M-1 \\ \\ \\ \\ 1 \\ M-1 \end{array}
 \end{array}
 \quad (A-10)$$

$\underbrace{\hspace{15cm}}$   
 M sets of N each

$$L = \begin{array}{cc} \left. \begin{array}{c} 0 \quad 0 \\ \vdots \quad \vdots \\ 0 \quad 0 \end{array} \right\} 3(M-1) \\ \hline k \quad k \quad \left. \right\} 1 \\ \hline \left. \begin{array}{cc} k^2 r_M^2 & k^2 r_M^2 \\ \vdots & \vdots \\ k^2 r_M^2 & k^2 r_M^2 \end{array} \right\} N \\ \hline \underbrace{\hspace{10em}}_2 \end{array} \quad (A-11)$$

It follows that

$$C A^{-1} B = \left[ \begin{array}{ccc} k^2 \sum_{i=1}^M r_i^2 & \dots & k^2 \sum_{i=1}^M r_i^2 \\ \vdots & & \vdots \\ k^2 \sum_{i=1}^M r_i^2 & \dots & k^2 \sum_{i=1}^M r_i^2 \end{array} \right] \quad N \quad (A-12)$$

where each term in each sum has an undisplayed trigonometric factor. Therefore we conclude that each element of  $(D-CA^{-1}B)^{-1}$  is of the form  $U/k^2$ , where

$$U = \frac{\text{sum of products of order } (N-1) \text{ in } \sum_{i=1}^M r_i^2}{\text{sum of products of order } (N) \text{ in } \sum_{i=1}^M r_i^2} \quad (A-13)$$

For purposes of this article we care only about the first  $3M-2$  elements of  $dX$ ; these are determined by the two upper blocks of  $H^{-1}$ . Thus, if  $dX_1 \triangleq (dx_1, dy_1, d\phi_1)$ ,  $R \triangleq (k\cos\psi, k\sin\psi, 1)$ , and  $\delta P_1 \triangleq RdX_1$ , then

$$\delta P_1 = -R(A^{-1}; 0)_1(F\phi + LdX_m) - R(TCA^{-1}; T)_1(F\phi + LdX_m) \quad (A-14)$$

where the matrix subscript 1 denotes the  $1^{th}$  3-row submatrix, and  $T \triangleq A^{-1}B(D-CA^{-1}B)^{-1}$ . Note that  $(A^{-1}; 0)_1 L = 0$ , and that

$$(A^{-1}; 0)_1 F = \begin{bmatrix} 1/k & \dots & 1/k \\ 0 & 1/k & \dots & 1/k & 0 \\ 1 & \dots & 1 \end{bmatrix}$$

$1^{th}$  N-column submatrix

Therefore the first of the two terms in (A-14) is a linear combination of  $(\phi_{11} \dots \phi_{1N})$  as in the first term of (12);  $\alpha_j$  is independent of  $k$  and  $r_1$ , but includes a trigonometric factor involving  $\psi$ ,  $\{\psi_j\}$ , and  $\{\theta_1\}$ . The  $1^{th}$  3-row submatrix of the factor  $A^{-1}B$  in  $T$  is proportional to  $r_1$ . Therefore, the second of the two terms in (A-14) has a linear factor  $r_1$ . Examination of the matrix products in the second term of (A-14) shows that the portion associated with  $\phi$  is independent of  $k$  and the portion associated with  $dX_m$  is linear in  $k$ . Thus the form of (12) is established. Each of the coefficients  $\beta_{1qj}$  and  $\gamma_{1p}$  in (12) includes a factor of the form  $r_q U/k$  and a trigonometric factor involving  $\psi$ ,  $\{\psi_j\}$ , and  $\{\theta_1\}$ . Each of the coefficients  $\gamma_{1p}$  includes a factor of the form  $r_M U$  and a trigonometric factor involving  $\psi$ ,  $\{\psi_j\}$ , and  $\{\theta_1\}$ .

## 5. SYNTHETIC APERTURE NEAR-FIELD SELF-SURVEY\*

C. Nelson Dorny

Tianhu Lei

In previous articles we have described a general self-survey technique for self-cohering of nonrigid antenna systems [1]. In this article we extend that work to synthetic aperture systems and to near-field targets. We also demonstrate the capability of the technique with real synthetic aperture radar data.

### Near-Field Bistatic Receive-Only Array

Figure 5.1 defines the geometry of a random array and near-field point reflectors. The coordinates of the array elements and the point reflectors are known approximately, but not to the accuracy ( $\lambda/10$ ) necessary to permit direct computation of the phase shifts required for beamforming and imaging. The purpose of the self-survey is to generate sufficiently accurate array element coordinates to permit beamforming and imaging.

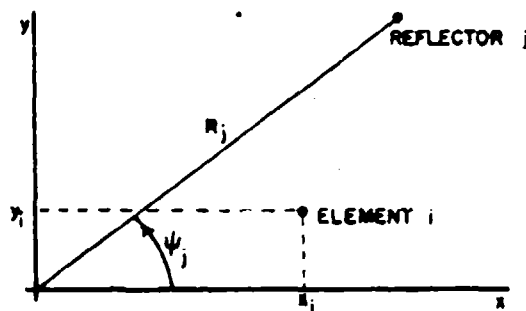


FIGURE 5.1 RANDOM ARRAY WITH NEAR-FIELD REFLECTORS

Assume a pulsed RF signal is transmitted from the reference element at the origin, and reflections from the targets are received at each element, including the reference element. Assume also that the reflected signals can be separated in range. The phases of the signals received at each of the elements are measured relative to the signal received at the reference element. The theoretical phase delay for the signal reflected from point  $j$  and received at element  $i$  is

$$P_{ij} = k[R_j - \sqrt{(R_j \cos \psi_j - x_i)^2 + (R_j \sin \psi_j - y_i)^2}] + \phi_i \quad (1)$$

\*This work is principally supported by the Air Force Office of Scientific Research under Contract No. AFOSR-82-0012.

where  $k = 2\pi/\lambda$  and  $\phi_1$  is the phase shift associated with carrying the reference signal from the reference element to the  $i^{th}$  element, either by cable or broadcast [1]. The corresponding measured value of the phase delay in (1) is denoted  $\phi_{1j}^m$ . The phase shifts associated with transmission and with reflection from the targets are removed by the phase comparison process. The phase shift associated with the receiver is included in  $\phi_1$ .

The self-survey technique consists in choosing values of the variables  $(x_i, y_i)$ ,  $i = 1, \dots, N$ , and  $(R_j, \psi_j)$ ,  $j = 1, \dots, M$  in such a way as to minimize

$$Q = \sum_{i=1}^N \sum_{j=1}^M (P_{1j} - \phi_{1j}^m)^2 \quad (2)$$

The minimization is carried out by applying Newton's method to the set of nonlinear equations obtained by equating to zero the partial derivatives of  $Q$  with respect to  $x_i$ ,  $y_i$ ,  $\phi_1$ ,  $R_j$ ,  $\psi_j$ .

The minimization in (2) is essentially a multilateration process. Thus the distances from elements to point targets must be known accurately a priori (to approximately  $\lambda/2$ ) to determine the actual phase delays  $\phi_{1j}^m$ , rather than the mod  $2\pi$  values which are obtained from the phase measurement process. The equations derived from (2) have a unique solution if appropriate baseline variables are measured a priori.

If  $R_j \rightarrow \infty$ , (1) reduces to the far-field phase difference

$$P_{1j} = k[x_1 \cos \psi_j + y_1 \sin \psi_j] + \phi_1 \quad (3)$$

Lee [1] analyzed the self-survey process in detail for far-field point targets (or beacons). He demonstrated satisfactory convergence properties of the Newton iteration, and derived the effect of phase measurement errors on the computed coordinates. He concluded that the technique will determine the element coordinates sufficiently accurately to form high quality beams within the angular spread of the point targets used for the self-survey phase data.

It can be shown that different coordinate systems must be used for the elements and the reflectors or else the equations will be degenerate. We choose to use rectangular coordinates for element positions and polar coordinates for reflector positions.

The phase  $P_{1j}$  of (1) and the associated self-survey process apply not only

to real receive-only arrays with fixed transmitter at the reference element, but also to equivalent synthetic aperture systems. That is, if the reference element at the origin transmits repetitively and the sequence of reflections is received both at the reference element and at a single moving receiver, then  $P_{ij}$  of (1) corresponds to the phase difference which exists when the receiver is at the  $i^{th}$  position  $(x_i, y_i)$ . Thus the self-survey process can be used to survey the sequence of positions of the moving receiver.

#### Near-Field Monostatic Transmit/Receive Array

Suppose a single transmit/receive element transmits a sequence of RF pulses and receives the reflections from the point targets as it traverses a path beginning at the origin. In Figure 4.1, element  $i$  would represent the position of the element during transmission and reception of the  $i^{th}$  pulse. The round trip phase delay for the  $i^{th}$  position is

$$\hat{P}_{ij} = 2k \sqrt{(R_j \cos \psi_j - x_i)^2 + (R_j \sin \psi_j - y_i)^2} + \phi_j \quad (4)$$

where  $\phi_j$  includes the phase delays in the transmitter and receiver (which are independent of  $i$  and  $j$ ) and the phase delay owing to the reflection process at the target (which we assume varies from target to target, but does not vary significantly with array element position). The measured phase delay, adjusted to reflect actual delay rather than the mod  $2\pi$  phase measurement alone, is denoted  $\hat{\phi}_{ij}^m$ . A self-survey could be performed for this synthetic-aperture system by carrying out the minimization of (2) with phase relations (4) instead of phase relations (1).

An alternative approach to self-survey with the monostatic synthetic-aperture system is to subtract the round trip phase delay  $\hat{P}_{ij}$  from the corresponding phase delay at a reference element position  $\hat{P}_{oj}$  for each of the transmitted signals in (4), thereby producing

$$P_{ij} = \hat{P}_{oj} - \hat{P}_{ij} = 2k[R_j - \sqrt{(R_j \cos \psi_j - x_i)^2 + (R_j \sin \psi_j - y_i)^2}] \quad (5)$$

The self-survey process consists in measuring  $\phi_{ij}^m = \hat{\phi}_{oj}^m - \hat{\phi}_{ij}^m$ , then minimizing (2). The structure of (5) is essentially the same as the structure of (1); it differs only in the factor 2 and in the missing cable delay  $\phi_1$ . Thus essentially the same computer algorithm can be used for self-survey of the bistatic array and the monostatic array. Note that the synthetic-aperture

equations (5) would also apply to a real transmit-receive array if transmissions occurred sequentially, element by element.

In the subtracted-reference version (5), it is a differential distance from element position to point-target position that determines the phase delay  $P_{ij}$ , whereas in the non-subtracted version (4) it is the absolute distance that determines the phase delay  $\hat{P}_{ij}$ . Consequently, the subtracted reference version is less sensitive to the absolute position of the point targets. That is, if the a priori measurements of the point-target positions and element positions are not sufficiently accurate, the conversions of the  $\text{mod } 2\pi$  measurements of round-trip phases to true delays are ambiguous. However, the portions of the ambiguities which are owing to the target position measurement errors are approximately the same for all element positions. Therefore, the conversion of the subtracted-reference  $\text{mod } 2\pi$  measurement of round trip phase to a true delay is much less likely to be ambiguous.

#### Simulation of Subtracted-Reference Synthetic-Aperture Self-Survey

The subtracted-reference self-survey algorithm was tested for a number of different planar geometries, each consisting of seven elements and four point targets. In each geometry the array elements were somewhat linear in placement and the targets were grouped within a  $10^\circ$  field of view somewhat toward broadside. The error-free subtracted-reference phase delay measurements were simulated. One of the seven elements was selected as the origin and another was chosen as a baseline element with measured coordinates. Thus there were eighteen equations to be solved by the Newton iteration. For each geometry the algorithm was tested using a variety of initial guess values for the element positions and point-target positions. The guess positions deviated from the true positions by as much as twenty-five wavelengths. (However, since the phase delays were error free, no delay ambiguity was introduced by use of these large initial position errors.)

For those sets of initial guesses which lead to convergence,  $Q$  converged to within  $10^{-10}$  within seven to eight iterations. The regions of convergence for the array elements and the point targets had the shapes and sizes shown in Figure 5.2. Note that from a convergence standpoint the most stringent requirement on a priori knowledge of element position is in the direction toward the target region; the tightest requirement on a priori knowledge of target

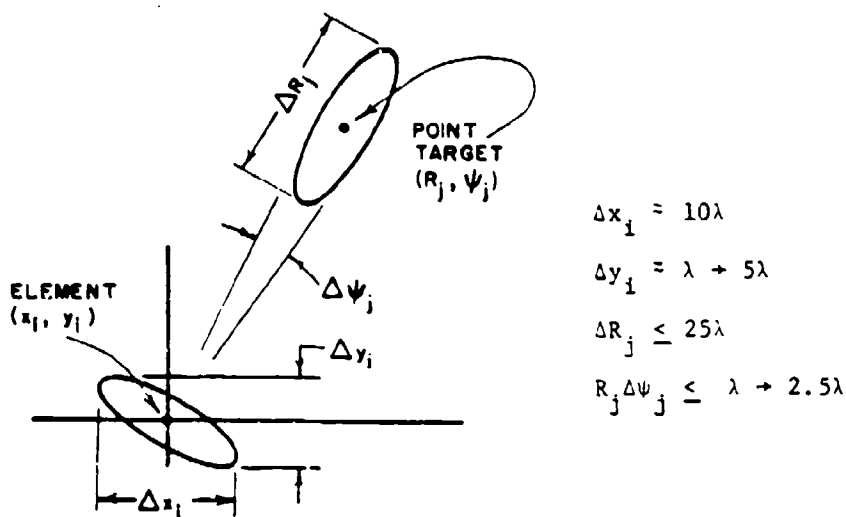


FIGURE 5.2 REGIONS OF CONVERGENCE FOR ELEMENTS AND POINT TARGETS

position is in the cross-range direction. It appears that the a priori position knowledge can be in error by at least one wavelength for each of the elements and positions without affecting convergence.

The algorithm was also tested for various geometries using simulated phase measurements with random phase errors. In each case the geometrically correct positions were used as initial guess values. In all cases the algorithm converged within two to three iterations. The tests were carried out for phase error sets with rms values less than or equal to 0.5 rad. The rms of the resulting errors in the element positions was less than 0.2 wavelengths for uniformly distributed phase errors and less than 0.8 wavelengths for normally distributed phase errors. Some of the tests used the geometry of the Valley Forge Research Center test site (shown in Figure 5.5). For this geometry the element-position and point-target position errors which were introduced by the simulated phase measurement errors exhibited the patterns shown in Figure 5.3. These error patterns are consistent with theoretical sensitivity analysis. For the VFRC geometry and the theoretical difference phase (5) it can be shown that

$$\frac{\partial x_1}{\partial p_{1j}} / \frac{\partial y_1}{\partial p_{1j}} \approx 2.16, \quad \frac{\partial R_j}{\partial p_{1j}} / \frac{\partial \psi_j}{\partial p_{1j}} R_j \approx 30 \quad (6)$$

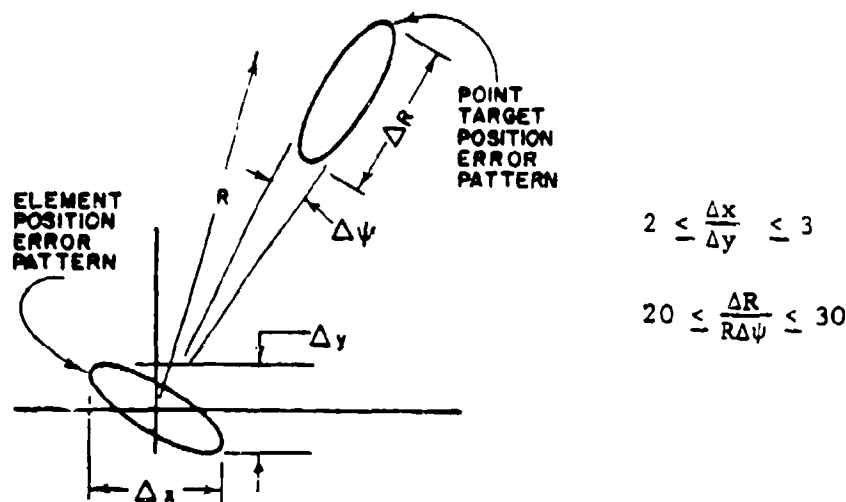


FIGURE 5.3 DISTRIBUTION OF SELF-SURVEY POSITION ERRORS (OWING TO PHASE MEASUREMENT ERROR).

#### Array Radiation Patterns

After the positions of the elements are determined by self-survey, the computed element positions can be used to compute the phase delays necessary to cohere the array at any (near-field) point within the angular spread of the target points used for the self-survey. Of course, for near-field focusing the concept of a beam is not well defined. Rather we must speak of a focal region. We present the equations for the focal patterns for both the bistatic and the monostatic (synthetic-aperture) arrays.

Assume free space propagation, no medium or system losses, isotropic reflectors and omnidirectional antenna elements, with the geometry shown in Figure 5.4. Suppose we wish to focus a bistatic receive-only array. The signals received at the elements must be individually delayed and added together. The phase delay (relative to the reference element at the origin) to apply to the signal received at element 1 for focus at  $(R^*, \psi^*)$  is  $-kd_1^*$ . By a method similar to that used to derive the radar equation [2], it can be shown that the bistatic near-field radiation pattern for focus at the point  $(R^*, \psi^*)$  is

$$A_B(R, \psi) = \left( \frac{R^*}{R} \right) \left( \frac{\sum_{i=0}^N \frac{1}{L_i} \exp[jk(L_i - L_1^*)]}{\sum_{i=0}^N \frac{1}{L_i^*}} \right) \quad (7)$$

where  $L_1^*$  and  $L_1$  can be expressed in terms of  $R^*$ ,  $\psi^*$ ,  $R$ ,  $\psi$ ,  $x_1$ , and  $y_1$ .

On the other hand, suppose we wish to focus a monostatic synthetic-aperture array. In order to focus the array at the point  $(R^*, \psi^*)$  we phase delay the signal received at the  $i^{th}$  position of the element by the amount  $-2kd_1^*$ , relative to the reference element position, before adding of signals across the aperture. The corresponding monostatic near-field radiation pattern for focusing of the synthetic-aperture array is

$$A_M(R, \psi) = \frac{\sum_{i=0}^N \frac{1}{L_1^*} \exp[j2k(L_1 - L_1^*)]}{\sum_{i=0}^N \frac{1}{L_1^*}} \quad (8)$$

Note that the monostatic synthetic-aperture radiation pattern (8) differs from the bistatic receive-only radiation pattern (7) primarily in the factor 2 in the exponents of  $L_1$  and  $L_1^*$ . As a consequence, the distinctive difference between the monostatic pattern and the bistatic pattern is an approximate halving of the beamwidth in the synthetic aperture case.

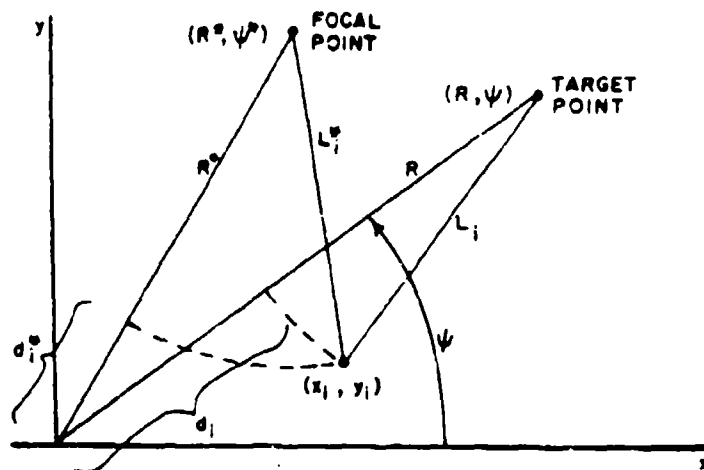


FIGURE 5.4 GEOMETRY FOR NEAR-FIELD FOCUSING

#### Experimental Self-Survey and Beamforming

Figure 5.5 shows the geometry of a monostatic synthetic-aperture experiment which was carried out at the VFRC test site. X-band (3cm) data were taken with a single moving transmitter/receiver at 100 random positions along an approximately linear path [3]. Reflections from a region containing corner reflectors were received at each element position. The amplitude and phase of the return

were measured at the centers of sixteen range bins, each 9 m in length. The field of view of the transmitter/receiver was  $8^\circ$ . The element positions were measured to within approximately 1 cm. The corner reflector positions were measured to within approximately 4 cm.

Seven element positions and four reflectors were selected for use in the self-survey. The measured positions were used to compute element-to-reflector distances in order to convert the mod  $2\pi$  phase measurements to true phase delays. One element position was selected as the reference position. For each range bin of each of the six non-reference element positions the measured phase was rotated by subtracting the phase at the corresponding range of the reference element signal. This subtraction process produced measurements of the subtracted-reference phase delay (5). The reference subtraction process

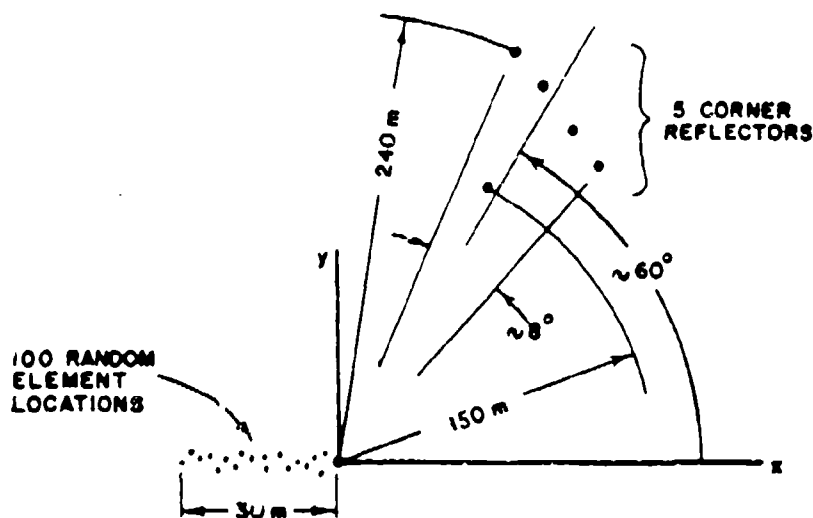


FIGURE 5.5 GEOMETRY OF X-BAND SYNTHETIC APERTURE EXPERIMENT

should have removed any delay ambiguity that might have existed in the direct element-to-reflector phase delays owing to the large inaccuracy in the reflector position measurements, because the reflector position error would cause essentially the same ambiguity error in the computed values of all the reflector-to-element phase delays.

The subtracted-reference phase-delay data for the six elements and four reflectors were used in the self-survey algorithm to obtain computed values of element positions and reflector positions, using the measured positions as initial values for the Newton iteration. One of the element positions was selected as the baseline element, and consequently its coordinates were not computed in the self-survey process. The computed positions satisfied  $Q < 1.45$  rad

where  $Q$  is defined in (2). Thus the rms of the computed values of the phase errors ( $P_{ij} = \phi_{ij}^m$ ) is only  $14^\circ$ . The rms of the difference between measured element positions and computed element positions was less than 0.6 wavelengths. Thus the computed solution fits the measured phase data very well, and agrees with the measured position data to within the accuracy of the position measurements.

The 6 element positions computed via the self-survey were used with the phase delays described in connection with the monostatic synthetic-aperture radiation pattern (8) to electronically scan the focal point of the array on a cross-range path through one of the reflectors, by selecting from the sixteen range bins of directly-measured amplitude and phase data for each of the 6 element positions. The 6 elements were spread over a 22-meter aperture. Thus the far-field region was at least 10 km from the array. The scanned image of the corner reflector is shown in Fig. 5.6a. The cross-range focal width (or beamwidth) is 0.7 milliradian and the rms sidelobe level is -7.3 dB. Although the reflector, at 240 m range, was in the near field, these measured beam parameters are close to those predicted for a linear random six-element array that is perfectly focused in the far field, namely 0.693 mrad and -7.7 dB [4]. According to far-field random array theory, the 0.4 dB difference in gain relative to sidelobe level is consistent with random phase errors with rms value  $17^\circ$ . This level of phase error is consistent with the  $14^\circ$  rms phase errors found during the self-survey computation. That is, according to the tolerance theory for far-field self-survey equations [1], phase errors in the self-survey phase measurements cause errors in the computed positions which, in turn, lead to phase errors during beamforming that are of the same level ( $14^\circ$ ) as phase errors in the self-survey phase measurements. The target signals measured during the imaging process are presumed to contain independent phase errors of the same level ( $14^\circ$ ) as the self-survey signals. Therefore, the rms value of the sum of the two sets of phase errors would be expected to be approximately  $\sqrt{2}(14^\circ) = 20^\circ$ .

The imaging process was repeated using the measured element positions rather than the element positions obtained by self-survey. The results are shown in Figure 5.6b. Note the significant reduction in gain (or the equivalent increase in sidelobe level). The gain is down, relative to a perfectly focused array, by 1.8 dB. According to far-field random array theory, a gain reduction of this size is consistent with random phase errors with rms value  $37^\circ$ . The improved focus due to the self-survey is apparent.

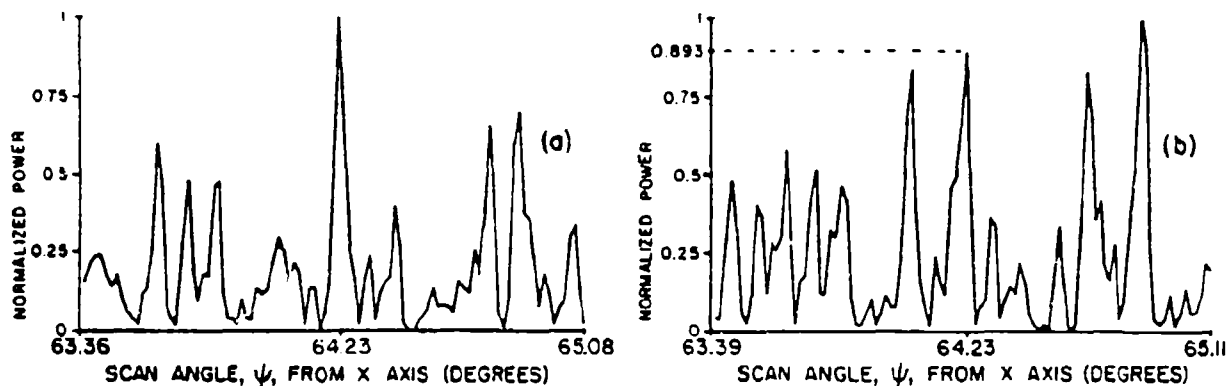


FIGURE 5.6 IMAGES OF CORNER REFLECTOR AT RANGE 240 m  
 (a) Element positions from self-survey  
 (b) Measured element positions

Figure 5.7 shows the -1 dB level curve of the image of the corner reflector obtained by performing several scans at different focal ranges using the element positions from the self-survey. Table 5.1 shows the position of the peak intensity in the image of Figure 5.7; it also shows the position of the corner reflector as measured and as computed by the self-survey process. According to the tolerance theory for the far-field region [1], errors in measurement of the baseline element position and errors in the self-survey phase

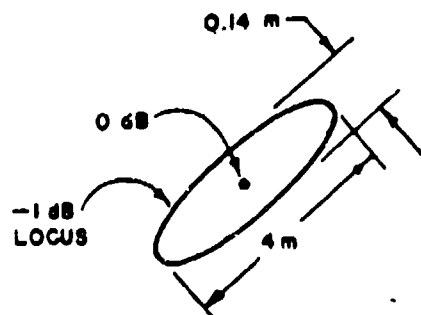


FIGURE 5.7 LEVEL CURVE OF CORNER REFLECTOR IMAGE

measurements each corrupt the computed element positions in such a way as to cause errors in the computed reflector direction and also errors in the beam-pointing angle during imaging.

The variations in beam pointing angle shown in Table 5.1 are in the order of 0.3 mrad. According to the far-field tolerance theory, this error is too large to be caused by the 14° phase errors arising from the self-survey process.

The theory also shows that a 0.3 mrad pointing error is consistent with a 0.5 cm error in position of the baseline element. These numbers were verified by computer simulation for the near-field geometry of the experiment. Thus, the accuracy of the target reflector location is consistent with the accuracy in measurement of the element positions.

	$R^*$ (Meters)	$\psi^*$ (Radians)
Measured	235.43	1.1214
From Self-Survey	236.49	1.1208
From Image	236.49	1.1211

TABLE 5.1 CORNER REFLECTOR POSITION

It is apparent that the self-survey process is effective with real radar data. The array which consisted of these six elements was also used to image the region containing the fifth corner reflector at range 150 m (Figure 5.5). This reflector was not used in the self-survey process; it was smaller than the other four. The intensity of the received returns was  $< \frac{1}{10}$  of those from the larger corner reflectors. Consequently, at the array the reflections were not distinguishable from the clutter.

The resulting image is shown in Figure 5.8. Table 5.2 shows the accuracy of location of the reflector.

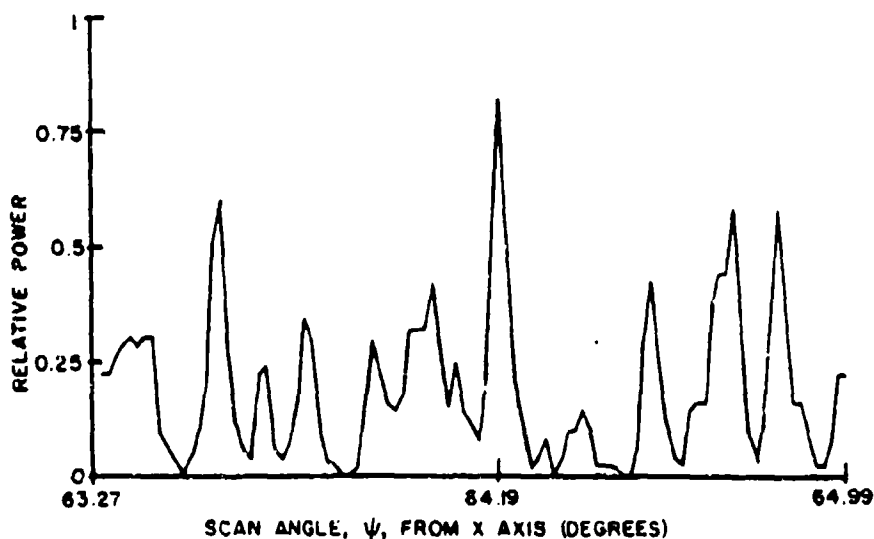


FIGURE 5.8 IMAGE OF WEAK CORNER REFLECTOR AT RANGE 150 m (UNNORMALIZED).

	$R^*$ (Meters)	$\psi^*$ (Radians)
Measured	149.47	1.1202
From Image	149.42	1.1963

TABLE 5.2 THE FIFTH CORNER REFLECTOR POSITION

The self-survey process is being repeated for a number of other sets of 6 elements. The sets of computed positions will be used simultaneously to form a focused beam with lower sidelobe level.

C. Nelson Dorny  
Tianhu Lei

#### REFERENCES

- [1] E. A. Lee, "A Generalized Self-Survey Technique for Self-Cohering of a Large Array," Doctoral Dissertation in Electrical Engineering and Science, University of Pennsylvania, Report UP-VFRC-30-81, Aug. 1981.
- [2] H. I. Skolnick, Introduction to Radar Systems, McGraw-Hill, New York, Chapter 2, 15-20 (1980).
- [3] D. Carlson, "High Resolution Airborne Imaging Radar System," Valley Forge Research Center Quarterly Progress Report No. 32, 15 Feb. 1980.
- [4] B. D. Steinberg, Principles of Aperture and Array System Design, John Wiley and Sons, Inc., New York, Chapter 3, 40-52, Chapter 8, 139-166 (1976).

# 8. LOSSY TRANSMISSION LINE MODEL OF A MICROSTRIP SLOT ANTENNA\*

Moshe Kisliuk

Microstrip-fed slot antennas can be used as radiating elements of large air-borne, or spaceborne, conformal adaptive arrays at frequencies ranging from UHF (0.5 GHz) to EHF (150 GHz). Compared to microstrip "patch" antennas they require less space, and preliminary investigations [1,2] show that they might operate at wider frequency bands.

The radiation pattern of a microstrip slot antenna had been measured and reported in [1], and it does not differ from the pattern of conventional slot antennas.

The input impedance of microstrip slot antennas has been studied in [1] and [2], but the obtained results do not take into account the thickness of the copper cladding and the width of the folded microstrip lines around the slot ("a" in Figure 8.1).

An approximate method for the evaluation of the input impedance of a microstrip slot antenna is presented. The method is based on the lossy transmission line model of slot radiators.

The upper view of a slot antenna fed by a 50  $\Omega$  microstrip line is shown in Figure 8.1.

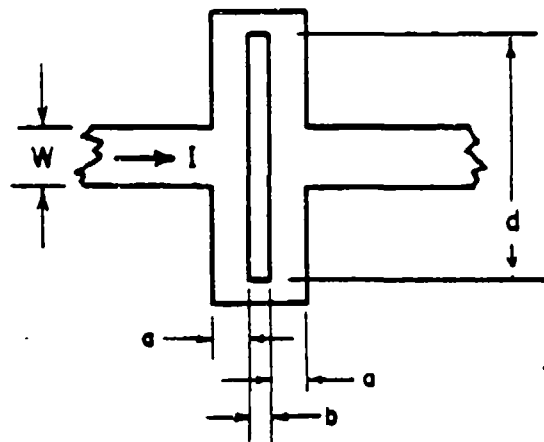


FIGURE 8.1. MICROSTRIP-FED SLOT ANTENNA

The radiating slot and the metallic strips on both sides of the slot form a

\*This work was supported by the Air Force Office of Scientific Research under Grant No. AFOSR-82-0012 with funding assistance from Air Force Wright Aeronautical Laboratories, Wright-Patterson Air Force Base, Ohio, and Rome Air Development Center, Griffiss Air Force Base, NY; also by Office of Naval Research Grant No. N00014-79-C-0505 with funding assistance from Naval Air Development Center, Warminster, PA and Naval Air Systems Command, Washington, D. C.

transmission line of coplanar strips (CPS) [3]. The propagation constant of lossless coplanar strips is [4]

$$\beta_0 = \frac{2\pi}{\lambda} \sqrt{\epsilon_e} \quad (1)$$

where  $\lambda$  is the free space wavelength, and

$$\epsilon_e \approx (\epsilon_r + 1)/2 \quad (2)$$

is the equivalent dielectric constant. The characteristic impedance of lossless coplanar strips is [4]

$$Z_0 = (120\pi/\sqrt{\epsilon_e})J(m), \quad (3)$$

where

$$J(m) = \pi/\ln \left( 2 \frac{1 + \sqrt{1-m^2}}{1 - \sqrt{1-m^2}} \right) \quad (4)$$

$$m = b/(b + 2a). \quad (5)$$

The complex propagation constant and characteristic impedance of lossy CPS are

$$\tilde{Z}_0 = Z_0(1 - js)^{-1/2} \quad (6)$$

$$\gamma = j\beta_0(1 - js)^{1/2} \quad (7)$$

where

$$s = 2 \frac{\alpha}{\beta_0} \sqrt{1 + (\alpha/\beta_0)^2}, \quad (8)$$

and  $\alpha$  is the attenuation constant that accounts for the radiation losses of the slot, as well as for the intrinsic losses of the CPS.

$$\alpha = \alpha_{\text{rad}} + \alpha_i, \quad (9)$$

$$\alpha_i \approx 9.2 \cdot 10^{-4} \frac{1}{\text{mm}} [4, \text{p.288}]$$

The simplest way to calculate  $\alpha_{\text{rad}}$  at near resonant frequencies is to assume that the slot is fed by a voltage source  $V_0$  (e.g., coaxial cable), as shown in Figure 2.

The voltage distribution on the slot is

$$V(z) = V_0 \sinh[\gamma(d/2 - |z|)]/\sinh(\gamma d/2), \quad (10)$$

but it is possible to assume that the voltage along the slot has a conventional

sinusoidal distribution

$$V(z) = V_0 \sin[\beta_0(d/2 - |z|)] / \sin(\beta_0 d/2). \quad (11)$$

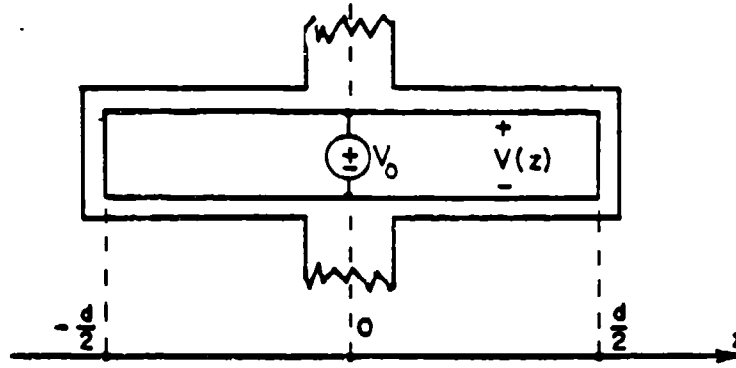


FIGURE 8.2 CENTER-FED SLOT ANTENNA

The power radiated into free space by a center-fed resonant slot with a sinusoidal voltage distribution is [2]

$$P_r = |V_0|^2 (\beta + k) \{ \text{Cin}[(\beta + k)d] - \text{Cin}[(\beta - k)d] \} / 8\pi\beta\eta \quad (12)$$

where  $k$  and  $\eta$  are the free space propagation constant and intrinsic impedance, respectively, and the function

$$\text{Cin}(x) = \int_0^x (1 - \cos u) du / u \quad (13)$$

is tabulated in mathematical handbooks. The average power delivered to the lossy transmission line by the voltage source in Figure 8.2 is

$$P_{in} = |V_0|^2 \text{Re} \left[ \frac{1}{Z_0 \tanh(\gamma d/2)} \right]^* \quad \text{or} \quad (14)$$

$$P_{in} = |V_0|^2 \frac{\tanh(\alpha d/2)}{Z_0} \quad (15)$$

Combining (15) and (12), we obtain

$$\alpha_{rad} = \frac{2}{d} \tanh^{-1} \left\{ \frac{Z_0 (1 + k/\beta)}{8\pi\eta} [\text{Cin}((\sqrt{\epsilon_e} + 1)\pi) - \text{Cin}((\sqrt{\epsilon_e} - 1)\pi)] \right\} \quad (16)$$

or

$$\alpha_{rad} = \frac{2}{d} \tanh^{-1} (Z_0 \cdot 4.3894 \cdot 10^{-4}). \quad (17)$$

The slot radiator is excited by the folded microstrip lines surrounding the

slot. Figure 8.3 shows one of these folded microstrip lines which excites the upper half of the slot.

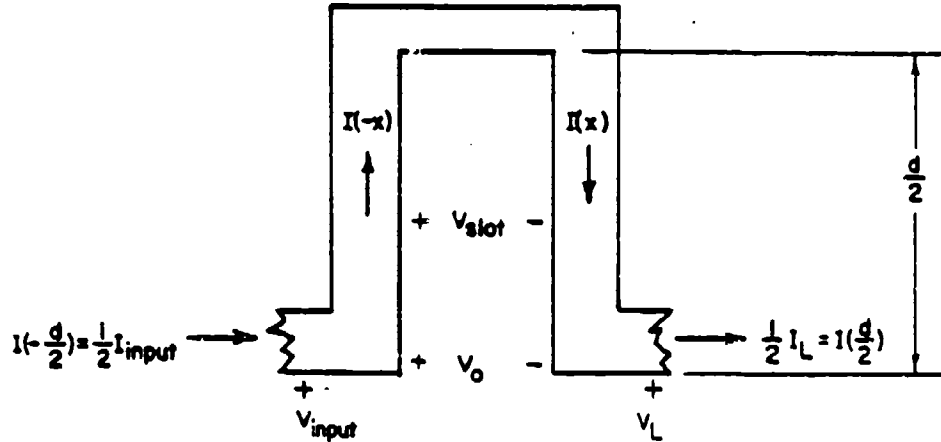


FIGURE 8.3 FOLDED MICROSTRIP LINE AROUND HALF OF A SLOT RADIATOR

Conventional transmission line analysis shows that the voltage and the current of the folded microstrip line in Figure 8.3 are given by

$$V(x) = V_L \{ \cos[\beta_F(d/2 - x)] + j \frac{Z_F}{2Z_L} \sin[\beta_F(d/2 - x)] \} + AV_o \left\{ \frac{\sinh(\gamma x)}{\sinh(\gamma d/2)} - \cos[\beta_F(d/2 - x)] + \frac{\gamma \sin[\beta_F(d/2 - x)]}{\beta_F \tanh(\gamma d/2)} \right\} \quad (18a)$$

$$I(x) = \frac{I_L}{2} \{ \cos[\beta_F(d/2 - x)] + j \frac{2Z_L}{Z_F} \sin[\beta_F(d/2 - x)] \} + jA \frac{V_o}{Z_F} \left\{ \frac{\gamma}{\beta_F} \left[ \frac{\cosh(\gamma x)}{\sinh(\gamma d/2)} - \frac{\cos[\beta_F(d/2 - x)]}{\tanh(\gamma d/2)} \right] - \sin[\beta_F(d/2 - x)] \right\} \quad (18b)$$

where  $Z_F$  and  $\beta_F$  are the characteristic impedance and propagation constant of the lossless folded microstrip,  $\gamma$  is the complex propagation constant of the slot (see equation 6),

$$A = \frac{Z_F \beta_F (1 - js)}{Z_0 \beta_0 [(\beta_0 / \beta_F)^2 - 1 + js]}, \quad (19)$$

and  $V_0$  is the voltage across the slot at its center.

$Z_0$ ,  $\beta_0$ ,  $\alpha$ , and  $s$  are the parameters of the coplanar strips (CPS). The quasi-static approximation for  $V_0$  yields

$$V_0 = V_{\text{input}} - V_L. \quad (20)$$

The voltage and the current of the folded microstrip lines at the input reference plane (Figure 8.3) are

$$V_{\text{input}} = V_L [\cos(\beta_F d) + j \frac{Z_F}{2Z_L} \sin(\beta_F d) + T] / (1 + T), \quad (21a)$$

$$T = A [2\cos^2(\beta_F d/2) - \frac{\gamma \sin(\beta_F d)}{\beta_F \tanh(\gamma d/2)}] \quad (21b)$$

$$I_{\text{input}} = I_L (\cos(\beta_F d) + j2 \frac{Z_L}{Z_F} \sin(\beta_F d) + jA \frac{2Z_L}{Z_F} (\frac{V_{\text{input}}}{V_L} - 1) [\frac{2\gamma \sin^2(\beta_F d/2)}{\beta_F \tanh(\gamma d/2)} - \sin(\beta_F d)]). \quad (22)$$

The input impedance of the radiating slot is

$$Z_{\text{input}} = \frac{V_{\text{input}}}{I_{\text{input}}}, \quad (23)$$

and is readily obtained from equations (21) - (23) for different values of the "load impedance" (Figure 8.3), which is the input impedance of the stub terminating the slot antenna. Due to the coupling between the arms of the folded microstrip line, design equations for its characteristic impedance ( $\beta_F$ ) and propagation constant ( $Z_F$ ) will be different from the ones used for straight microstrip lines [3,4], and further research on the influence of the coupling is needed to find these parameters.

Input impedance and pattern tests were performed at VFRC on a microstrip slot antenna of the form shown in Figure 8.4. The antenna model was mounted on 0.062-inch, 5870 "Duroid", and was tested over the 2 to 4 GHz frequency range; Table 8.1 lists the Z and X inputs over this range.

TABLE 8.1  
INPUT IMPEDANCE OF  
MICROSTRIP SLOT ANTENNA

GHz	Z input	X input
2.0	0.57	-0.03
2.1	0.58	+0.03
2.2	0.60	+0.06
2.3	0.63	+0.10
2.4	0.66	+0.15
2.5	0.72	+0.16
2.6	0.75	+0.16
2.7	0.80	+0.18
2.8	0.85	+0.17
2.9	0.90	+0.16
3.0	0.91	+0.14
3.1	1.00	+0.12
3.2	1.04	+0.10
3.3	1.07	+0.09
3.4	1.08	+0.10
3.5	1.1	+0.12
3.6	1.11	+0.15
3.7	1.14	+0.20
3.8	1.18	+0.25
3.9	1.26	+0.32
4.0	1.43	+0.40

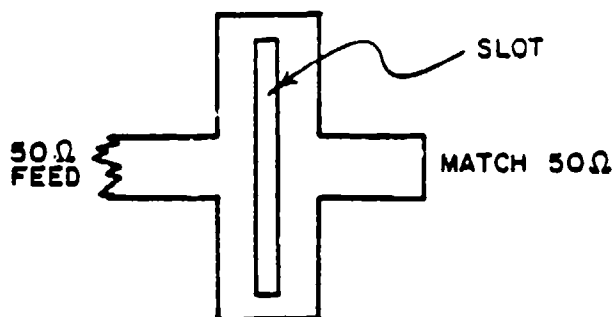


FIGURE 8.4 MICROSTRIP SLOT ANTENNA

From these measurements and continuing investigations, this antenna appears to be a broadband element. We measured a voltage standing wave ratio of less than 1.5 over the range from 2.4 to 4 GHz when the microstrip slot antenna was positioned in a matched 50-ohm line.

Moshe Kisliuk

#### REFERENCES

- [1] K. Solbach, "Microstrip Franklin Antenna," IEEE Trans. A&P, Vol. AP-30, No. 4, July 1982, pp. 773-775.
- [2] M. Kisliuk, "The Conformal Microstrip Slot Antenna," 1983 Intl. Symp. on Antennas & Propagat., Vol. 1, Houston, Texas, pp. 166-169.
- [3] K. C. Gupta, R. Garg, and I. T. Bahl, Microstrip Lines and Slotlines, Ch. 7, Artech House, Dedham, MA, 1979.
- [4] F. E. Gardiol and T. F. Zürcher, "HP-65 Program Computes Microstrip Impedance," Microwaves, Dec. 1977, pp. 186-187.

## Eliminating Reference Loop Phase Shift in Adaptive Arrays

Y. BAR-NESS, Senior Member, IEEE  
Drexel University

Adaptive array processors utilizing the Widrow LMS algorithm with an internally generated reference signal have been shown to be subject to weight cycling caused by phase shift in the reference extracting loop. Adaptive compensation schemes that eliminate the reference loop phase shift are suggested here. Two such schemes are proposed. They differ in the amount of hardware complexity needed as well as in the rate at which each one eliminates the phase shift. Computer calculations are used to compare the rates of convergence of the two schemes.

Manuscript received October 7, 1980; revised July 13, 1981.

This work was principally supported by the Air Force Office of Scientific Research under Grant AFOSR-78-1688.

Author's address: Dept. of ECE, Drexel University, Philadelphia, PA 19104. The work was done while the author was with the Valley Forge Research Center, Moore School of Electrical Engineering, University of Pennsylvania (on leave of absence from the School of Engineering, Tel Aviv University, Tel Aviv, Israel).

0018-9251/82/0100-0115 \$00.75 © 1982 IEEE

### I. INTRODUCTION

The desire to extract more information from existing space-time fields has led to the consideration of optimum array processors. Adaptive arrays are then the obvious realization of the optimum array processors for nonstationary backgrounds.

Such adaptive array processors are particularly useful in communication systems for automatic beam steering and interference cancellation. For such applications the least mean square (LMS) algorithm of Widrow et al. [1] is widely used. However, the realization of this algorithm requires a "reference signal" [2]. If this signal is a perfect replica of the desired signal to be received, then at the array output all the components which are uncorrelated with the desired signal (interference) will be suppressed. Such an ideal reference signal is not generally available, however. If it were available, there would be no need for a receiver and receiving array. To overcome this difficulty different approaches were used. Griffiths [3], for example, modified the Widrow-Hoff LMS algorithm so that a direct estimate of the cross covariance vector of the input and the desired signal might be used instead. In certain cases, as in the problem of extracting signals of known statistics from additive independent background noise, it may be shown that this cross covariance vector is a function of only the known signal statistics. Thus it can be accurately estimated even though it is not directly measurable. In the general case, the signal spatial or temporal structure may be assumed; however, the unknown signal level creates the same problem as with the Widrow-Hoff algorithm.

In communication systems the reference signal can be obtained naturally from the array output. For this to be possible, the desired signal must differ in some way from the interference, so that suitable processing of the array output can leave the desired signal unchanged while altering or suppressing the interference. Such a condition occurs, for example, when the desired signal is narrowband and the interference is broadband. Also, if the signal has a spread spectrum, then multiplying the array output by the right code will spread the interference bandwidth, collapse the desired signal spectrum, and provide again the condition of narrowband signal and broadband interference [4].

For extracting the reference signal from the array, a reference channel containing RF components such as a bandpass filter, mixers, etc., is needed. These components will introduce a phase shift of the reference signal with respect to the desired signal at the output of the array. This phase shift will depend on the instantaneous frequency of the signal as well as on the characteristics of the RF components. A priori unknown frequency changes of the signal (because of Doppler shift, transmitter frequency error, or receiver

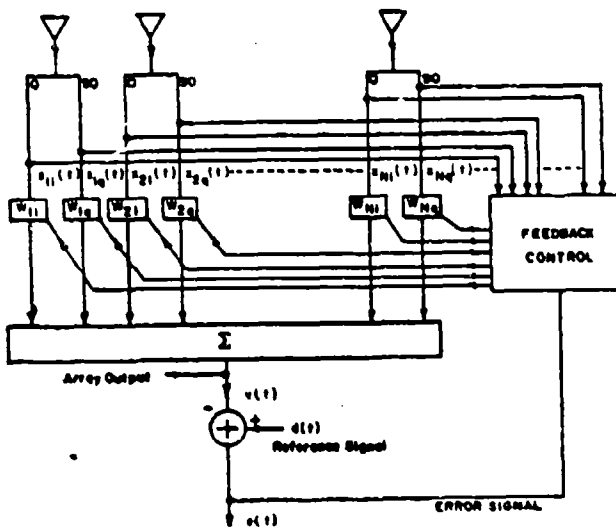


Fig. 1. Quadrature weighted adaptive array.

local oscillator frequency errors) will make pre-adjustments of these phase shifts impossible.

DiCarlo and Compton [5] studied the effect of a constant phase shift in the reference signal loop for a one- and a two-element array, and DiCarlo [6] generalized this result to the case of the  $N$ -element array. They show that such a phase shift causes the array weights to cycle. Using a simple model based on CW signals they showed that the array weights cycle with frequency and amplitude that depend on the main feedback loop gain and the reference loop phase shift. The main effect of this cycling is that the frequency of the desired signal at the array output is not the same as that at the array input. Particularly, systems using frequency modulation will be most susceptible, since the array alters the frequency deviation. Finally, these studies showed that the frequency at which the weights cycle increased as the number of array elements increased. To overcome this difficulty they suggest a compromise in the design of the reference loop filter (this filter contributes most of the phase shift). A highly selective bandpass filter is desired to eliminate as much interference from the reference signal as possible. However, the narrow filter bandwidth may cause a larger phase offset.

The purpose of this work is to suggest compensation schemes that might be used to prevent weight cycling and frequency distortion. First we present the mathematical formulation of a multielement adaptive array in which the reference signal is extracted from the array output as was done in [5, 6], and under the same assumptions. Then to overcome the reference loop phase shift problem, this loop is adaptively phase compensated to eliminate this phase shift. Two different adaptive compensation schemes are proposed. Both schemes annihilate the loop phase shift in the steady state. They differ, however, in the amount of hardware complexity needed as well as in the rate at which each one eliminates the phase shift. Depending

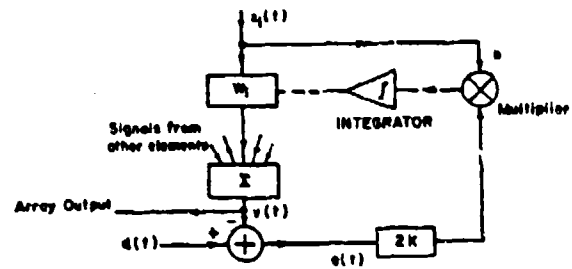


Fig. 2. Main feedback loop for LMS algorithm realization.

on the system parameters and the amount of complexity allowed, one scheme or the other might be used. It is also shown that the output signal-to-noise ratio is not affected by these compensating schemes. Finally, using computer simulation, the rate of convergence of the two schemes is compared.

## II. REFERENCE SIGNAL EXTRACTION SCHEME

The general configuration of the narrowband adaptive array processor is shown in Fig. 1. The input of each array element is split into in-phase and quadrature components, resulting in  $2N$  inputs to the processor ( $N$  is the number of elements in the array). Each of these inputs  $x_{iI}(t)$  or  $x_{iQ}(t)$  is weighted by a real factor  $w_{iI}(t)$  or  $w_{iQ}(t)$ , respectively, and then summed to produce the array output  $v(t)$ . The difference between the array output and the reference signal  $d(t)$  is the error signal  $e(t)$ . The error signal  $e(t)$  adjusts, through feedback loops, the different weights  $w_{iI}(t)$ , and  $w_{iQ}(t)$  so that its mean-square error  $e^2(t)$  is minimized. Using the analytic signals' representations, we can write for the array output

$$v(t) = x'(t)w(t) \quad (1)$$

where  $w(t)$  is the complex weight vector  $w(t) = \{w_1(t), w_2(t), \dots, w_N(t)\}$ ,  $w_i(t) = w_{iI}(t) + jw_{iQ}(t)$ , and  $x(t)$  is the analytic signal associated with the input. The transpose is indicated by  $\tau$ . Also we have

$$e(t) = d(t) - x'(t)w(t) \quad (2)$$

where  $e(t)$  and  $d(t)$  are the analytic signals associated with the error and reference signal, respectively.

In this representation an algorithm must be used to minimize  $|e(t)|^2$  where the overbar stands for the expected value. This can be done by using the steepest descent algorithm. That is

$$dw(t)/dt = -k \nabla w |e(t)|^2 \quad (3)$$

where  $\nabla w$  is the gradient with respect to  $w$  and is understood to be a complex vector whose components are the gradients with respect to the real and imaginary parts of  $w$ , respectively, and  $k$  is the main feedback loop gain. Following the derivation in [1] we obtain

$$dw(t)/dt = 2ix^*(t)e(t). \quad (4)$$

This is the complex LMS algorithm whose equivalent feedback network is displayed in Fig. 2. Substituting

for  $e(t)$  from (2) we get the differential equation that governs the weight vector  $w(t)$ <sup>1</sup>

$$dw(t)/dt + 2kR_s w(t) = 2kR_{sd} \quad (5)$$

where  $R_s = E[x^*(t)x(t)]$  is the input covariance matrix and  $R_{sd} = E[x^*(t)d(t)]$ . For the case of a single CW signal arriving at angle  $\psi$  to broadside we have<sup>2</sup>

$$x(t) = A/\sqrt{2}P + N(t) \quad (6)$$

where  $N(t) = \{n_1(t), \dots, n_N(t)\}$  is the noise process vector,  $P = \{1, \exp(-ja_1), \exp(-ja_2), \dots, \exp(-ja_{N-1})\}$ ,

$$a_i = (2\pi L_i/\lambda_c) \sin \psi \quad (7)$$

where  $\lambda_c$  is the free space wavelength at frequency  $\omega_c$ , and  $L_i$  is the distance between the  $i$ th and the first element. With this

$$R_s = \Phi + \sigma_n^2 I \quad (8)$$

where  $\Phi = A^2/2P^*P$ , and  $A$  is the signal amplitude. In (8) we also used  $E[n_i(t)n_j^*(t)] = \sigma_n^2$  for  $i = j$  and zero for  $i \neq j$ . Therefore (5) can be written as

$$dw(t)/dt + 2k(\Phi + \sigma_n^2 I)w(t) = 2kR_{sd} \quad (9)$$

When the array output  $v(t)$  is processed to produce a reference signal [5] as in Fig. 3, then

$$d(t) = a(P^*w(t)/|P^*w(t)|) \exp(-j\phi) \quad (10)$$

where  $a$  is a constant depending on the limiter level and filter attenuation and  $\phi$  is a phase shift introduced by the reference loop. Notice that due to the filtering process,  $d(t)$  in (10) is assumed noise free.<sup>3</sup> Obviously, noise in the reference signal loop will have an effect on the overall system performance. This effect is not considered in this paper. Analyzing this scheme, DiCarlo [5] showed that the complex weight vector  $w(t)$  converges to a limit cycle. That is, it oscillates with a radian frequency dependent upon the reference loop phase shift offset  $\phi$ , the loop gain  $k$ , the thermal noise power  $\sigma_n^2$ , and the total signal power  $NA^2/2$ . As a result, the frequency of the desired signal at the output is shifted by an amount that depends on these factors. Although the actual value of  $\phi$  may be small, other system parameters might be such that the effect of the resulting frequency translation would be intolerable.

<sup>1</sup>Notice that in obtaining (5), an assumption commonly made in the analysis of adaptive arrays is used. That is, the weight and signal processes are independent.

<sup>2</sup>We assumed without loss of generality that  $x(t)$  contains no interference. In fact, the interference term will only change the matrix  $\Phi$ . Similarly, it is assumed that the reference loop filter sufficiently filters out the interference.

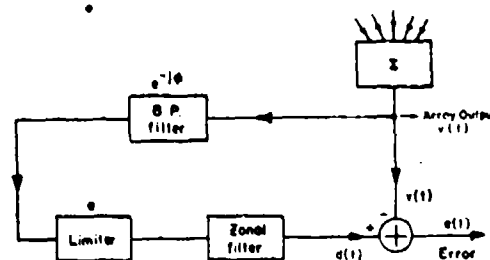


Fig. 3. Reference signal loop.

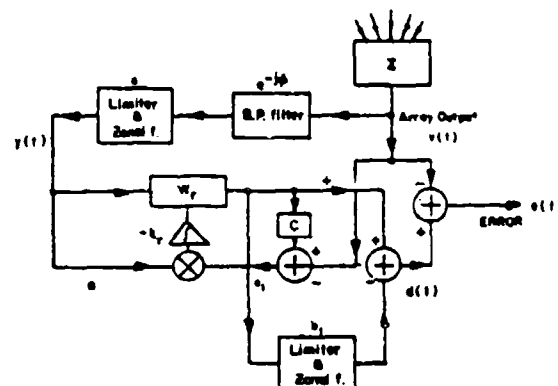


Fig. 4. Phase-compensated reference signal loop—first scheme.

### III. PHASE-COMPENSATED REFERENCE SIGNAL LOOPS

To cope with the problem of weight cycling due to the nonzero phase shift of the bandpass filter used to extract the reference signal in Fig. 3, we propose to use phase compensation by adding a complex weight  $w_r$ . Since the bandpass filter phase shift may not be known a priori or may even be of nonstationary character due to frequency error or modulation,  $w_r$  must be adaptively controlled to follow the variation in phase shift. A similar LMS algorithm might be used in controlling  $w_r$ . Accordingly, two different compensation schemes are proposed.

The first scheme leads to a set of equations governing the main and compensating weights which are linear in the amplitude of these weights, while the second scheme leads to a set of nonlinear equations. Both schemes drive the weight to a steady state stable point, independent of the filter phase shift. Therefore a total compensation of this phase shift results, together with the elimination of frequency shift and distortion that this phase shift was causing. The realization of the two schemes was motivated by the requirement of controlling the compensating weight  $w_r$  so that phases in two proper points in the reference loop will be equalized. This is done by the natural way of using a correlation loop (multiplier and integrator). The first scheme (Fig. 4), which might look rather mysterious, was a direct implementation of the mathematics involved in the requirement of making the system equation [(30)–(33)] linear in the amplitudes of weights  $q(t)$  and  $q_r(t)$ . The second scheme (Fig. 6) is rather self-explanatory.

### A. First Compensation Scheme

The reference signal loop is depicted in Fig. 4, from which one can easily see that the reference loop weight  $w_r$  is governed by

$$dw_r(t)/dt = -2k_r y^*(t) e_1(t) \quad (11)$$

where, as in (10),

$$y(t) = a(P^* w(t)/|P^* w(t)|) \exp(-j\phi) \quad (12)$$

and

$$e_1(t) = cy(t)w_r(t) - x^*(t)w(t). \quad (13)$$

The reference signal  $d(t)$  becomes

$$\begin{aligned} d(t) &= y(t)w_r(t) - b_1 y(t)w_r(t)/|y(t)w_r(t)| \\ &= y(t)[w_r(t) - b_1 w_r(t)/a|w_r(t)|] \end{aligned} \quad (14)$$

where we used  $|y(t)| = a$ . Using the definition of  $R_{rr}$  we get, after substituting for  $y(t)$  from (12),

$$\begin{aligned} R_{rr} &= E[x^*(t)P^* w(t)/|P^* w(t)|][aw_r(t) \\ &\quad - b_1 w_r(t)/|w_r(t)|] \exp(-j\phi). \end{aligned}$$

Using (6) and the definition of  $\Phi$  we have

$$\begin{aligned} R_{rr} &= (\sqrt{2}/A)[\Phi w(t)/|P^* w(t)|][aw_r(t) \\ &\quad - b_1 w_r(t)/|w_r(t)|] \exp(-j\phi). \end{aligned}$$

Thus (9) becomes

$$\begin{aligned} dw(t)/dt + 2k(\Phi + \sigma_r^2 I)w(t) &= (2k\sqrt{2}/A) \\ &\quad [\Phi w(t)/|P^* w(t)|][aw_r(t) - b_1 w_r(t)/|w_r(t)|] \\ &\quad \exp(-j\phi). \end{aligned} \quad (15)$$

Using (13) for  $e_1(t)$ , (11) becomes

$$dw_r(t)/dt = -2k_r y^*(t)[cy(t)w_r(t) - x^*(t)w(t)]$$

and with (12) we obtain, after some algebraic manipulation,

$$\begin{aligned} dw_r(t)/dt &= -2k_r[ca^2 w_r(t) \\ &\quad - (a\sqrt{2}/A)w_r(t)\Phi w(t)\exp(j\phi)/|P^* w(t)|] \end{aligned} \quad (16)$$

where the prime stands for transpose conjugate.

Equations (15) and (16) govern the main feedback loop weight vector  $w(t)$  and the reference loop weight  $w_r(t)$ , respectively.

The matrix  $\Phi$  is Hermitian having rank equal to

one. Therefore, there exists a constant unitary matrix  $Q$  such that  $Q^* \Phi Q = \Lambda$  where  $\Lambda$  is a diagonal matrix with only one nonzero element  $\lambda_N$ .

Premultiply (15) by  $Q^*$  and we get

$$\begin{aligned} d\Gamma(t)/dt + 2k(\Lambda + \sigma_r^2 I)\Gamma(t) &= 2k[\Lambda\Gamma(t)/|\Gamma(t)\Lambda\Gamma(t)|^{1/2}] \\ &\quad \cdot [aw_r(t) - b_1 w_r(t)/|w_r(t)|] \exp(-j\phi) \end{aligned} \quad (17)$$

where

$$\Gamma(t) = Q^* w(t) \quad (18)$$

and we also used the fact that

$$\begin{aligned} |P^* w(t)| &= (\sqrt{2}/A)|w(t)\Phi w(t)|^{1/2} \\ &= (\sqrt{2}/A)|\Gamma^*(t)\Lambda\Gamma(t)|^{1/2}. \end{aligned}$$

Similarly, (16) becomes

$$\begin{aligned} dw_r(t)/dt + 2k_r ca^2 w_r(t) &= 2k_r a[\Gamma^*(t)\Lambda\Gamma(t)/|\Gamma^*(t)\Lambda\Gamma(t)|^{1/2}] \exp(j\phi). \end{aligned} \quad (19)$$

Let  $\Gamma(t) = [\gamma_1(t), \dots, \gamma_N(t)]$ , then (17) and (19) can be written as (from [6])

$$d\gamma_i(t)/dt + 2k\sigma_r^2 \gamma_i(t) = 0, \quad i = 1, 2, \dots, N-1 \quad (20)$$

$$\begin{aligned} d\gamma_N(t)/dt + 2k(\lambda_N + \sigma_r^2)\gamma_N(t) &= 2ka\sqrt{\lambda_N}[\gamma_N(t)/|\gamma_N(t)|][aw_r(t) \\ &\quad - b_1 w_r(t)/|w_r(t)|] \exp(-j\phi) \end{aligned} \quad (21)$$

$$dw_r(t)/dt + 2k_r ca^2 w_r(t) = 2k_r a\sqrt{\lambda_N}|\gamma_N(t)| \exp(j\phi). \quad (22)$$

Notice that in (20) we have used the fact that  $\lambda_i = 0$  for  $i = 1, 2, \dots, N-1$ . The solution of (20) is given by

$$\gamma_i(t) = \gamma_i(0) \exp(-2k\sigma_r^2 t). \quad (23)$$

To solve the other system of differential equations (21) and (22) we define

$$\gamma_N(t) = q(t) \exp[-j\theta(t)] \quad (24)$$

$$w_r(t) = q_r(t) \exp[-j\psi(t)]. \quad (25)$$

With this (21) and (22) become

$$\begin{aligned} (d/dt)\{q(t) \exp[-j\theta(t)]\} + 2k(\lambda_N + \sigma_r^2)q(t) \exp[-j\theta(t)] &= 2k\sqrt{\lambda_N} \exp\{-j[\theta(t) + \phi(t) + \psi(t)]\}[aq_r(t) - b_1] \end{aligned} \quad (26)$$

$$(d/dt)\{q(t) \exp[-j\psi(t)]\} + 2k\alpha^2 q(t) \cdot \exp[-j\psi(t)] = 2k\alpha\sqrt{\lambda_w} \exp[j\phi(t)] q(t). \quad (27)$$

Evaluating the derivative and multiplying through by  $\exp[j\theta(t)]$  gives

$$\begin{aligned} dq(t)/dt - jq(t)[d\theta(t)/dt] + 2k(\lambda_w + \alpha^2)q(t) \\ = 2k\sqrt{\lambda_w} \exp\{-j[\phi(t) + \psi(t)]\} [aq(t) - b_1]. \end{aligned} \quad (28)$$

Similarly, evaluating the derivative and multiplying through by  $\exp[j\psi(t)]$  produces

$$\begin{aligned} dq(t)/dt - jq(t)[d\psi(t)/dt] + 2k\alpha^2 q(t) \\ = 2k\alpha\sqrt{\lambda_w} \exp\{j[\phi(t) + \psi(t)]\} q(t). \end{aligned} \quad (29)$$

Equating the real and imaginary parts of the right and left sides of (28) and (29) we obtain

$$\begin{aligned} dq(t)/dt + 2k(\lambda_w + \alpha^2)q(t) &= 2k\sqrt{\lambda_w} [aq(t) - b_1] \\ &\cos[\phi(t) + \psi(t)] \end{aligned} \quad (30)$$

$$\begin{aligned} dq(t)/dt + 2k\alpha^2 q(t) &= 2k\alpha\sqrt{\lambda_w} q(t) \cos[\phi(t) + \psi(t)] \\ &\quad (31) \end{aligned}$$

$$q(t)[d\theta(t)/dt] = 2k\sqrt{\lambda_w} \sin[\phi(t) + \psi(t)][aq(t) - b_1] \quad (32)$$

$$q(t)[d\psi(t)/dt] = 2k\alpha\sqrt{\lambda_w} \sin[\phi(t) + \psi(t)] q(t). \quad (33)$$

Dividing (31) by (33) and multiplying through by  $d\psi(t)/dt$ , we get

$$\begin{aligned} [dq(t)/dt]/q(t) + 2k\alpha^2 &= -\cot[\phi(t) + \psi(t)][d\psi(t)/dt] \\ \text{or} \\ d \ln[q(t)]/dt + 2k\alpha^2 &= -d \ln\{\sin[\phi(t) + \psi(t)]/dt\} \end{aligned} \quad (34)$$

where we assumed that  $\phi(t)$  is constant or very slowly varying so that  $d\phi(t)/dt \approx 0$ . The solution of (34) is given by

$$q(t) \sin[\phi(t) + \psi(t)] = c_0 \exp(-2k\alpha^2 t) \quad (35)$$

where  $c_0 = q(0) \sin[\psi(0) + \psi(0)]$ . Substituting the value of  $q(t)$  from (35) into (33) we get

$$\begin{aligned} (d\psi/dt)/\sin^2[\phi(t) + \psi(t)] \\ = (-k\alpha\sqrt{\lambda_w}/c_0) q(t) \exp(2k\alpha^2 t) \end{aligned}$$

or

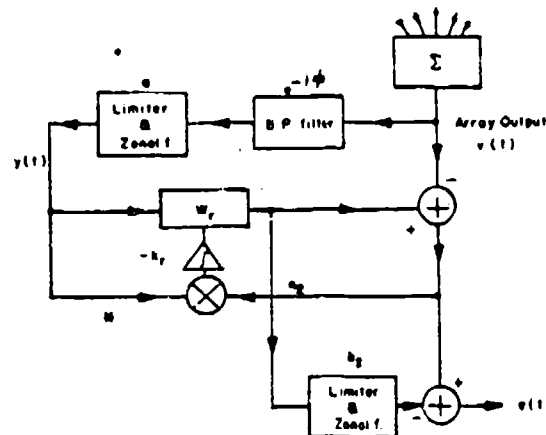


Fig. 5. Phase-compensated reference signal loop—first scheme,  $c = 1$ .

$$\begin{aligned} \cot[\phi(t) + \psi(t)] &= \\ \frac{[q(0) \cos(\phi_0 + \psi_0) + 2k\alpha\sqrt{\lambda_w} \int_0^t q(\tau) \exp(2k\alpha^2 \tau) d\tau]}{q(0) \sin(\phi_0 + \psi_0)} \end{aligned} \quad (36)$$

If  $q(t)$  is bounded away from zero,<sup>1</sup> then for sufficiently large  $t$  we have

$$\phi(t) \approx -\psi(t) \quad (37)$$

in which case (30) and (31) become

$$\begin{aligned} (d/dt) \begin{bmatrix} q(t) \\ q(t) \end{bmatrix} &= \begin{bmatrix} -2k(\lambda_w + \alpha^2) & 2k\alpha\sqrt{\lambda_w} \\ 2k\alpha\sqrt{\lambda_w} & -2k\alpha^2 \end{bmatrix} \cdot \\ \begin{bmatrix} q(t) \\ q(t) \end{bmatrix} &+ \begin{bmatrix} -kb_1\sqrt{\lambda_w} \\ 0 \end{bmatrix}. \end{aligned} \quad (38)$$

For this linear system to have an asymptotically stable singular point, it is necessary and sufficient that the system matrix eigenvalues have a negative real part. It can easily be shown that this is equivalent to the condition

$$c(\lambda_w + \alpha^2)/\lambda_w > 1. \quad (39)$$

Notice that if  $c$  were chosen to equal one, so that the scheme of Fig. 4 were simplified (Fig. 5), then the eigenvalues of the matrix in (38) would depend on the noise power  $\alpha^2$ . Particularly when  $\alpha^2$  is almost zero, then one of these eigenvalues will be approximately zero unless the loop gains are chosen to be very large. This means that, depending on the noise power, the system may become very sluggish. Furthermore, one can show that  $\lambda_w = NA^2/2$ , and therefore for a stable system it is necessary and sufficient to have

<sup>1</sup>This can be obtained by choosing a nonzero initial value for  $p(t)$ .

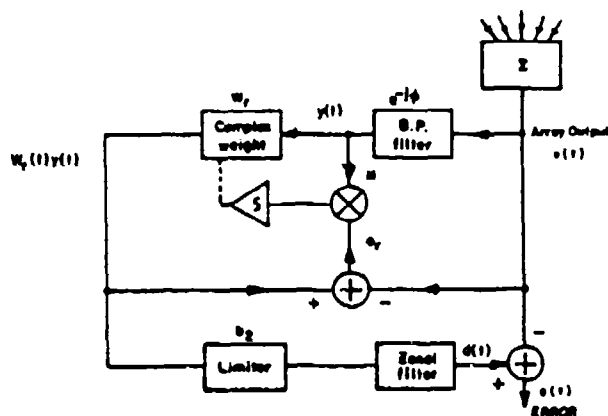


Fig. 6. Phase-compensated reference signal loop—second scheme.

$$c > 1/(1 + 2\sigma_n^2/NA^2).$$

Obviously  $c > 1$  is sufficient for stability with any signal-to-noise ratio. In this case  $q(t)$  and  $q_r(t)$  will converge exponentially to their steady state value given by

$$\begin{bmatrix} q(t) \\ q_r(t) \end{bmatrix} = -1/[c(\lambda_N + \sigma_n^2) - \lambda_N] \begin{bmatrix} c/2k & \sqrt{\lambda_N}/2akr \\ \sqrt{\lambda_N}2ak & (\lambda_N + \sigma_n^2)/2k, a^2 \end{bmatrix} \begin{bmatrix} -2kb_1\sqrt{\lambda_N} \\ 0 \end{bmatrix} \quad (41)$$

$$\begin{aligned} \lim_{t \rightarrow \infty} q(t) &= cb_1\sqrt{\lambda_N}/[c(\lambda_N + \sigma_n^2) - \lambda_N] \\ &= (b_1\sqrt{\lambda_N}/AN)[1/(1 - 1/c) + 2\sigma_n^2/NA^2] \end{aligned} \quad (42)$$

$$\lim_{t \rightarrow \infty} q_r(t) = (b_1\lambda_N/a)/[c(\lambda_N + \sigma_n^2) - \lambda_N]. \quad (43)$$

To conclude, we notice that under the condition discussed regarding the system parameters, the array main weight  $w(t)$  and reference loop weight  $w_r(t)$  converge to a steady-state stable value, resulting in the elimination of weight cycling.

## B. Second Compensation Scheme

A different reference signal loop is given in Fig. 6. With this the reference loop weight  $w_r$  is governed by

$$dw_r(t)/dt = -2k_r y^*(t) e_2(t) \quad (44)$$

where

$$y(t) = (A/\sqrt{2}) P^* w(t) \exp(-j\phi) \quad (45)$$

and

$$e_2(t) = y(t)w_r(t) - x^*(t)w(t). \quad (46)$$

The reference signal  $d(t)$  becomes

$$\begin{aligned} d(t) &= b_2 y(t) w_r(t) / |y(t) w_r(t)| \\ &= b_2 [P^* w(t) / |P^* w(t)|] \cdot [w_r(t) / |w_r(t)|] \exp(-j\phi). \end{aligned}$$

Thus

$$R_w = (b_2 \sqrt{2}/A) [\Phi w(t) / |P^* w(t)|] [w_r(t) / |w_r(t)|] \cdot \exp(-j\phi) \quad (47)$$

and (9) becomes

$$\begin{aligned} dw(t)/dt + 2k(\Phi + \sigma_n^2) w(t) &= (2kb_2 \sqrt{2}/A) \\ &\times [\Phi w(t) / |P^* w(t)|] [w_r(t) / |w_r(t)|] \exp(-j\phi). \end{aligned} \quad (48)$$

Using (46) in (44) gives

$$dw_r/dt = -2k_r [|y(t)|^2 w_r(t) - y^*(t) x^*(t) w(t)]$$

and using (45) we get

$$\begin{aligned} dw_r(t)/dt &= -2k_r [|A/\sqrt{2}| P^* w(t)|^2 w_r(t) \\ &- w(t) \Phi w(t) \exp(j\phi)]. \end{aligned} \quad (49)$$

Using the same transformation as before we end up with

$$d\gamma_i(t)/dt + 2k\sigma_n^2 \gamma_i(t) = 0, \quad i = 2, N-1 \quad (50)$$

$$\begin{aligned} d\gamma_N(t)/dt + 2k(\lambda_N + \sigma_n^2) \gamma_N(t) &= 2kb_2 \sqrt{\lambda_N} [\gamma_N(t) / |\gamma_N(t)|] [w_r(t) / |w_r(t)|] \\ &\cdot \exp(-j\phi) \end{aligned} \quad (51)$$

$$\begin{aligned} dw_r(t)/dt + 2k\lambda_N |\gamma_N(t)|^2 w_r(t) &= 2k\lambda_N |\gamma_N(t)|^2 \\ &\cdot \exp(j\phi). \end{aligned} \quad (52)$$

Using the polar representation of  $\gamma_N(t)$  and  $w_r(t)$  as in (24) and (25), respectively, and after equating the real and imaginary parts, we end up with

$$\begin{aligned} dq(t)/dt + 2k(\lambda_N + \sigma_n^2) q(t) &= 2kb_2 \sqrt{\lambda_N} \\ &\cdot \cos[\phi(t) + \psi(t)] \end{aligned} \quad (53)$$

$$\begin{aligned} dq_r(t)/dt + 2k\lambda_N q_r^2(t) q_r(t) &= 2k\lambda_N q_r^2(t) \\ &\cdot \cos[\phi(t) + \psi(t)] \end{aligned} \quad (54)$$

$$q(t)[d\theta(t)/dt] = 2kb_2 \sqrt{\lambda_N} \sin[\phi(t) + \psi(t)] \quad (55)$$

$$q_1(t)[d\psi(t)/dt = -2k\lambda_N q_2^2(t) \sin[\phi(t) + \psi(t)]. \quad (56) \quad \text{Thus}$$

Using steps similar to those that led to (34), we get

$$d \ln \{q_1(t) \sin[\phi(t) + \psi(t)]\} / dt = -2k\lambda_N q_2^2(t)$$

whose solution is given by

$$q_1(t) \sin[\phi(t) + \psi(t)] = c_0 \exp[-2k\lambda_N \int_0^t q_2^2(\xi) d\xi]. \quad (57)$$

Substituting for  $q_1(t)$  from (57) into (56) we get

$$\begin{aligned} \cot[\phi(t) + \psi(t)] &= \{q_1(0) \cos(\phi_0 + \psi_0) \\ &+ 2k\lambda_N \int_0^t q_2^2(\tau) \exp[2k\lambda_N \int_0^\tau q_2^2(\xi) d\xi] d\tau\} / \\ &q_1(0) \sin(\phi_0 + \psi_0). \end{aligned} \quad (58)$$

It is obvious that the right-hand term goes to infinity, and we have  $\lim_{t \rightarrow \infty} \psi(t) = -\phi(t)$  unless  $q_2(t)$  converges to zero for finite  $t$ . In this case we get from (53) and (54)

$$\begin{aligned} \lim_{t \rightarrow \infty} q_1(t) &= b_2 \sqrt{\lambda_N} / (\lambda_N + \sigma_n^2) \\ &= (b_2 \sqrt{2} / AN) [1 / (1 + 2\sigma_n^2 / NA^2)] \end{aligned} \quad (59)$$

$$\lim_{t \rightarrow \infty} q_2(t) = 1. \quad (60)$$

To conclude we notice that, similar to the previous case,  $w(t)$  and  $w_1(t)$  converge to a steady-state value resulting in the elimination of weight cycling.

### C. Performance Comparison

Comparing (59) with (42) we notice that the first scheme requires larger control weights, unless we make  $c$  very large. Equations (36) and (58) describe the process of compensation of phase shift in reference loops of the first and second schemes, respectively. They both present a nondecreasing function that diverges to infinity. If the rate of change of one function is greater than the rate change of the other for every  $t$ , then the corresponding scheme is preferable since it will decrease distortion in the desired signal output faster than the other. To check for this we can take the derivative with respect to  $t$  of (36) and (58), respectively,

$$R_1(t) = 2k\lambda_N q_1(t) \exp(2k\lambda_N t) / q_1(0) \sin(\phi_0 + \psi_0) \quad (61)$$

$$\begin{aligned} R_2(t) &= 2k\lambda_N q_2^2(t) \exp[2k\lambda_N \int_0^t q_2^2(\xi) d\xi] / \\ &q_1(0) \sin(\phi_0 + \psi_0) \end{aligned} \quad (62)$$

where  $q_1(t)$  and  $q_2(t)$  are the solutions of the system of equations (30) to (33), and (53) to (56), respectively.

$$\begin{aligned} R_1(t) / R_2(t) &= [a q_1(t) / \sqrt{\lambda_N} q_2^2(t)] \\ &\cdot \exp[2k\lambda_N t - \lambda_N \int_0^t q_2^2(\xi) d\xi] \end{aligned} \quad (63)$$

or

$$\begin{aligned} R_1(t) / R_2(t) &\geq [a q_1(t) / \sqrt{\lambda_N} \|q_2(t)\| q_2(t)] \\ &\cdot \exp\{2k\lambda_N [ca^2 - \lambda_N \|q_2(t)\|^2] t\} \end{aligned} \quad (64)$$

where we used  $\|q_2(t)\| \geq q_2(t)$  for every  $t$ ;  $\|\cdot\|$  is the supremum norm. Using (53) we show in the Appendix that

$$\|q_2(t)\| \leq q_2(0) + b_2 \sqrt{\lambda_N} / (\lambda_N + \sigma_n^2). \quad (65)$$

Therefore for  $q_2(0) = 0$  by choosing  $a$  such that

$$a > \lambda_N b_2 / (\lambda_N + \sigma_n^2) \quad (66)$$

we get

$$a^2 > \lambda_N \|q_2(t)\|^2. \quad (67)$$

Hence for  $c > 1$ , (64) becomes

$$R_1(t) / R_2(t) \geq d_1 [q_1(t) / q_2(t)] \exp(2k\lambda_N t) \quad (68)$$

where  $d_1 \geq 1$  and  $d_1 > 0$ . Now from (42) and (59) we have for  $b_1 = b_2$  (by so selecting the limiter levels),  $q_1(\infty) \geq q_2(\infty)$ . Therefore it is most probable (except possibly for a very small  $t$ ) that  $R_1(t) \geq R_2(t)$  for almost every  $t \geq 0$ , i.e., it appears that we have a better performance with the first scheme than with the second. To have (66) satisfied for any noise power  $\sigma_n^2$ , it is sufficient to require  $a > b_2$ . Obviously this condition is sufficient, but not necessary, for the first scheme arrangement to perform better than the second scheme.

### IV. ARRAY OUTPUT SIGNAL-TO-NOISE RATIO

The complex envelope of the desired signal at the array output is given by

$$s(t) = v_1(t) = (A/\sqrt{2}) P^* w(t) = (A/\sqrt{2}) P^* Q \Gamma(t)$$

and in the steady state, by using (23)

$$\lim_{t \rightarrow \infty} s(t) = (A/\sqrt{2}) P^* q_1 \gamma_N(\infty)$$

where  $q_1$  is the last column of the matrix  $Q$ . By its definition  $Q^* \Phi Q = (A^2/2) Q P^* P^* Q = \Lambda$ ; therefore  $(A/\sqrt{2}) P^* q_1 = \sqrt{\lambda_N}$

and

$$\lim_{t \rightarrow \infty} s(t) = \gamma_N(\infty) \sqrt{\lambda_N}.$$

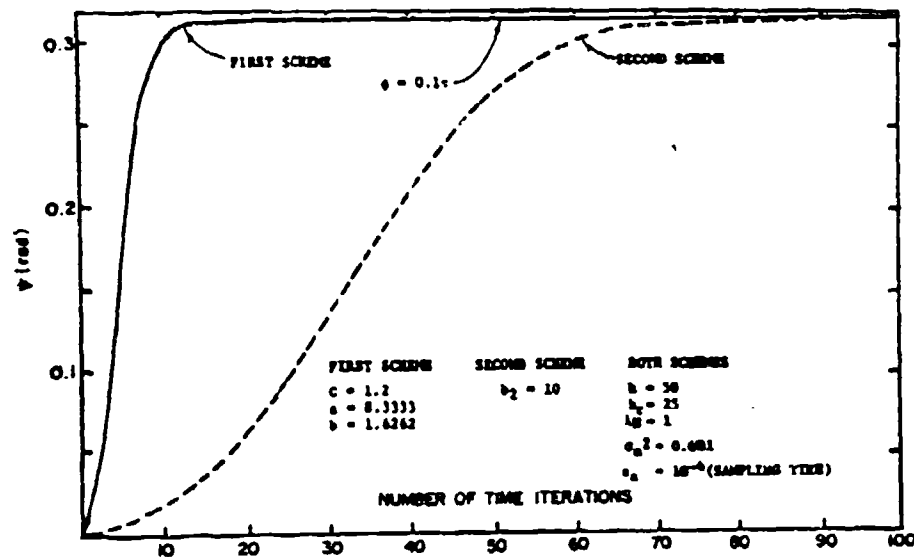


Fig. 7. Compensation convergence curves.

The output signal power  $S_o = |\gamma_N(\infty)|^2 \lambda_N$  while the noise power is given by  $N_o = \sigma_n^2 |\gamma_N(\infty)|^2$ . Hence:

$$S_o/N_o = \lambda_N/\sigma_n^2 = NA^2/2\sigma_n^2.$$

This is true independently of the way the reference loop was compensated.

## V. COMPUTER COMPUTATION

The system sets of (30)-(33) and (53)-(56) for the first and second compensation schemes, respectively, were solved using a digital computer. The array parameters used in both schemes were

$$k = 50; \quad k_r = 25; \quad \lambda_N = 1; \quad \sigma_n^2 = 0.01.$$

For the first scheme we used

$$a = 8.33; \quad b_1 = 1.6767; \quad c = 1.2.$$

For the second scheme we used  $b_2 = 10$ . For the derivative operation the approximation used was  $df/dt \approx (f_{i+1} - f_i)/s_s$  with  $s_s = 10^{-4}$ . The results of only one set of parameters are reported here. Nevertheless, the computations give some feeling that confirms the analysis. Actual system simulation of some real scenario, which might include desired signal modulation, is planned in a future research and is felt inappropriate in this stage of the work.

### A. Computation Results

1) With  $\phi = 0.1\pi, 0.2\pi, 0.3\pi, 0.4\pi$ , and  $0.5\pi$  both schemes had  $\psi(t)$  converging to  $-\phi$ . The difference was in the rate of convergence. While with the first scheme,  $\psi(t)$  converged to  $-\phi$  in 50 time iterations, it

took 150 time iterations for the second scheme to converge.\* Fig. 7 depicts the convergence curve of these two schemes. Notice the superiority of the first scheme despite the use of parameters ( $b_1 = 10, a = 8.33$ ) which do not satisfy the condition in (68).

However, the computer result showed that other system parameters, namely  $q(t)$ ,  $\hat{q}(t)$ , and  $\theta(t)$ , converge to their final value in a shorter time with the second scheme than with the first. With the first scheme, for example, these parameters converge in 6200 time iterations, while with the second scheme, it took 150 time iterations for  $q(t)$  to converge and 1200 time iterations for  $\theta(t)$  and  $\hat{q}(t)$  to converge.

2) Changing the noise power  $\sigma_n^2$  ( $=0.001, 0.01$ , and  $0.1$ ) had only a small effect on the rate of convergence of  $\psi(t)$  with both schemes. It had slightly more effect on the final values of  $q(t)$  and  $\hat{q}(t)$  of the first scheme. It had even less effect on these values for the second scheme. This is in agreement with the calculated final values of (42) and (43) for the first scheme and of (59) and (60) for the second scheme.

3) The effect of the parameter  $c$  on the stability of the first scheme was examined. With  $c = 0.9$ ,  $q(t)$  and  $\hat{q}(t)$  did not converge; with  $c = 1.1$ ,  $q(t)$  reached very close to the final value with 7500 time iterations, and with  $c = 1.2$ , 6200 time iterations were required.

## VI. CONCLUSION

Two schemes were suggested for the compensation of the phase shift introduced by the bandpass filter and other RF components in the reference signal loop. An adaptively controlled complex weight was used for compensation. It was shown that this weight converges to a value that makes the total phase shift of

\*Convergence to within 0.001 of the final value of  $\phi$ .

the reference loop zero, and therefore eliminates the main loop cycling, which causes frequency distortion of the desired signal at the array-output. Although the first scheme required more hardware complexity, it had the advantage of faster elimination of phase shift in the loop. Computer analysis confirmed these results.

## APPENDIX

The solution of (53) is given by

$$q(t) = \exp[-2k(\lambda_n + \sigma_n^2)t] \left\{ \int 2kb_2 \sqrt{\lambda_n} \cos[\phi(t) + \psi(t)] \right. \\ \times \exp[-2k(\lambda_n + \sigma_n^2)t] dt + q(0) \} \\ |q(t)| \leq 2kb_2 \sqrt{\lambda_n} \int_0^t \exp[-2k(\lambda_n + \sigma_n^2)t] dt + q(0) \\ = b_2 \sqrt{\lambda_n} / (\lambda_n + \sigma_n^2) + q(0).$$

This is true for any  $t$ ; hence

$$\|q(t)\| \leq b_2 \sqrt{\lambda_n} / (\lambda_n + \sigma_n^2) + q(0).$$

## REFERENCES

- [1] Widrow, B., McCool, J., and Ball, J. (1975)  
The complex LMS algorithm.  
*Proceedings of the IEEE*, Apr. 1975, 63, 719-720.
- [2] Reigler, R.L., and Compton, R.T., Jr. (1973)  
An adaptive array for interference rejection.  
*Proceeding of the IEEE*, June 1973, 61, 748.
- [3] Griffiths, L.J. (1969)  
A simple adaptive algorithm for real time processing in antenna arrays.  
*Proceedings of the IEEE*, Oct. 1969, 57, 1696-1794.
- [4] Compton, R.T., Jr. (1978)  
An adaptive array in spread spectrum communication.  
*Proceedings of the IEEE*, Mar. 1978, 66, 289.
- [5] DiCarlo, D.M., and Compton, R.T., Jr. (1978)  
Reference loop phase shift in adaptive arrays.  
*IEEE Transactions on Aerospace and Electronic Systems*, July 1978, AES-14, 599-607.
- [6] DiCarlo, D.M. (1979)  
Reference loop phase shift in an  $N$ -element adaptive array.  
*IEEE Transactions on Aerospace and Electronic Systems*, July 1979, AES-15, 576-582.



Y. Bar-Ness (M'69—SM'78) was born in Iraq, received the B.Sc. and M.Sc. degrees in electrical engineering from the Technion, Israel, in 1958 and 1963, respectively, and the Ph.D. degree in applied mathematics from Brown University, Providence, R.I., in 1969.

He has worked for the RAFAEL, Armament Development Authority, Israel, in the fields of communication and control and as a Chief Engineer of the Nuclear Medicine Department, Elscint Ltd., Haifa, Israel, in the field of control and image and data processing. In 1973 he joined the School of Engineering, Tel Aviv University, Israel, where he is an Associate Professor in control and communication systems. During 1978/1979 he was on sabbatical with the Division of Applied Mathematics, Brown University. Currently he is on leave of absence with the Department of System Engineering and the Valley Forge Research Center of the University of Pennsylvania, Philadelphia. His interests include coherent communications, phase-locked systems, signal processing, discrete control, and adaptive systems and arrays.

Dr. Bar-Ness is a member of Sigma Xi.

# Distortion Estimation of SAW Time Inversion System Based on Delta Function Approximation

HAGIT MESSER, STUDENT MEMBER, IEEE, AND YEHESKEL BAR-NESS, SENIOR MEMBER, IEEE

**Abstract**—Time inversion can be obtained using surface acoustic wave (SAW) devices with no more than two chirp filter elements. This time inversion method is based on the fact that the Fourier transform of a linear frequency modulated (FM) signal, whose envelope is modulated by a given time function, has (approximately) the time-inverted function as its amplitude. The different distortions inherent in the method are discussed. Procedures are suggested to eliminate some of these distortions, while others, inherent due to the approximation used, are estimated. It is shown that the average of the output distortion is upper-bounded by  $w^2/16\mu$ , where  $w$  is the signal bandwidth and  $\mu$  is the chirp filter's dispersive slope. Simulation results supplement the analysis.

## INTRODUCTION

THE time-inverted replica of a given signal is very important in many signal processing applications. Using surface acoustic wave (SAW) components, Nudd *et al.* [1] applied two identical inverse chirp-transform systems to a real time signal and obtained an output that is the time-inverted replica of the input. However, implementing the system using chirp devices requires at least four chirp filters. Arsenaute, *et al.* [2] used the Fresnel transform to obtain time inversion with three chirp filters. Recently, a new SAW time inversion system was

proposed [3]. It is based on the fact that the Fourier transform of a linear frequency modulated (FM) signal, which is envelope-modulated by a given time function, is (approximately) the time-inverted replica of the function. The idea is based on a certain approximated limit expression for the delta function [4]. A detailed comparison between the various time inversion methods was recently published in [5].

Here, a general analysis is presented for time inversion systems based on delta function approximation [3]. Two types of distortions are shown to result—*image distortion* and *delta function approximation distortion*—and expressions describing them are derived. Conditions are established for the elimination of image distortion using time gating. To estimate the second type of distortion, upper bounds are established on its time average. These bounds depend on the signal energy, the squared signal bandwidth, and the filter's slope. Using computer simulations, the time average of the delta function approximation distortion is computed for different values of signal bandwidth and filter dispersive slopes, and a comparison is made with the calculated upper bounds.

## SYSTEM ANALYSIS

Consider the system shown in Fig. 1 and let

$$f(t) = f(t), t_0 \leq t \leq t_0 + T$$

$$= 0, \text{ elsewhere} \quad (1)$$

$$m(t) = \exp [j\tau(\omega_1 \pm 2\mu(t - 2t_1 - T_1))]$$

$$+ cc, \quad t_1 \leq t \leq t_1 + T_1$$

$$= 0, \text{ elsewhere} \quad (2)$$

Manuscript received May 15, 1981. This work was supported in part by the Air Force Office of Scientific Research under Contract No. AFOSR-78-3688.

H. Messer is with the School of Engineering, Tel Aviv University, Ramat-Aviv 69978, Israel.

Y. Bar-Ness is with the Valley Forge Research Center, Moore School of Electrical Engineering, University of Pennsylvania, Philadelphia, PA 19104, on leave from: the Department of Electronic Systems, School of Engineering, Tel Aviv University, Ramat-Aviv 69978, Israel.

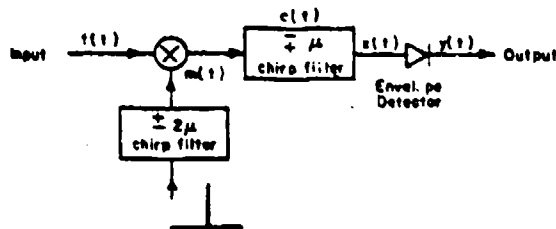


Fig. 1. Block diagram of system.

$$c(t) = \exp [j(\omega_2 \mp \mu(t - 2t_2 - T_2))] + cc, \quad t_2 \leq t \leq t_2 + T_2$$

$$= 0, \quad \text{elsewhere} \quad (3)$$

where  $cc$  stands for complex conjugate,  $f(t)$  is the input signal to be inverted,  $m(t)$  is the chirp modulation signal,  $c(t)$  is the chirp filter impulse response, respectively.  $\omega_1$ ,  $T_1$ , and  $t_1$ ,  $i = 1, 2$ , are the chirp filter's center frequencies, time dispersions, and minimum impulse response delay times, respectively. Notice the use of the double dispersion slope in the first chirp filter. The plus-minus signs mean that it is possible to have either up or down chirps.

The output of the system  $x(t)$  is given by

$$x(t) = (f(t) * m(t)) * c(t) \quad (4)$$

where the asterisk denotes the convolution. Substituting for  $c(t)$  and  $m(t)$  from (2) and (3), we obtain after some algebraic manipulations

$$x(t) = \exp [j(\omega_2 t \mp \mu t(t - 2t_2 - T_2))] (A(\Omega_1) + B(\Omega_2)) + cc \quad (5)$$

where

$$\Omega_1 = -\omega_1 + \omega_2 \mp 2\mu \left( t - (t_2 + t_2) - \frac{2T_1 + T_2}{2} \right)$$

$$\Omega_2 = \omega_1 + \omega_2 \mp 2\mu \left( t - (t_2 - 2t_1) - \frac{T_2 - 2T_1}{2} \right)$$

and  $A(\omega)$  and  $B(\omega)$  are the Fourier transforms of  $a(t) = f(t) \exp(\pm j\mu t^2)$  and  $b(t) = f(t) \exp(\mp j\mu t^2)$ , respectively.

Define the function

$$g(t, \mu) = \sqrt{\pm \mu / j\pi} \exp(\pm j\mu t^2). \quad (6)$$

Its Fourier transform is given by

$$G(\omega, \mu) = \exp(\mp j\omega^2 / 4\mu). \quad (7)$$

Using Taylor series expansion about  $1/\mu = 0$ , we have

$$G(\omega, \mu) = \sum_{n=0}^{\infty} \frac{1}{n!} \left( \mp j \frac{\omega^2}{4\mu} \right)^n$$

$$= \sum_{n=0}^{\infty} \frac{1}{n!} \exp\left(\pm j \frac{\pi n}{2}\right) \frac{1}{(4\mu)^n} (j\omega)^{2n}. \quad (8)$$

Now

$$\mathcal{F}\{r(t) \exp(\pm j\mu t^2)\} \triangleq \int_{-\infty}^{\infty} r(\tau) \exp(\pm j\mu \tau^2) \exp(-j\omega \tau) d\tau$$

$$= \sqrt{j\pi/\pm \mu} \exp(\mp j\omega^2 / 4\mu) \int_{-\infty}^{\infty} r(\tau) \left[ \sqrt{\pm \mu / j\pi} \exp\left(\pm j\mu \left(\tau \mp \frac{\omega}{2\mu}\right)^2\right) \right] d\tau \quad (9)$$

where  $\mathcal{F}$  stands for the Fourier transform. Using Parseval's formula together with (6) and (7), the integral in (9) becomes

$$\frac{1}{2\pi} \int_{-\infty}^{\infty} R(\Omega) \exp\left(\pm j \frac{\Omega^2}{4\mu}\right) \exp\left(\pm j \frac{\omega}{2\mu} \Omega\right) d\Omega$$

where  $R(\omega)$  is the Fourier transform of  $r(t)$ . Using (8), we have

$$\mathcal{F}\{r(t) \exp(\pm j\mu t^2)\} = \frac{1}{2\pi} \sqrt{j\pi/\pm \mu} \exp\left(\mp j \frac{\omega^2}{4\mu}\right) \cdot \int_{-\infty}^{\infty} R(\Omega) \sum_{n=0}^{\infty} \frac{1}{n!} \left(\pm j \frac{\Omega^2}{4\mu}\right)^n \exp\left(\pm j \frac{\omega}{2\mu} \Omega\right) d\Omega \quad (10)$$

or using the fact that

$$\sqrt{\pm j} = \exp\left(\mp j \left(2n - \frac{1}{2}\right) \frac{\pi}{2}\right),$$

we have

$$\mathcal{F}\{r(t) \exp(\pm j\mu t^2)\} = \frac{1}{2\pi} \sqrt{\frac{\pi}{\mu}} \sum_{n=0}^{\infty} \exp\left(\mp j \left(\frac{\omega^2}{4\mu} + \left(3n - \frac{1}{2}\right) \frac{\pi}{2} \cdot \frac{1}{n!} \cdot \frac{1}{(4\mu)^n}\right)\right) \cdot \int_{-\infty}^{\infty} R(\Omega) (j\Omega)^{2n} \exp\left(\pm j \frac{\omega}{2\mu} \Omega\right) d\Omega. \quad (11)$$

Finally, recognizing the last integral as the inverse Fourier transform, (11) yields

$$\mathcal{F}\{r(t) \exp(\pm j\mu t^2)\} = \sqrt{\frac{\pi}{\mu}} \sum_{n=0}^{\infty} \exp\left(\mp j \left(\frac{\omega^2}{4\mu} + \left(3n - \frac{1}{2}\right) \frac{\pi}{2} \cdot \frac{1}{n!} \cdot \frac{1}{(4\mu)^n}\right)\right) \cdot r^{(2n)}\left(\pm \frac{\omega}{2\mu}\right) \quad (12)$$

where

$$r^{(2n)}\left(\pm \frac{\omega}{2\mu}\right) = \frac{d^{2n}}{dt^{2n}} r(t) \Big|_{t=\pm \omega/2\mu}.$$

Applying this result to  $A(\omega)$  and  $B(\omega)$ , we obtain from (5)

$$x(t) = \sqrt{\frac{\pi}{\mu}} \sum_{n=0}^{\infty} \frac{1}{n!} \left[ \frac{1}{(4\mu)^n} \cos \phi_1 f^{(2n)}\left(\pm \frac{\Omega_1}{2\mu}\right) + 3^{-(n+1/2)} \cos \phi_2 \cdot f^{(2n)}\left(\mp \frac{\Omega_2}{6\mu}\right) \right] \quad (13)$$

where

$$\begin{aligned}\phi_1 &= (2\omega_2 - \omega_1) t \mp 2\mu t (t - 2(t_1 + t_2) - (T_1 + T_2)) \\ &\mp \psi_1 \mp \left(3n - \frac{1}{2}\right) \frac{\pi}{2} \\ \phi_2 &= \frac{2\omega_2 - \omega_1}{3} t \mp \frac{2\mu}{3} t (t - 2(t_1 + t_2) - (T_1 + T_2)) \\ &\pm \psi_2 \pm \left(3n - \frac{1}{2}\right) \frac{\pi}{2}\end{aligned}\quad (14)$$

and

$$\begin{aligned}\psi_1 &= \frac{1}{4\mu} \left( \omega_2 - \omega_1 \pm 2\mu \left( 2t_1 + t_2 + \frac{2T_1 + T_2}{2} \right) \right)^2 \\ \psi_2 &= \frac{1}{12\mu} \left( \omega_1 + \omega_2 \mp 2\mu \left( 2t_1 - t_2 + \frac{2T_1 - T_2}{2} \right) \right)^2.\end{aligned}$$

Thus,  $x(t)$  is composed of two terms. The first term includes chirp signals centered around the frequency  $2\omega_2 - \omega_1$ , whose dispersive slopes are  $2\mu$ , and shifted in phase by  $\mp(\pi/2)$  with respect to one another. The envelopes of these chirp signals are delayed time-inverted replicas of the input and its even derivatives. Similarly, the second term contains chirp signals centered around the frequency  $(2\omega_2 - \omega_1)/3$ , whose dispersive slopes are  $2\mu/3$ , and phase-shifted by  $\pm\pi/2$  with respect to one another. The envelopes of these signals are delayed replicas of the input signal and its even derivatives, which are time-scaled but not time-inverted. Notice, however, that the delay resulting from the first group of signals is different from that of the second group. Hence, the second sum of  $x(t)$  represents a distortion term which we call *image distortion*.

For  $n = 0$ , the first term in (13) is the desired signal, which is given by

$$\begin{aligned}x_d(t) &= \sqrt{\frac{\pi}{\mu}} \cos \left[ (2\omega_2 - \omega_1) t \mp 2\mu t (t - 2(t_1 + t_2) \right. \\ &\quad \left. - T_1 + T_2) \mp \psi_1 \pm \frac{\pi}{2} \right] f \left( \pm \frac{\omega_2 - \omega_1}{2} \right. \\ &\quad \left. - t + 2t_1 + t_2 + \frac{2T_1 + T_2}{2} \right).\end{aligned}\quad (15)$$

Notice that for large enough  $\mu$ , terms with  $n \neq 0$  may be neglected from the first sum in (13). Also under this condition, the image distortion terms will vanish except for the first one:

$$\begin{aligned}x_I(t) &= \sqrt{\frac{\pi}{3\mu}} \cos \left[ \frac{2\omega_2 - \omega_1}{3} t \mp \frac{2}{3} t (t - 2(t_1 + t_2) \right. \\ &\quad \left. - (T_1 + T_2)) \pm \psi_2 \mp \frac{\pi}{2} \right] \\ &\quad \cdot f \left( \mp \frac{\omega_1 + \omega_2}{6\mu} + \frac{t}{3} - \frac{2t_2 - 4t_1 + T_2 - 2T_1}{6} \right).\end{aligned}\quad (16)$$

Now, if the system bandwidth (which depends on  $\mu$ ) is much larger than the input signal bandwidth, then it might be possible to use a delta function as an approximation for  $g(t, \mu)$  in

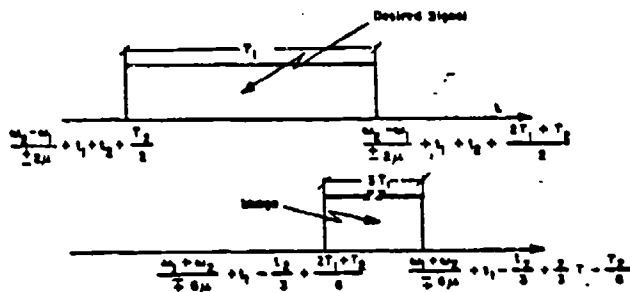


Fig. 2. Relative time intervals of desired and imaged signals.

(6). In this case (refer to [3]) we have

$$\mathcal{F}(r(t) \exp(\pm j\mu t^2)) = \sqrt{\frac{j\pi}{\pm\mu}} \exp\left(\mp j \frac{\omega^2}{4\mu}\right) \cdot r\left(\pm \frac{\omega}{2\mu}\right) \quad (17)$$

for any slowly varying function,  $r(t)$  and large  $\mu$ . Applying this approximation to  $A(\omega)$  and  $B(\omega)$  in (5),  $x(t)$  will include only  $x_d(t)$  and  $x_I(t)$  (of (15) and (16), respectively). In the sequel, the first sum in (13), except for  $x_d(t)$ , will be called *delta function approximation distortion*.

#### ELIMINATION OF IMAGE DISTORTION

Because of the difference in envelope delays of the image distortion and the desired signal, it is possible to eliminate the distortion terms by using time gating. To derive the conditions that are necessary for time gating, Fig. 2 depicts the timing relations between the desired and imaged signals. It shows the case where  $t_0 = t_1$ , namely, the input starts at the same time when the sampling chirp  $m(t)$  begins and lasts for a time not less than the sampling time  $T_1$ . Clearly, to be able to use time gate for image elimination, we must have either

$$\begin{aligned}t_1 + t_2 + \frac{2T_1 + T_2}{2} \pm \frac{\omega_2 - \omega_1}{2\mu} &\leq t_1 - \frac{t_2}{3} \\ &+ \frac{2T_1 - T_2}{6} \mp \frac{\omega_1 + \omega_2}{6\mu}\end{aligned}$$

or

$$t_1 + t_2 + \frac{T_2}{2} \pm \frac{\omega_2 - \omega_1}{2\mu} \geq t_1 - \frac{t_2}{3} + \frac{20T_1 - T_2}{6} \mp \frac{\omega_1 + \omega_2}{6\mu}$$

By rearranging, we have

$$\pm 2\mu (2t_2 + T_1 + T_2) \leq \omega_1 - 2\omega_2$$

or

$$\pm 2\mu (2t_2 + T_2 - 5T_1) \geq \omega_1 - 2\omega_2. \quad (18)$$

#### ESTIMATION OF DELTA FUNCTION APPROXIMATION DISTORTION

Using the fact that the first term of the sum in (10) is given by

$$\frac{1}{2\pi} \int_{-\infty}^{\infty} R(\Omega) \exp\left(\pm j \frac{\omega}{2\mu} \Omega\right) d\Omega = r\left(\pm \frac{\omega}{2\mu}\right)$$

we have

$$\begin{aligned} \mathcal{F}\{r(t) \exp(\pm j\mu t^2)\} &= \sqrt{\frac{j\pi}{\pm\mu}} \exp\left(\mp j \frac{\omega^2}{4\mu}\right) \left[ r\left(\pm \frac{\omega}{2\mu}\right) \right. \\ &\quad \left. + \frac{1}{2\pi} \sum_{n=1}^{\infty} \frac{1}{n!} \left(\frac{\pm j}{4\mu}\right)^n \int_{-\infty}^{\infty} \right. \\ &\quad \left. \cdot \Omega^{2n} R(\Omega) \exp\left(\pm j \frac{\omega}{2\mu} \Omega\right) d\Omega \right]. \end{aligned} \quad (19)$$

Assuming that the image distortion is removed, the output envelope  $y(t)$  of the system in Fig. 1 can be obtained from (5) together with (19):

$$\begin{aligned} y(t) &= f(T' - t) + \frac{1}{2\pi} \sum_{n=1}^{\infty} \frac{1}{n!} \left(\frac{j}{4\mu}\right)^n \int \Omega^{2n} F(\Omega) \\ &\quad \cdot \exp\left(j \frac{\Omega}{2\mu} \Omega\right) d\Omega \end{aligned} \quad (20)$$

where

$$T' = 2t_1 + t_2 + \frac{2T_1 + T_2}{2} \pm \frac{\omega_2 - \omega_1}{2\mu}. \quad (21)$$

Thus, the error (distortion)  $\epsilon(t)$  caused by the delta function approximation is given by the second term in (20). Using triangle and Schwarz inequalities, we get

$$\begin{aligned} |\epsilon(t)| &\leq \frac{1}{2\pi} \sum_{n=1}^{\infty} \left[ \int \left| \frac{1}{n!} \left(j \frac{\Omega}{4\mu}\right)^n \right|^2 d\Omega \right. \\ &\quad \left. \cdot \int |F(\Omega) \exp[j(T' - t)\Omega]|^2 d\Omega \right]^{1/2} \\ &= \frac{1}{2} \sum_{n=1}^{\infty} \left[ \left(\frac{1}{n! (4\mu)^n}\right)^2 \int \Omega^{4n} d\Omega \int |F(\Omega)|^2 d\Omega \right]^{1/2} \end{aligned} \quad (22)$$

Since  $f(t)$  is band-limited to  $w$ , the first integral equals

$$\frac{w}{4n+1} \left(\frac{w}{2}\right)^{4n}.$$

The second integral is the energy  $E$  of the input signal  $f(t)$ . Hence, (22) yields

$$\begin{aligned} |\epsilon(t)| &\leq \sum_{n=1}^{\infty} \left[ Ew \frac{1}{4n+1} \left(\frac{1}{n!} \left(\frac{w^2}{16\mu}\right)^n\right)^2 \right]^{1/2} \\ &= \sqrt{Ew} \sum_{n=1}^{\infty} \frac{1}{n!} \left(\frac{w^2}{16}\right)^n \frac{1}{\sqrt{4n+1}}. \end{aligned} \quad (23)$$

Equation (23) provides a uniform bound on the distortion of the delta function approximation, and hence it is also a bound for the average distortion,

$$\frac{1}{T} \int_0^T |\epsilon(t)| dt.$$

Also, notice that

$$\sum_{n=1}^{\infty} \frac{1}{n!} \left(\frac{w^2}{16}\right)^n \frac{1}{\sqrt{4n+1}} < \sum_{n=1}^{\infty} \frac{1}{n!} \left(\frac{w^2}{16\mu}\right)^n = \exp\left(\frac{w^2}{16\mu}\right) - 1$$

and therefore we have another bound, namely,

$$|\epsilon(t)| \leq \sqrt{Ew} \left( \exp\left(\frac{w^2}{16\mu}\right) - 1 \right). \quad (24)$$

Using Cauchy inequality in (23) we get

$$\begin{aligned} |\epsilon(t)| &\leq \sqrt{Ew} \left[ \sum_{n=1}^{\infty} \left( \frac{1}{\sqrt{4n+1}} \cdot \frac{1}{n!} \right)^2 \right]^{1/2} \\ &\quad \cdot \left[ \sum_{n=1}^{\infty} \left( \frac{w^2}{16\mu} \right)^{2n} \right]^{1/2} \\ &= \sqrt{Ew} \cdot 0.48 \cdot \frac{w^2/16\mu}{[1 - (w^2/16\mu)^2]^{1/2}}. \end{aligned} \quad (25)$$

Notice that for (25) to apply, we must have  $w^2/16\mu < 1$ . The three bounds of (23), (24), and (25) are depicted in Fig. 3.

#### COMPUTER SIMULATION RESULTS

The system of Fig. 1 was simulated on a digital computer. The chirp filters were modeled by their impulse responses, as in (2) and (3), the basic parameters being

$$\omega_1 = \omega_2 = 2\pi (60 \text{ MHz})$$

$$t_1 = t_2 = 0$$

$$\mu \triangleq \mu_0 = 0.2 \text{ MHz}/\mu\text{s}$$

$$T_1 = 6.25 \mu\text{s}$$

$$T_2 = 25 \mu\text{s}.$$

The input signal was of the form

$$\begin{aligned} f(t) &= \sin(\pi/T_1)t + 0.5 \sin(2\pi/T_1)t, \quad 0 \leq t < T_1 \\ &= 0, \text{ elsewhere} \end{aligned} \quad (26)$$

where  $T_1 = T_1$ . Fig. 4 shows the input signal in the time and frequency domains.

The continuous signals  $f(t)$ ,  $m(t)$ , and  $c(t)$  were sampled every  $0.01 \mu\text{s}$ , and the sampled product of  $f(t)$  and  $m(t)$  was convolved with the sampled  $c(t)$  using fast Fourier transform (FFT), by multiplying them in the frequency domain and then finding the inverse transformation using inverse fast Fourier transform (IFFT).

To show the effect of  $w^2/16\mu$  on the output distortion, the simulation was run four times, each with a different  $\mu$  ( $\mu_0$ ,  $\mu_0/2$ ,  $\mu_0/4$ ,  $\mu_0/5$ ) and all with the same input signal (of bandwidth  $w$ ). Since  $B = 2\mu T$ , changing  $\mu$  while keeping  $T$  (the chirp filter dispersive time) fixed means that the filter bandwidth is changed. Fig. 5 depicts the input and the output of the system for each case. The lower traces show  $x(t)$  (refer to Fig. 1) while the upper trace shows  $m(t)$  modulated by  $f(t)$ , which is the input to the convolving chirp filter  $c(t)$ .

To calculate the amount of distortions, the output was envelope-detected by finding the maximum value of 25 points

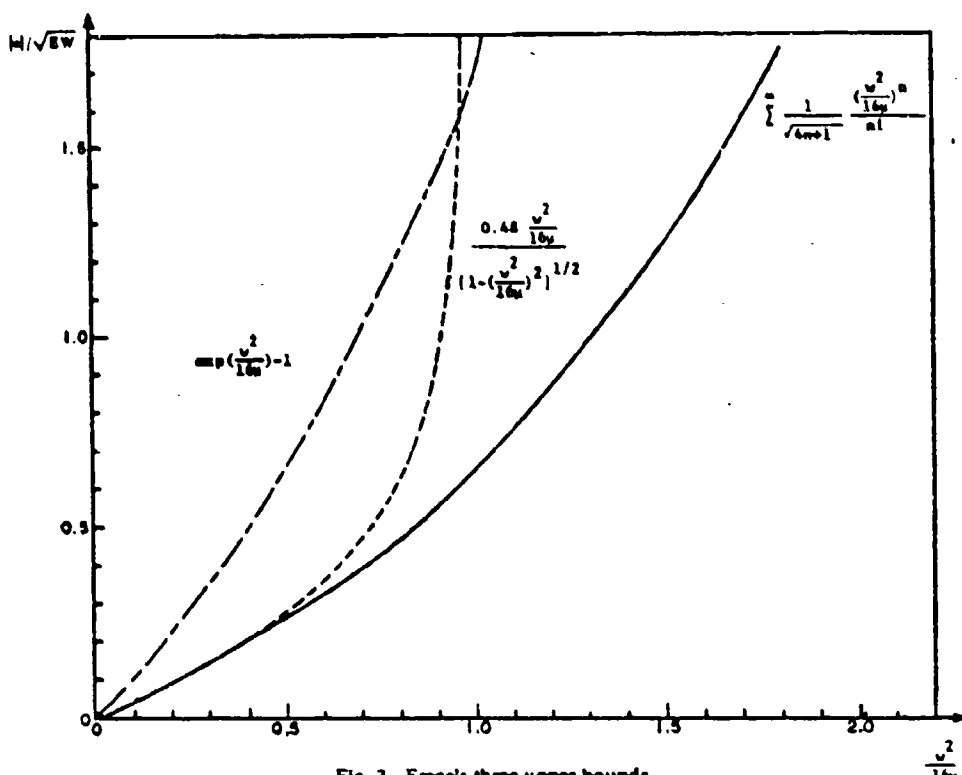


Fig. 3. Error's three upper bounds.

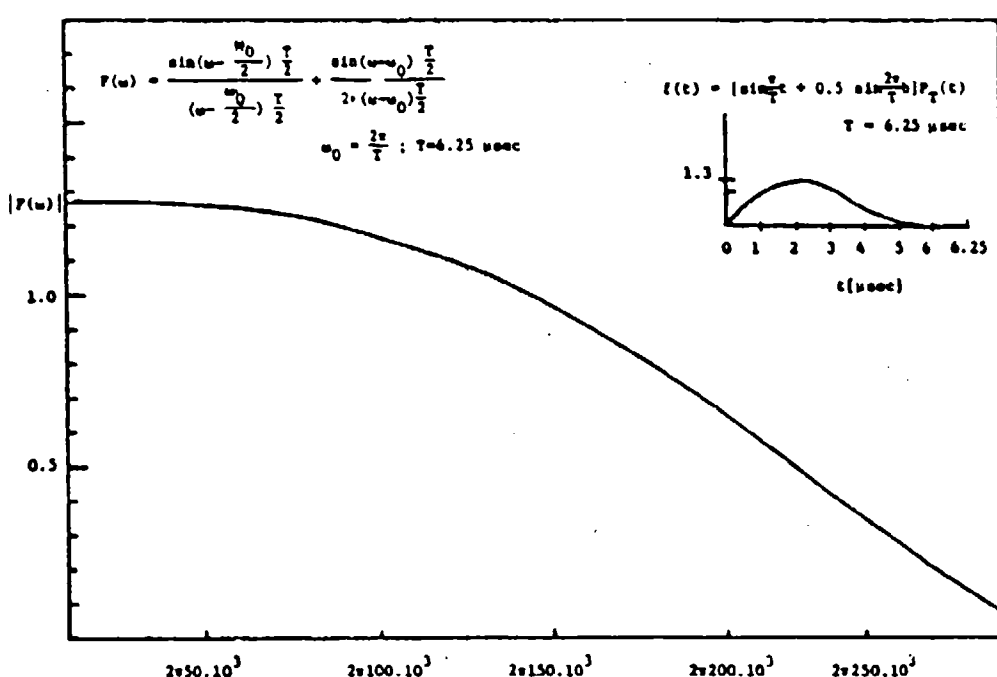


Fig. 4. Simulated input signal in time and frequency domains.

in  $x(t)$ ; this was then used as the new value for the envelope detected output, and the procedure repeated for the next 25 points, and so on. The constant delay between the input and output was then eliminated, and the envelope-detected output compared with the time-inverted replica of the input. This was done for all the cases shown in Fig. 5 and repeated for a

different input signal,  $f(t)$  of (26) with  $T_i = (2/3)T_1$ . The error is calculated by

$$\gamma = \frac{1}{N} \sum_{k=1}^N |f(T_i - k) - y(k)| \quad (27)$$

where  $y(k)$  is the envelope-detected desired output without

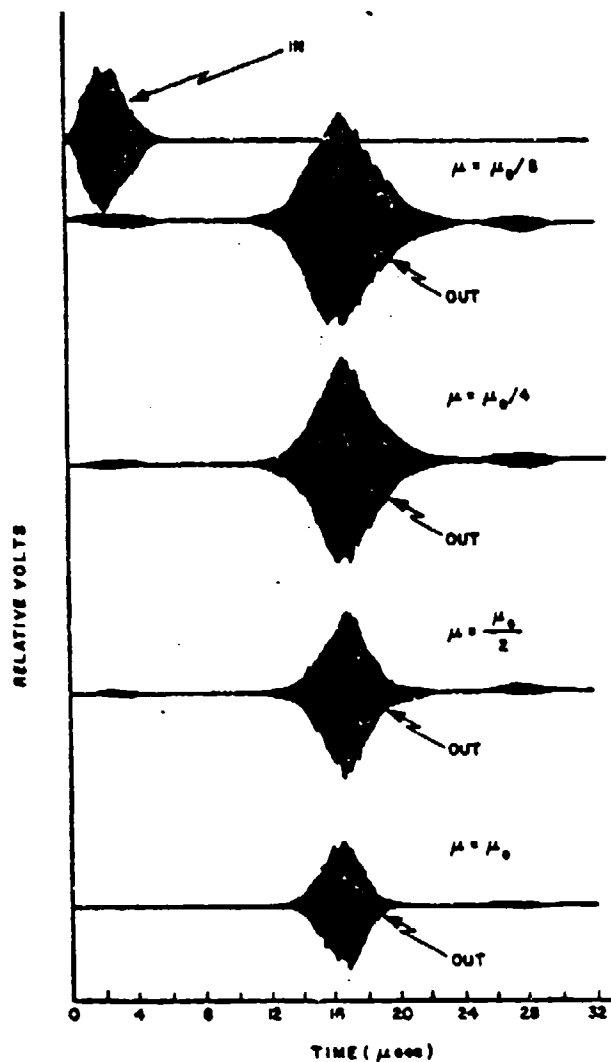


Fig. 5. Effect of  $w^2/16\mu$  on output distortion.

the constant delay, with  $f(k)$  and  $y(k)$  being of same magnitude. Thus,  $\gamma$  represents the average error

$$\frac{1}{T} \int_0^T |e(t)| dt$$

in the sampled form.

Fig. 6 depicts  $\gamma$  as a function of  $\mu$  for the two different inputs, of bandwidths  $w_1$  and  $w_2$ ,  $w_2 > w_1$ , as well as showing the theoretical upper bounds on the error, calculated for the two cases using (23).

#### DISCUSSION AND CONCLUSION

The output distortions in delta function approximation time inversion systems were examined. It was shown that the image distortion can be eliminated using a time gate or by using a bandpass filter at the output, with bandwidth  $w$  centered at  $2\omega_2 - \omega_1$ , when  $2(2\omega_2 - \omega_1)/3 > 2w/3$ .

The delta function approximation distortion cannot be re-

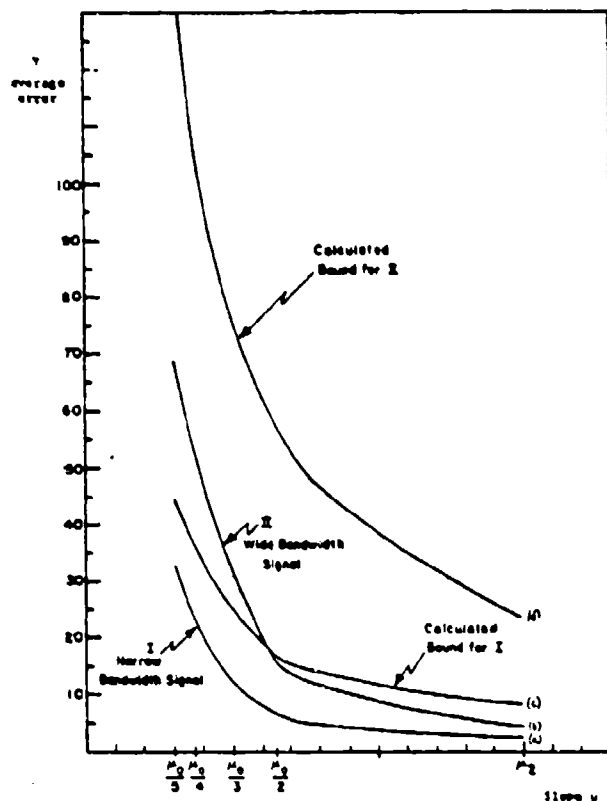


Fig. 6. Average error as function of  $\mu$  for fixed  $w$ . (a) Simulation results for  $w_1$ . (b) Simulation results for  $w_2 > w_1$ . (c) Calculated upper bound for  $w_1$ . (d) Calculated upper bound for  $w_2 > w_1$ .

moved because  $\mu$  is finite. It was shown, however, that the error caused by this distortion is upper-bounded, and the bound grows with  $w^2/16\mu$ . Computer simulation results were shown to support this theory. Thus Fig. 5 shows that for fixed  $w$ , the distortions grow with  $1/\mu$ , and from Fig. 6 it can be shown that for fixed  $\mu$ , the average error grows with  $w$ . Furthermore, the simulated average error was shown to be bounded by the calculated theoretical bounds.

These results mean that if an input signal of a certain time duration needs to be time-inverted, the system of Fig. 1 is satisfactory if the chirp filter's bandwidth is much larger than the bandwidth of the input signal. If such filters do not exist or are too expensive, another time inversion system can be used [5]. However, more chirp filters will be required.

#### REFERENCES

- [1] G. R. Nudd and O. W. Otto, "Chirp signal processing using acoustic surface wave filters," *Proc. 1975 IEEE Ultrason. Symp.*, pp. 944-950.
- [2] D. R. Arsenault and P. Das, "SAW Fresnel transform devices and their applications," *Proc. 1977 IEEE Ultrason. Symp.*, pp. 1264-1270.
- [3] H. Messer, Y. Bar-Ness, and H. Gilboa, "New SAW time inversion system," *Electron. Lett.*, vol. 15, pp. 214-215, 1979.
- [4] A. Papoulis, *Signal Analysis*. New York: McGraw-Hill, 1977, pp. 267-271.
- [5] H. Messer and Y. Bar-Ness, "Different time-inversion methods using SAW devices," *Proc. 11th IEEE Convention*, Tel-Aviv, Israel, 1979.

# WIDEBAND INSTANTANEOUS FREQUENCY MEASUREMENTS (IFM) USING SAW DEVICES\*

Y. Bar-Ness\*\*

Dept. of Systems Engineering  
The Moore School of Electrical Engineering  
University of Pennsylvania  
Philadelphia, Pennsylvania 19104

H. Messer

Dept. of Electrical Communication  
Control and Computer Systems  
School of Engineering  
Tel-Aviv University  
Tel-Aviv Isreal

## Abstract

A popular method of performing frequency measurement is by using the autocorrelation of the signal to be measured with a delayed (fixed delay) version of the same signal. A disadvantage of this approach is the ambiguity in the result unless the input bandwidth is limited.

Instead, a variable delay line controlled by a feedback arrangement is proposed in this work. This approach using SAW components for the voltage controlled delay line (VCDL) is shown to provide a wide-band measurement with no ambiguity. Systems with different feedback loop filters are analyzed and compared. Some computer simulations and experimentally set-up results are also included.

## 1. Introduction

Frequency measuring systems are important in many applications. One popular method of performing such measurements is to autocorrelate the signal to be measured with a delay version of the same signal. Such a system arrangement which is depicted in figure 1 is usually termed instantaneous frequency measurement (IFM). The output voltage can be related to multivalues of the incoming signal frequency unless the possible bandwidth of frequencies is limited. In fact, unambiguous measurement can be obtained only if the input bandwidth  $\Delta f$  is less than  $1/2\tau$  where  $\tau$  is the fixed delay. Furthermore, the relation between the output voltage and the frequency to be measured is highly nonlinear unless further restriction on bandwidth is imposed.

In recent years [1] surface acoustic wave (SAW) components were used to advantage in many different applications in communication and signal processing. One of these components which is widely used in analog processing is the chirp filter (see for example [2]). A system that performs the function of a voltage controlled delay line VCDL can be procured using a cascaded arrangement of two chirp filters [3,4].

\*This work is partially supported by the Air Force Office of Scientific Research under grant No. AFOSR-78-3688.

\*\*Currently on leave of absence from School of Engineering, Tel-Aviv University.

In this work we consider the use of a variable delay line for IFM. The correlator output is filtered and fed-back to control the delay line. This feedback system that mathematically resembles a Frequency Modulation Feedback (FMB) arrangement enables one to obtain wideband IFM. In fact, such an arrangement might be used as well in other applications such as in wideband FM detection. SAW voltage controlled delay line will be utilized as a variable delay. The work includes setting up the dynamic equations of different loop filters. The phase plane representation is used to determine the singularities of the system and to aid in combating the ambiguity problem. A comparison of performance with different loop filters is made by considering the necessary limitations needed to have unambiguous measurements, as well as by the acquisition time of the system, i.e. the time that it takes for the output (measuring) voltage to get sufficiently close to its final value.

It is shown that with proper selection of the chirp filters used in the VCDL, the correspondence of input frequency to voltage output is unique, and hence the ambiguity problem is eliminated. It is also shown that the frequency measuring bandwidth, which practically equals the VCDL bandwidth, is essentially large and depends only on the chirp filter parameters.

Computer simulation and experimental results support the theory.

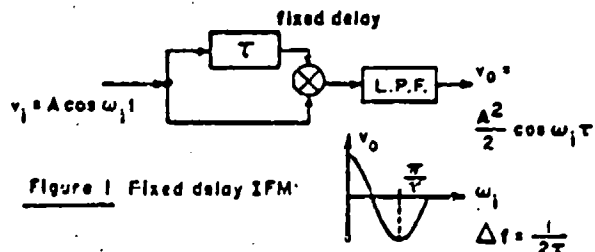


Figure 1 Fixed delay IFM

## 2. System Block Diagram and Equation

The block diagram of a variable delay IFM is depicted in figure 2. The VCDL is considered composed of a frequency controlled variable delay line (FCDL) and a voltage controlled oscillator. If the loop gain is sufficiently large or the loop filter includes a pole at zero, the system steady state is at a point where the autocorrelation of

the input is close to or at zero. Particularly for a single tone input, the autocorrelation function is a sine wave with the same frequency as the input. Using the relation between the output voltage  $v_o(t)$  and the signal autocorrelation's, zero crossing we facilitate our frequency measurements.

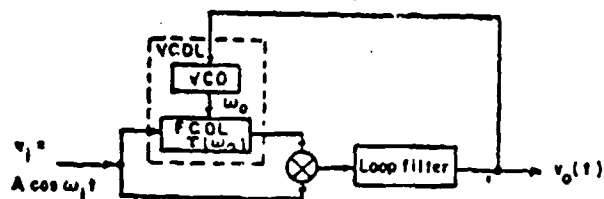


Figure 2 Variable delay IFM

The VCDL characteristic is given by [4]

$$\tau(\omega_o) = c_1 + c_2 \omega_o, \quad \omega_o = k_v v_o \quad (1)$$

where  $k_v$  is the VCO gain and  $c_1$  and  $c_2$  are constants which depend on the FCOL's chirp filter parameters. The general loop equation is

$$v_o(t) = kF(p) v_i(t) v_1(t - c_1 - c_2 k_v v_o(t)) \quad (2)$$

or

$$\omega_o(t) = k_1 F(p) v_i(t) v_1(t - c_1 - c_2 \omega_o(t)) \quad (3)$$

where  $F(p)$  with  $p \Delta d/dt$ , is the Heaviside operator representing the loop filter transfer function and  $k = k_1 k_v$  represents the total loop gain.

For frequency measurement we assume  $v_i = A \cos \omega_1 t$  where  $f_1 = \omega_1/2\pi$  is the input frequency to be measured. With this (3) becomes

$$\omega_o(t) = k_1 F(p) \cos[\omega_1(c_1 - c_2 \omega_o(t))] \quad (4)$$

where we neglect the double frequency terms and let  $A = \sqrt{2}$ . Together with  $v_o = \omega_o/k_v$ , this adynamic equation determines the transient as well as the steady state components of the output measurement voltage as a function of input frequency,  $\omega_1$ , to be measured. This, obviously, depends on the filter transfer function  $F(p)$ . In the next sections we discuss in some detail the case when this filter is formed of a perfect integrator and only present some result related to the cases with other different filter transfer functions.

### 2.1 The Perfect Integrator Loop Case

For this case  $F(p) = 1/p$  and (4) becomes

$$\dot{\omega}_o(t) = k_1 \cos[\omega_1(c_1 + c_2 \omega_o(t))] \quad (5)$$

where  $\dot{\omega}_o(t) = d\omega_o(t)/dt$ . This is a first order non-linear differential equation, whose solution is

$$\omega_o(t) = \frac{1}{c_2} \left[ \frac{(4n+1)\pi}{2\omega_1} - c_1 \right] + \frac{1}{\omega_1} \left[ \tan^{-1} \tan\left(-\frac{\pi}{4} + \frac{\omega_1}{2}(c_1 + c_2 \omega_o(0))\right) \right] e^{-\omega_1 c_2 k_1 t} \quad (6)$$

and for  $c_2 k_1 > 0$  we have for the steady state

$$\omega_{oss} = \frac{1}{c_2} \left[ \frac{(4n+1)\pi}{2\omega_1} - c_1 \right] \quad (7)$$

or for the output voltage

$$v_{oss} = \frac{1}{c_2 k_v} \left[ \frac{(4n+1)\pi}{2\omega_1} - c_1 \right] \quad (8)$$

That is, the output depends inversely on the input signal frequency with ambiguities resulting from the different possible values of  $n$ . To investigate the characteristics of the solution, we use the phase plane representation of (5) as it is done in figure 3. Clearly, the system will settle in the steady state at one of the stable singular points of (7) depending on the initial value  $\omega_o(0)$ . If we choose the stable point corresponding to  $n=0$  as our desired solution we must limit  $\omega_o(0)$  to the region

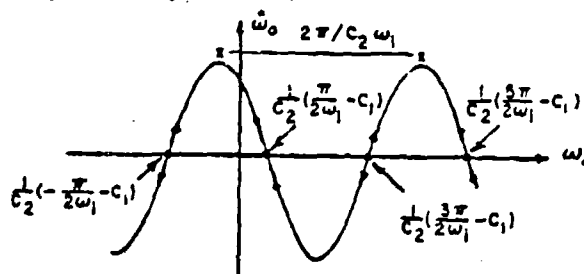


Figure 3 Phase plane of the system's dynamic equation with perfect integrator

$$-\frac{1}{c_2} \left( \frac{\pi}{2\omega_1} + c_1 \right) < \omega_o(0) < \frac{1}{c_2} \left( \frac{3\pi}{2\omega_1} - c_1 \right) \quad (9)$$

for any  $\omega_1$ ,

$$\omega_c - \frac{\Delta\omega}{2} \leq \omega_1 \leq \omega_c + \frac{\Delta\omega}{2} \quad (10)$$

where  $\Delta\omega$  is the input (radian)bandwidth and  $\omega_c$  is the center frequency of this band. The smallest region for  $\omega_o(0)$  is given from (9) by

$$-\frac{1}{c_2} \left[ \frac{\pi}{2(\omega_c + \Delta\omega/2)} - c_1 \right] < \omega_o(0) < \frac{1}{c_2} \left[ \frac{3\pi}{2(\omega_c + \Delta\omega/2)} - c_1 \right] \quad (11)$$

which leads to a VCO output frequency range

$$\omega_o = \frac{2\pi}{(\omega_c + \Delta\omega/2) c_2} \quad (12)$$

and VCO center frequency,

$$\omega_v = \frac{1}{c_2} \left( \frac{\pi}{2(\omega_c + \Delta\omega/2)} - c_1 \right) \quad (13)$$

This limitation on the output frequency of VCO is not sufficient to obtain a unique singular stable point solution, unless we assure that the stable point for the extreme case with  $\omega_1 = \omega_c - \frac{\Delta\omega}{2}$  stays within the region of (11). That is

$$\frac{1}{c_2} \left[ \frac{\pi}{2(\omega_c - \Delta\omega/2)} - c_1 \right] < \frac{1}{c_2} \left[ \frac{3\pi}{2(\omega_c + \frac{\Delta\omega}{2})} - c_1 \right] \quad (14)$$

or

$$\Delta\omega/\omega_c < 1 \quad (15)$$

which means the input bandwidth has to be limited to less than 100% of its center frequency. However, the system bandwidth is limited by the VCDL bandwidth which is less than 100% and (15) follows.

For a SAW voltage controlled delay line we have [4]  $c_2 = 1/2\mu$ , when  $\mu$  is the chirp filter slope and,

$$B_s = \Delta\omega = 2\mu T - \Delta\omega_0 \quad (16)$$

where  $B_s$  is the bandwidth of the VCDL (for a configuration with two identical chirp filters) and  $2\mu T$  is the bandwidth of the chirp filters. Substituting (12) into (16), we obtain after some algebraic manipulation

$$\Delta\omega^2 + 2\Delta\omega(\omega_c - \mu T) + 4\mu(2\pi - T\omega_c) = 0 \quad (17)$$

which has a positive solution,

$$\Delta\omega = \mu T - \omega_c + \sqrt{(\mu T - \omega_c)^2 - 8\mu\pi} \quad (18)$$

provided  $\mu T + \omega_c \geq 2/2\mu\pi$ . This is the system bandwidth, which is very close to the filter's bandwidth  $2\mu T$  if the second term under the root sign is sufficiently small.

Beside the system bandwidth, another important parameter in designing IFM is the acquisition time,  $T_a$ . This will be defined as the time it takes the system to reach a state where the output voltage gets to 90% of its final steady state value. One can show, using (5), that the time  $T_a$  that it takes  $v_o(t)$  to get to the value  $v_{op} = v_o(T_p)$ , starting at  $v_o(0) = 0$ , is given by

$$T_p = \int_0^{T_p} dt = \frac{1}{c_2 k \omega_1} \ln \left( \frac{\tan[-\frac{\pi}{2} + \omega_1(c_1 + c_2 k v_{op})]}{\tan[-\frac{\pi}{4} + \frac{\omega_1 c_1}{2}]} \right) \quad (19)$$

Using (8) we have for  $n = 0$

$$T_a = -\frac{1}{c_2 k \omega_1} \ln(\alpha) \quad (20)$$

where

$$\alpha = \frac{\tan(0.005 \omega_1 c_1 - 0.025\pi)}{\tan(0.5 \omega_1 c_1 - 0.25\pi)} \quad (21)$$

From which we notice that the acquisition time depends on the VCDL parameters  $c_1$  and  $c_2$  as well as on the loop gain  $k$  and the measured input frequency  $\omega_1$ . For any input frequency,  $T_a$  is larger when  $c_2$  and  $k$  are smaller.

## 2.2 Other loop filtering cases

We consider two additional kinds of loop filters in this section;

$$a. F(p) = \frac{p+a}{p}$$

Equation (4) becomes,

$$\dot{\omega}_o(t) = \frac{a k_1 \cos[\omega_1(c_1 + c_2 \omega_o(t))]}{1 + \omega_1 c_2 k \sin[\omega_1(c_1 + c_2 \omega_o(t))]} \quad (22)$$

The steady state solutions of this equation are the same as those of the previous case, so that the whole discussion concerning the suitable design that leads to non-ambiguous solutions applies to this case as well. However the acquisition time is different and given by

$$T_a = -\frac{1}{a c_2 k \omega_1} \ln[\alpha \beta^B] \quad (23)$$

where  $\alpha$  as in (21),

$$\beta = \frac{\cos(0.1 \omega_1 c_1 + 0.45\pi)}{\cos(\omega_1 c_1)} \quad (24)$$

and

$$B = \omega_1 c_2 k \quad (25)$$

Comparing (22) with (20) we conclude the following,

$$\frac{\ln \beta}{\ln \alpha} > \frac{a-1}{B} \Rightarrow T_{a1} < T_{a2} \quad (26)$$

$$\frac{\ln \beta}{\ln \alpha} > \frac{a-1}{B} \Rightarrow T_{a1} > T_{a2} \quad (27)$$

where  $T_{a1}$  and  $T_{a2}$  are the acquisition times of the previous and the current loop filter cases, respectively. That is with the same system's parameters and input frequency, different value of  $a$  (the zero of the loop filter) can make either of these cases have smaller acquisition time



8. A NULLING TECHNIQUE FOR MICROWAVE IMAGING WITH A RANDOM THINNED ARRAY.\*

C. Nelson Dorny

Lih-Tyng Hwang

INTRODUCTION

Target Model for Microwave Imaging

Microwave images differ from optical images. The wavelengths of light are much smaller than those of microwaves. Most objects are sufficiently rough at optical wavelengths to scatter light, permitting formation of visual images of objects. At microwave wavelengths many objects have smooth surfaces which do not scatter radiation, but reflect it quasi-specularly. An aircraft imaged by a radio camera is an example: it contains flat surfaces such as the fuselage and some small details such as windows, edges and corners on the aircraft. A microwave antenna "sees" the fuselage only when a specular return is received. The flat surface appears "black" except in a narrow viewing sector. In this situation, a strong highlight within the image is a function of transmitter-object-receiver geometry, and therefore does not necessarily help the user in identifying the object. The weaker signals received from the small scattering objects (if strong enough to be visible) tend to outline the object being viewed; their relative locations are not affected by the geometry. They generally can provide information for object recognition. Since the scattering sources are weak relative to the highlights, wide dynamic range of the target echoes becomes the first assumption in the target model. Since highlights tend to appear only over a very narrow angle in the image and since the scattering objects tend to be small and isolated, we model targets for microwave imaging by a set of discrete point scatterers.

Conventional Spatial Signal Processing

We have modeled a target scene by a discrete set of scatterers with wide dynamic range. Assume the targets are in the far field of the array. Then the scene function can be written as

$$s(u) = \sum_{k=1}^K a_k \delta(u - u_k) \quad (1)$$

Where  $u = \sin\theta$ ,  $\theta$  is the angle measured from the broadside of the antenna array,  $a_k$  is the complex strength of the  $k^{th}$  target at "angle"  $u_k$ , and  $K$  is the number of targets.

\*This work is supported by the Air Force Office of Scientific Research, under Grant No. AFOSR-82-0012.

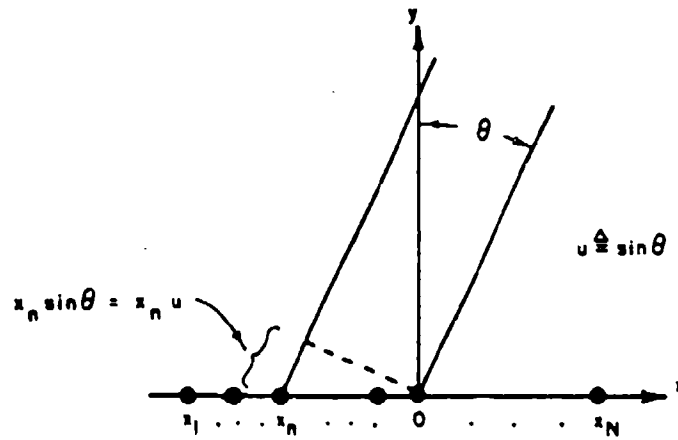


FIGURE 8.1 ARRAY GEOMETRY

Let  $x_n$  denote the position of the  $n^{th}$  element of the array as shown in Figure 8.1. The signal received at the  $n^{th}$  element can be represented as

$$S(x_n) = \sum_{k=1}^K a_k e^{-j \frac{2\pi}{\lambda} x_n u_k} \quad (2)$$

$S(x_n)$  is the Fourier transform of the scene function. To image the scene, that is, to estimate the magnitudes, phases and directions of the target scatterer, the conventional approach is to take the inverse Fourier transform of the aperture distribution  $S(x_n)$ , as shown in Figure 8.2.

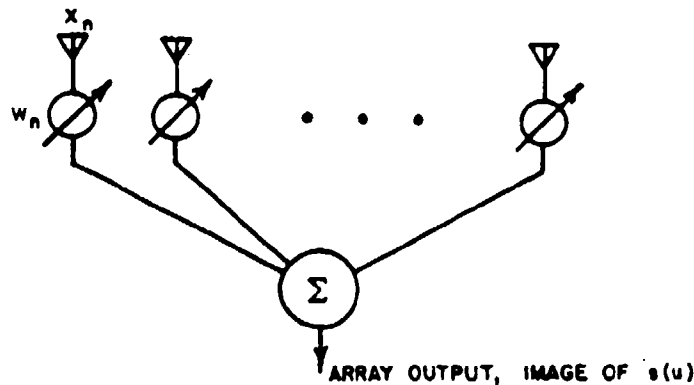


FIGURE 8.2 CONVENTIONAL SPATIAL SIGNAL PROCESSING

Assuming no noise and no element position error, the image of  $s(u)$  is,

$$\begin{aligned} \hat{s}(u) &= \frac{1}{N} \sum_{n=1}^N e^{j \frac{2\pi}{\lambda} x_n u} \left( \sum_{k=1}^K a_k e^{-j \frac{2\pi}{\lambda} x_n u_k} \right) = \sum_{k=1}^K a_k f(u - u_k) \\ &= f(u) * \sum_{k=1}^K a_k \delta(u - u_k) \end{aligned} \quad (3)$$

where  $f(u)$  is the array factor. The equation says that the image of  $s(u)$  is a summation of weighted and shifted array factors. If  $f(u)$  were a delta function, we would obtain a perfect image. Because of the finite size of the antenna array,  $f(u)$  is only an approximation of the delta function; it possesses a mainbeam with finite width and sidelobes. We cannot image a scene exactly by using a finite size antenna array.

#### Random Thinned Array

The requirement of a large antenna array is imposed through the need for good resolution. The resolution is determined by the width of the mainbeam of the array factor. The beamwidth is  $\lambda/L$ , where  $\lambda$  is the wavelength of the microwave signal and  $L$  is the size of the antenna array. Microwave wavelengths run from about 1 to 30 cm. To achieve a beamwidth (or resolving power) of  $10^{-4}$  rad, which is common for a camera lens, a microwave aperture has to be 100 m to 3 km in size. Because of this large size, the elements must be placed conformal to the terrain. We assume they are randomly placed. To build a filled array of this size would take  $2 \times 10^4$  elements, a number which is too large and impractical. The array must be thinned drastically. Randomness and thinning are two basic requirements which we impose in constructing an antenna array for high angular resolution microwave imaging. The effect of thinning is to increase the sidelobe level of the array.

#### What is the problem?

Due to drastic thinning of the array, high peak sidelobes emerge in the array factor. Since an image consists of the sum of the mainbeam response and the sidelobe response of targets, if the mainbeam response of a small target is smaller than the sidelobe response of a strong target, the small target is not distinguishable. We use the output of a random thinned array for a test scene to illustrate this point. The characteristics of the array and the target scene are:

Array aperture size =  $1000 \lambda$ : resolution 1 mr.

Number of elements = 45: average sidelobe level, -17 dB; peak sidelobe level, -7 to -10 dB.

(Table continued)

Test Scene (4 scatterers):		
Direction ( $\theta_k$ )	$a_k$	
	Magnitude	Phase
1.5 mr	0 dB	$-6^\circ$
4.3	-3	$160^\circ$
8.0	-12	$35^\circ$
12.4	-38	$45^\circ$

The image of the scene obtained via the 45-element array is shown in Figure 8.3.

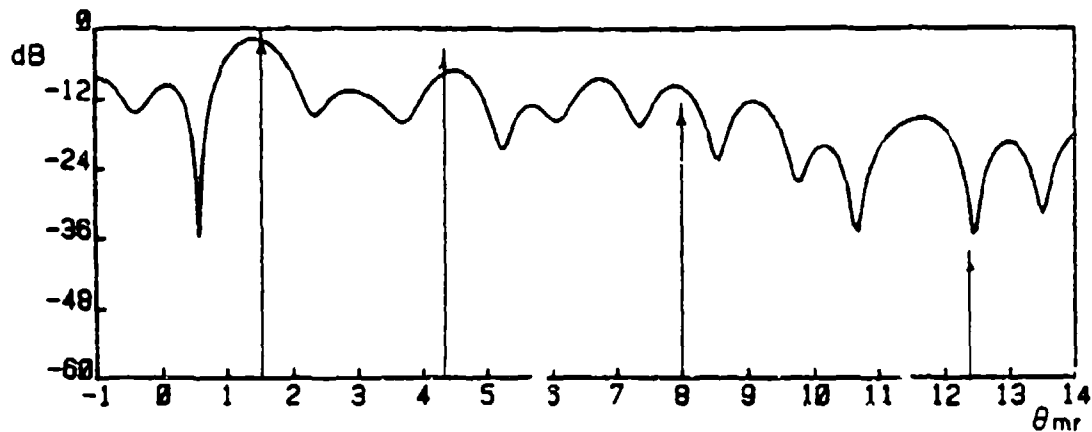


FIGURE 8.3 SCENE IMAGE USING 45-ELEMENT ARRAY. (Arrows denote magnitudes and positions of scatterers.)

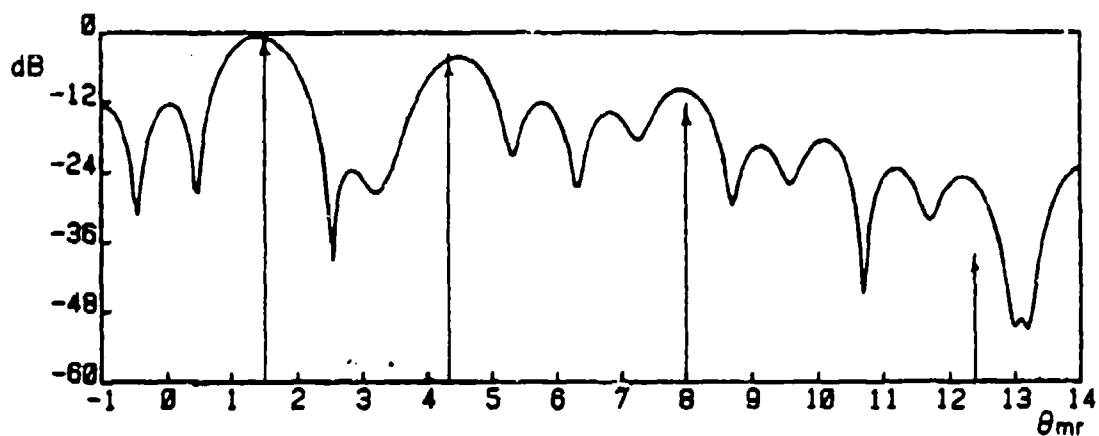


FIGURE 8.4 SCENE IMAGE USING 360-ELEMENT ARRAY.

If we estimate the locations of the targets on the basis of the strength of the output, the third and fourth targets will be incorrectly located. Since the fourth target is well below the average sidelobe level, we do not expect to be able to observe it. The third is higher than the average sidelobe level, but

is below the peak sidelobe level. We wish to observe it. Increasing the number of elements will reduce the sidelobe level of the array factor and permit observation of the third target (Figure 3.4). But increasing the number of elements means increasing the cost of the array. The object of this work is to image a wide dynamic range scene with relatively few elements.

#### How to solve the problem

An image consists of the sum of the mainbeam response and sidelobe response of the targets. It is the sidelobe response of a strong target that causes the difficulty in observing a small target. If we are able to estimate the parameters of the strongest target, the response coming from that target can be eliminated. We can either subtract an estimate of the array response to the large target from the original array output, or we can scan the mainbeam across the scene while maintaining a null in the estimated direction of the large target. Either approach provides a second image in which the sidelobe response of the strongest target is reduced. Consequently, we would expect the second strongest target to be prominent. By applying this target elimination technique repeatedly, we are able to determine the target information sequentially.

The first method, which does target subtraction, is called the clean technique and is being developed by Jenho Tsao. The second method, which fixes a null in the estimated target direction while scanning the mainbeam across the scene, we refer to as the nulling technique; it was conceived by De Yuan Ho. We have extended his work and are developing a theoretical analysis for the technique. The sequential nulling technique, which is the main theme of the proposal, is introduced in the following section.

#### THE SEQUENTIAL NULLING TECHNIQUE

First, the direction of the peak of the conventional array output is determined. It becomes the first (strongest) estimated target direction. In the second scan, a null is fixed in that estimated strong-target direction while scanning the mainbeam cross the scene. The algorithm which establishes a null in the estimated target direction and a mainbeam in the scanning direction is described in [2] and [12]. The second-strongest target direction is determined from the second scan. In the third scan, two nulls are fixed, in the direction of the two largest targets. By performing the nulling technique

repeatedly, a sequence of estimated target directions is determined. The technique stops when the array output (the total energy in the remaining image) is sufficiently small to indicate that all targets have been nulled. We note that at each step where we estimate a target direction by finding the peak of the output scan, we also obtain an estimate of the magnitude and phase of the target by taking the magnitude and phase of the output scan in that direction. The technique is summarized in the following flow chart, Figure 8.5.

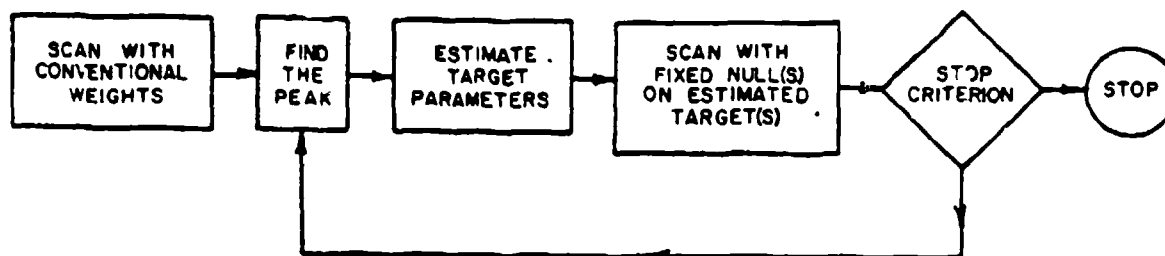


FIGURE 8.5 FLOW CHART OF THE SEQUENTIAL NULLING ALGORITHM

#### Simulation Results

##### (a) Ideal case

Assume that there is essentially no noise in the received signals and that the element positions are known exactly ( $\text{SNR} = 40 \text{ dB}$ ,  $\sigma_{\Delta x} = 0$ ,  $\sigma_{\Delta y} = 0$ ). The resulting estimates of the target parameters are:

<u>Direction (mr)</u>	<u>Magnitude (dB)</u>	<u>Phase</u>
1.44	0	-8.31°
4.28	-1.5	160.34°
8.06	-9.8	35.33°
-.05	-25.0	6.94°

The directions and phases of the first three targets are accurately determined. The errors in estimated target directions are less than 1/20 beamwidth. By comparison with the true scene data (preceding Figure 8.3) we see that the fourth target estimate is incorrect because the summation of leakages through the nulls is larger than the strength of the fourth target.

(b) Realistic Cases

In this portion of the simulation, the effect of noise and the effect of element position error on the nulling technique are examined. With noise in the received signals, but no element position error ( $\sigma_{\Delta x} = 0$ ,  $\sigma_{\Delta y} = 0$ ), the results are:

	<u>SNR = 10 dB</u>	<u>SNR = 0 dB</u>	<u>True Scene</u>
Estimated	1.44	1.46	1.5
Target	4.25	4.27	4.3
Directions	8.02	12.32	8.0
(mr)	12.32	7.85	12.4

The nulling technique appears to tolerate noise well. The theoretical basis for this noise performance is given later. It is worthwhile to point out that the nulling technique has self-correcting capability. In the SNR = 0 dB example, the technique missed the third strongest target at the third scan, but found it in the fourth scan. A technique for differentiating between the false and true targets has been developed by De Yuan Ho. With element position uncertainties but essentially no noise (SNR = 40 dB), the results are:

	<u><math>\sigma_{\Delta x} = 10\lambda</math>, <math>\sigma_{\Delta y} = 0</math></u>	<u><math>\sigma_{\Delta x} = 0</math>, <math>\sigma_{\Delta y} = \lambda</math></u>
Estimated	1.55	-.3
Target	4.30	11.55
Directions	7.98	3.68
(mr)	.60	14.25

It is apparent that the basic nulling technique can tolerate serious element position error in the direction perpendicular to the beam but cannot tolerate significant element position error in the direction along the beam. This phenomenon results from the fact that a position error in the direction along the beam causes much more phase error than does an identical position error in the direction perpendicular to the beam.

It is well known that in the absence of null control, the adaptive beacon forming and scanning process can compensate for the phase error caused by position error in the direction along the beam. We have implemented adaptive beacon forming and scanning together with the nulling technique. In the flow chart of Figure 8.5 the conventional scan is preceded by adaptive beacon forming. Then the scanning with nulls becomes somewhat more complicated. The results of a simulation of this implementation are shown below. This simulation uses essentially no noise (SNR = 40dB) but includes serious element position error in the beam direction.

		$\sigma_{\Delta x} = 0, \sigma_{\Delta y} = 10\lambda$
Estimated Target Direction (mr)	{	1.44
		4.28
		8.06
		-0.05

Initial theoretical observations concerning the adaptive beacon forming and scanning process in the nulling context are given in the next section. We conclude this section with the following observations:

- (1) The nulling technique can detect targets below the average sidelobe level in the presence of noise. From the simulation results we found that the nulling technique detected the third strongest target with strength -12 dB, which is below the expected peak sidelobe level (-10 to -7 dB), but above the average sidelobe level (-17 dB). We ran another simulation in which the third target had strength -20 dB. It was correctly estimated with the same array with signal-to-noise ratio 7 dB. The nulling technique, therefore, appears able to image a wide dynamic range scene with relatively few elements.
- (2) The technique has good noise tolerance.
- (3) The technique has good element position tolerance (with ABF)\*.
- (4) Although the technique processes (and nulls) only target directions, the target magnitudes and phases are obtained as well.
- (5) The technique has self-correcting capability.

\*ABF = Adaptive Beam-Forming

## THEORETICAL CONSIDERATIONS

We have seen the effects of noise and element position errors on the success of the nulling technique. Initial theories for these effects are presented later in this section. Even in the absence of noise and element position error, the accuracy of the nulling technique is affected by other system limitations. We examine them in detail in the following. Lastly, since we have assumed that the scene consists of a collection of discrete targets, the impact of the various target distributions on the applicability of the nulling technique is discussed.

### Array output asymmetry and mainbeam imperfection

In the initial scan, the unconstrained radiation pattern is used. In the absence of element noise and element position error, the mainbeam of the unconstrained radiation pattern is symmetrical about the pointing direction, the magnitude in the pointing direction is maximal (equal to 1), and the phase in that direction is zero. Such a mainbeam is able to find a lone target exactly. However, there are sidelobe responses from the other targets while the mainbeam is scanning. The sidelobe response is added to the mainbeam response, resulting in error in target direction estimation. Therefore, in the absence of element noise and element position error, the error in the first scan (the error in the first target estimate) is due entirely to array output asymmetry caused by sidelobe response.

In the second scan, a null is fixed in the estimated target direction as the mainbeam scans. Since there is a slight difference between the true target direction and the estimated target direction, leakage through the null results. This leakage is added to the mainbeam response of the second strongest target. Thus, the array output asymmetry in the second scan is caused by a combination of the sidelobe response and the null leakage. In the absence of element noise and element position error, there is a third source of error in the second scan, namely, asymmetry of the mainbeam about the pointing direction. The null-constrained radiation pattern is formed by summing several weighted unconstrained radiation patterns, shifted to the null directions. Because of the different weights and (probably) asymmetrical null positions with respect to the pointing direction of the mainbeam, the mainbeam of the constrained radiation pattern will be asymmetrical about the desired pointing direction. This phenomenon is pronounced when the main beam pointing direction

is moved within one beamwidth of a null. Figure 8.6 illustrates this phenomenon.

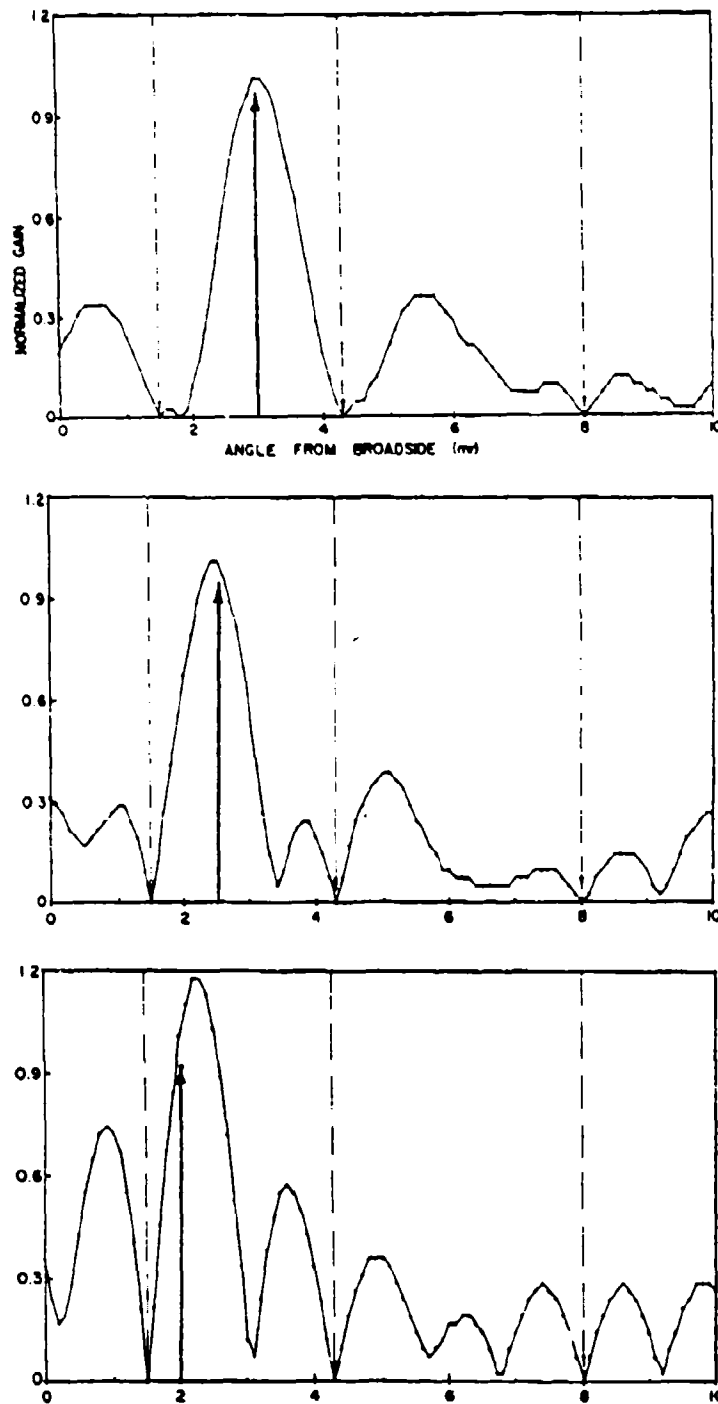


FIGURE 8.6 NULL-CONSTRAINED ARRAY PATTERNS. (Solid arrows denote pointing directions; dashed arrows denote fixed null directions. Coordinate units are the same for all three patterns.)

In the figure the nulls remain fixed but the desired pointing directions are moved. Note that the magnitudes in the respective desired pointing directions are unity, but the maxima do not occur in those directions.

For the subsequent scans, the error phenomena are essentially the same, but the accumulation of null leakages can increase to the point that the probability of false target estimation becomes high for scenes with high dynamic range. Of course, the true targets may still be detected on subsequent scans. The number of nulls also has an effect on the constrained radiation pattern. This can be seen from Figure 8.7. When the number of degrees of freedom (number of elements minus number of nulls) decreases, we have less control over the shape of the constrained radiation pattern.

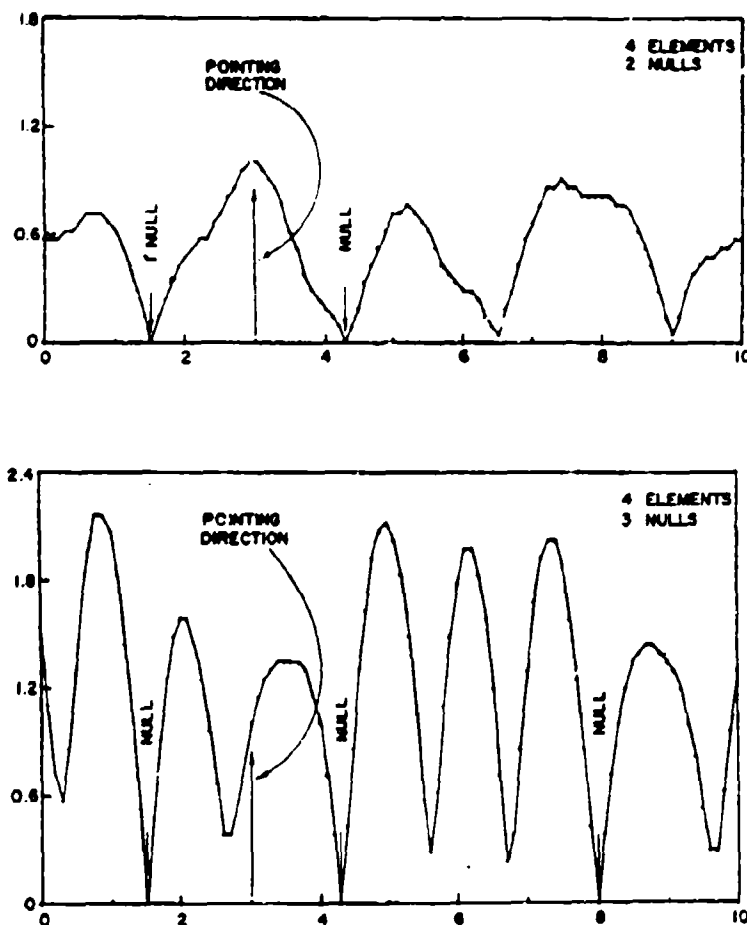


FIGURE 8.7 NULL-CONSTRAINED RADIATION PATTERNS  
(Coordinate units are the same as those on Figure 8.6.)

### Noise Properties

It is shown in [3] that conventional coherent spatial signal processing with an N-element array will improve the signal-to-noise ratio of the individual received signals by a factor of N. A single target is assumed in the derivation. It is stated in [8] that if the array output SNR is below about 5 dB when the beam is pointed at the weaker source, then the weak source cannot be detected. These two theories should apply, almost unchanged, to our nulling technique. We expect to be able to show that the SNR gain of the null-constrained array equals the number of degrees of freedom N-M, where M is the number of constrained nulls. The ability to observe a weak target depends on the SNR of that weak source. Assuming that we are able to null the stronger targets perfectly, the following rule can be used to predict the capability of the nulling technique to find the weak target:

Array SNR (weak target)

$$= \underbrace{10 \log(N-M)}_{\text{Array Gain}} + \underbrace{\text{SNR}(\text{element})}_{\text{Relative to strongest target}} - \text{Dynamic Range (of weak target)} > -5 \text{ dB}$$

In the earlier simulation results, we are able to observe the third target, whose amplitude is 12 dB below the strongest target, by using the 45-element array and 3 nulls ( $10 \log(45-3) = 16$  dB) with a 0 dB element signal-to-noise ratio (relative to the strongest target). The left-hand side of the inequality is  $16 + 0 - 12 = 4$ , which essentially satisfies the criterion for observation of the weak target. We tried unsuccessfully to resolve the third target after reducing its amplitude to 20 dB below the strongest target with the same array under the same SNR. This result agrees with the criterion since the left-hand side equals  $16 + 0 - 20 = -4$ , which is significantly smaller than 5. After we increased the SNR to 7 dB, we were able to resolve the third (-20 dB) target. In this case, the left-hand side equaled  $16 + 7 - 20 = 3$ , which is close to 5. Therefore, the detectability criterion appears to reliably predict the capability of the nulling technique. We will develop the theoretical noise properties for a null-controlled radiation pattern to see if the form used above is correct.

### Element Position Error

It has been shown in the simulation that the adaptive beacon forming and scanning process compensates for phase error caused by element position error

in both the beam and cross-beam directions, even if the radiation pattern is null-constrained. We show mathematically how the ABF process is carried out and how it reduces the effects of position errors.

Assuming a single target with complex amplitude  $a_T$  at  $\theta_T$ , the image produced by the conventional scanning process is

$$\hat{s}(\theta) = \frac{1}{N} \sum_{n=1}^N e^{j \frac{2\pi}{\lambda} x_n \sin \theta} (a_T e^{-j \frac{2\pi}{\lambda} x_n \sin \theta_T})$$

The term in parenthesis is the signal received at the  $n^{\text{th}}$  element, and the pre-multiplier  $e^{j \frac{2\pi}{\lambda} x_n \sin \theta}$  is the weight for beam forming at angle  $\theta$ . Since the element position is not known exactly, the calculated weight becomes  $e^{j \frac{2\pi}{\lambda} \hat{x}_n \sin \theta}$ , where  $\hat{x}_n$  is the estimated element position. The above expression becomes

$$\begin{aligned} \hat{s}(\theta) &= \frac{1}{N} \sum_{n=1}^N e^{j \frac{2\pi}{\lambda} \hat{x}_n \sin \theta} (a_T e^{-j \frac{2\pi}{\lambda} x_n \sin \theta_T}) \\ &= a_T \frac{1}{N} \sum_{n=1}^N e^{j \frac{2\pi}{\lambda} x_n (\sin \theta - \sin \theta_T)} \cdot e^{j \frac{2\pi}{\lambda} \Delta x_n \sin \theta} \end{aligned}$$

The phase error  $\frac{2\pi}{\lambda} \Delta x_n \sin \theta$  occurs as a result of the element position error. The effect of phase error on the array output is treated in Chapter 13 of [9]. We show in the following how the effect of position error can be reduced by implementing the ABF process.

Assume a strong reflector (beacon) can be made available at angle  $\theta_b$  in the vicinity of the single target. The image is then

$$\hat{s}(\theta) = \frac{1}{N} \sum_{n=1}^N e^{j \frac{2\pi}{\lambda} x_n \sin \theta} (a_T e^{-j \frac{2\pi}{\lambda} x_n \sin \theta_T} + a_b e^{-j \frac{2\pi}{\lambda} x_n \sin \theta_b})$$

Since the complex amplitude  $a_b$  of the beacon is large compared to  $a_T$ , we can ignore the target signal and measure  $a_b$  and  $\frac{2\pi}{\lambda} x_n \sin \theta_b$  accurately at each element. Therefore, we can form a mainbeam at  $\theta_b$  adaptively without using the element position. The image function can be rewritten in the form

$$\begin{aligned} \hat{s}(\theta) &= \frac{1}{N} \sum_{n=1}^N e^{j \frac{2\pi}{\lambda} x_n (\sin \theta - \sin \theta_b)} \cdot e^{j \frac{2\pi}{\lambda} x_n \sin \theta_b} \\ &\quad \cdot (a_T e^{-j \frac{2\pi}{\lambda} x_n \sin \theta_T} + a_b e^{-j \frac{2\pi}{\lambda} x_n \sin \theta_b}) \end{aligned}$$

The second factor on the right-hand side (RHS) is the phase adjustment necessary to beamform at the beacon; these phases are direct measurements of the ABF signal at each element. The first factor on the RHS is the phase adjustment required to scan the beam from  $\theta_b$  to  $\theta$ . Computation of this phase adjustment requires estimates of the element positions and beacon direction. Since the element positions are not known exactly, the scanning weight is obtained by using the estimated element position,  $\hat{x}_n$ .

We turn off the beacon while scanning the beam from  $\theta_b$  to  $\theta$  to obtain

$$\begin{aligned}\hat{s}(\theta) &= \frac{1}{N} \sum_{n=1}^N e^{j \frac{2\pi}{\lambda} \hat{x}_n (\sin\theta - \sin\theta_b)} \cdot e^{j \frac{2\pi}{\lambda} x_n \sin\theta_b} (a_T e^{-j \frac{2\pi}{\lambda} x_n \sin\theta_T}) \\ &= a_T \frac{1}{N} \sum_{n=1}^N e^{j \frac{2\pi}{\lambda} x_n (\sin\theta - \sin\theta_T)} \cdot e^{j \frac{2\pi}{\lambda} \Delta x_n (\sin\theta - \sin\theta_b)}\end{aligned}$$

The phase error, after ABF and scanning, becomes  $\frac{2\pi}{\lambda} \Delta x_n (\sin\theta - \sin\theta_b)$ . Since  $\theta_b$  is in the neighborhood of the target region, this error is greatly reduced as compared with the error  $\frac{2\pi}{\lambda} \Delta x_n \sin\theta$  which occurs without ABF.

Similar logic applies to the image obtained via the null-constrained radiation pattern. The image obtained with a null-constrained radiation pattern for a single target is

$$\hat{s}(\theta) = \frac{1}{N} \sum_{n=1}^N (B_{M+1} e^{j \frac{2\pi}{\lambda} x_n \sin\theta} + \sum_{m=1}^M B_m e^{j \frac{2\pi}{\lambda} x_n \sin\hat{\theta}_m}) (a_T e^{-j \frac{2\pi}{\lambda} x_n \sin\theta_T})$$

where  $\hat{\theta}_1, \hat{\theta}_2, \dots, \hat{\theta}_M$  are the desired null directions and  $\theta$  is the scanning direction (mainbeam pointing direction).  $B_1, B_2, \dots, B_M, B_{M+1}$  are the complex weights required to place nulls in directions  $\hat{\theta}_1, \hat{\theta}_2, \dots, \hat{\theta}_M$  and the unit gain (essentially the mainbeam) in direction  $\theta$ . An algorithm for calculating the  $\{B_m\}$  is given in [12]. Each  $B_m$  is a function of  $\{\hat{\theta}_m\}$ ,  $\theta$ , and  $\{x_n\}$ .  $B_m$  must be updated for each scanning angle  $\theta$  even though the null directions  $\{\hat{\theta}_m\}$  and element positions  $\{x_n\}$  do not change during the scan. If the number of elements is much greater than the number of nulls,  $B_{M+1}$  is approximately equal to 1; it is always real.  $|B_m|$  is approximately the sidelobe level of the array. We use  $\hat{B}_m$  to indicate that these weights are calculated by using the estimated element positions  $\{\hat{x}_n\}$ . When the element positions are not known exactly,

$$\begin{aligned}\hat{s}(\theta) &= \frac{1}{N} \sum_{n=1}^N (\hat{B}_{M+1} e^{j \frac{2\pi}{\lambda} \hat{x}_n \sin \theta} + \sum_{m=1}^M \hat{B}_m e^{j \frac{2\pi}{\lambda} \hat{x}_n \sin \hat{\theta}_m}) (a_T e^{-j \frac{2\pi}{\lambda} x_n \sin \theta_T}) \\ &= a_T \sum_{m=1}^{M+1} \hat{B}_m \cdot \left[ \frac{1}{N} \sum_{n=1}^N e^{j \frac{2\pi}{\lambda} x_n (\sin \hat{\theta}_m - \sin \theta_T)} \cdot e^{j \frac{2\pi}{\lambda} \Delta x_n \sin \hat{\theta}_m} \right]\end{aligned}$$

where we let  $\hat{\theta}_{M+1} = \theta$ . The exponent  $\frac{2\pi}{\lambda} \Delta x_n \sin \hat{\theta}_m$  in the last factor is the phase error.

If we have a strong reflector in direction  $\theta_b$ , we can beamform adaptively at  $\theta_b$  and then scan to  $\theta$ . The array output becomes

$$\begin{aligned}\hat{s}(\theta) &= \frac{1}{N} \sum_{n=1}^N \left[ \hat{B}_{M+1} e^{j \frac{2\pi}{\lambda} \hat{x}_n (\sin \theta - \sin \theta_b)} + \sum_{m=1}^M \hat{B}_m e^{j \frac{2\pi}{\lambda} \hat{x}_n (\sin \hat{\theta}_m - \sin \theta_b)} \right] \\ &\quad \cdot e^{-j \frac{2\pi}{\lambda} x_n \sin \theta_b} \cdot (a_T e^{-j \frac{2\pi}{\lambda} x_n \sin \theta_T})\end{aligned}$$

The first factor (in square brackets) is the scanning weight for each element. The weights are calculated from the estimated element positions  $\{\hat{x}_n\}$ , the desired null directions  $\{\hat{\theta}_m\}$ , and  $\{\hat{B}_m\}$ . The second factor is the phase shift that is required to beamform at the beacon. This quantity is measured directly in the ABF process. It can be accurately measured if the beacon is a good phase synchronizing source. The last term is the received signal. After manipulation, again letting  $\hat{\theta}_{M+1} = \theta$ ,  $\hat{s}(\theta)$  becomes

$$\hat{s}(\theta) = a_T \sum_{m=1}^{M+1} \hat{B}_m \left[ \frac{1}{N} \sum_{n=1}^N e^{j \frac{2\pi}{\lambda} x_n (\sin \hat{\theta}_m - \sin \theta_T)} \cdot e^{j \frac{2\pi}{\lambda} \Delta x_n (\sin \hat{\theta}_m - \sin \theta_b)} \right]$$

After ABF and scanning, the phase error is  $\frac{2\pi}{\lambda} \Delta x_n (\sin \hat{\theta}_m - \sin \theta_b)$ , which is greatly reduced as compared with the previous phase error  $\frac{2\pi}{\lambda} \Delta x_n \sin \hat{\theta}_m$ . Since  $\theta_b$  is in the vicinity of the target,  $(\sin \hat{\theta}_m - \sin \theta_b)$  is a very small quantity; it reduces the effect of element position error  $\Delta x_n$ . The formulation easily extends to two- or three-dimensional arrays by carrying the  $y_n$  and  $z_n$  terms. The ABF process also reduces the effect of element position errors  $\Delta y_n$  and  $\Delta z_n$ .

### Target Model

We have assumed that a scene is a collection of discrete targets. If two targets are closer together than one beamwidth of the array radiation pattern, the array output will have only one peak. If we put a null in that peak direction, the null leakage will be large. Therefore, we may need to use a null sector instead of a point null. The feasibility of using a null sector is under investigation.

### RESEARCH PLAN

I. Theoretical Analysis. Determine the theoretical limitations to target detectability and accuracy via the nulling technique caused by:

1. The array output asymmetry owing to the sidelobe response.
2. The null leakage owing to errors in target direction estimation.
3. Mainbeam imperfection in the null-constrained radiation pattern.
4. Noise.
5. Element position errors (assuming use of adaptive beacon forming and scanning of the null-constrained radiation pattern).

#### II. Practical Evaluation

1. Evaluate the processing requirements for practical implementation of the nulling technique.
2. Test the technique on real data from the Valley Forge Research Center.

III. Algorithm Development. To the extent possible within time limitations, attempt to:

1. Incorporate into the algorithm De Yuan Ho's technique for differentiating true targets from false targets.
2. Determine the feasibility of prescribing a null sector in order to null two targets which are closer together than one beamwidth.

Lih-Tyng Hwang

### REFERENCES

- [1] R. E. Collin and F. J. Zucker, Antenna Theory, Part I and II, McGraw-Hill, New York, 1969.
- [2] M. DonVito, "Methods of Sidelobe Clutter Reduction," Master's Thesis, The Moore School, University of Pennsylvania, 1977.
- [3] T. A. Dzekov, "Microwave Holographic Imaging of Aircraft with Spaceborne Illumination Source," Ph.D. Dissertation, The Moore School, University of Pennsylvania, 1976.
- [4] J. Freedman, "Resolution in Radar Systems," Proc. IRE, 39, 813-818, 1951.
- [5] D. L. Margerum, "Self-Phased Arrays," Chap. 5 of Microwave Scanning Antennas, Vol. 3, R. C. Hansen, Ed., Academic Press, 1966.

(Continued)

# REFERENCES (Continued)

- [6] J. C. Lim and D. E. N. Davies, "Synthesis of a Single Null Response in an Otherwise Omnidirectional Pattern Using a Circular Array," Proc. IEEE, 122 (4), 349-352, 1975.
- [7] R. Mitchell, "Models of Extended Targets and Their Coherent Radar Images," Proc. IEEE, 62, 754-758, 1974.
- [8] B. D. Steinberg, "The Effects of Relative Source Strength and Signal-to-Noise Ratio on Angular Resolution of Antennas," Proc. IEEE, 62, 758-762, 1974.
- [9] B. D. Steinberg, Principles of Aperture and Array System Design, John Wiley, New York, 1976.
- [10] B. D. Steinberg and D. Y. Ho, "Image Feedback Control of a Self-Cohering Random Antenna Array," VFCR QPR No. 23, p. 84, 15 Nov. 1977.
- [11] B. D. Steinberg and D. Y. Ho, "Adaptive Learning System for the Radio Camera," VFCR QPR No. 27, 58-64, 15 Nov. 1978.
- [12] B. D. Steinberg and D. Y. Ho, "A Sidelobe Suppression Technique for the Radio Camera," VFCR QPR No. 29, 76-84, 15 May 1979.
- [13] B. D. Steinberg, "Radar Imaging from a Distorted Array: The Radio Camera Algorithm and Experiments," IEEE Trans. Antennas Propagat., Vol. AP-29, 740-748, Sept. 1981.
- [14] H. Steyskal, "Synthesis of Antenna Patterns with Prescribed Nulls," IEEE Trans. Antennas Propagat., Vol. AP-30, 273-279, 1982.
- [15] S. H. Taheri and B. D. Steinberg, "Tolerances in Self-Cohering Antenna Arrays of Arbitrary Geometry," IEEE Trans. Antennas Propagat., Vol. AP-24, 733-739, 1976.
- [16] W. M. Waters, "Adaptive Radar Beacon Forming," IEEE Trans. Aeros. Elect. Syst., Vol. AES-6, 503-513, 1970.

# 7. A NULLING TECHNIQUE FOR MICROWAVE IMAGING WITH A RANDOM THINNED ARRAY\*

C. Nelson Dorny

Lih-tyng Hwang

## INTRODUCTION

Reference [1] introduced a sequential nulling technique for microwave imaging with a random thinned array. The direction of the peak of the conventional scanned array output is used as an estimate of the first (strongest) target direction. The target scene is then scanned a second time (perhaps by merely reprocessing the same received data used in the first scan) while maintaining a null in the estimated direction of the first target, thereby locating the second-strongest target. The process is repeated until all targets are located or the noise/artifact level is reached.

Reference [1] describes the sources of error which corrupt the sequential imaging process. The first source of error is the error in estimated direction of the first target owing to the sidelobe response from other targets. This article derives an estimate of that directional error. It is shown that this error can be expected to be in the order of 0.05 beamwidths for most scenes.

### Direction Estimation Error in the First Scan

The power output of an array for a scene consisting of  $K$  point targets is

$$P(u) = \left( \sum_{k=1}^K a_k f(u-u_k) \right) \left( \sum_{k=1}^K a_k f(u-u_k) \right)^* \quad (1)$$

where  $u = \sin\theta$ ,  $\theta$  is the angular direction relative to broadside,  $a_k$  is the complex strength of  $k^{\text{th}}$  target,  $u_k$  is direction of the  $k^{\text{th}}$  target, and  $f(u)$  is the unconstrained radiation pattern. The first target direction estimate  $\hat{u}_1$  is the central peak of the array power output. That is,

$$P'(u) \Big|_{u=\hat{u}_1} = 0 \quad (2)$$

The difference  $\Delta u_1 = \hat{u}_1 - u_1$  is the estimation error. Assuming  $\hat{u}_1$  is close to  $u_1$ ,  $\Delta u_1$  can be explicitly expressed through the following linear approximation:

$$P''(u) \Big|_{u=u_1} = \frac{P' \Big|_{u=\hat{u}_1} - P' \Big|_{u=u_1}}{\hat{u}_1 - u_1} = - \frac{P' \Big|_{u=u_1}}{\Delta u_1} \quad \text{or} \quad \Delta u_1 = - \frac{P'}{P''} \Big|_{u=u_1} \quad (3)$$

\*This work is supported by the Air Force Office of Scientific Research under Grant No. AFOSR-82-0012, the Office of Naval Research under Grant No. N00014-79-C-0505, and the Army Research Office under Contract DAAC29-81-K-0105.

Computer simulations for specific arrays demonstrate that (3) is a good approximation for values of  $\Delta u_1$  much smaller than the beamwidth. The results on the left of Table 7.1 are obtained by searching for the peak of the array output. Those on the right are obtained by using (3). The scene contains two targets: one at 1.5 mr (0 dB,  $-6^\circ$  relative phase), the other at 4.3 mr ( $-3$  dB,  $160^\circ$  relative phase). The array consists of 45 identical elements randomly distributed over a linear aperture of 1000 wavelengths. Thus the array beamwidth is 1 mr with a peak sidelobe level of approximately  $-7$  dB. Five different sets of random element positions were simulated. The simulated and approximated values of  $\Delta u_1$  are identical to within about 0.01 beamwidth or less. Thus, we conclude that (3) gives a good approximation to the real estimation error.

Trial	$\hat{u}_1$	$\Delta u_1$ (simulated)	$\Delta u_1$ (linear approximation)
#1	1.427 mr	-.073 mr	-.073 mr
2	1.528	.028	.041
3	1.399	-.101	-.093
4	1.377	-.123	-.122
5	1.41	-.09	-.106
Average ( $\Delta \hat{u}_1$ )		-.072 mr	-.07 mr

TABLE 7.1 DIRECTION ESTIMATION ERROR  $\Delta u_1$  FOR A SPECIFIC TWO-TARGET SCENE

#### Simplification of the Two-Target Case

For an arbitrary two-target scene (and small  $\Delta u_1$ ), the analytical estimate (3) can be expressed

$$\Delta u_1 = - \frac{\frac{|a_2|}{|a_1|} N_{12} + \left(\frac{|a_2|}{|a_1|}\right)^2 N_2}{\frac{2\pi}{\lambda} \left[ D_1 + \frac{|a_2|}{|a_1|} D_{12} + \left(\frac{|a_2|}{|a_1|}\right)^2 D_2 \right]} \quad (4)$$

Where  $a_k$  is the strength of target  $k$ ,  $k = 1, 2$ , and where we define

$$N_{12} = \sum_{i=1}^N \sum_{j=1}^N (x_i - x_j) \sin\left(\frac{2\pi}{\lambda} x_j (u_2 - u_1) + (a_1 - a_2)\right)$$

(Continued)

$$\begin{aligned}
N_2 &= \frac{1}{2} \sum_{i=1}^N \sum_{j=1}^N (x_i - x_j) \sin\left(\frac{2\pi}{\lambda} (x_i - x_j) (u_1 - u_2)\right) \\
D_{12} &= \sum_{i=1}^N \sum_{j=1}^N (x_i - x_j)^2 \cos\left(\frac{2\pi}{\lambda} x_j (u_2 - u_1) + (a_1 - a_2)\right) \\
D_1 &= \frac{1}{2} \sum_{i=1}^N \sum_{j=1}^N (x_i - x_j)^2 \\
D_2 &= \frac{1}{2} \sum_{i=1}^N \sum_{j=1}^N (x_i - x_j)^2 \cos\left(\frac{2\pi}{\lambda} (x_i - x_j) (u_1 - u_2)\right)
\end{aligned} \tag{5}$$

and  $a_k$  is the phase of target  $k$ ,  $x_1$  and  $x_j$  are random element positions.

Figure 7.1 shows the ideal array output for two targets of equal strength, one beamwidth apart. The two targets are not resolvable if they are of equal phase. The equal phase case is the most difficult case for target location or separation. For two targets having the same strength and same phase, the separation required for resolution of the targets is about 1.5 beamwidths (Figure 7.2). This observation confirms the conclusion in [2], which states that the required separation for equal-strength sources is about 1.5 to 2 beamwidths. There is no need, therefore, to be concerned about target estimation error  $\Delta u_1$  for equal strength targets if the target spacing is less than 2 beamwidths.

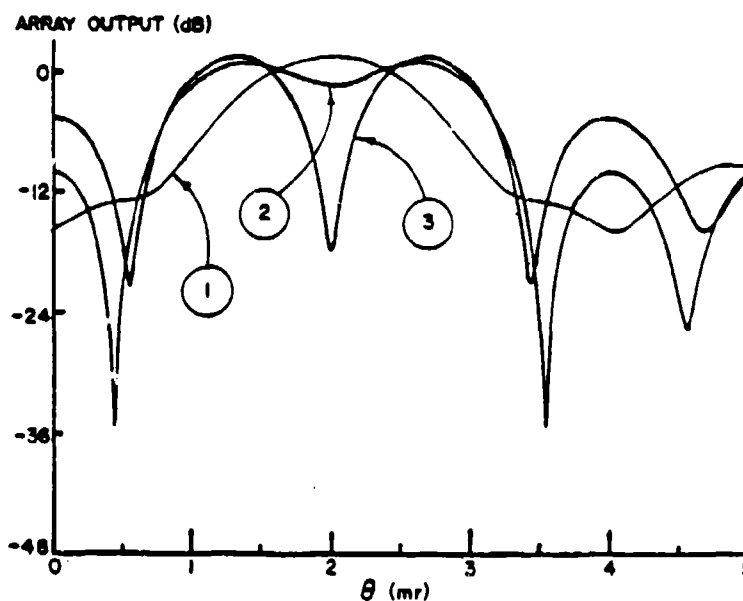


FIGURE 7.1 ARRAY OUTPUTS FOR TWO TARGETS OF EQUAL STRENGTH, 1 Mrad APART, USING A 1 Mrad BEAMWIDTH.  
 ①  $b = a_2 - a_1 = 0$ ; ②  $b = 90^\circ$ ; ③  $b = 180^\circ$ .

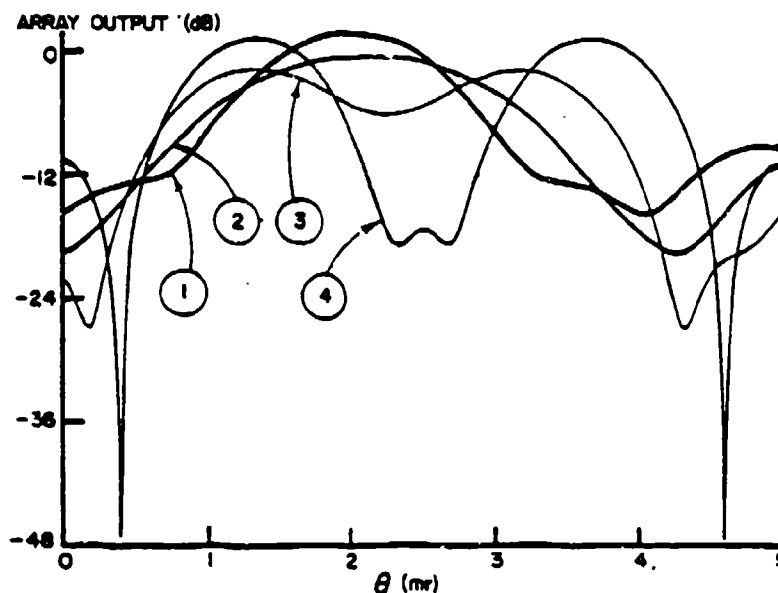


FIGURE 7.2 ARRAY OUTPUTS FOR TWO TARGETS OF EQUAL STRENGTH, SAME PHASE, USING A 1 Mrad BEAMWIDTH.  
 ①  $u_{21} = u_2 - u_1 = 1.0$  bw; ②  $u_{21} = 1.2$  bw;  
 ③  $u_{21} = 1.5$  bw; ④  $u_{21} = 2.0$  bw.

Typically, the scene (target locations, phases and strengths) and the array (element positions) are random. Since the number of array elements is large and the elements are roughly uniformly distributed, the array beam properties closely approximate the expected properties of a random array. According to [3], the expected value of the power pattern of a random array is identical with the design power pattern (that of a filled array with the same aperture). Therefore, we replace each of the quantities in (4) by its expected value with respect to array element position. That is, we take the ensemble averages over element position  $x_1$ . These expected values are:

$$N_{12} = E\{N_{12}\} = \frac{(\cos \frac{aL}{2} - \frac{2}{aL} \sin \frac{aL}{2})}{aL} \cdot \cos b \cdot (N^2 - N) \cdot L$$

$$N_2 = E\{N_2\} = \frac{\sin aL - \frac{2}{aL} (1 - \cos aL)}{a^2 L^2} \cdot (N^2 - N) \cdot L$$

$$D_1 = E\{D_1\} = \frac{1}{12} \cdot (N^2 - N) L^2 \quad (6)$$

(Continued)

(6) Continued

$$D_{12} = E(D_{12}) = \frac{2\left[\frac{3}{aL} \cos \frac{aL}{2} + \left(1 - \frac{6}{a^2 L^2}\right) \sin \frac{aL}{2}\right]}{3aL} \cos b \cdot (N^2 - N)L^2$$

$$D_2 = E(D_2) = \frac{\left[\left(\frac{6}{a^2 L^2} - 1\right) \cos aL - \frac{6}{a^2 L^2} + \frac{4}{aL} \sin aL\right]}{a^2 L^2} (N^2 - N)L^2 \quad (6)$$

where  $a = \frac{2\pi}{\lambda}(u_2 - u_1)$  and  $b = (a_2 - a_1)$ .

$E(D_1)$  is nonrandom. The expected values of the other terms depend upon the two-target scene (random target spacing  $a$  and target phase difference  $b$ ). For the worst case of two targets with equal phase ( $\cos b = 1$ ), Figures 7.3 and 7.4 show how the terms in the numerator and the denominator vary with the target spacing. In the numerator,  $E(N_{12})$  dominates, while in the denominator

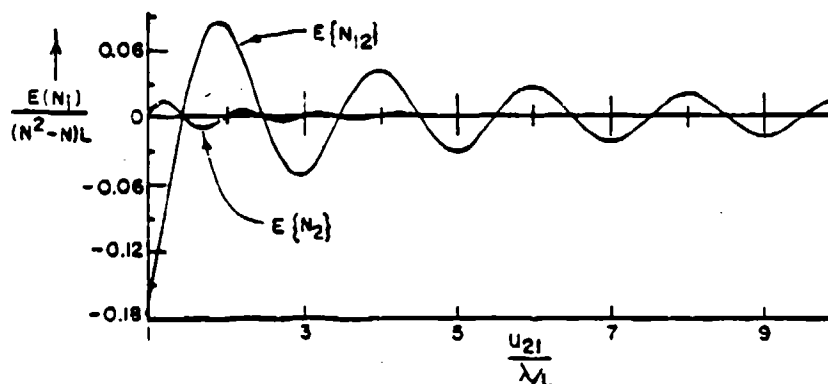


FIGURE 7.3 EXPECTED VALUES OF NORMALIZED TERMS IN THE NUMERATOR

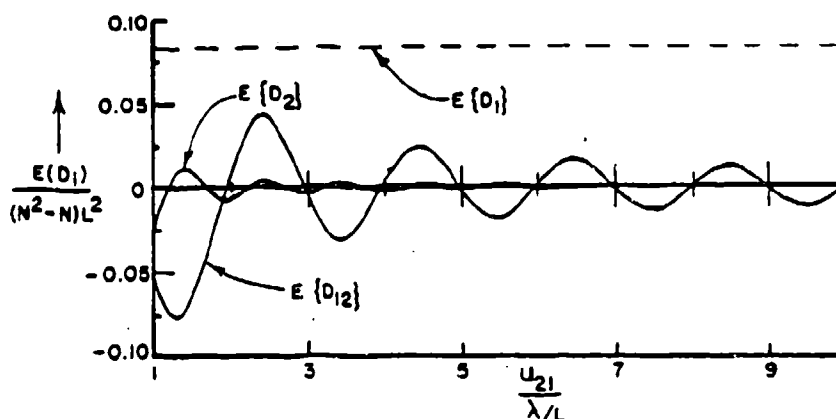


FIGURE 7.4 EXPECTED VALUES OF NORMALIZED TERMS IN THE DENOMINATOR

$E\{D_1\}$  is dominant. Therefore  $\Delta u_1$  can be approximated (for any target phase difference and target strength ratio, and for  $u_1$  in the near sidelobe region) by

$$\Delta u_1 = - \frac{\frac{|a_2|}{|a_1|} \cdot E\{N_{12}\}}{\frac{2\pi}{\lambda} \cdot D_1} \cdot \left( -\frac{3}{\pi} \right) \cdot \frac{\cos \frac{aL}{2} - \frac{2}{aL} \sin \frac{aL}{2}}{\frac{aL}{2}} \cdot \cos b \cdot \frac{\lambda}{L} \quad (7)$$

where we have treated the denominator as a nonrandom value. According to the above derivation, (7) is a good approximation to  $\Delta u_1$  if the second target strength is small compared to the first target strength, or if the spacing between two targets is larger than 2 beamwidths.

#### Simulation of the Two-Target Case

We check this conclusion by computer simulation. The value of  $\Delta u_1$  vs target spacing  $u_{21}$  is determined by simulation for 5 different 45-element, 1000-wavelength random arrays, for two different target strength ratios. Figures 7.5 and 7.6 compare the simulations (averaged over the 5 arrays) to the estimate given by (7): (These figures are on the following page, together for comparison). It is clear from Figures 7.5 and 7.6 that (7) is a good approximation if the target spacing is larger than 2 beamwidths. The approximation is even better if the targets have unequal strengths. Equation (7) can be used to predict the  $\Delta u_1$  for any target pair. We concentrate on the worst-case situation -- equal-strength, equal-phase targets, separated by 2 beamwidths -- (shown in Figure 7.5). Then  $\Delta u_1 \leq 0.16$  beamwidths. This number is a bound on the possible values of  $\Delta u_1$  as long as the targets are not closer than 2 beamwidths. The rms of the worst-case target pair of Figure 7.5, taken over spacings  $u_{21}$  between 2-10 beamwidths, is 0.049 beamwidths. This number represents a reasonable estimate of  $\Delta u_1$  if the target spacing is not known. Computer simulations for a  $1000\lambda$  array with 20, 45, and 90 elements for  $u_{21} = 2.8, 9.5,$  and  $10$  beamwidths show that  $\Delta u_1$  is accurately predicted by (7) and is not affected by the number of elements  $N$ . Of course, the variation in  $\Delta u_1$  from one realization to another is inversely proportional to  $\sqrt{N}$ . For  $N=45$  the variation in  $u_1$  is in the order of 0.05 beamwidths. Thus, for  $N > 100$  we can ignore the variance and expect (7) to give a good estimate of  $\Delta u_1$ .

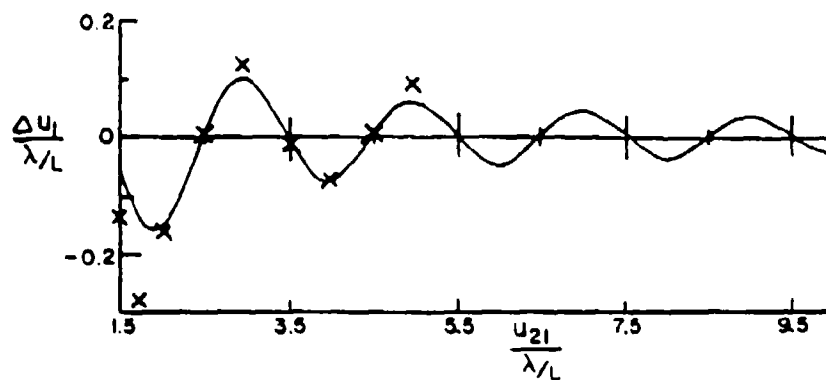


FIGURE 7.5  $\Delta u_1$  VS TARGET SPACING (NORMALIZED) FOR TWO EQUAL-STRENGTH, EQUAL-PHASE TARGETS. (SOLID CURVE DENOTES APPROXIMATION (7); X DENOTES AVERAGE OF SIMULATIONS.)

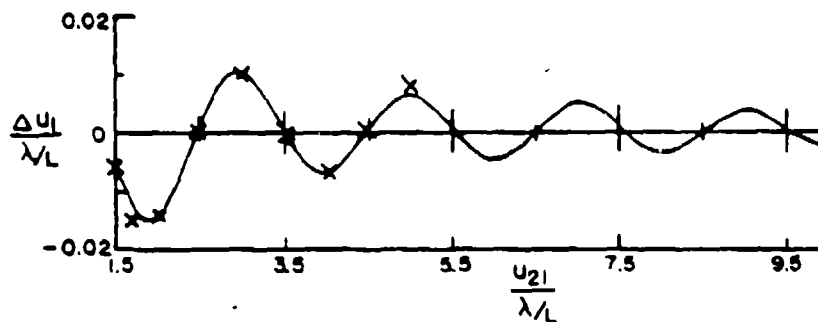


FIGURE 7.6  $\Delta u_1$  VS TARGET SPACING (NORMALIZED) FOR TWO EQUAL-PHASE TARGETS (ONE 0 dB, THE OTHER -20 dB). SOLID CURVE DENOTES APPROXIMATION (7); X DENOTES AVERAGE OF SIMULATIONS.)

#### Multiple Targets

The three-target version of (4) has also been derived, and the corresponding curves equivalent to Figures 7.3 and 7.4 computed. These curves demonstrate that for each additional target an additional numerator term equivalent to  $N_{12}$  must be included in (7). The denominator is still dominated by the constant term  $D_1$ . All other terms can be neglected. This conclusion applies in all cases except a specific periodic placement of many identical targets.

The component of the estimation error  $\Delta u_1$  corresponding to each target will depend on the separation from the first target in the manner illustrated in Figures 7.5 and 7.6. Thus the component owing to the third target may either add to or subtract from the component owing to the second target. In

general, for  $M$  point targets of equal strength and phase, random positioning of the targets should result in an rms value of  $\Delta u_1$  which is  $\sqrt{M-1}$  times the value shown in (7). For most target scenes normal variation in target strength will lead to lower estimation errors. Thus we would expect  $0.05 \sqrt{M-1}$  beamwidths to be a conservative estimate of  $\Delta u_1$  in the multitarget case.

#### SUMMARY

We have shown that the effect of the sidelobe response on the direction estimation error in the first scan of the sequential nulling technique depends on the number of targets, target phase differences, target strengths and target spacings, but normally does not depend on array element placement. A quantitative expression for the estimation error has been derived and a practical, simplified, approximate expression has been obtained. For two equal-strength targets separated by more than 2 beamwidths, the worst possible estimation error is 0.16 beamwidths, and the rms (over target spacing) for the worst-case target pair is approximately 0.05 beamwidths. Additional targets of equal strength (again the worst case), will cause a total estimation error  $\Delta u_1$  of approximately  $0.05 \sqrt{M-1}$  beamwidths, where  $M$  is the number of targets.

Lih-tyng Hwang

#### References

- [1] C. N. Dorny and L. T. Hwang, "A Nulling Technique for Microwave Imaging with a Random Thinned Array," Valley Forge Research Center QPR No. 42, Oct. - Mar. 1983, pp. 92-108.
- [2] B. D. Steinberg, "The Effects of Relative Source Strength and Signal-to-Noise Ratio on Angular Resolution of Antenna," Proc. IEEE, 62, 1974, pp. 758-762.
- [3] B. D. Steinberg, Principles of Aperture and Array System Design, John Wiley & Sons, Inc., New York, 1976, pp. 139-146.

# Sidelobe Reduction of Random Arrays by Element Position and Frequency Diversity

BERNARD D. STEINBERG, FELLOW, IEEE, AND ELSAYED H. ATTIA, STUDENT MEMBER, IEEE

**Abstract**—The high sidelobes of random, thinned arrays can be reduced through the use of diversity techniques. Element position diversity and frequency diversity are considered in this paper. Image artifacts due to the high sidelobes change their locations from image to image when the element positions are altered or the operating frequency is changed. Superimposing or averaging images tends to build up stable, correct portions of an image while reducing, by smoothing, the image artifacts. In principle, all the sidelobe crests can be reduced to the average background level and all the troughs in the side radiation pattern will rise to this level. The theory, supported by simulation experiments, indicates that dual position diversity reduces the sidelobe level by 2 to 2 1/2 dB, depending upon array size. Higher order position diversity reduces the sidelobe level several dB further. Under frequency diversity it is found that when  $Q$ , the reciprocal of the fractional bandwidth, is less than the array size  $L/\lambda$  (measured in units of wavelength), the peak sidelobe power level is approximately  $N^{-1} \ln Q$ , where  $N$  is the number of array elements. For larger values of  $Q$ , the level asymptotes approximately to  $N^{-1} \ln(L/\lambda)$ .

## I. INTRODUCTION

DIVERSITY techniques are proven tools for enhancement of stable components of signals or images in a stochastic background. Required is some parameter (space, time, frequency, polarization, etc.) in which the undesired signal component becomes decorrelated through variation of the parameter. Space diversity upon reception was introduced early in HF radio communication to reduce the effect of random signal fading [1]. Angle diversity has proven useful in tropospheric scatter communication [2]. Frequency and polarization diversity also are useful [3]. Even the integration of successive radar echoes in a background of noise or time-varying clutter is a temporal form of diversity [4]. More recently, RF phase diversity has been found indispensable in obtaining stable maximum entropy images [5].

The high sidelobes of random, thinned arrays can be reduced through the use of diversity techniques. Element position diversity and frequency diversity are examined in this paper. The side radiation pattern of such an array is a random process whose peak levels can easily be 10 dB higher than its average [6], [7]. The specific locations of the high sidelobes depend upon the specific locations of the antenna elements and the operating frequency. Variation of the element locations or operating frequency does not alter the average sidelobe level nor the remaining statistics of the side radiation pattern; it does, however, alter the sidelobe locations. Hence, image artifacts due to high sidelobes in a large imaging array will change their locations from

image to image provided that the element positions are altered or the operating frequency is changed. The true components of the image, those associated with main-lobe response, do not change under either diversity scheme. Hence, superimposing or averaging such images tends to build up stable, correct portions of the image while reducing, by smoothing, the image artifacts.

Element position diversity can be applied in any array problem in which the antenna elements are on separate platforms or vehicles which have independent motions. One example is a random field of sonobuoys freely drifting in the ocean. The geometry of the sonobuoy field varies with time. Successive images formed from the outputs of such a system at intervals of time exceeding the correlation time of the array geometry will exhibit image artifacts due to the high sidelobes in different locations. Noncoherently averaging such successive images would be useful. Another illustration is a huge radar phased array deployed on many ships in a task force. The individual receiving elements would be placed on different ships. One ship would carry the transmitter.

Two separate questions are important to a designer. The first question is how valuable is it to change the system design, which always is a costly process, from one without diversity to one which permits the introduction of diversity techniques. If the answer to the first question indicates sufficient value to alter the system to accommodate diversity, the second question is how much diversity should be included.

This paper places the subject on a quantitative basis. A theory is derived for the reduction of the peak sidelobe of a thinned, random array as a function of the number  $M$  of independent rearrangements of  $N$  antenna elements, with the individual radiation patterns averaged incoherently. Two different theoretical techniques are used. First, because of the known (Rayleigh) shape of the probability density function (pdf) of random samples of the amplitude of the side radiation pattern, the effect of smoothing two such samples upon the peak sidelobe level (PSL) is calculated. Next, it is recognized that the pdf of the average of several independent variates tends toward the Gaussian distribution. Thus averaging or superimposing many images changes the amplitude distribution from Rayleigh to approximately Gaussian. Upward- and downward-biased asymptotic statistical estimators of the peak are calculated. Computer simulation experiments verify both parts of the theory.

Both coherent and noncoherent combining of the frequency components of a wide-band source can be used to achieve frequency diversity. Coherent combining results when a wide bandwidth signal is radiated. In noncoherent combining the signal constituents are separately radiated, each producing its own radiation pattern and the resulting power patterns averaged. While the behavior of the peak sidelobe level is found to be similar in both cases, coherent combining reduces the average sidelobe level in the far sidelobe region as well.

Manuscript received September 20, 1982; revised June 3, 1983. This work was supported by the U.S. Army Research Office under Contract DAAC29-81-K-0105, by the Office of Naval Research under Contract N00014-79-C-0505, and by the Air Force Office of Scientific Research under Grant AFOSR-78-3688.

The authors are with the Valley Forge Research Center, Moore School of Electrical Engineering, University of Pennsylvania, Philadelphia, PA 19104.

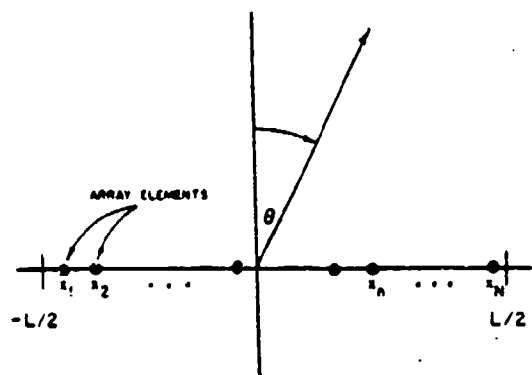


Fig. 1. Geometry of the random array.

## II. BASIC THEORY OF RANDOM ARRAYS

Consider the geometry shown in Fig. 1 where a linear array is formed by distributing  $N$  isotropic elements at random over the aperture length.<sup>1,2</sup> We limit ourselves here to the case where all the elements have identical monochromatic excitations. Although generalizations are possible, the details become somewhat more involved. Within an unimportant constant of proportionality, the resulting complex amplitude of the far field in a direction making an angle  $\theta$  with broadside can be written as [7]

$$F(\theta) = \sum_{n=1}^N e^{jkx_n \sin \theta} \quad (1)$$

where  $k = 2\pi/\lambda$  is the wavenumber associated with the wavelength  $\lambda$  and  $x_n$  is the  $n$ th element position which is chosen according to some probability density function covering the interval  $[-L/2, L/2]$  where  $L$  is the array length.

Defining  $u = \sin \theta$ , (1) can be rewritten as

$$F(u) = \sum_{n=1}^N e^{jkx_n u} = \sum_{n=1}^N \cos(kx_n u) + j \sum_{n=1}^N \sin(kx_n u) \\ = a(u) + jb(u). \quad (2)$$

Note that  $u$  is defined over the interval  $[-1, 1]$ . It follows also that  $|F(-u)| = |F(u)|$ . Therefore, it is sufficient to consider the radiation pattern  $F(u)$  only over the interval  $[0, 1]$ .

The radiation pattern  $F(u)$ , as given by (2), is a complex random process. For the special case where element locations are independent and uniformly distributed<sup>3</sup> over the interval  $[-L/2, L/2]$ , the expected values of the processes  $a(u)$  and  $b(u)$  are

[7], [11]

$$E\{a(u)\} = \frac{N \sin(\pi u L / \lambda)}{\pi u L / \lambda} = N \operatorname{sinc}(uL/\lambda) \quad (3)$$

and

$$E\{b(u)\} = 0. \quad (4)$$

The processes  $a(u)$  and  $b(u)$ , for a given value of  $u$ , are sums of  $N$  independent, identically distributed random variables. When  $N$  is large, the central limit theorem justifies approximating  $a(u)$  and  $b(u)$  as Gaussian random variables. The mean of  $a(u)$ , as given by (3), is approximately zero for  $u$  greater than a few beamwidths (the nominal beamwidth is  $\lambda/L$ ). Furthermore, for imaging problems in which high angular resolution is demanded,  $\lambda/L \ll 1$ . Thus in most of the sidelobe region, the two orthogonal components of  $F(u)$  are approximately zero-mean wide sense stationary Gaussian random processes. For a given  $u$ , the magnitude of  $F(u)$  is known to be Rayleigh distributed [12]. Let us denote the magnitude pattern as  $A(u) \triangleq |F(u)|$ . The probability density function of  $A$  will be given by [6], [7]

$$p(A) = \frac{2A}{N} \exp(-A^2/N). \quad (5)$$

It follows that the mean square value  $\overline{A^2}$ , which is the average sidelobe power level, is  $N$ . The average  $\overline{A} = \sqrt{\pi N}/2$ . Hence, the variance is  $\sigma^2 = \overline{A^2} - \overline{A}^2 = N(1 - \pi/4)$ .

## III. DUAL POSITION DIVERSITY

Given two independent random arrays of the same length  $L$  and having  $N$  elements each, the incoherently averaged side radiation pattern is  $A(u) = 1/2[A_1(u) + A_2(u)]$  where  $A_1(u)$  and  $A_2(u)$  are the component magnitude patterns. We define the peak sidelobe tolerance  $A_0$  as that sidelobe level which will not be exceeded in more than some prespecified fraction of array designs. The probability that a single sample of the random process  $A(u)$  does not exceed  $A_0$  is given by

$$\Pr \left\{ \frac{A_1}{2} + \frac{A_2}{2} \leq A_0 \right\} = \int_0^{A_0} \int_0^{A_0 - y_1} p(y_1, y_2) dy_1 dy_2 \quad (6)$$

where  $y_1 = A_1/2$ ,  $y_2 = A_2/2$  and  $p(y_1, y_2)$  is the joint pdf of the two random variables  $y_1$  and  $y_2$ . Since the element locations of each array are assumed to be chosen independently,  $y_1$  and  $y_2$  are independent random variables. Furthermore, each of them is Rayleigh distributed with mean square value of  $N/4$ . Thus (6) becomes

$$\Pr \{A < A_0\} = \int_0^{A_0} \int_0^{A_0 - y_1} \frac{2y_1}{N/4} e^{-\frac{y_1^2}{N/4}} \cdot \frac{2y_2}{N/4} e^{-\frac{y_2^2}{N/4}} dy_1 dy_2 = 1 - e^{-\frac{A_0^2}{N}} \\ - \sqrt{\pi/2} \left( \frac{2A_0}{\sqrt{N}} \right) e^{-\frac{A_0^2}{N}} \operatorname{erf} \left( \frac{A_0}{\sqrt{N/2}} \right). \quad (7)$$

Equation (7) gives the probability that an arbitrary sample of the averaged side radiation pattern does not exceed  $A_0$ . We are interested in calculating the probability that no such sample will exceed this level: the result of this calculation is the con-

<sup>1</sup> Mutual coupling is excluded. Realistic radiators exhibit nonisotropic radiation patterns which are not identical, and which experience mutual coupling between themselves as well as to the local environment. The effects of these phenomena are beyond the scope of the paper. The interested reader is referred to [7] for discussions of these topics as they pertain to random, thinned arrays.

<sup>2</sup> Another deviation from practical design in this paper is the implicit assumption that the antenna elements may be arbitrary close to each other. As a practical matter, if two randomly chosen antenna locations are spaced by less than the physical size of an antenna element, one of the positions may be eliminated and a new one selected. Provided that the antenna is very large compared to element size, the effect on the statistics of the process can be ignored.

<sup>3</sup> The uniform distribution is the most common distribution of element positions of random arrays [7].

fidence level that accompanies the specification of  $A_0$ . To do this we first sample, conceptually, the side pattern  $n$  times at the minimum interval in  $u$  that assures that the samples are independent. The probability is calculated that none of the  $n$  independent samples exceeds  $A_0$ . The estimate that is obtained is downward biased because, with unity probability, the largest sample falls somewhat below the crest of the largest sidelobe. For  $n$  independent samples

$$\beta = [\Pr(A < A_0)]^n \quad (8)$$

is the probability that none exceeds  $A_0$ . From (7) and (8) we get

$$1 - \beta^{1/n} = e^{-A_0^2/2} + \sqrt{2\pi} B_2 e^{-1/2 B_2^2} \operatorname{erf}(\sqrt{2} B_2) \quad (9)$$

where  $B_2 = A_0^2/N$ . This quantity is an estimate of the peak sidelobe power level, at a level of confidence  $\beta$ , normalized to the number of array elements  $N$ . Note that  $N$  no longer represents the average power level of the resulting side radiation pattern. The average power level has dropped to  $(\pi/8 + 1/2) N$  due to averaging.

The number of independent samples  $n$  of the side radiation pattern for the case of a single random array steered to broadside is given by the array parameter  $n = L/\lambda$  [6], [7]. It is clear that this number will remain the same after the averaging of two independent patterns. For given values of  $L/\lambda$  and  $\beta$ , (9) can be solved numerically for  $B_2$ . In most practical situations where high angular resolution is required and a high confidence level is specified, values of  $n$  and  $\beta$  are such that  $B_2 > 2$  (e.g., for  $L/\lambda = 100$  and  $\beta = 0.9$ ,  $B_2 = 4.25$ ). Thus  $\operatorname{erf}(\sqrt{2} B_2) \approx 1$  and (9) can be simplified to

$$B_2 \approx \frac{1}{2} \ln \left( \frac{\sqrt{2\pi}}{1 - \beta^{1/n}} \right) + \frac{1}{2} \ln B_2 \quad (10)$$

which can be solved numerically for  $B_2$ .

A downward-biased estimator for the peak-sidelobe power normalized to the number of array elements was derived in [6] for the case of a single array (without diversity, which can be called diversity of order one). That quantity was denoted by  $B$ . Here, in the context of diversity, we will identify  $B_1$  with  $B$ . Thus,  $B_1$  is given by [6]

$$B_1 = -\ln(1 - \beta^{1/n}). \quad (11)$$

The bottom row of Table I shows the ratio  $B_1/B_2$  in decibels as a function of array length for a value of the confidence level  $\beta = 0.9$ .

Table I shows that an improvement of 2-2.5 dB in the peak sidelobe response due to dual incoherent element position diversity is possible. This is quite significant since the improvement in peak sidelobe level due to doubling the number of elements in a single array is just 3 dB. A further insight into (10) can be gained if we use (11) to rewrite (10) as

$$B_2 = \frac{1}{2} B_1 + \frac{1}{2} \ln \sqrt{2\pi} + \frac{1}{2} \ln B_2. \quad (12)$$

We note that the term  $1/4 \ln B_2$  is always the order of 0.5. Thus (12) becomes

$$B_2 \approx \frac{1}{2} B_1 + 1. \quad (13)$$

Equation (13) says that the improvement due to dual diversity asymptotically approaches 3 dB as  $B_1$  increases due to an increase in  $L/\lambda$ ,  $\beta$  or both.

In the following section the theory is extended to higher orders

TABLE I  
IMPROVEMENT IN PEAK SIDELobe LEVEL DUE TO DUAL DIVERSITY ( $\beta = 0.9$ )

$L/\lambda$	10	$10^2$	$10^3$	$10^4$	$10^5$
$B_1$	4.36	6.86	9.16	11.46	13.76
$B_2$	3.01	4.25	5.46	6.66	7.86
$10 \log B_1/B_2$	1.8	2.08	2.24	2.36	2.44

of diversity. In the original theory the peak sidelobe level  $A_0^2$  was normalized to the average sidelobe power level, forming the estimator  $B = A_0^2/N$  [6]. Following diversity combining  $N$  is no longer the average sidelobe power level and, therefore,  $B$  loses some of its physical significance. In the following section, we employ two new estimators.  $B_L(M) = B_M/N = A_0^2/N^2$  is a downward-biased estimator for the peak sidelobe normalized to the power of the main beam ( $u = 0$ ). The subscript  $L$  (for lower) indicates that the estimator is biased downward, while  $M$  is the order of diversity.  $B_H(M)$ , similarly defined ( $H$  is for higher), is an upward-biased estimator. It is seen below that the estimators are very close to each other and that the results of simulation experiments fall between them.

#### IV. HIGHER ORDER POSITION DIVERSITY

After  $M$ -fold averaging of independent side radiation patterns, the amplitude distribution changes from Rayleigh to approximately Gaussian ( $M \geq 5$ ). The average values of the two distributions are the same ( $\bar{A} = \sqrt{\pi N}/2$ ), while the variance becomes

$$\sigma_M^2 = \frac{\sigma^2}{M} = \frac{N}{M} (1 - \pi/4). \quad (14)$$

Hence, the resulting pdf takes the form

$$p_M(A) \approx \frac{1}{\sqrt{2\pi}\sigma_M} \exp \left[ -\frac{(A - \bar{A})^2}{2\sigma_M^2} \right], \quad M \geq 5 \quad (15)$$

where  $A$  denotes the  $M$ -fold averaged magnitude of the side radiation pattern. This is depicted in Fig. 2, along with the original Rayleigh distribution.

We follow a strategy similar to that developed in the preceding section. We define  $A_0$  as the peak sidelobe tolerance at a certain confidence level.

Let  $\alpha$  be defined as

$$\begin{aligned} \alpha &= \Pr(A > A_0) = \int_{A_0}^{\infty} p_M(A) dA \\ &= \int_{A_0}^{\infty} \frac{1}{\sqrt{2\pi}\sigma_M} e^{-\frac{(A - \bar{A})^2}{2\sigma_M^2}} dA \\ &= \frac{1}{2} \operatorname{erfc} \left( \frac{A_0 - \bar{A}}{\sqrt{2}\sigma_M} \right). \end{aligned} \quad (16)$$

Equation (16) gives the probability that an arbitrary sample of the average side radiation pattern exceeds the specified peak sidelobe  $A_0$ . The complement of (16),  $1 - \alpha$ , is the probability that such a sample is less than  $A_0$ . Once more, we sample, conceptually, the side radiation pattern at the minimum interval

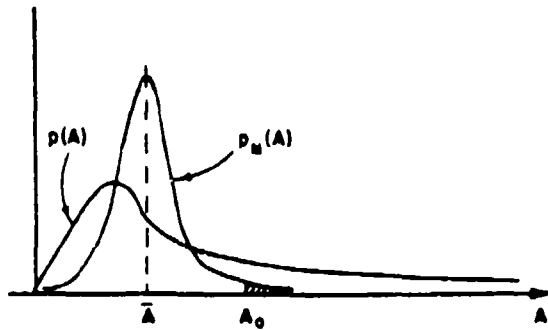


Fig. 2. Probability density function before ( $p(A)$ ) and after ( $p_M(A)$ ) averaging.

in  $u$  for which the samples are independent. For  $n$  such samples

$$\beta = (1 - \alpha)^n = \left[ 1 - \frac{1}{2} \operatorname{erfc} \left( \frac{A_0 - \bar{A}}{\sqrt{2\sigma_M^2}} \right) \right]^n$$

is the probability that none exceeds  $A_0$ . Once more, for large  $\beta$ , a necessary condition for satisfactory system design  $\alpha \ll 1$ , which implies that we can use the approximate expression

$$\operatorname{erfc}(x) \approx \frac{e^{-x^2}}{x\sqrt{\pi}} \quad \text{for } x \gg 1.$$

Thus we obtain

$$\alpha \approx \frac{e^{-b}}{\sqrt{\pi b}}$$

where

$$b = \frac{(A_0 - \bar{A})^2}{2\sigma_M^2} \quad (17)$$

and hence

$$\beta = \left[ 1 - \frac{e^{-b}}{2\sqrt{\pi b}^{1/2}} \right]^n$$

Solving for  $b$

$$b + \frac{1}{2} \ln b = -\ln 2\sqrt{\pi}(1 - \beta^{1/n}) \quad (18)$$

where  $n$  remains  $L/\lambda$ . Equation (18) is solved numerically for  $b$  for given values of  $\beta$  and  $L/\lambda$ . From (14) and (17)

$$b = \frac{M(A_0^2 - 2\bar{A}A_0 + \bar{A}^2)}{2(1 - \pi/4)N} \quad (19)$$

Solving (19) for  $A_0^2/N^2$

$$B_L(M) \triangleq \frac{A_0^2}{N^2} = \frac{1}{N} \left[ \frac{\pi}{4} + \frac{\sqrt{\pi(2 - \pi/2)b}}{\sqrt{M}} + \frac{(2 - \pi/2)b}{M} \right] \quad (20)$$

Equation (20) is one of the main results of this section.  $B_L$  is a downward-biased estimator of the peak sidelobe to main lobe power ratio as a function of diversity order  $M$ .

In Appendix I, we calculate an asymptotic upward-biased estimator of the peak sidelobe to main lobe power ratio. The calculations are based upon the theory of level crossings of random processes and yield the second main result of this section:

$$B_H(M) = \frac{1}{N} \left[ \frac{\pi}{4} + \frac{\sqrt{\pi(2 - \pi/2)b'}}{\sqrt{M}} + \frac{(2 - \pi/2)b'}{M} \right] \quad (21)$$

where  $b'$  is calculated differently (see Appendix I).

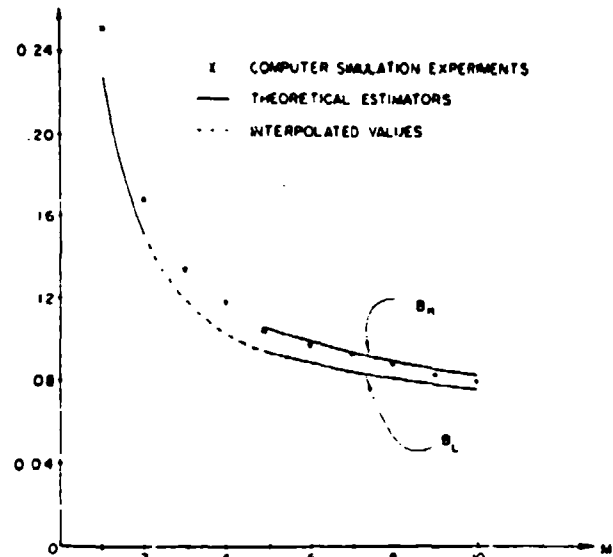


Fig. 3. Peak sidelobe to main lobe power ratio ( $N = 20$ ,  $\beta = 0.9$ ,  $L_e/\lambda = 10$ ), as a function of diversity order  $M$ .

In order to check the validity of (10), (20), and (21), computer simulation experiments were carried out in which a set of 1000 random arrays was formed by generating independent random numbers to represent element positions uniformly distributed throughout the aperture length. In order to get a fairly thinned array, values of  $N = 20$  and  $L/\lambda = 100$  were used. Stationarity was assumed, and side radiation patterns were calculated on a small interval in  $u$  space. Since stationarity is increasingly more valid further from the origin, the interval  $[0.9, 1.0]$  was chosen. For each value of  $M \in [1, 10]$ , 100 experiments were conducted in each of which a different group of  $M$  magnitude patterns (computed in the interval  $[0.9, 1.0]$ ) were averaged and the peak sidelobe found. Empirical cumulative distribution functions of the peak sidelobe level were formed from each set of 100 data points. Points in Fig. 3 represent the normalized level which exceeded the peak sidelobe level of 90 percent ( $\beta = 0.9$ ) of the experiments as a function of  $M$ . Solid curves in Fig. 3 represent theoretical estimates given by (10), (20) and (21), calculated for this value of  $\beta = 0.9$ . In (42), an interval length  $l = 0.1$  was assumed, while in (18), we took  $n = 0.1L/\lambda$ . This makes Fig. 3 correspond to an array of equivalent length  $L_e = 10\lambda$ . We see that all the experimental values fall between  $B_H$  and  $B_L$ , in good agreement with the theories that led to both of them.

Fig. 4 shows  $B_L$  as a function of diversity order  $M$  with  $L/\lambda$  as a parameter. Note that these curves become practically indistinguishable with large  $M$ , unlike the situation without diversity combining. This means that with a fixed number of array elements, element position diversity permits thinning the aperture significantly by increasing array length and thereby improving its resolving power, without deteriorating the peak sidelobe response appreciably.

Fig. 5 shows the improvement in the peak sidelobe level per doubling of the diversity order  $M$  for different values of  $L/\lambda$ .

## V. PRINCIPLES OF FREQUENCY DIVERSITY

There is a basic difference between frequency diversity and element position diversity in the manners in which they influence the images. In the latter case, radiation patterns formed from

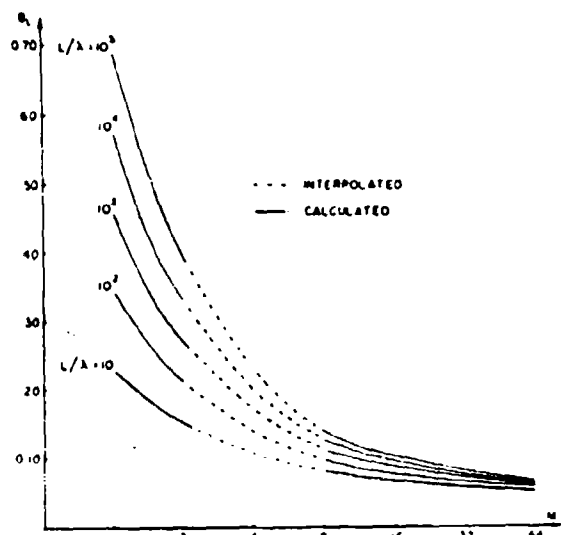


Fig. 4. Downward-biased estimate of the peak sidelobe to main lobe power ratio as a function of diversity order  $M$  ( $N = 20$ ,  $\beta = 0.9$ ).

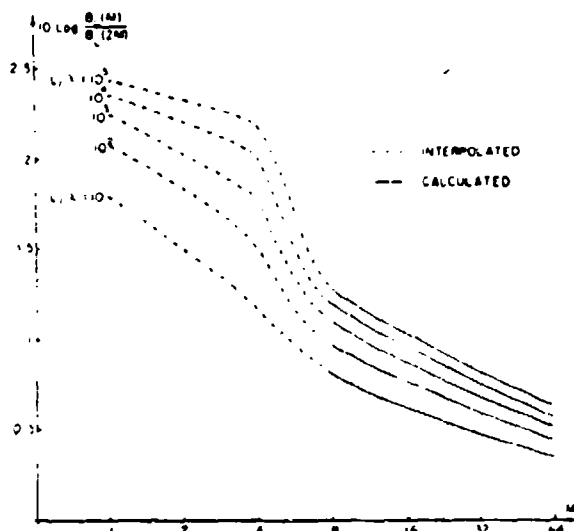


Fig. 5. Improvement in peak sidelobe level per doubling of diversity order ( $\beta = 0.9$ ).

different sets of element positions drawn from the same statistics have nearly identical main lobes and first few sidelobes (depending on the number of elements and the amplitude or density taper employed), while the remaining portions of the side radiation patterns are decorrelated. Radiation patterns obtained at two different frequencies from a single array also exhibit similar properties in the main lobe and first few sidelobes. However, the remainder of the sidelobe pattern does not fully decorrelate with a change of frequency; instead, the correlation progressively decreases with angle from the main lobe at a rate determined by the  $Q$  (reciprocal fractional bandwidth) of the radiation.

The theory presented here is an asymptotic low  $Q$  ( $Q \rightarrow 0$ ) wide-band theory. The earlier monochromatic theory [6], [7] may be considered an asymptotic narrow-band theory ( $Q \rightarrow \infty$ ). The transition region occurs when  $Q$  is in the neighborhood of the array size as measured in units of wavelength. Experi-

mental computer simulations validate the asymptotic theories. Neither theory, however, predicts a peculiar overshoot-under-shoot characteristic which exists in the transition region.

Both coherent and noncoherent combining of the frequency components of a wide-band source can be used to achieve frequency diversity. Coherent combining results when a wide bandwidth signal is radiated. In noncoherent combining the signal constituents are separately radiated, each producing its own radiation pattern, and the resulting power patterns averaged. Frequency hopping is an example of noncoherent frequency diversity. Notwithstanding the intrinsic difference between them, their effects upon the high sidelobes prove to be essentially the same. The peak-to-average sidelobe power-level ratio of a one-dimensional random array is approximately  $\ln n$  plus a small additive term. The array parameter  $n$  of a random array is  $(L/\lambda)(1 + |u_0|)$  where  $u_0 = \sin^{-1} \theta_0$  and  $\theta_0$  is the beamsteering angle measured from the normal to the array [6], [7].  $L/\lambda$  is the order of the number of sidelobes when the radiation is monochromatic and the elements are isotropic. Except for the first few sidelobes, the statistics of the sidelobes are the same everywhere in the pattern.  $L/\lambda$  is approximately the number of independent locations in the side radiation pattern at which the peak sidelobe can occur.

Bandwidth reduces the number of likely locations of the peak. The radiation patterns of a random array at two different wavelengths  $\lambda_1$ ,  $\lambda_2$  will have identical shapes but their abscissa scales differ by the factor  $\lambda_1/\lambda_2$ . Since the abscissa scale of the radiation pattern is linear with frequency, the radiation patterns become progressively different at angles away from the main lobe. If radiation patterns having these characteristics are averaged, the near portion would remain unchanged while in the distant sidelobe region, peaks would reduce and the valleys would fill in. The largest sidelobe, therefore, would, after averaging, most likely fall in the near-sidelobe region. By reducing the extent of the visible region in which the largest sidelobe is likely to occur, the effective array parameter  $n$  is also reduced. Since the peak sidelobe is approximately proportional to  $\ln n$ , the sidelobe level is also reduced.

An initial estimate of the extent of the reduction in the array parameter is made by calculating the number of lobes of the radiation pattern which occur before the two patterns have slipped by the order of one-half to one lobe. Because sidelobes are nominally spaced by one beamwidth, the  $p$ th sidelobe at  $\lambda = \lambda_1$  occurs approximately at angle  $p\lambda_1/L$ . At the same angle the sidelobe number at  $\lambda = \lambda_2$  is  $(p\lambda_1/L)/(\lambda_2/L) = p\lambda_1/\lambda_2$ .

The angle  $u_p$  at which the number of lobes at  $\lambda_1$  and  $\lambda_2$  differ by, say,  $1/2$  or  $1$  defines the transition between the portions of the radiation patterns which are nearly the same ( $u < u_p$ ). The approximate number of lobes within this region is found by equating  $p + 1/2$  or  $p + 1$  to  $p\lambda_1/\lambda_2$ , from which  $p \approx Q/2$  or  $Q$  where  $Q$  is the reciprocal of the fractional bandwidth.

The number  $p$  is the number of sidelobes left relatively unchanged by widening the spectral width of the radiation, while the remainder of the radiation pattern tends to be smoothed toward the average sidelobe level. The array parameter  $n$  reduces from approximately  $L/\lambda$  to approximately  $Q$ . Hence, the power ratio of the peak sidelobe to the average sidelobe, minus a small additive constant, becomes approximately  $\ln Q$  rather than  $\ln (L/\lambda)$ . In general, the signal spectrum will consist of more than two frequency components. Although the highly

correlated sidelobe region is not clearly defined in the general case, we still expect  $n$  to be proportional to  $Q$ , i.e.,  $n = \alpha Q$  where  $\alpha$  depends on the spectrum shape and lies in the neighborhood of unity. Therefore  $\ln \alpha$  will contribute to the additive constant. Computer simulation experiments verify the linear relationship between the peak sidelobe level and  $\ln Q$ .

## VI. COHERENT COMBINING

The argument above generally pertains both to coherent and noncoherent combining. The detailed correlations between radiation patterns at different frequencies differ for the two cases, and are now developed.

The manner in which the sidelobe radiation patterns decorrelate with frequency can be calculated from the cross correlation function of two patterns at two different frequencies. The frequencies are distinguished in the equations below by subscripts 1 and 2:

$$R_{12} = E(F_1 F_2^*) = NE\{e^{-j\Delta\omega x u/c}\} + (N^2 - N) \cdot E\{e^{j\omega_0 x u/c}\}E\{e^{-j(\omega_0 + \Delta\omega)x u/c}\} \quad (22)$$

where  $f_0 = \omega_0/2\pi$  is either one of the frequencies and  $\Delta f = \Delta\omega/2\pi$  is the frequency separation. Let  $x$  be distributed uniformly in the interval  $[-L/2, L/2]$ . Then

$$E\{e^{-j\Delta\omega x u/c}\} = \frac{1}{L} \int_{-L/2}^{L/2} e^{-j\Delta\omega x u/c} dx = \frac{\sin(\Delta\omega Lu/2c)}{\Delta\omega Lu/2c}$$

and hence we get

$$R_{12} = N \frac{\sin(\Delta\omega Lu/2c)}{\Delta\omega Lu/2c} + (N^2 - N) \frac{\sin(\omega_0 Lu/2c)}{\omega_0 Lu/2c} \cdot \frac{\sin[(\omega_0 + \Delta\omega)Lu/2c]}{(\omega_0 + \Delta\omega)Lu/2c} \quad (23)$$

For a low density array  $N \ll L/\lambda$  and a high  $Q$  ( $\omega_0 \gg \Delta\omega$ ); the second term in (23) is much smaller than the first one for values of  $u$  a few beamwidths away from the main lobe. Then

$$R_{12} \approx N \frac{\sin(\Delta\omega Lu/2c)}{\Delta\omega Lu/2c} \quad (24)$$

and the patterns are decorrelated when

$$\Delta\omega Lu/2c = \pi \quad (25)$$

for then  $R_{12} = 0$ . Equation (25) can be written in terms of the frequency separation required to achieve decorrelation at and beyond a given value of  $u$

$$\Delta f = \frac{\Delta\omega}{2\pi} = \frac{c}{Lu} = \frac{f\lambda}{Lu} \quad (26)$$

or in terms of the  $Q$  of the microwave source

$$Q = \frac{f}{\Delta f} = \frac{Lu}{\lambda} \quad (27)$$

In (27)  $u$  is the angle beyond which the sidelobe patterns are decorrelated and  $u/(1 + |u_0|)$ ,  $u_0$  = beamsteering angle, is the fraction of the visible region in which the sidelobes are not de-

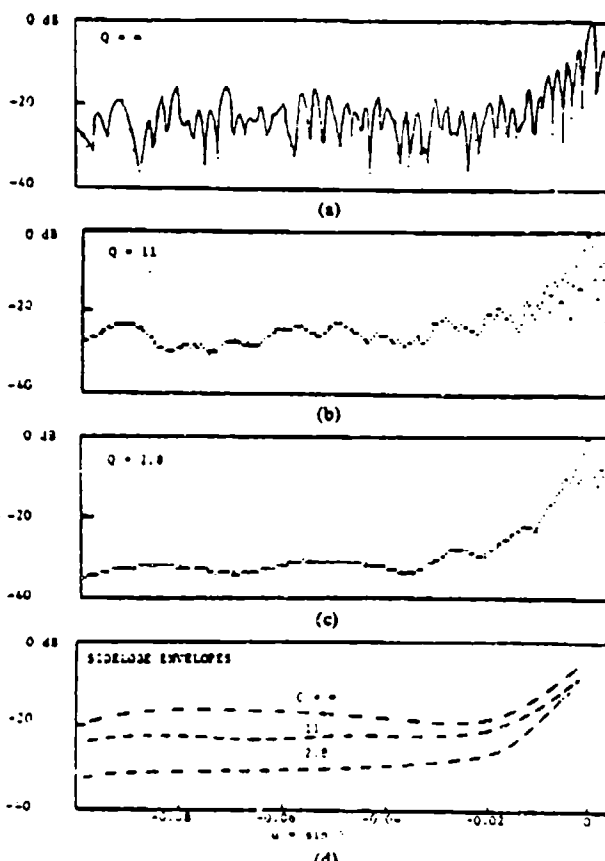


Fig. 6. Effect of bandwidth on side radiation pattern. 800 wavelength random array. 200 elements.

correlated. Since the array parameter with monochromatic radiation is  $n = (L/\lambda)/(1 + |u_0|)$ , the effective or reduced array parameter

$$n' = n \frac{u}{1 + |u_0|} = \frac{Lu}{\lambda} = Q \quad (28)$$

and the power ratio of the peak sidelobe to the average level, minus some small additive constant becomes approximately  $\ln Q$ . Thus both calculations lead to the same result.

It is evident that large bandwidth is helpful in reducing the peak sidelobe by reducing the array parameter. However, the payoff is relatively slow because of the logarithmic relation between PSL and the array parameter  $n$ . For example, the expected value of PSL/ASL of a narrow-band random array in which the aperture size  $L = 10^3 \lambda$  is 13.5 (calculated from [6] or [7]). If the signal bandwidth is increased to 1 percent of the carrier frequency ( $Q = 100$ ), the expected value of the peak drops to 6.6, a reduction of 3 dB. A further broadening of the bandwidth by a factor of 10 reduces PSL only by another 2 dB.

Fig. 6 shows the effect of bandwidth upon a thinned, random array. The radiation patterns are of a 200 element linear random array 800 wavelengths long for three different signal bandwidths. In Fig. 6(a) the signal is monochromatic while the  $Q$  in Fig. 6(b) is 11 and in Fig. 6(c) it is 2.8. The ragged sidelobe behavior of Fig. 6(a) nearly disappears when the  $Q$  is lowered to that of Fig. 6(c). The reduction in the sidelobe envelope is evident in the composite plot shown in Fig. 6(d). Although we are mainly interested in the reduction of the high sidelobes which occur

in the near sidelobe region, it is worthwhile to notice that the average level of the distant sidelobes has also reduced appreciably.

## VII. NONCOHERENT COMBINING

The alternative to coherent utilization of the entire spectrum of the signal is noncoherent frequency diversity combining, which generally is a more practical technique. This is because wide-band frequency-hopping generators are more common than broad-band generators of modulated microwave waveforms. The available waveform is a succession of narrow-band signals (such as RF pulses) at frequencies  $f_1, f_2, \dots$ , and  $f_M$ . The receiving system images on each pulse and then superimposes the images.

The frequency separation  $\Delta f$  which results in independence in the sidelobe region may be calculated from the cross correlation function as was done above for the wideband signal waveform. However, the cross correlation must be calculated between the power patterns at the two frequencies rather than the complex radiation patterns. As is seen below, decorrelation occurs at the same frequency separation as for coherent frequency diversity.

Writing the radiation pattern as the sum of two quadrature, frequency-dependent components  $a(u) + jb(u)$ , the power pattern is

$$p(u) = a^2(u) + b^2(u). \quad (29)$$

The correlation function between patterns with different wave-numbers is (dropping the angular variable)

$$\begin{aligned} R_{12} &= E\{p(k_1)p(k_2)\} = E\{a^2(k_1)a^2(k_2)\} \\ &\quad + E\{a^2(k_1)b^2(k_2)\} + E\{b^2(k_1)a^2(k_2)\} \\ &\quad + E\{b^2(k_1)b^2(k_2)\}. \end{aligned} \quad (30)$$

Since  $a$  and  $b$  are Gaussian, the fourth moment theorem

$$\begin{aligned} E\{x_1 x_2 x_3 x_4\} &= E\{x_1 x_2\}E\{x_3 x_4\} + E\{x_1 x_3\}E\{x_2 x_4\} \\ &\quad + E\{x_1 x_4\}E\{x_2 x_3\} - 2\mu_1 \mu_2 \mu_3 \mu_4 \end{aligned} \quad (31)$$

is applied and with assumptions similar to those made for the coherent case, we get

$$R_{12} \approx N^2 \left( 1 + \left[ \frac{\sin(\Delta\omega L u / 2c)}{\Delta\omega L u / 2c} \right]^2 \right). \quad (32)$$

The constant additive term is the square of the nonzero mean of the power pattern and plays no part in the decorrelation of the pattern with frequency. The second term is the square of (24). Hence the power patterns become decorrelated at the same frequency separation that decorrelates the complex radiation pattern, namely that value given by (26).

The equivalence between coherent combining (wideband waveform) when a square law detector is employed and noncoherent combining (frequency hopping) of spectral components is established from a waveform analysis. Let  $u(t)$  be the waveform radiated from a source at  $u = u_0$ . The wave received at the  $n$ th element is  $u(t + t_n)$  where  $t_n = x_n u_0 / c$  is the differential travel time from the source. Let  $T_n = x_n u / c$  be the steering delay for the  $n$ th element for the arbitrary steering direction  $u$ . The array output following square law detection and integration is

$$p(u; u_0) = \int \sum_{m=1}^N \sum_{n=1}^N u(t + t_m - T_m) u^*(t + t_n - T_n) dt. \quad (33)$$

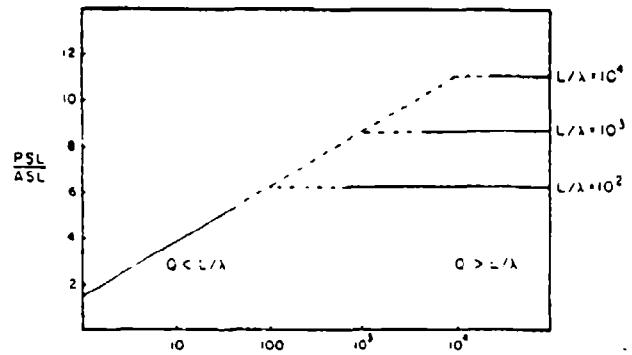


Fig. 7. Expected asymptotic peak sidelobe behavior as a function of the fractional signal bandwidth ( $Q^{-1}$ ) and array size ( $L/\lambda$ ).

Let  $V(\omega) = F\{u(t)\}$  be the Fourier spectrum of  $u(t)$ . By Parseval's theorem (33) equals

$$p(u; u_0) = \frac{1}{2\pi} \int \sum_m \sum_n |V(\omega)|^2 e^{j\omega(t_m - T_m - t_n + T_n)} d\omega. \quad (34)$$

The exponential term is recognized as the wide-band equivalent of the monochromatic function  $\exp[jk(x_n - x_m)(u - u_0)]$ ; as in the monochromatic theory, the double sum of that function is the power pattern. Thus

$$p(u; u_0) = \frac{1}{2\pi} \int |V(\omega)|^2 |F(u - u_0; \omega)|^2 d\omega \quad (35)$$

in which  $|F|^2$  is the power pattern at frequency  $\omega$  when the array is steered to  $u_0$ .

Now let

$$V(\omega) = V_0 \sum_{g=-G/2}^{G/2} \delta(\omega - \omega_0 - g\omega_\Delta). \quad (36)$$

The radiation consists of  $G + 1$  spectral lines spaced by  $\omega_\Delta$  occupying a band  $W = G\omega_\Delta$ . Then

$$p(u; u_0) \propto V_0^2 \sum_{g=-G/2}^{G/2} |F(u - u_0; \omega_0 + g\omega_\Delta)|^2. \quad (37)$$

Equation (37) is the sum of  $G + 1$  power patterns, which is exactly the same output obtained when the spectral lines are radiated sequentially. Thus simultaneous transmission (wide-band signal) followed by square law detection and integration, and sequential transmission (frequency hopping), result in the same system output.

Since both coherent and noncoherent frequency diversity combining exhibit similar decorrelation properties, a single test of the theory suffices. Fig. 7 shows the predicted asymptotic behavior as a function of  $Q$ . The ordinate is the power ratio of the peak-to-average sidelobe level. The abscissa is logarithmic in  $Q$ . When  $Q < L/\lambda$  the curve should rise linearly with  $\ln Q$  and be independent of  $L/\lambda$ . In the high  $Q$  region the curves should be independent of  $Q$  and should be spaced by  $\ln(L/\lambda)$ . Note that Fig. 7 is independent of  $N$ . This should be approximately the case for  $5 < N < L/\lambda$ . The lower limit is required for the applicability of the central limit theorem which was used to derive the statistics of the side radiation pattern. The upper limit insures that the array is thinned enough so that the stationary part of the side radiation pattern extends to most of the  $u$ -space.

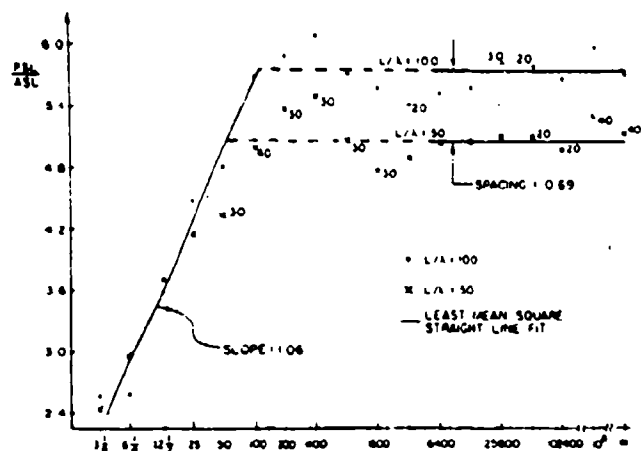


Fig. 8. PSL/ASL versus  $Q$  in computer simulation frequency hopping experiment. Each datum point is the average of 10 samples (unmarked) or 20-40 samples (as indicated).  $N = 30$ ,  $\beta = 0.5$ .

The results of many frequency-hopping simulation experiments for  $L/\lambda = 50$  and  $100$  are shown in Fig. 8. The expected asymptotic behavior is evident. The slope of the portion linear with  $\ln Q$  in the low  $Q$  region is  $1.06$ , in close agreement with theory, which predicts a slope approximately equal to unity. In the high- $Q$  region the asymptotic spacing, based on linear least mean squares fits to the data points, is  $0.69$ , which exactly equals the predicted spacing of  $\ln(100/50)$ . The central region exhibits an overshoot-undershoot characteristic which cannot be predicted from the asymptotic theory.

### VIII. CONCLUSION

Element position diversity is shown to be useful in reducing the peak sidelobe level of random arrays. Dual diversity reduces the peak sidelobe by 2 to 2.5 dB. The improvement grows with antenna size. The asymptotic improvement is 3 dB, which is exactly the improvement that would be obtained by coherent combining of the signals received by both antennas. Thus the process is asymptotically efficient. For higher orders of diversity, the peak sidelobe approaches the average sidelobe power level. Two closely spaced asymptotic estimators have been derived, one downward-biased and the other upward-biased. The two estimators bound the computer simulation results. The derived expressions are valid whenever the diversity order  $M$  is greater than or equal to five.

Wide-band frequency diversity also reduces the high sidelobe level of the random, thinned array. The behavior of the peak sidelobe level is found to be similar under both coherent and non-coherent frequency diversity. An important difference between them, however, is that coherent combining reduces the average level of the distant sidelobes as well. In monochromatic theory, the peak sidelobe power level is found to be proportional to  $\ln L/\lambda$  plus a small constant. The theory developed in this paper shows that the peak sidelobe power level is proportional to  $\ln Q$  plus another small constant when  $Q < L/\lambda$ . (The proportionality constant in both cases is  $N^{-1}$  where  $N$  is the number of elements.  $Q$  is the reciprocal fractional bandwidth and  $L/\lambda$  is the array size in units of wavelengths.) Thus the peak sidelobe level first rises logarithmically with  $Q$  and then asymptotes to a value determined by array size and number of elements. The transition takes place in the neighborhood of  $Q \approx L/\lambda$ .

Simulation experiments confirm both asymptotic theories

( $Q \rightarrow 0$  and  $Q \rightarrow \infty$ ). An overshoot-undershoot phenomenon occurs in the transition region unaccounted for by either theory.

### APPENDIX I

#### AN ASYMPTOTIC UPWARD-BIASED ESTIMATE

In this appendix, an asymptotic upward-biased estimator is calculated based on the theory of level crossings of random processes. The expected number of upcrossings of a certain level by the random process  $A(u)$  is first calculated, then a relation is established between this quantity and the probability that the process will remain below that particular level. This will lead to the definition of our estimator.

As noted before, except for a few beamwidths centered around the main beam, the side radiation pattern of a thinned random array can be considered a stationary random process. After  $M$ -fold incoherent averaging of independent side radiation patterns, the amplitude distribution changes from Rayleigh to approximately Gaussian of mean  $\bar{A} = \sqrt{\pi N/2}$  and variance  $\sigma_a^2 = N(1 - \pi/4)/M$ . In an interval of length  $l$ , the expected number of upcrossings of the level  $A_0$  by the random process  $A(u)$  is given by [13]

$$E\{U_{A_0}\} = l \int_0^\infty |A'| p(A_0, A') dA' \quad (38)$$

where  $p(A, A')$  is the joint pdf of the random variables  $A(u)$  and  $A' = dA(u)/du$ . Since differentiation is a linear operation,  $A(u)$  will also be approximately Gaussian; furthermore, since a stationary random process and its derivative are uncorrelated [14],  $A(u)$  and  $A'(u)$  are independent. Thus we can write

$$p(A, A') = p_a(A) \cdot p_a'(A') \\ = \frac{1}{2\pi\sigma_a\sigma_{a'}} \exp \left[ -\left( \frac{(A - \bar{A})^2}{2\sigma_a^2} + \frac{A'^2}{2\sigma_{a'}^2} \right) \right] \quad (39)$$

where  $\sigma_{a'}^2$  is the variance of the Gaussian random variable  $A'$ . Substituting (39) in (38) and performing the integration we get

$$E\{U_{A_0}\} = \frac{l}{2\pi} \cdot \frac{\sigma_{a'}}{\sigma_a} \exp \left[ -\frac{(A_0 - \bar{A})^2}{2\sigma_a^2} \right] \quad (40)$$

Substituting  $\sigma_a^2 = N(1 - \pi/4)/M$  in (40) and solving for  $A_0^2/N^2$  we obtain

$$B_H(M) \triangleq \frac{A_0^2}{N^2} = \frac{1}{N} \left[ \frac{\pi}{4} + \frac{\sqrt{\pi(2 - \pi/2)b'}}{\sqrt{M}} + \frac{(2 - \pi/2)b'}{M} \right] \quad (41)$$

where

$$b' = \ln \left[ \frac{l}{2\pi(1 - \beta)} \cdot \frac{\sigma_{a'}}{\sigma_a} \right] \quad (42)$$

and

$$\beta \triangleq 1 - E\{U_{A_0}\}. \quad (43)$$

Since we are interested in the peak of the process, we consider only levels  $A_0$  which are high with respect to the expected value of  $A(u)$ . It is shown in [15], [11], and [17] that for such high levels, the expected number of local maxima above  $A_0$  approaches the expected number of upcrossings of  $A_0$ . Also, [11] shows that the expected value  $E\{U_{A_0}\}$  of the number of upcrossings in the sidelobe region is an upper bound on the probability  $P\{U_{A_0} \geq 1\}$  of at least one upcrossing of  $A_0$  in the same region. In order to show this, let  $P_k$  be the probability of exactly  $k$  upcrossings of  $A$ . Thus  $E\{U_{A_0}\} = \sum_{k=0}^\infty k P_k$ , and

$P(U_{A_0} > 1) = \sum_{k=1}^{\infty} P_k$ . Therefore,  $P(U_{A_0} > 1) < E(U_{A_0})$  and  $E(U_{A_0})$  is an upperbound on  $P(U_{A_0} > 1)$ . We expect that this bound becomes tight for small values of  $E(U_{A_0})$  because, in this case, the probability of obtaining more than one upcrossing in the sidelobe region is negligible compared to the probability of obtaining zero or one upcrossing [11]. Also, it is clear that  $\beta \geq P(U_{A_0} = 0)$ , which is the probability that the process will remain below the level  $A_0$ , and we expect the two sides of the inequality to become very close to each other for values of  $\beta$  close to unity.

From (41) and (42), we see that  $B_H$  is a monotonically increasing function of  $\beta$ . Thus, if we define  $\beta' = P(U_{A_0} = 0)$  then the corresponding normalized level  $B'_H$  will satisfy  $B'_H < B_H$  since  $\beta' < \beta$ . Thus,  $B_H$  is always an upward biased estimate of  $B'_H$ .

Next we turn to the problem of calculating the ratio  $\sigma_a'/\sigma_a$  in (42). The variance of  $A'(u)$  is  $\sigma_a'^2 = -R_a''(0)$  where  $R_a''(u) = d^2 R_a(u)/du^2$  is the second derivative of the autocorrelation function of  $A(u)$  [16]. Also, since differentiation is a linear operation, it is clear that  $\sigma_a'^2 = K^2 \sigma_a^2$  where  $K^2$  is a constant of proportionality. Since a closed form expression for  $R_a(u)$  in the case of incoherent averaging is not available, simulation experiments were conducted to determine the constant  $K$  for an assumed uniform distribution of element positions. A value of  $K = 2.77 L/\lambda$  was found (see Appendix II). Since  $A(u)$  is the average of  $M$  amplitude patterns, each of which is symmetric around  $u = 0$ , then  $A(u)$  is also symmetric and it is sufficient to consider the range  $u \in [0, 1]$ . As noted before, for a thinned array, the stationary part of the side radiation pattern starts a few beamwidths from the origin; thus  $l$  in (42) can be written as  $l = 1 - \alpha\lambda/L$  where  $\alpha$  is a number the order of three. Also for most practical applications  $\lambda/L \ll 1$ , and we can take  $l \approx 1$ .

Equation (41) is the main result of this appendix. For a given confidence level  $\beta$ , it gives an upward-biased estimate of the power ratio of the peak sidelobe to the main lobe as a function of diversity order  $M$ .

## APPENDIX II EVALUATING THE CONSTANT $K$

The ratio  $K = \sigma_a'/\sigma_a$  in (40) was found through computer simulation experiments. Use has been made of the relation  $\sigma_a'^2 = -R_a''(0)$ . For the  $M$ -fold averaged process  $A(u) = 1/M \sum_{i=1}^M A_i(u)$ , the autocorrelation function is

$$\begin{aligned} R_a(u_1, u_2) &= E(A(u_1)A(u_2)) \\ &= \frac{1}{M^2} E\left\{\left(\sum_{i=1}^M A_i(u_1)\right)\left(\sum_{j=1}^M A_j(u_2)\right)\right\} \\ &= \frac{1}{M} R(u_1, u_2) + \left(1 - \frac{1}{M}\right) \overline{A(u_1)A(u_2)}, \end{aligned}$$

where  $\overline{A(\cdot)}$  is the expected value of any of the  $M$  independent magnitude patterns. We assume  $u_1, u_2 > \lambda/L$  and  $L/\lambda \gg 1$ , implying that the processes are stationary and  $R(u_1, u_2) = R(u)$  where  $u = u_1 - u_2$ . Also  $\overline{A(u_1)A(u_2)} = \sqrt{\pi N}/2 \approx \text{constant}$ . Thus we get

$$\begin{aligned} R_a''(u) &= \frac{1}{M} R''(u) \\ \text{and} \\ \sigma_a'^2 &= -\frac{1}{M} R''(0). \end{aligned} \quad (44)$$

but since

$$\sigma_a^2 = \frac{1}{M} \sigma^2, \quad (45)$$

we obtain

$$\frac{\sigma_a'^2}{\sigma_a^2} = -\frac{R''(0)}{\sigma^2}. \quad (46)$$

Thus the ratio  $\sigma_a'/\sigma_a$  is not a function of  $M$ . Also, it is easy to see that this ratio does not depend on  $N$ . Equation (46) is the basis for the simulation experiments. Fixing  $L/\lambda$ , the  $u$ -space autocorrelation function was calculated for several 20 element arrays; attention was focused on the region around the origin. The outcomes of 10 experiments were averaged and the resulting autocorrelation function was used to calculate  $K = \sigma_a'/\sigma_a$  through (46), where a sixth-order polynomial was used to fit the data and approximate  $R(u)$ . The above was repeated for eight different values of  $L/\lambda$ . A regression procedure yielded the value  $K = 2.77 L/\lambda$ .

## REFERENCES

- [1] E. J. Baghdady, Ed., *Lectures on Communication System Theory*. New York: McGraw-Hill, 1961.
- [2] P. F. Panter, *Communication System Design: Line-of-Sight and Troposcatter Systems*. New York: McGraw-Hill, 1972.
- [3] M. Schwartz, W. R. Bennett, and S. Stein, *Communication Systems and Techniques*. New York: McGraw-Hill, 1966.
- [4] R. S. Berkowitz, *Modern Radar*. New York: Wiley, 1965.
- [5] W. F. Gabriel, "Spectral analysis and adaptive array superresolution techniques," *Proc. IEEE*, vol. 68, pp. 654-666, June 1980.
- [6] B. D. Steinberg, "The peak sidelobe of the phased array having randomly located elements," *IEEE Trans. Antennas Propagat.*, vol. AP-20, Mar. 1972.
- [7] —, *Principles of Aperture and Array System Design*. New York: Wiley, 1976.
- [8] E. Yadin-Jadlovker, "Phase synchronizing distributed, adaptive airborne antenna arrays," Ph.D. dissertation, Univ. Pennsylvania, 1981.
- [9] B. D. Steinberg and E. Yadin, "Radio camera experiment with airborne radar data," *Proc. IEEE*, vol. 70, pp. 96-98, Jan. 1982.
- [10] —, "Distributed airborne array concepts," *IEEE Trans. Aerosp. Electron. Syst.*, vol. AES-18, no. 2, pp. 219-227, Mar. 1982.
- [11] M. B. Donvito and S. A. Kassam, "Characterization of the random array peak sidelobe," *IEEE Trans. Antennas Propagat.*, vol. AP-27, May 1979.
- [12] J. B. Thomas, *An Introduction to Statistical Communication Theory*. New York: Wiley, 1969.
- [13] I. F. Blake and W. C. Lindsey, "Level crossing problems for random processes," *IEEE Trans. Inform. Theory*, vol. IT-19, pp. 295-315, May 1973.
- [14] R. E. Ziemer and W. H. Tranter, *Principles of Communications*. Boston, MA: Houghton Mifflin, 1976.
- [15] S. O. Rice, "The mathematical analysis of random noise," *Bell Systems Tech. J.*, vol. 23, pp. 282-332, 1944, and vol. 24, pp. 46-156, 1945.
- [16] A. Papoulis, *Probability, Random Variables and Stochastic Processes*. New York: McGraw-Hill, 1965.
- [17] L. G. Sodin, "Statistical analysis of nonequidistant linear antenna arrays," *Radio Eng. Electron. Phys.*, vol. 11, pp. 1715-1720, Nov. 1966.

Bernard D. Steinberg (S'48-A'50-SM'64-F'66), for a biography please see page 748 of the September 1981 issue of this TRANSACTIONS.



Elsayed H. Attia (S'83) was born in Zagazig, Egypt, on November 14, 1954. He received the B.Sc. and M.Sc. degrees in electrical engineering from Cairo University, Egypt, in 1977 and 1979, respectively.

Since 1980, he has been enrolled in the Ph.D. program at the Moore School of Electrical Engineering, University of Pennsylvania, Philadelphia. He is now with the Valley Forge Research Center group, working on microwave imaging projects.